Nanogenerators

for Self-powered Devices and Systems

Zhong Lin Wang

School of Materials Science and Engineering
Georgia Institute of Technology, Atlanta GA USA

(first edition, June 2011)

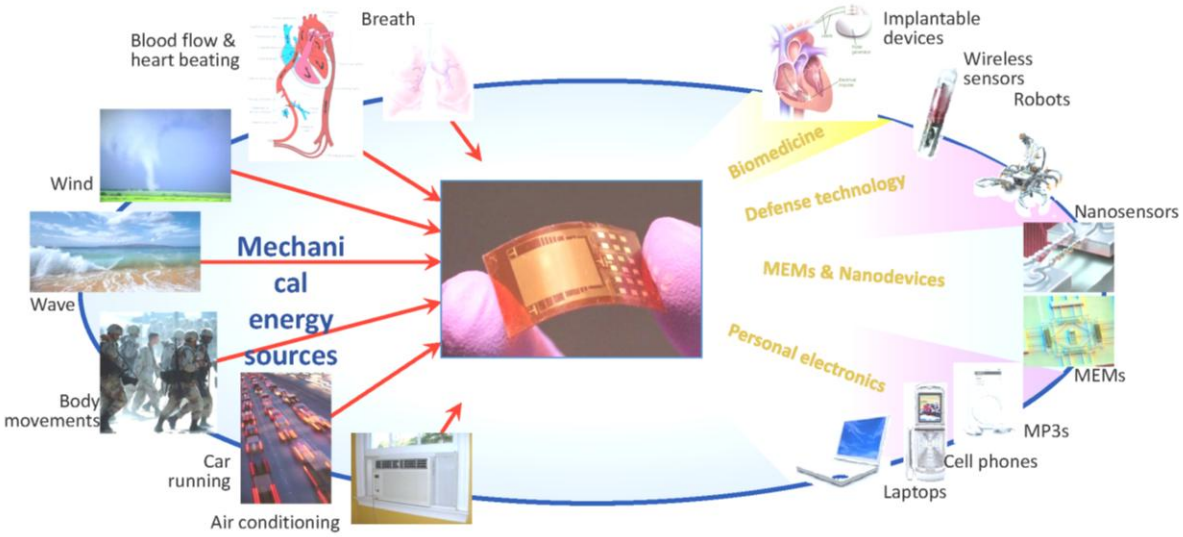

Published by

Georgia Institute of Technology, Atlanta, USA

SMARTech digital repository, 2011.

Site for down load: http://hdl.handle.net/1853/39262

ISBN 978-1-4507-8016-2

Preface

Ever since we demonstrated the first *nanogenerators* using piezoelectric nanowires for converting mechanical energy into electricity (Wang & Song, *Science*, 312, 242-246 (2006)), a great interest has been excited worldwide for developing various approaches for energy harvesting. A key idea presented in the 2006 paper is the *self-powered nanotechnology*, aiming at powering nanodevices/nanosystems using the energy harvested from the environment in which the systems are suppose to operate. We have published a series of papers during a period of 6 years covering the basic theory, mechanism, engineering scale up and potential applications of nanogenerators (see Appendix). To provide a comprehensive and coherent review about the development of nanogeneratos, I have organized this book based on our published papers. The readers are encouraged to referring to the original papers for details and citations.

While authoring this book, I decide to use a new format of distribution. Instead of selling hard copies, I like to distribute this book free of charge through the internet so that it can benefit a wider range of readers. Although the readers may free download this book and use it for non-commercial purposes, we own the copyright of the book and preserve the right of making any revisions and changes. The official publisher of the book is Georgia Institute of Technology.

Please use the following phrase if one cites this book in official publications: Zhong Lin Wang, *Nanogenerators for self-powered devices and systems*, Georgia Institute of Technology, SMARTech digital repository, 2011 (http://hdl.handle.net/1853/39262).

Finally, I like to thank my group members and collaborators who contributed to the development of nanogenerators and piezotronics (not in particular order): Jinhui Song, Xudong Wang, Rusen Yang, Yong Qin, Jun Zhou, Youfan Hu, Sheng Xu, Yaguang Wei, Yong Ding, Puxian Gao, Jr-Hau He, Peng Fei, Yan Zhang, Jin Liu, Will Hughes, Zhou Li, Yifan Gao, Wenzhuo Wu, Qing Yang, Guang Zhu, Zetang Li, Changshi Lao, Ming-Pei Lu, Cheng Li, Chen Xu, Ben Hansen, Yi-Feng Lin, Giulia Mantini, Shisheng Lin, Joon Ho Bae, Minbaek Lee, Chi-Te Huang, Sihong Wang, Ying Liu, Zhiyuan Gao, Yudong Gu, Jung-il Hong, Yolande Berta, Yue Zhang, Robert Snyder, Lih-J. Chen, S.-Y. Lu, Li-Jen Chou, Aurelia Wang and many others. We acknowledge generous financial support from DARPA, NSF, DOE, NASA, Airforce, NIH, Samsung, MANA NIMS, Chinese Academy of Sciences and Chinese Scholars Council. I like to thank Georgia Tech and the Center for Nanostructure Characterization (CNC) for support in facility and infrastructure.

Lastly and most importantly, I thank my wife and our daughters for their years support and understanding. It was not been possible to carry out such a research without their support.

Zhong Lin (Z.L.) Wang
Georgia Institute of Technology, USA
e-mail: zlwang@gatech.edu
Personal website: http://www.nanoscience.gatech.edu/zlwang/

About the author

Dr. Zhong Lin (ZL) Wang is the Hightower Chair in Materials Science and Engineering, Regents' Professor, Engineering Distinguished Professor and Director, Center for Nanostructure Characterization, at Georgia Tech. Dr. Wang is a foreign member of the Chinese Academy of Sciences, member of European Academy of Sciences, fellow of American Physical Society, fellow of AAAS, fellow of Microscopy Society of America and fellow of Materials Research Society. He has received the 2001 S.T. Li prize for Outstanding Contribution in Nanoscience and Nanotechnology, the 1999 Burton Medal from Microscopy Society of America, and the 2009 Purdy award from American ceramic society.

Dr. Wang has made original and innovative contributions to the synthesis, discovery, characterization and understanding of fundamental physical properties of oxide nanobelts and nanowires, as well as applications of nanowires in energy sciences, electronics, optoelectronics and biological science. His discovery and breakthroughs in developing nanogenerators establish the principle and technological road map for harvesting mechanical energy from environment and biological systems for powering a personal electronics. His research on self-powered nanosystems has inspired the worldwide effort in academia and industry for studying energy for micro-nano-systems, which is now a distinct disciplinary in energy research and future sensor networks. He coined and pioneered the field of piezotronics and piezo-phototronics by introducing piezoelectric potential gated charge transport process in fabricating new electronic and optoelectronic devices. This breakthrough progress has important applications in smart MEMS/NEMS, nanorobotics, human-electronics interface and sensors. Wang also invented and pioneered the *in-situ* technique for measuring the mechanical and electrical properties of a single nanotube/nanowire inside a transmission electron microscope (TEM). Dr. Wang entire publications have been cited for over 43,000 times by July, 2011. The H-index of his citations is 100. Details can be found at: http://www.nanoscience.gatech.edu/zlwang

List of Contents

Nanogenerators for Self-powered Devices and Systems

Chapter 1

Introduction

1.1. Powering of nanodevices

With the threatening of global warming and energy crises, searching for renewable and green energy resources is one of the most urgent challenge to sustainable development of human civilization [1, 2]. At the large-scale, besides the well known energy resources that power the world today, such as petroleum, coal, hydraulic, natural gas and nuclear, active research and development are being taken in exploring alternative energy resources such as solar, geothermal, biomass, nuclear, wind, and hydrogen. At a much smaller scale, energy and technologies are desperately needed for independent, sustainable, maintain-free and continuous operations of implantable biosensors, ultrasensitive chemical and biomolecular sensors, nanorobotics, micro-electromechanical systems, remote and mobile environmental sensors, homeland security and even portable/wearable personal electronics. A nanorobot, for example, is proposed to be a smart machine that may be able to sense and adapt to the environment, manipulate objects, taking actions and perform complex functions, but a key challenge is to find a power source that can drive the nanorobot without adding much weight. An implanted wireless biosensor, for example, requires a power source, which may be provided directly or indirectly by charging of a battery. In general, the size of the battery is much larger than the size of the nanodevices, which largely dictates the size of the entire system.

The near future research is the integration of multi-functional nanodevices into a nanosystem so that it can function as a living species with capabilities of sensing, controlling, communicating and actuating/responding. A nanosystem is composed of not only nanodevices but also nano-power-source (or nano-battery). But the small size of the nano-battery largely limits the life-time of the battery. It is highly desired for wireless devices and even required for implanted biomedical systems to be self-powered without using battery, which not only can largely enhance the *adaptability* of the devices but also greatly reduce the size and weight of the system. Therefore, it is desperate to develop nanotechnology that harvests energy from the environment for self-powering these nanodevices.[3] The goal for nanotechnology is to build self-powered nanosystems that exhibit ultrasmall size, supersensitivity, extraordinary multi-functionality and extremely low power consumption. As a result, the energy harvested from the environment may be sufficient to power the system.

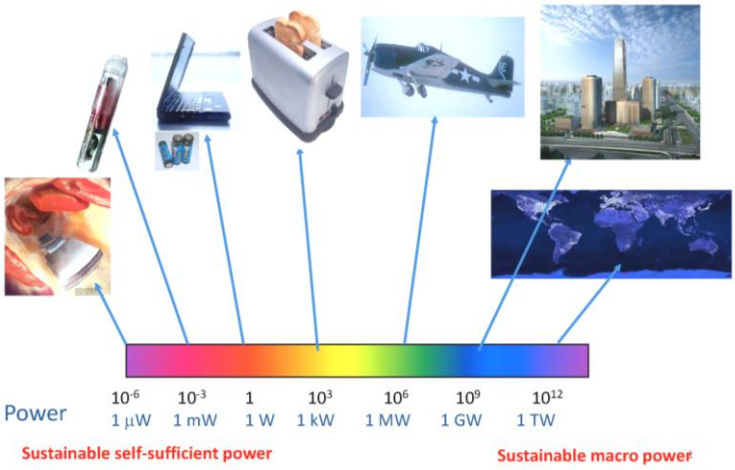

Figure 1.1. The scale of operation power. The magnitude of power needed for meet certain operation depending critically on the scale and applications. At the global range, TW magnitude of energy is needed, but for driving small devices, micro-Watt energy is needed although the sum of the energy for running such devices in total may not be huge. The energy requried for the operation of such systems is indispensible and even priceless . Differnet approches have to be delovoped to solve the world energy problem at all scales.

1.2. Self-powered sensor network

and systems

A nanosystem is an integration of multi-functional nanodevices with the capability to sense, control, communicate and actuate/respond. Their low power consumption means it is possible to use the energy harvested from the environment to power such a system. Power on the scale of microwatts is usually needed for independent, sustainable, maintain-free operations of implantable biosensors, remote and mobile environmental sensors, nanorobotics, micro-electromechanical systems, and even portable/wearable personal electronics. A nanorobot, for example, could sense and adapt to the environment, manipulate objects, taking actions and perform complex functions, but a key challenge is to find a power source that can drive a nanorobot without adding too much weight. Self-powered sensors, meanwhile, are needed for monitoring oil/gas transportations line over long distances.

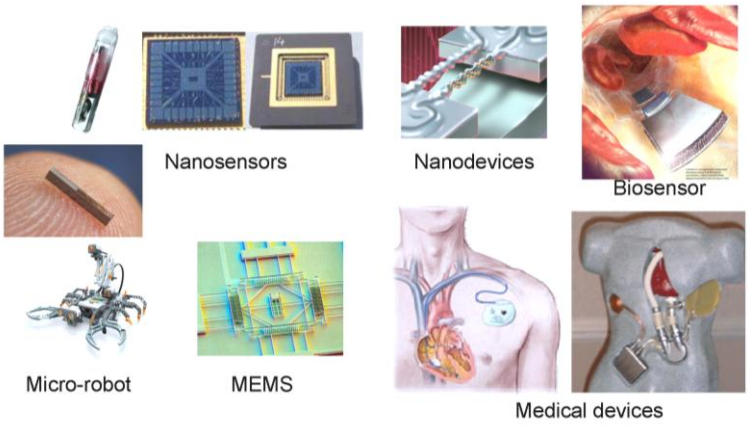

Figure 1.2. Many devices made based on nanotechnology may need micro- to milli-Watt scale power to operate. Although the required power is small, it has to have it regardless the cost! Although battery is a great choice in most of cases, harvesting energy from environment may entirely replace battery and/or extend the life time of the battery for sustainable operation.

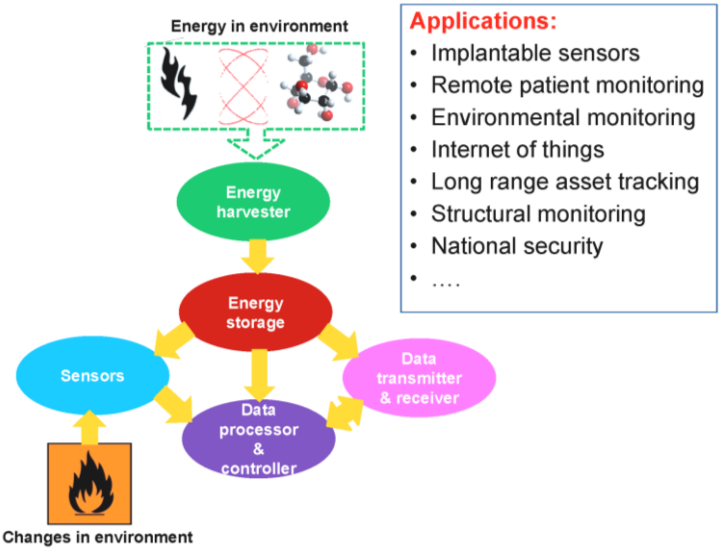

Figure 1.3. A self-powered sensor system and its potential applications.

Self-powered sensors are a key component of the *defect tolerant sensor networks*, which use information sensing equipment such as radio frequency identification (RFID), sensors, global positioning systems (GPS) and laser scanners to connect objects with the internet to carry out communication, identification, positioning, tracking, monitoring and management. By replacing the traditional finite number of discrete sensors with a large number of independent and mobile sensors distributed in the field, a statistical analysis of the signals collected through the internet over the distributed sensors can give precise and reliable information. An internet of things that can correlate everyday objects and devices to large databases and networks (the internet) are the future of health care, medical monitoring, infrastructure/environment monitoring, product tracking, and smart home.

However, such a sensor network will be almost impractical if each sensor has to be powered by a battery because of the huge number and also environmental and health concerns. Therefore, new

technologies that can harvest energy from the environment as *sustainable self-sufficient micro/nano-power* sources offer a possible of solution. But the mechanical energy available in our environment has a wide spectrum of frequencies and time-dependent amplitudes. This type of energy is called *random energy* and can come from irregular vibrations, light airflow, noise and human activity.

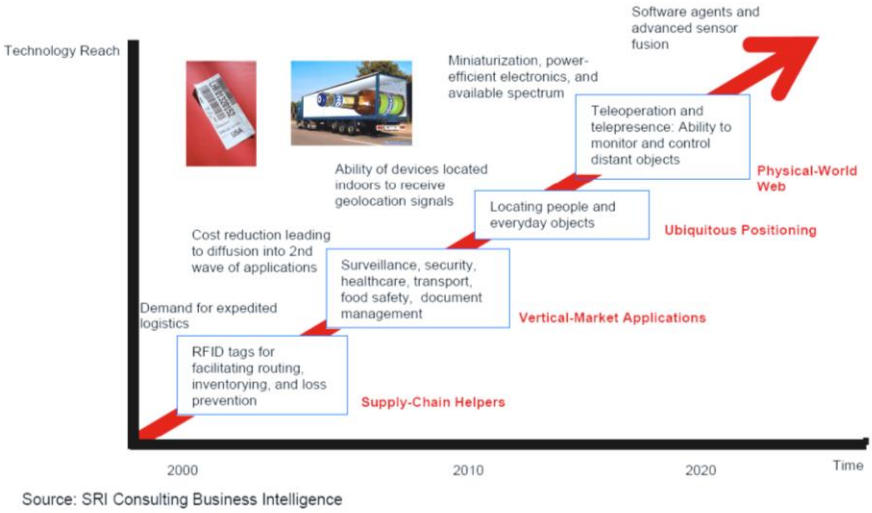

Figure 1.4. Potential application of self-powered system in sensor network.

The working mode of a wireless sensor can have an active mode but most importantly, a standby mode, during which the device is at "sleeping" with minimum energy consumption. The power generated by an energy havester may not be sufficient to continuously drive the operation of a device, but an accumulation of charges generated over a period of time is sufficient to drive the device for a few seconds. This could be of practical use for devices that have standby and active modes, such as glucose and blood pressure sensors, or even personal electronics such as blue tooth transmitters (driving power ~5 mW; data transmission rate ~ 500 kbits/s; power consumption 10 nW/bit), which are only required to be in active mode periodically. The energy generated when the device is in standby mode is likely to be sufficient to drive the device when it is in active mode.

Figure 1.5. Battery is one of the best choices for many personal electronics and small electronics, the replaing, recycling and disposal can be a huge environmental problem.

1.3. Harvesting mechanical energy

Photovoltaic, thermal electricity and electromagnetic induction are the well established technologies for energy harvesting, why do we need to harvest mechanical energy? We now consider the following occasions. In a case of individual sensors are difficult to get to (e.g. in hostile territory), or if the sensor network consists of a large number of nodes distributed over a large geographic area, then it may not be possible to replace batteries when required. A self sufficient power source deriving its power from the environment and thus not requiring any maintenance would be very desirable. In order for any system to be self sufficient, it must harness its energy from its surrounding environment and store this harnessed energy for later use. A nanorobot, for example, is proposed to be a smart machine that may be able to sense and adapt to the environment, manipulate objects, taking actions and perform complex functions, but a key challenge is to find a power source that can drive the nanorobot without adding much weight. If a nanorobot is placed in the body for performing sensing, diagnostic and

therapeutic action, one can easily introduces it in the body, but it will be rather difficult/impossible to fish it out to replace the battery. In the context of military sensing/surveillance node placement may be in difficult to reach locations, may need to be hidden, and may be in the environment of dusty, rainy, dark and/or deep forest. This precludes the use of solar cell technologies because light is typically not available. Methods of energy harvesting that might be applicable to the problem at hand may include systems utilizing random vibration (e.g. vibrations near a roadway), temperature gradients (e.g. ground temperature is fairly constant sufficiently below the surface), or any other phenomenon that could be exploited to provide energy. Therefore, it is highly desired to develop technology for harvesting mechanical energy.

Table 1.1. Sources of mechanical energy around us each and every day that can be harvested for electricity

Human body/motion	Transportation	Infrastructures	Industry	Environment
Breathing, blood flow/pressure, exhalation, walking, arm motion, finger motion, jogging, talking …	Aircraft, automobile, train, tires, tracks, peddles, brakes, tubine enginin, vibration, noises …	Bridges, roads, tunnels, farm, house structure, control-switch, water/gas pipes, AC system …	Motors, compressors, chillers, pumps, fans, vibrations, cutting and dicing, noise…	Wing, ocean current/wave, acoustic wave…

Table 1.2. Mechanical energy from typical body motions and the theoretically exlectricity that can be generated.

Activity	Mechanical energy	Electrical energy	Electricity generated per movement
Blood flow	0.93 W	0.16 W	0.16 J
Exhalation	1.00 W	0.17 W	1.02 J
Breath	0.83 W	0.14 W	0.84 J
Upper limbs	3.00 W	0.51 W	2.25 J
Finger type	6.9-19 mW	1.2-3.2 mW	226-406 uJ
Walk	67 W	11-39 W	18.8 J

What types of mechanical energies are we aiming at to harvest? There are abundant amount and types of mechanical energy exist in our living environment, such as light wind, body movement, muscle stretching, acoustic/ultrasonic waves, noises, mechanical vibrations, and blood flow. The sources of mechanical energy we are looking at have the following characteristics. First, the magnitude of such energy could be small and tiny, which may exclude the application of some conventional energy harvesting technologies because the available mechanical force may not be strong enough to drive the generator. Second, the frequency range of the available signal can be quite wide, and most of the energy is in low-frequency range. This requires a technique that operates from low (~Hz) to relatively high (~kHz) frequency range. Finally, the situation of the environment can vary. This requires a technique that has a

high adoptability. The nanogenerator we developed in the last 7 years is a potential technology for solving these problems.

1.4. The nanogenerator

We first proposed the self-powered nanotechnology in 2006, and we had developed the nanogenerator for the self-powered system. The nanogenerator converts random mechanical energy into electric energy using piezoelectric zinc oxide nanowire arrays. The mechanism of the nanogenerator relies on the piezoelectric potential created in the nanowires by an external strain: a dynamic straining of the nanowire results in a transient flow of the electrons in the external load because of the driving force of the piezopotential. The advantage of using nanowires is that they can be triggered by tiny physical motions and the excitation frequency can be one Hz to thousands of Hz, which is ideal for harvesting random energy in the environment. By integrating the contribution from thousands of nanowires, a gentle straining can output 1.2 V, which can drive an LED and a small liquid crystal display.

The discovery of nanogenerators is the top 10 world discoveries in science according to academicians of Chinese Academy of Science. The fiber based nanogenerator was elected as one of the top progresses in physics in 2008 by *Physics World*.[4, 5] The nanogenerator has been selected as the top 10 sci-fi discoveries that can have the equal importance as the invention of cell phones in 10-30 years, according to *New Scientist*. The nanopiezotronics is the top 10 emerging technologies in 2009 according to *MIT Technology Review*. The nanogenerator was among the top 20 discoveries in nanotechnologies that you may not known by *Discovery* Magazine (2010), and it is now in the top six future and emerging technologies selected by European Commission for support in the next 10 years [6].

The development process of the nanogenerator is a scientific story. The objective of this book is to introduce the fundamentals of the nanogenerator. We start from the very basic materials growth, followed by the description of the physical mechanism and basic theory. Then we will demonstrate the engineering approaches for achieving high output power. Lastly, we will present the hybridization of the nanogenerators with other energy harvesting techniques. Finally, we will show the prototype self-powered systems. The objective of the book is to serve as a fundamental text for teaching undergraduate students, graduate students and general researchers of how we have systematically developed the theory and technology of the nanogenerators.

---

[1] See the special issue on Sustainability and Energy, *Science*, Feb. 9 2007.

[2] See special issue on Harnessing Materials for Energy, *MRS Bulletin* **33** (4), 2008.

[3] Z.L. Wang, *Scientific American* **82**, Jan. 2008.

[4] Top 10 future technologies by New Scientists: http://www.newscientist.com/article/mg20126921.800-ten-scifi-devices-that-could-soon-be-in-your-hands.html?full=true

[5] MIT Technology Review: top 10 emerging technology in 2009: http://www.technologyreview.com/video/?vid=257=

[6] Digital Agenda: Commission selects six future and emerging technologies (FET) projects to compete for research funding: http://europa.eu/rapid/pressReleasesAction.do?reference=IP/11/530&format=HTML&aged=0&language=en&guiLanguage=en

Chapter 2

Nanomaterials for nanogenerator

ZnO, as an important semiconducting material, has a wide range of applications in optics, optoelectronics, sensors, actuators, energy, biomedical sciences and spintronics [1]. ZnO exhibit the most splendid and abundant configurations of nanostructures that one material can form. ZnO is one of the few dominant nanomaterials for nanotechnology. Based on bibliometric data from information-services provider Thomson Reuters [2], the number of publications and the cross-referenced areas based on ZnO nanostructures are as large and as important as literature in quantum computing, carbon nanotube, semiconductor thin films, and dark matter. There are a few existing excellent reviews related to nanowire growth and characterization especially about ZnO [3, 4**,** 5, 6 **,** 7**,** 8**,** 9]. As for the purpose of this book, we will mainly focus on the synthesis of nanowires especially aligned arrays via a vapor-liquid-solid (VLS) or vapor-solid-solid growth process.

2.1 Crystal structure of ZnO

Under conventional conditions, ZnO has the wurtzite structure, which has a hexagonal unit cell with space group *C6mc* and lattice parameters a = 0.3296, and c = 0.52065 nm. The oxygen anions and Zn cations form a tetrahedral unit. The entire structure lacks of central symmetry. The structure of ZnO can be simply described as a number of alternating planes composed of tetrahedrally coordinated O^{2-} and Zn^{2+} ions, stacked alternatively along the *c*-axis (Fig. 2.1a).

Although the entire unit cell of ZnO is neutral, the distribution of the cations and anions could take specific configuration as determined by crystallography, so that some surfaces can be terminated entirely with cations or anions, resulting in positively or negatively charged surfaces, called polar surfaces. The polar charge dominated surfaces can give some unique growth phenomena, as will be illustrated later. The most common polar surface is the basal plane. The oppositely charged ions produce positively charged Zn-(0001) and negatively charged O-$(000\bar{1})$ polar surfaces, resulting in a normal dipole moment and spontaneous polarization along the *c*-axis as well as a divergence in surface energy. To maintain a stable structure, the polar surfaces generally have facets or exhibit massive surface reconstructions, but ZnO ±(0001) are exception, which are atomically flat, stable and without reconstruction [10**,** 11]. Understanding the superior stability of the ZnO ±(0001) polar surfaces is a forefront research in today's surface physics [12**,**13**,**14**,**15].

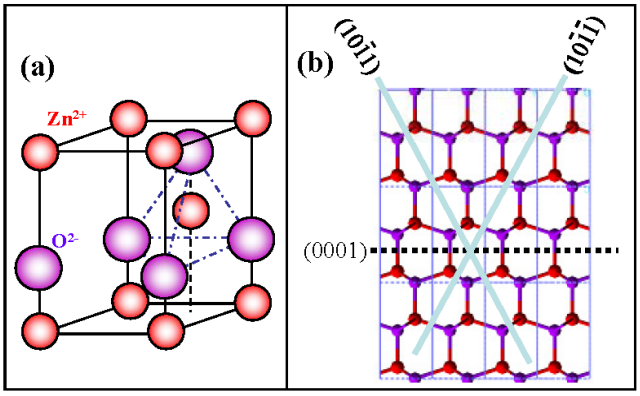

Figure 2.1. (a) Wurtzite structure model of ZnO, which has non-central symmetry and piezoelectric effect. (b) The three types of facets of ZnO nanostructures: ±(0001), $\{2\bar{1}\bar{1}0\}$ and $\{01\bar{1}0\}$.

Another polar surface is the $\{01\bar{1}1\}$. By projecting the structure along $[1\bar{2}10]$, as shown in Fig. 2.1b, beside the most typical ±(0001) polar surfaces that are terminated with Zn and oxygen, respectively, ±$(10\bar{1}1)$ and ±$(10\bar{1}\bar{1})$ are also polar surfaces. The $\{10\bar{1}1\}$ type surfaces are not common for ZnO, but they have been observed in a nanohelical structure [16]. The charges on the polar surfaces are ionic charges, which are non-transferable and non-mobile. Because the interaction energy among the charges depends on the distribution of the charges, the structure is arranged in such a configuration to minimize

the electrostatic energy. This is the main driving force for growing the polar surface dominated nanostructures.

Structurally, ZnO has three-types of fast growth directions: <2 $\bar{1}$ $\bar{1}$ 0> (±[2 $\bar{1}$ $\bar{1}$ 0], ±[$\bar{1}$ 2 $\bar{1}$ 0], ±[$\bar{1}$ $\bar{1}$ 20]); <01 $\bar{1}$ 0> (±[01 $\bar{1}$ 0], ±[10 $\bar{1}$ 0], ±[1 $\bar{1}$ 00]); and ±[0001]. Together with the polar surfaces due to atomic terminations, ZnO exhibits a wide range of novel structures that can be grown by tuning the growth rates along these directions. One of the most profound factors determining the morphology involves the relative surface activities of various growth facets under given conditions. Macroscopically, a crystal has different kinetic parameters for different crystal planes, which are emphasized under controlled growth conditions. Thus, after an initial period of nucleation and incubation, a crystallite will commonly develop into a three-dimensional object with well-defined, low-index crystallographic faces. Figures 2.2(a-c) show a few typical growth morphologies of 1D nanostructures for ZnO. These structures tend to maximize the areas of the {2 $\bar{1}$ $\bar{1}$ 0} and {01 $\bar{1}$ 0} facets because of lower energy. The morphology shown in Fig. 2.2d is dominated by the polar surfaces, which can be grown by introducing planar defects parallel to the polar surfaces [17]. Planar defects and twins are usually observed parallel to the (0001) plane, but dislocations are rarely seen. A detailed analysis about the defects in ZnO nanostructures can be found from [18].

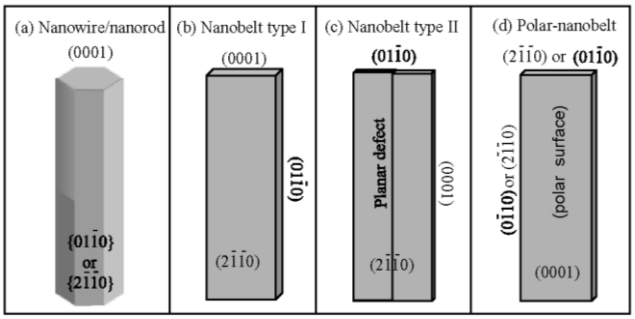

Figure 2.2. Typical growth morphologies of one-dimensional ZnO nanostructures and the corresponding facets.

2.2 Nanowire/nanobelt grown by vapor-solid-solid process

Vapor-solid growth process is a simple and effective method for the growth of oxide nanostructures without using catalyst [19]. There are two approach for vaporizing the source material, thermal vaporization and laser ablation. The thermal vaporization technique is a simple process, in which powder source material(s) is vaporized at elevating temperature and then the resultant vapor phase(s) condenses under certain conditions (temperature, pressure, atmosphere, substrate, etc.) to form the desired product(s) (Fig. 2.3). The morphology and phase structure of the synthesized product(s) depend on the source materials, growth temperature, temperature gradient, substrate, gas flow rate and pressure.

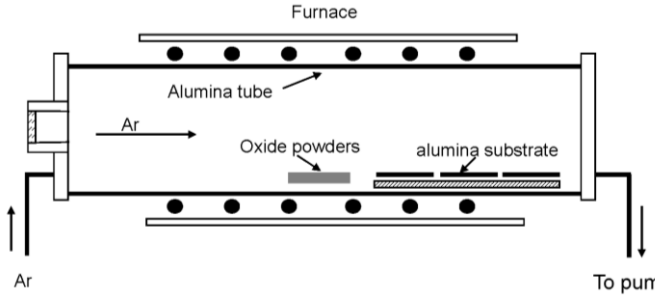

Figure 2.3. The furnace system for growth of nanowires by VLS and VSS process.

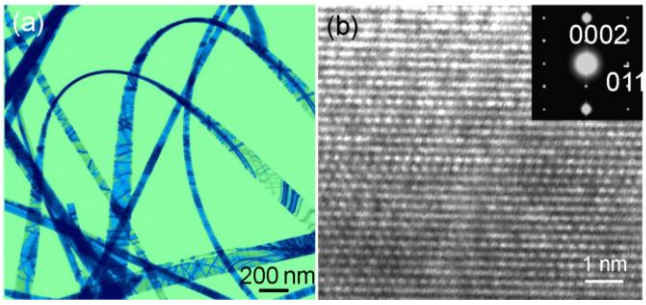

Figure 2.4. (a) Low magnification TEM image of ZnO nanobelts grown by vapor-solid process without using catalyst. (b) High-resolution TEM image of the nanobelt.

Thermal evaporation of ZnO powders (purity: 99.99%; melting point: 1975 °C) at 1400 °C resulted in ultra-long ZnO nanobelts (Fig. 2.4a). The as-synthesized oxide nanobelts are pure, structurally uniform, single crystalline and

most of them free from dislocations. A ripple-like contrast appeared in the TEM image is due to strain resulted from the bending of the belt. Occasionally, some planar defects, such as twins and stacking faults are found, but there is no line defect. Point defects, such as oxygen vacancies, should be present, which greatly affect the transport properties of the NBs. The NBs have a rectangular-like cross-section with typical widths of 30 - 300 nm, width-to-thickness ratios of 5 - 10 and lengths of up to a few millimeters. High-resolution TEM (HRTEM) and electron diffraction studies show that the ZnO nanobelts are structurally uniform and single crystalline (Fig. 2.4b).

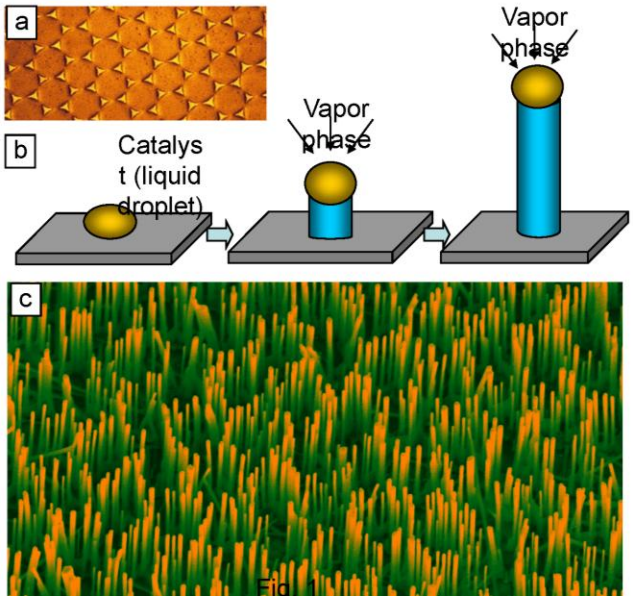

Figure 2.5. (a) SEM image of aligned ZnO nanowires grown on sapphire substrate using a thin layer of gold as catalyst. (b) SEM images of gold catalyst patterns using PS sphere monolayer as mask. (c) SEM image of aligned ZnO nanorods grown with a honeycomb pattern.

2.3 Nanowire arrays grown by vapor-liquid-solid process

Growth of aligned nanowires is important for the nanogenerators, light-emitting diodes and field effect transistors. Aligned growth of NWs can be achieved with the use of substrates and catalyst particles or seeds. The large-scale perfect vertical alignment of ZnO nanowires has been firstly demonstrated on *a*-plane ((11 $\bar{2}$ 0) crystal surface) orientated single-crystal aluminum oxide (sapphire) substrates [20]. Gold nanoparticles were used as catalysts (Fig. 2.5a). The growth is initiated and guided by the Au particle and the epitaxial relationship between ZnO and Al_2O_3 leads to the alignment (Fig. 2.5b).

Unlike the normal vapor-liquid-solid (VLS) process, a moderate growth rate is required for the alignment since the catalyst needs to be molten, form alloy and precipitate step by step to achieve the epitaxial growth of ZnO on sapphire surface. Therefore, a relatively low growth temperature was always applied to reduce the vapor concentration. Mixing ZnO with carbon powder, which is so-called carbon-thermal evaporation, can reduce the vaporization temperature from 1300 ℃ to 900 ℃,

$$ZnO(s) + C(s) \xleftrightarrow{900^{o}C} Zn(v) + CO(v) \qquad (2.1)$$

The above reaction is reversible in a relatively lower temperature. So when the Zn vapor and CO were transferred to the substrate region, they could react and became back to ZnO, which could be absorbed by gold catalyst and eventually formed ZnO NWs through VLS process. The detailed growth conditions can be found in our previous publications.

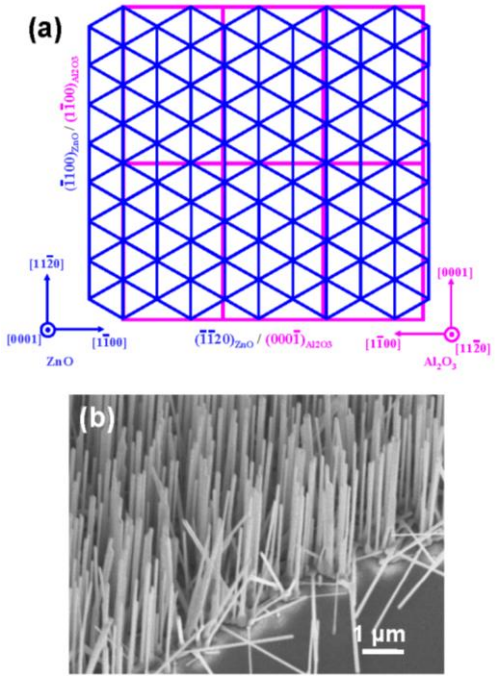

Figure 2.6. (a) Relationship between the lattices of alumina substrate and ZnO nanowires. (b) Nanowire arrays grown by a

The catalyst can also be pre-patterned by lithography or self-assembly techniques. For example, a two-dimensional, large-area, self-assembled and ordered monolayer of submicron polystyrene spheres was formed on sapphire substrate as a mask, through which a thin layer of gold was deposited. After etching away the spheres, a hexagonal network of gold layer was achieved (Figure 2.5a) [21], catalyzed by which, the as-grown aligned NWs exhibited the same honeycomb-like distribution (Figure 2.5c). All of the NWs are perpendicular to the substrate surface and the darker dot on the top of each nanowire is the gold catalyst. In this process, the growth spots were dictated by the existence of catalyst. If the applied catalyst was just a thin layer of gold, the distribution of the NWs would be random (Figure 2.6).

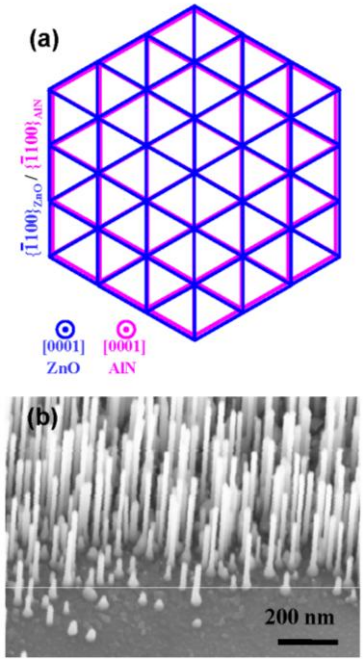

Figure 2.7. (a) Relationship between the lattices of alumina substrate and ZnO nanowires. (b) Nanowire arrays grown by a vapor solid process.

Epitaxial relationship between the substrate surface and ZnO nanowires determines whether there will be an aligned growth and how well the alignment can be. The successful alignment of ZnO NWs on sapphire and nitride substrates is attributed to the very small lattice mismatches between the substrates and ZnO. In the case of sapphire, $(11\bar{2}0)$ plane orientated substrate is always used because the smallest lattice mismatch is along the *c*-axis of Al_2O_3 and *a*-axis of ZnO (Fig. 2.6). The epitaxial relationship between ZnO NW and *a*-plane sapphire substrate are $(0001)_{ZnO} \parallel (11\bar{2}0)_{Al_2O_3}$, $[11\bar{2}0]_{ZnO} \parallel [0001]_{Al_2O_3}$. The lattice mismatch between $4[01\bar{1}0]_{ZnO}$ ($4 \times 3.249 = 12.996$Å) and $[0001]_{Al_2O_3}$ (12.99 Å) is almost zero, which confined the growth orientation of ZnO NWs. Nevertheless, since the $(11\bar{2}0)$ plane of Al2O3 is a rectangular lattice but the (0001) plane of ZnO is a hexagonal lattice, this epitaxial relationship can only hold in one direction.

Aligned ZnO NWs have been successfully grown on sapphire, GaN, AlGaN and AlN substrates [22] through a VLS process, where the crystal structure of substrate is crucial for the orientation of NWs. The growth direction is controlled by the epitaxial relationship between the substrate and NWs (Fig. 2.7); while the aligning quality is controlled by many other factors. We have performed a systematic investigation on the growth conditions, which were attributed to three basic terms: chamber pressure, oxygen partial pressure [23] and thickness of catalyst layer [24].

2.4 Nanowire arrays grown by pulse laser deposition

Pulse laser deposition (PLD) is a popular technique for thin film deposition ever since its demonstration as growing high-quality superconductive thin films. PLD can be used for deposition of a wide range of materials, such as ceramic oxides, nitride films, metallic films and superlattices. For our NW growth using PLD, a KrF excimer laser (Coherent Compex 205, wavelength of 248 nm) was used as the ablation source to focus on a ceramic target, which is a stack of ZnO powerder, and the incident fluence was approximately 3 J/cm^2. The key point for growing vertically aligned NWs is in-situ fabrication of a textured ZnO buffer layer on a silicon substrate before switching to the condition for the growth of NWs.

The topology of the NW array can be controlled by four parameters: substrate temperature (T), growth pressure, the flow ratio of argon and oxygen, laser repetition frequency [25]. At a laser repetition frequency of 5 Hz and a flowing mixture of Ar and O_2 at a flow ratio of 6:1 with a total pressure of 5.0 Torr, the SEM images of the NWs produced at a series of Ts are shown in Fig. 2.8a-d. At a T of 700 ^oC, a film with a rough surface was obtained (Fig. 2.8a). When T was increased to 750 ^oC, NWs were formed with a typical length of ~800 nm (Fig. 2.8b). Longer NWs of lengths ~2-3 μm were grown at 800 ^oC (Fig. 2.8c). Further increasing Ts to 850 ^oC merged a few NWs together (Fig. 2.8d). On the other hand, by fixing T at 800 ^oC, the dependence of the aspect ratio on the growth pressure was revealed. As the growth pressure increased to 6.0 Torr, slimmer NWs (Fig. 2.8e) were formed. While larger diameter NWs were obtained at 4.0 Torr (Fig. 2.8f). The aspect ratio can thus be controlled by adjusting the T and growth pressure.

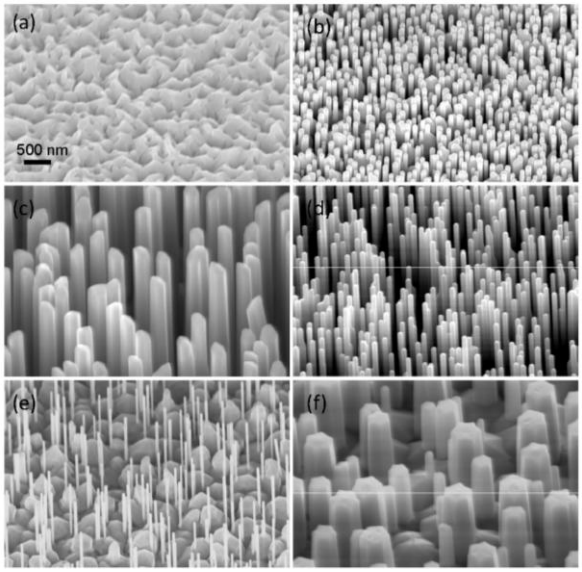

Figure 2.8. SEM tilted views of the NWs grown at (a) 700 ^oC, (b) 750 ^oC, (c) 800 ^oC, (d) 850 ^oC, the growth pressure was 5 Torr. (e), (f) NWs array grown at 6.0 Torr and 4.0 Torr at 800 ^oC. All of the images use one scale bar of 500 nm. A mixture of argon and oxygen with flow ratio of 6 is used as working gas and the laser repetition frequency is 5 Hz. The target is lithium doped $Zn_{0.95}Mg_{0.05}O$ (0.5 at.% doping concentration of Li).

2.5 Nanowire arrays grown by chemical approach

2.5.1 Basic approaches

2.5.1.1 Seeded Growth

One main advantage of wet chemical growth is that it can be achieved independent of the substrate by employing ZnO seeds in the form of thin films or nanoparticles. In this way, the nucleation step is bypassed and only the necessary conditions for growth are considered. Alignment of the ZnO nanocrystals occurs on flat surfaces regardless of their crystallinity or surface chemistry, including ZnO and Al_2O_3 single crystals, transparent conducting oxides such as indium tin oxide (ITO) and fluorine-doped tin oxide (FTO), amorphous oxides including glass and Si with its native oxide, and the oxide-free metals such as Au and Ti. However, this approach typically requires higher temperature substrate processing. ZnO seeds must be annealed at 150 ℃ to improve particle adhesion to the substrate and ZnO nanorod vertical alignment is improved by textured ZnO seeds annealed at 350 ℃.

2.5.1.2 Au/Polyimide

ZnO synthesis can also be carried out on catalysts such as Au, Ag, and Pt. Such metals can be deposited onto polymeric substrates as thin films to achieve nanowire growth. In this case, the surface roughness of the thin film must be carefully controlled to promote nucleation. In addition, the nanowire orientation is largely a function of the surface topography. In order to achieve vertically-aligned nanowires, an appropriate process flow must be employed for smooth substrate surfaces.

2.5.1.3 Electrochemical deposition

Electrochemical deposition of ZnO is a powerful technique for achieving large area, uniform nanorod synthesis. However, it requires a conductive substrate and materials which can withstand acid reaction environments. Typically, a $ZnCl_2$/KCl electrolyte is bubbled with O_2 to maintain an oxygen saturated electrolyte. A standard three electrode setup with a saturated Ag/AgCl reference electrode and Pt counter

electrode is often used in conjunction with potentiostat to control the current-voltage characteristics throughout the process.

In addition, the nucleation and growth rate of ZnO can be enhanced by electrochemical methods in a solution of zinc nitrate and HMTA. As mentioned previously, Weintraub et. al. used an electrochemical technique combined with a patterned substrate to achieve individual ZnO nanorod growth. In this case, the applied potential causes an increased OH^- concentration by the reduction of NO_3^- in an electrochemical reaction at the negative electrode. As such the reaction would proceed as follows:

$$NO_3^- + H_2O + 2e^- \rightarrow NO_2^- + 2OH^- \quad (2.2)$$

$$Zn^{2+} + 2OH^- \rightarrow ZnO + H_2O \quad (2.3)$$

The HMTA still promotes 1-D growth by capping the non-polar facets and providing a hydroxide source. This method is particularly useful because enhanced nucleation can be achieved without the use of seeds. Seeding often requires a high temperature annealing step (>200 ℃) making it difficult to use polymer seeded substrates. Therefore, the electrochemical approach which can be carried out on any conductive substrate makes it useful for growth on conductive polymers.

2.5.1.4 Zinc nitrate hexahydrate and hexamethylenetetramine

The most commonly used chemical agents for the hydrothermal synthesis of ZnO nanowires are probably Zinc nitrate hexahydrate and hexamethylenetetramine**[**26**,** 27**]**. The chemistry of the growth has already been well documented. Zinc nitrate hexahydrate salt provides Zn^{2+} ions required for building up ZnO nanowires. Water molecules in the solution provide O^{2-} ions. Even though the exact function of hexamethylenetetramine during the ZnO nanowire growth is still unclear, it is believed to act as a weak base, which would slowly hydrolyze in the water solution and gradually produce OH^-. This is critical in the synthesis process because, if the hexamethylenetetramine hydrolyzes very fast and produces a lot of OH^- in a short period of time, the Zn^{2+} ions in solution would precipitate out very quickly due to the high pH environment, which would have little contribution to the ZnO nanowire oriented growth, and eventually results in fast consumption of the nutrient and prohibits further growth of ZnO nanowires.

$$(CH_2)_6N_4 + 6\ H_2O \leftrightarrow 4\ NH_3 + 6\ HCHO \quad (2.4)$$

$$NH_3 + H_2O \leftrightarrow NH_3 \cdot H_2O \quad (2.5)$$

$$NH_3 \cdot H_2O \leftrightarrow NH_4^+ + OH^- \quad (2.6)$$

$$Zn^{2+} + 2\ OH^- \leftrightarrow Zn(OH)_2 \quad (2.7)$$

$$Zn(OH)_2 \leftrightarrow ZnO + H_2O \quad (2.8)$$

The growth process of ZnO nanowires can be controlled through the five chemical reactions listed above. All of the five reactions are actually in equilibrium and can be controlled by adjusting the reaction parameters, such as precursor concentration, growth temperature and growth time, in order to push the reaction equilibrium forward or backward. In general, precursor concentration determines the nanowire density. Growth time and temperature control the ZnO nanowire morphology and aspect ratio.

For simplicity of description, we use Si substrate to describe the experimental procedure and to illustrate the effects of various experimental parameters on the growth. A piece of Si (100) wafer substrate was cleaned by a standard cleaning progress. First, the wafer was ultrasonicated consecutively in acetone, ethanol, IPA (isopropyl alcohol) and de-ionized water each for 10 minutes, then blew dry by dry nitrogen gas and then baked on hotplate at 200 ℃ for 5 minutes to get rid of any adsorbed moisture. Then, a 50 nm thick layer of Au was deposited on top of the Si wafer by magnetron plasma sputtering, which is expected to act as an "intermediate-layer" to assist the growth. Between the Si wafer and Au layer, 20 nm of Ti was deposited as an adhesion layer to buffer the large lattice mismatch between Si(100) surface with native oxide on and Au(111) surface and to improve the interface bonding. Then the

substrate was annealed at 300 ℃ for 1 hour. The next step is to prepare the nutrient solution. The nutrient solution was composed of a 1 to 1 ratio of zinc nitrate and hexamethylenetetramine (HMTA). The substrate was put face down at the top of the nutrient solution surface. Due to surface tension, the substrate could float at the top of the solution surface. The annealing process helps the as-deposited Au layer to form a uniform crystalline thin layer on the surface of Si substrate, which is critical in the oriented growth of aligned ZnO NWs.

The growth process of ZnO NWs can be controlled through the five chemical reactions listed above. All of the five reactions are actually in equilibrium and can be controlled by adjusting the reaction parameters, such as precursor concentration, growth temperature and growth time, in order to push the reaction equilibrium forward or backward. In general, precursor concentration determines the NW density (Fig. 2.9a-c). Growth time and temperature control the ZnO NW morphology and aspect ratio.

The density of ZnO NWs on the substrate could be controlled by the initial concentration of the zinc salt and HMTA. To explore the relationship between the precursor concentration and the density of the ZnO NW arrays, a series of experiments were performed by varying the precursor concentration but keep the ratio constant between the zinc salt and HMTA. Experimental results show that the density of the NW arrays is closely related to the precursor concentration. Detailed analysis of the measured data is shown in Fig. 2.9d (red line). From 0.1 mM to 5 mM, the ZnO NWs density, defined as number of NWs per 100 μm^2, increases dramatically, possibly for the following reasons. Zinc chemical potential inside the solution body increases with zinc concentration. To balance the increased zinc chemical potential in solution, more nucleation sites on the substrate surface will be generated. So, the density of ZnO NWs increases. When further increasing the zinc concentration, the density of ZnO NWs remains approximately steady with a little tendency of decrease. The steady/saturated density may be understood from the nucleation and growth process. The NW density is decided by the number of nuclei formed at the very beginning of the growth, which continued to grow and form nanorods (shorter NWs). The arrival of more ions on the substrate may not initiate new nuclei at a later stage because of two possible reasons. One, with consideration the critical size required for a nucleus to grow into a crystal, no new nanorods would form if the sizes of the nuclei are smaller than the critical size. Second, due to the existence of the first group of grown nanorods, the newly arrived ions on the substrate have higher probability to reach the existing NWs rather than to the newly formed nuclei, thus, the size of the nuclei may not exceeds the critical size and they will eventually dissolve into the solution body. In such cases, a continuous increase in solution concentration may not increase the density of the NWs when its density is larger than the saturation density. This also explains why the grown NWs in our experiments have fairly uniform height. Even though the density of the ZnO NW remains steady at high precursor

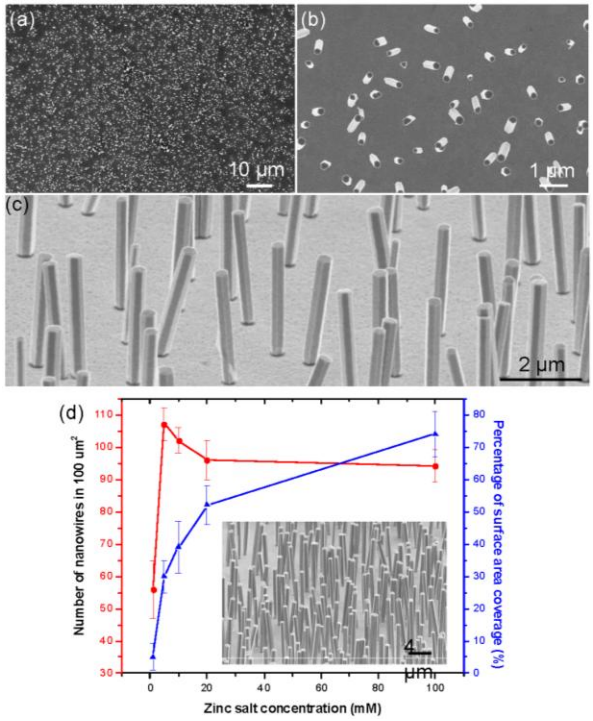

Figure 2.9. A general view of as grown ZnO nanowire arrays at 5mM, growing 24 hours at 70 ℃: (a) top view; (b) enlarged top view; (c) with a 60 ° tilt. (d) Density varied with concentration: Plot of ZnO nanowire density in a 100 μm^2 area (red line) and plot of area percentage covered by ZnO nanowires (blue line). Each data point was obtained from 4 different areas. Inset is a typical image of ZnO nanowires grown at 5 mM.

concentration level, the surface coverage percentage increases slightly due to the lateral growth of the NWs (Fig. 2.9d, blue line).

2.5.2 Patterned growth of vertically aligned nanowire array

To grow high-quality patterned ZnO NW arrays, we need an approach that can meet the following three requirements. First, the growth has to be at low temperature so that the NWs can be integrated with general substrates. Second, the NWs have to be grown following a designed pattern, with a high degree control in size, orientation, dimensionality, uniformity and possibly shape. Finally, the catalyst may need to be eliminated for integrating with silicon based technology. Our approach is based on electron-beam lithography and a low temperature hydrothermal method to achieve patterned and aligned growth of ZnO NWs at < 100 ℃ on general inorganic substrates, such as Si and GaN, without using a catalyst [28]. For the epitaxial growth, the Si doped n-type GaN substrate used here was fabricated by growing 2 μm thick GaN on c plane sapphire by metal organic chemical vapor deposition. Then the GaN substrate was also cleaned by the standard cleaning progress.

The substrate was then spun on a 50 nm thick layer of PMMA. Then the substrate was baked on a hotplate at 180 ℃ for 2 minutes. The patterned was defined by an array of circle with 100 nm in diameter, and 1μm in pitch. The dose used here was ranged from 300 $\mu C/cm^2$ to 600 $\mu C/cm^2$. After electron beam exposure, the substrate was developed in a mixture of 1:3 (in volume) ratio of IPA (isopropyl alcohol) and MIBK (Methyl isobutyl ketone) for 1 minute. No oxygen plasma treatment was performed.

Now the substrate is ready for hydrothermal growth of ZnO nanowire arrays. The nutrient solution used here was composed of 5 mmol/L 1:1 ratio of zinc nitrate and HMTA (hexamethylenetetramine). The patterned GaN substrate was put floating on top of the nutrient solution surface. The whole system was heated up to 70 ℃ for 24 hours for growing multiple ZnO nanowires out of one single spot on Si wafer, and to 95 ℃ for 24 hours for both one ZnO nanorod in one single spot on Si wafer on and GaN substrate. Figure 2.10 show the aligned ZnO NW array grown on a GaN on sapphire substrate. The as grown NWs have a complete control in size, dimension and orientation.

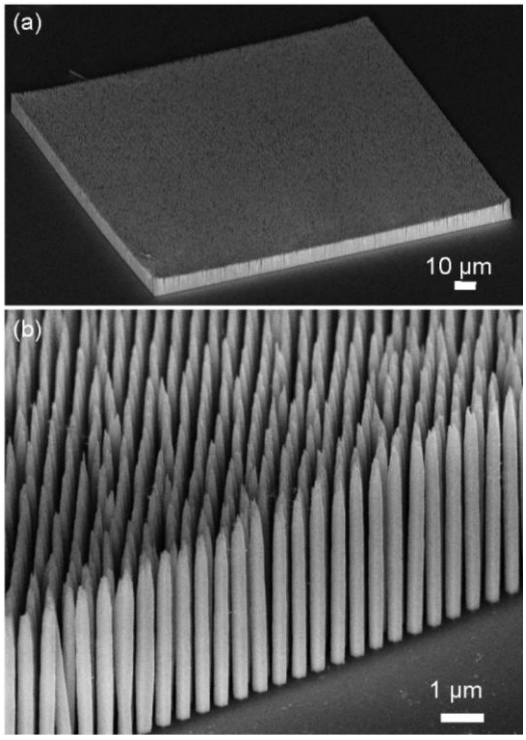

Figure 2.10. (a) Low magnification and (b) high magnification SEM images of the ZnO NW arrays grown on a GaN substrate using a hydrothermal approach.

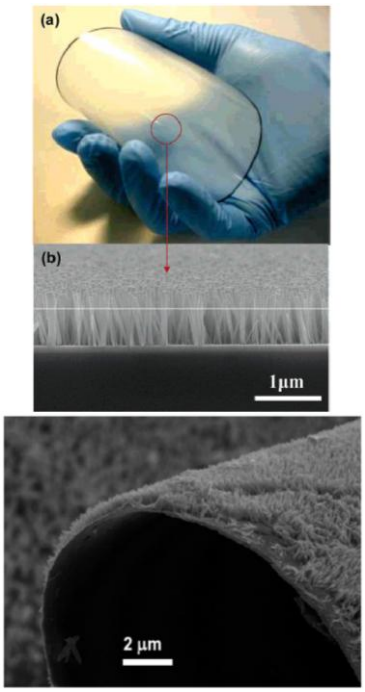

Figure 2.11. ZnO NW arrays grown on a flexible substrate using a hydrothermal approach.

2.5.3 Growth on flexible substrates

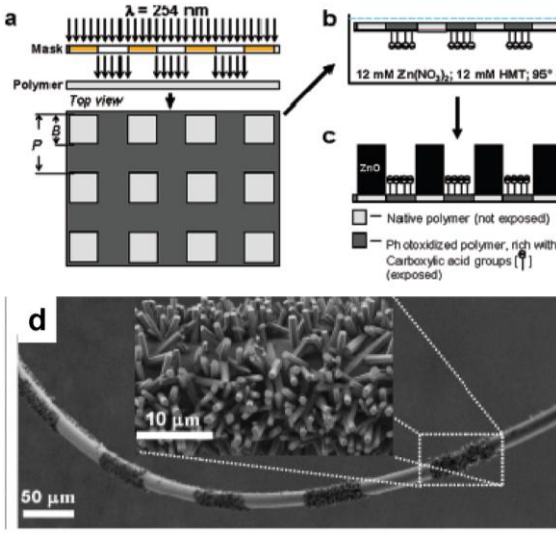

Figure 2.12. Patterned growth of ZnO NW arrays grown on a fiber. From [33].

ZnO nanorods can be synthesized on organic substrates in a variety of fashions. ZnO seeds can by sputtered at room temperature on virtually any substrate leading to high density nanorod growth. For example, Liu et. al. successfully carried out synthesis on a 4" thermoplastic polyurethane substrate as seen in Figure 2.11 [29]. The technique is general and substrates such as polyimide, polystyrene, polyethylene terepthalate, and polyethylene napthalate are just a few examples of substrates seen in the literature. In addition, ZnO nanorods can be electrochemically deposited provided that the flexible substrate is either conductive or pre-coated with a metal or a transparent conducting oxide such as ITO. A typical experimental step would consist of a $ZnCl_2$/KCl electrolyte with O_2 bubbled into the solution to maintain an oxygen saturated electrolyte. A standard three electrode setup with a saturated Ag/AgCl reference electrode and Pt counter electrode is often used. Typical potentials are approximately -1 V. ZnO nanorods electrochemically deposited on an Au film with a curvature of radius less than 10 μm have been achieved.

2.5.4 Growth of nanowire arrays on microfibers

Patterned growth of ZnO nanowire arrays has been achieved by using patterned gold catalysts, seed layers [30], and SAMs (self-assembled monolayer) [31]. Morin et al., developed a simple catalyst-free process that could not only be used on flat polymer films but also on microfibers [32]. Their main working principle is that by employing UV radiated polymer surfaces, the region where has been radiated generates carboxylic group on top of the polymer surface, while the unexposed region remains unchanged. Astonishingly, ZnO nanowire arrays could only nucleate and grow selectively onto the regions where there are no carboxylic groups. It is because that protonated hexamethylenetetramine species would combine with those surface carboxylic acid groups thus blocking the nucleation of ZnO in these UV radiated regions. This explanation makes sense very well. Based on the reported pKa of hexamethylenetetramine (5.4-5.5), and the measured pH of 6.6 at their reaction conditions, approximately 7 % of the hexamethylenetetramine species present should be protonated.

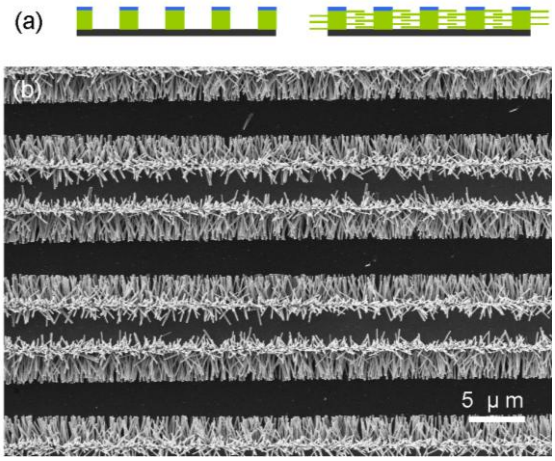

Figure 2.13. (a) Schematic steps for growing patterned and laterally aligned ZnO NW arrays. (b) SEM image of ZnO nanowire arrays grown laterally on Si substrate.

In their experiments, they use single filaments of polyester (polyethylene terephthalate or PET), which are the material to go ZnO nanowire arrays onto, are cleaned by a standard cleaning procedure. First, they are sonicated the filaments in acetone for 20 minutes, then rinsed with distilled water and then baked at 60 ℃ for at least 24 hours to get rid of any absorbed moisture. To do surface functionalization, a single filament is strung through slits in a PC backing film and then do photo oxidation using a UV lamp with wavelength at 254 nm at a nominal intensity of 18.5 mW/cm^2 for 50 minutes through a common photo

mask, as illustrated in Figure 2.12a. After that, the photo oxidized substrate was immersed into a 6 ml vial containing 3.5 ml of nutrient solution, which is composed of 1 to 1 ratio of zinc nitrate and hexamethylenetetramine. The morphology of the ZnO nanostructures could be varied by using different composition of the nutrient solution in their experiments. To grow ZnO nanorods, a solution of 12 mM zinc nitrate hexahydrate and 12 mM hexamethylenetetramine was used, while a mixed solution of 25 mM zinc nitrate hexahydrate, 25 mM hexamethylenetetramine, and 0.18 mM citric acid was used to produce ZnO plates, where citric acid acted as a capping agent to the basal planes of the nanowires to inhibit the axial growth of the nanowires, as will be discussed in later section. To avoid random deposition of the heterogeneously formed precipitates from the solution body, the substrate was positioned with the UV irradiated face facing downward[33]. After that, the sample was removed from the vial, rinsed with ethanol, and dried with N_2 gas, as shown in Figure 2.12b.

2.5.5 Patterned growth of laterally aligned nanowire array

The laterally aligned NWs were grown by using different materials to activate or inhibit the growth of nanowires [33]. Two materials are used here: ZnO seeds for the growth, and Cr layer for preventing the local growth. The first step for the growth is to fabricate a ZnO strip pattern covered with Cr at top (Fig. 2.13a). A (100) Si wafer was firstly cleaned in sequence with HF acid solution, acetone, isopropyl alcohol and ethanol. A photoresist was spun coated on the substrate to get a uniform layer. Then a pattern was produced using optical lithography. ZnO strips with Cr on top were achieved after lifting-off with aceton. Finally, the substrate was put into growth solution and aged for 12 hours at 80 ℃. To achieve uniform control over the growth rate by the concentration of the solution, the substrate was floated upside down on the solution surface with the patterned side facing downwards. Figure 2.13b is the laterally grown ZnO NW arrays on Si substrate. It can be seen that ZnO NW arrays grew from the lateral sides of the pattern with a good alignment. More than 70% nanowires are parallel to the substrate. Only a small fraction of disordered ZnO nanowires grew at the edge of the pattern. ZnO NWs have a diameter less than 200 nm and a length of about 4 microns. Hexagonal cross section of nanowires implies that *c* axis of ZnO NW is along its length direction.

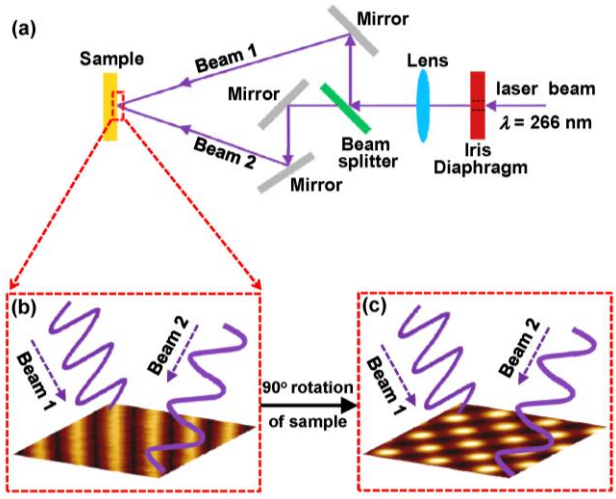

Figure 2.14. (a) Schematics of experimental setup for the laser interference patterning, which remains the same for both LIL and LIA approaches. A 10-ns pulsed Nd:YAG laser (Quanta-Ray PRO 290, Spectra Physics) with wavelength of 266 nm is used as the laser source. The primary laser beam (266 nm) was split into two coherent light beams (beam 1 and beam 2). (b) The interference between beam 1 and beam 2 formed a grating pattern on the photoresist layer (for LIL approach) or the substrate directly (for LIA approach), under a single laser pulse (10 ns) irradiation. (c) The sample was then rotated for 90° or at an arbitrary angle with a second exposure, and patterns of periodic nanodot arrays were formed on the photoresist layer or the substrate. The grating and nanodot patterns in Figure 1b and c were fabricated on SU 8 via LIL approach and acquired by a scanning probe microscope.

2.6 Growth of wafer level nanowire arrays by laser patterning

To achieve controllable growth of highly-ordered and aligned ZnO NW arrays with high-throughput and low-cost at large scale, it is necessary to adopt feasible combinations of patterning techniques and ZnO NWs synthesis methods. We demonstrate one such approach for patterned growth of vertically aligned ZnO nanowire arrays by combining laser interference lithography

(LIL) [34,35], which is a large-scale, fast, maskless, and noncontact nanopatterning technique, and HT growth of ZnO NWs either homoepitaxially on textured ZnO layer, which is also synthesized wet-chemically, or heteroepitaxially on GaN film. The substrates can be patterned with periodic ordered, variable spacing and symmetry over large areas of up to a 2-inch wafer by LIL. Perfectly aligned vertical ZnO NW arrays were then grown at predefined positions via a low temperature HT method without using catalyst but with control over orientation, dimension and location. As-synthesized NWs are highly uniform in length and diameter with perfect alignment, and are single crystals with growth direction along [0001].

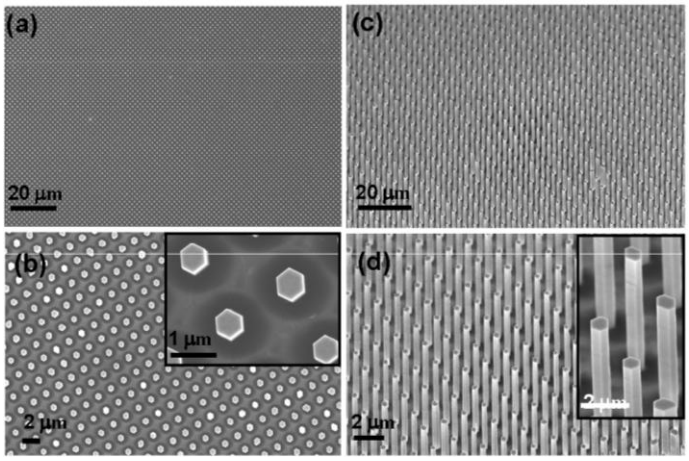

Figure 2.15. The heteroepitaxial growth of vertically aligned ZnO NW arrays on GaN substrate via LIL approach. (a) and (b) Top-view SEM images of vertically aligned ZnO NW arrays on GaN substrate in large-scale uniform pattern at different magnifications. (c) and (d) 45°-tilted-view SEM images of vertically aligned ZnO NW arrays on GaN substrate in large-scale uniform pattern at different magnifications.

The patterns for synthesis of ZnO NW arrays were prepared by LIL of the photoresist, which is a photochemical process similar to that in the state-of-art photolithography process. The epoxy-based negative photoresist SU-8, commonly used in the microelectronics industry, was adopted in our experiment. The LIL technique generates patterns on the photoresist masklessly. When exposed, SU-8's long molecular chains cross-link and cause the solidification of the exposed areas. After development, the exposed areas of SU-8 layer remained and served as the mask for the growth of ZnO NWs. The experimental setup for the laser interference patterning is shown in Figure 1a. A 10-ns pulsed Nd:YAG laser (Quanta-Ray PRO 290, Spectra Physics) with wavelength of 266 nm is used as the laser source. The primary laser beam (266 nm) was split into two coherent light beams (Figure 2.14a). Interference between the beams formed a grating pattern (Figure 2.14b) on the photoresist layer under a single laser pulse (10 ns) irradiation. The period of the pattern line spacing d is determined by the wavelength (λ) of the light and the half-angle (θ) between the two incident beams through the relationship $d=\lambda/2\sin(\theta)$. The sample was then rotated by 90° followed by a second exposure, and patterns of periodic nanodot arrays were formed on the photoresist layer (Figure 2.14c).

The patterned substrate was used to directly grow ZnO nanowires using chemical approach. The locations of the growth are defined by the pattern, and the orientation of the nanowires is dictated by the epitaxial relationship with the GaN substrate. The morphology and uniformity of the patterned NW arrays via LIL approach were examined and confirmed by SEM images (Figure 2.15). Almost all of the NWs have the same diameter and height. The aligned ZnO NW arrays were uniformly grown following the patterned holes with high-fidelity at diameter of ~600 nm (Figure 2.15b). All the NWs are perfectly aligned normal to the substrate and have the same height of ~5 μm (Figure 2.15c and 2.15d).

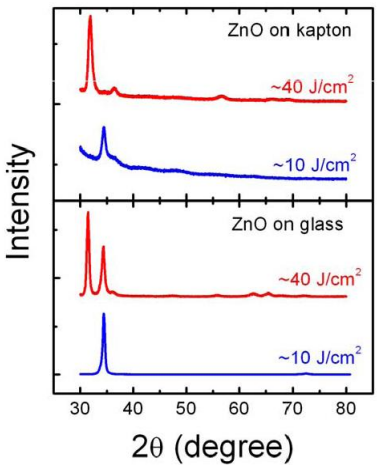

Figure 2.16. XRD spectra of ZnO films grown on kapton and glass substrates at high (40 J/cm^2) and low (10 J/cm^2) laser fluencies.

2.7 Textured ZnO film

One of the unique advantage of ZnO is that, when it is deposited into a film, the film is textured along [0001], so that the polar direction is aligned. Although the film has random orientations among the grains in *a*- and *b*-axes direction in plane, the normal direction of the deposited film is most likely to be c-axes. This characteristic is particularly important for applications in nanogenerators due to the crystallographic alignment and consequent alignment of piezoelectric "domains".

We use a ZnO film prepared by PLD as example to illustrate this characteristics [36]. The substrate used for the film can be kapton or glass but the texturing orientation depends on the flux of laser. X-ray diffraction spectra for the ZnO films deposited on kapton and glass substrates are shown in figure 2.16. Up to the maximum laser fluence of 45 J/cm2, the texture change from <001> toward <100> is noticeable but not as complete as in the case of ZnO films on Si substrates. It appears that higher laser fluence power is necessary to change the texture of ZnO film from (0001) to (1-100) completely on the glass and kapton substrates than on the Si substrates

References for Chapter 2:

[1] J. Jagadish and S.J. Pearton (ed), Elsevier. 2006.
[2] Physics World, October issue 36 (2008).
[3] C.M. Lieber and Z.L. Wang, *MRS Bulletin* **32**, 99 (2007).
[4] J.G. Lu, P.C. Chang, Z.Y. Fan, *Materials Science & Engineering R-Reports* ***52***, 49 (2006).
[5] Y.W. Heo, D.P. Norton, L.C. Tien, Y. Kwon, B.S. Kang, F. Ren, S.J. Pearton, J.R. LaRoche, *Materials Science and Engineering R* **47**, 1 (2004).
[6] N. Wang, Y. Cai, R.Q. Zhang, *Materials Science and Engineering R*, 60, 1 (2008).
[7] Z.L. Wang, *J. Nanoscience and Nanotechnology* **8**, 27 (2008).
[8] X.D. Wang, J.H. Song and Z.L. Wang, *J. Materials Chemistry* **17**, 711 (2007).
[9] Z.L. Wang, Materials Science and Engineering Report, **64** (issue 3-4), 33 (2009).
[10] O. Dulub, L. A. Boatner, and U. Diebold, *Surf. Sci.* **519**, 201 (2002).
[11] B. Meyer and D. Marx, *Phys. Rev. B.* **67**, 035403 (2003).
[12] P. W. Tasker, J. *Phys. C: Solid State Phys.* **12**, 4977 (1979).
[13] O. Dulub, U. Diebold and G. Kresse, *Phys. Rev. Letts.* **90**, 016102 (2003).
[14] A. Wander, F. Schedin, P. Steadman, A. Norris, R. McGrath, T. S. Turner, G. Thornton and N. M. Harrison, *Phys. Rev. Letts.* **86**, 3811 (2001).
[15] V. Staemmler, K. Fink, B. Meyer, D. Marx, M. Kunat, S. Gil Girol, U. Burghaus and Ch. Woll, *Phys. Rev. Letts.* **90**, 106102 (2003).
[16] R. S. Yang, Y. Ding and Z. L. Wang, *Nano Lett.* **4**, 1309 (2004).
[17] Y. Ding, X.Y. Kong, Z.L. Wang, *Phys. Rev. B* **70**, 235408 (2004).
[18] Y. Ding and Z.L. Wang, *Micron*, **40**, 335 (2009).
[19] Z. L. Wang, Z. W. Pan and Z. R. Dai, *Microsc. and Microanal.* **8**, 467 (2002).
[20] M.H. Huang, S. Mao, H. Feick, H.Q. Yan, Y.Y. Wu, H. Kind, E. Weber, R. Russo and P.D. Yang, *Science* **292**, 1897 (2001).
[21] X.D. Wang, C.J. Summers and Z.L. Wang, *Nano Letters* **3**, 423 (2004).
[22] X.D. Wang , J.H. Song , P. Li , J.H. Ryou , R.D. Dupuis , C.J. Summers and Z.L. Wang, J. *Am. Chem. Soc*. **127**, 7920 (2005).
[23] J.H. Song, X.D. Wang, E. Riedo and Z.L. Wang, J. *Phys. Chem. B.* **109**, 9869 (2005).

[24] X.D. Wang, J.H. Song, C.J. Summers, J.H. Ryou, P. Li, R.D. Dupuis, and Z.L. Wang, *J. Phys. Chem. B*, **110**, 7720 (2006).
[25] S. S. Lin, J. I. Hong, J. H. Song, Y. Zhu, H. P. He, Z. Xu, Y. G. Wei,Y. Ding, R. L. Snyder, and Z. L. Wang, *Nano Letters* **9**, 3877 (2009).
[26] L. Vayssieres, *Advanced Materials* **15**, 464 (2003).
[27] S. Xu, C. Lao, B.Weintraub, Z. L. Wang, *Journal of Materials Research* **23**, 2072 (2008).
[28] S. Xu, Y.G. Wei, M. Kirkham, J. Liu, W.J. Mai, R.L. Snyder, Z.L. Wang, *J. Am. Chem. Soc.* **130**, 14958 (2008).
[29] T. Y. Liu, H. C. Liao, C. C. Lin, S. H. Hu, S. Y. Chen, *Langmuir* **22**, 5804 (2006).
[30] Y. Tak, K.Yong, *Journal of Physical Chemistry B.* **109**, 19263 (2005).
[31] J. W. P. Hsu, J. R. Tian, N. C. Simmons, C. M. Matzke, J. A. Voigt, J. Liu, *Nano Letters* **5**, 83 (2005).
[32] S. A. Morin, F. F. Amos, S. Jin, *Journal of the American Chemical Society* **129**, 13776 (2007).
[33] Y. Qin, R.S. Yang and Z.L. Wang, *J. Physical Chemistry C*. **122**, 18734 (2008).
[34] D. Yuan, R. Guo, Y. Wei, W. Wu, Y. Ding, Z. L. Wang, S. Das, *Adv. Func. Materials* **20**, 3484 (2010).
[35] Y. Wei, W. Wu, R. Guo, D. Yuan, S. Das and Z. L. Wang, *Nano Letters* **10**, 3414 (2010).
[36] J. Hong, J. Bae, Z. L. Wang, R. L. Snyder, *Nanotechnology* **20**, 085609 (2009).

Chapter 3

Piezoelectricity and piezopotential

We first introduce the theory for piezoelectricity. Then the piezoelectric potential (piezopotential) produced by piezoelectric effect is derived for illustrating the principle of nanogenerators. In the literature, numerous theories for 1D nanostructure piezoelectricity have been proposed, including first-principles calculations [1, 2], MD simulations [3] and continuum models [4]. However, first-principle theory and MD simulation are difficult to be implemented to nanopiezotronics system (the typical dimension of which is ~ 50 nm in diameter and ~2 micron in length) due to the huge number of atoms. The continuum model proposed by Michalski 4 et al is relevant in that it gives a criterion to distinguish between mechanically dominated regime and electro-statically dominated regime. In this section we propose a continuum model for the electrostatic potential in a laterally bent NW. A perturbation technique is introduced to solve the coupled differential equations, and the derived analytical equation gives a result that is within 6% of that received from full numerical calculation. The theory directly establishes the physical basis of nanopiezotronics and nanogenerator as proposed previously [1].

3.1 Governing Equations

Our theoretical objective is to derive the relationship between the potential distribution in a NW and the dimensionality of the NW and magnitude of the applied force at the tip. For this purpose, we start from the governing equations for a static piezoelectric material, which are three sets: mechanical equilibrium equation (Eq. 3.1), constitutive equation (Eq. 3.2), geometrical compatibility equation (Eq. 3.3) and Gauss equation of electric field (Eq. 3.4). The mechanical equilibrium condition when there is no body force $\vec{f}_e^{(b)} = 0$ acting on the nanowire is:

$$\nabla \cdot \sigma = \vec{f}_e^{(b)} = 0, \qquad (3.1.1)$$

where σ is the stress tensor, which is related to strain ε, electric field $\vec{E}$ and electric displacement $\vec{D}$ by constitutive equations:

$$\begin{cases} \sigma_p = c_{pq}\varepsilon_q - e_{kp}E_k \\ D_i = e_{iq}\varepsilon_q + \kappa_{ik}E_k \end{cases} \qquad (3.1.2)$$

Here c_{pq} is the linear elastic constant, e_{kp} is the linear piezoelectric coefficient, and κ_{ik} is the dielectric constant. It must be pointed out that Eq. (3.1.2) does not contain the contribution from the spontaneous polarization introduced by the polar charge on the ± (0001) polar surfaces [5], which are the top and bottom ends of the NW, respectively. The validity of this approximation will be elaborated later. To keep the notation compact, the so-called Nye two-index notation [6] is used. By considering the C_{6v} symmetry of a ZnO crystal (with wurtzite structure), c_{pq}, e_{kp} and κ_{ik} can be written as:

$$c_{pq} = \begin{pmatrix} c_{11} & c_{12} & c_{13} & 0 & 0 & 0 \\ c_{12} & c_{11} & c_{13} & 0 & 0 & 0 \\ c_{13} & c_{13} & c_{33} & 0 & 0 & 0 \\ 0 & 0 & 0 & c_{44} & 0 & 0 \\ 0 & 0 & 0 & 0 & c_{44} & 0 \\ 0 & 0 & 0 & 0 & 0 & \frac{(c_{11}-c_{12})}{2} \end{pmatrix} \qquad (3.2.1)$$

$$e_{kp} = \begin{pmatrix} 0 & 0 & 0 & 0 & e_{15} & 0 \\ 0 & 0 & 0 & e_{15} & 0 & 0 \\ e_{31} & e_{31} & e_{33} & 0 & 0 & 0 \end{pmatrix} \tag{3.2.2}$$

$$\kappa_{ik} = \begin{pmatrix} \kappa_{11} & 0 & 0 \\ 0 & \kappa_{11} & 0 \\ 0 & 0 & \kappa_{33} \end{pmatrix} \tag{3.2.3}$$

The compatibility equation is a geometrical constraint that must be satisfied by strain ε_{ij} :

$$e_{ilm} e_{jpq} \frac{\partial^2 \varepsilon_{mp}}{\partial x_l \partial x_q} = 0 \tag{3.3}$$

In equation (3.3) the indices are in the normal definition and Nye notation is not used. e_{ilm} and e_{jpq} are Levi-Civita anti-symmetric tensors. For simplicity of the derivation, we assume that the NW bending is small.

Finally, by assuming no free charge $\rho_e^{(b)}$ in the nanowire, Gauss equation must be satisfied:

$$\nabla \cdot \vec{D} = \rho_e^{(b)} = 0 \tag{3.4}$$

This assumption restrict that the governing equation (3.4) applies to insulator piezoelectric materials. But this is a good start to develop more sophisticated models.

3.2 Theory for the first three orders of perturbations

The typical setup of a vertical piezoelectric nanowire that is transversely deflected by a force at the tip. Equations (3.1)-(3.4) along with appropriate boundary conditions give a complete description of a static piezoelectric system. However, the solution of these equations is rather complex, and analytical solution does not exist in many cases. Even for a two-dimensional (2-D) system, the solution would entail a partial differential equation of order six [7]. In order to derive an approximate solution of the equations, we apply a perturbation expansion of the linear equations to simplify the analytical solution [8]. Then, we will examine the accuracy of the perturbation theory in reference to the exact results calculated by finite element method.

In order to derive the piezoelectric potential distributed in the NW for the different orders of electro-mechanical coupled effect, we now introduce a perturbation parameter λ in the constitutive equations by defining $\tilde{e}_{kp} = \lambda e_{kp}$, which is introduced to trace the magnitudes of contributions made by different orders of effects in building the total potential. Consider a virtue material with linear elastic constant c_{pq}, dielectric constant κ_{ik} and piezoelectric coefficient $\tilde{e}_{kp}$. When $\lambda = 1$, this virtue material becomes the realistic ZnO. When $\lambda = 0$, it corresponds to a situation of no coupling between mechanical field and electric field. For virtue materials with λ between 0 and 1, the mechanical field and electric field are both functions of parameter λ, which can be written in an expansion form:

$$\begin{cases} \sigma_p(\lambda) = \sum_{n=0}^{\infty} \lambda^n \sigma_p^{(n)} \\ \varepsilon_q(\lambda) = \sum_{n=0}^{\infty} \lambda^n \varepsilon_q^{(n)} \\ E_k(\lambda) = \sum_{n=0}^{\infty} \lambda^n E_k^{(n)} \\ D_i(\lambda) = \sum_{n=0}^{\infty} \lambda^n D_i^{(n)} \end{cases} \tag{3.5}$$

where the superscript (n) represents the orders of perturbation results. By substituting Eq. (3.5) into Eq. (3.2) for a virtue material with piezoelectric coefficient $\tilde{e}_{kp}$, and comparing the terms in the equations that have the same order of λ, the first three orders of perturbation equations are given as follows:

0^{th} order:
$$\begin{cases} \sigma_p^{(0)} = c_{pq}\varepsilon_q^{(0)} \\ D_i^{(0)} = \kappa_{ik}E_k^{(0)} \end{cases} \tag{3.6}$$

1^{st} order:
$$\begin{cases} \sigma_p^{(1)} = c_{pq}\varepsilon_q^{(1)} - e_{kp}E_k^{(0)} \\ D_i^{(1)} = e_{kq}\varepsilon_q^{(0)} + \kappa_{ik}E_k^{(1)} \end{cases} \tag{3.7}$$

2^{nd} order:
$$\begin{cases} \sigma_p^{(2)} = c_{pq}\varepsilon_q^{(2)} - e_{kp}E_k^{(1)} \\ D_i^{(2)} = e_{kq}\varepsilon_q^{(1)} + \kappa_{ik}E_k^{(2)} \end{cases} \tag{3.8}$$

For equations (3.1), (3.3), (3.4), since there is no explicit coupling, no decoupling process is needed while seeking perturbation solution.

We now consider the solutions of the first three orders. For the 0^{th} order (Eq. 3.6), the solution is for a bent nanowire without piezoelectric effect, which means there is no electric field even with the presence of elastic strain. Here we ignore the contribution from the spontaneous polarization. For the case of ZnO NW, it normally grows with its c-axis parallel to the growth direction. The ±(0001) surfaces at the top and bottom end of the NW are terminated by Zn^{2+} and O^{2-} ions, respectively. The electric field due to spontaneous polarization arising from polar charges on the ±(0001) surface can be ignored for the following two reasons. First, since the NW has a large aspect ratio, the polar charges on the ± (0001) polar surfaces, which are the top and bottom ends of the NW in most of the cases, can be viewed as two point charges. Thus they do not introduce an appreciable intrinsic field inside of the NW. Second, the polar charges at the bottom end of the NW are neutralized by the conductive electrode; while the ones at the top of the NW may be neutralized by surface adsorbed foreign molecules while exposed to air. Further more, even the polar charges at the top end introduce a static potential, it will not contribute to the power generated but shift the potential base line by a constant value, which goes to the background signal, because the polar charges are present and remain constant regardless the degree of NW bending. Therefore, we can take $E_k^{(0)} = 0, D_i^{(0)} = 0$. Consequently, from Eqs. (3.7) and (3.8), we have $\sigma_p^{(1)} = 0$, $\varepsilon_p^{(1)} = 0$, $D_p^{(2)} = 0$, $E_p^{(2)} = 0$. Equations (3.6-3.7) thus become:

0^{th} order: $$\sigma_p^{(0)} = c_{pq}\varepsilon_q^{(0)} \quad (3.9)$$

1^{st} order: $$D_i^{(1)} = e_{kq}\varepsilon_q^{(0)} + \kappa_{ik}E_k^{(1)} \quad (3.10)$$

2^{nd} order: $$\sigma_p^{(2)} = c_{pq}\varepsilon_q^{(2)} - e_{kp}E_k^{(1)} \quad (3.11)$$

The physical meaning of these equations can be explained as follows. Under the different order of approximation, these equations correspond to the decoupling and coupling between the electric field and mechanical deformation: the 0^{th} order solution is purely mechanical deformation without piezoelectricity; the 1^{st} order is the result of direct piezoelectric effect that strain-stress generates an electric field in the NW; and the 2^{nd} order shows up the first feed back (or coupling) of the piezoelectric field to the strain in the material.

In our case as for nanowires bent by AFM tip, the mechanical deformation behavior of the material is almost unaffected by piezoelectric field in the NW. Therefore, as for the calculation of piezoelectric potential in the nanowire, the 1^{st} order approximation may be sufficient. The accuracy of this approximation will be examined in reference to full numerical solutions of the coupled equations (3.1-3.4).

3.3 Analytical solution for a vertical nanowire

To simplify the analytical solution, we assume that the nanowire has a cylindrical shape with a uniform cross-section of diameter *2a* and length l. To further simplify the derivation, we approximate the material elastic constants by an isotropic elastic modulus with Young's modulus E and Poisson ratio ν. This has been found to be an excellent approximation for ZnO. For the convenience of our calculation, we define $a_{pq}^{isotropic}$ to be the inverse of matrix $c_{pq}^{isotropic}$. The strain and stress relation is given by:

$$\begin{pmatrix} \varepsilon_{xx} \\ \varepsilon_{yy} \\ \varepsilon_{zz} \\ 2\varepsilon_{yz} \\ 2\varepsilon_{zx} \\ 2\varepsilon_{xy} \end{pmatrix} = \sum_q a_{pq}^{isotropic}\sigma_q = \frac{1}{E}\begin{pmatrix} 1 & -\nu & -\nu & 0 & 0 & 0 \\ -\nu & 1 & -\nu & 0 & 0 & 0 \\ -\nu & -\nu & 1 & 0 & 0 & 0 \\ 0 & 0 & 0 & 2(1+\nu) & 0 & 0 \\ 0 & 0 & 0 & 0 & 2(1+\nu) & 0 \\ 0 & 0 & 0 & 0 & 0 & 2(1+\nu) \end{pmatrix}\begin{pmatrix} \sigma_{xx} \\ \sigma_{yy} \\ \sigma_{zz} \\ \sigma_{yz} \\ \sigma_{zx} \\ \sigma_{xy} \end{pmatrix} \quad (3.12)$$

In the configuration of the nano-generator, the root end of the nanowire is affixed to a conductive substrate, while the top end is pushed by a lateral force f_y. We assume that the force f_y is applied uniformly on the top surface so that there is no effective torque that twists the nanowire. By Saint-Venant theory of bending [9], the stress induced in the nanowire is given by:

$$\sigma_{xz}^{(0)} = -\frac{f_y}{4I_{xx}}\frac{1+2\nu}{1+\nu}xy \quad (3.13.1)$$

$$\sigma_{yz}^{(0)} = \frac{f_y}{I_{xx}}\frac{3+2\nu}{8(1+\nu)}[a^2 - y^2 - \frac{1-2\nu}{3+2\nu}x^2] \quad (3.13.2)$$

$$\sigma_{zz}^{(0)} = -\frac{f_y}{I_{xx}}y(l-z) \quad (3.13.3)$$

$$\sigma_{xx}^{(0)} = \sigma_{xy}^{(0)} = \sigma_{yy}^{(0)} = 0 \qquad (3.13.4)$$

where $I_{xx} = \int_{CrossSection} x^2 dA = \frac{\pi}{4} a^4$

Eq. (3.13) is the 0th order mechanical solution to equations (3.1), (3.3) and (3.12). Because Saint-Venant principle is used to simplify the boundary condition, solution Eq. (3.13) is valid only for regions far away from the affixed end of the nanowire. Here by "far away" we mean a distance large enough in comparison to the NW diameter. Later, full numerical calculation shows that it would be safe to use Eq. (3.13) when the distance from the substrate is larger than twice the NW diameter.

Eqs. (3.4) and (3.10) give the direct piezoelectric behavior. By defining a remnant displacement $\vec{D}^R$ as

$$\vec{D}^R = e_{kq} \varepsilon_q^{(0)} \hat{i}_k \qquad (3.14)$$

we have:

$$\nabla \cdot (D_i^R + \kappa_{ik} E_k^{(1)}) = 0 \qquad (3.15)$$

From Eqs. (3.14), (3.13), (3.12) and (3.2.2), the remnant displacement is:

$$\vec{D}^R = \begin{pmatrix} -\frac{f_y}{I_{xx} E}(\frac{1}{2} + \nu) e_{15} xy \\ \frac{f_y}{I_{xx} E}(\frac{3}{4} + \frac{\nu}{2}) e_{15}(a^2 - y^2 - \frac{1-2\nu}{3+2\nu} x^2) \\ \frac{f_y}{I_{xx} E}(2\nu e_{31} - e_{33}) y(l-z) \end{pmatrix} \qquad (3.16)$$

It should be noted that it is the divergence of $\vec{D}^R$ rather than $\vec{D}^R$ itself that induces $E_k^{(1)}$. If we simply assume $E_k^{(1)} = (\kappa_{ik})^{-1} D_i^R$, we would arrive at an absurd electric field with non-zero curl. Instead, by defining a remnant body charge:

$$\rho^R = -\nabla \cdot \vec{D}^R \qquad (3.17)$$

and remnant surface charge:

$$\Sigma^R = -\vec{n} \cdot (0 - \vec{D}^R) = \vec{n} \cdot \vec{D}^R, \qquad (3.18)$$

Eq. (3.15) will be transformed into an elementary electrostatic problem with Poisson equation:

$$\nabla \cdot (\kappa_{ik} E_k^{(1)} \vec{i}_i) = \rho^R \qquad (3.19)$$

with charge given by Eq. (3.18) on the cylindrical surface of the nanowire. From Eqs. (3.17) and (3.16), we have

$$\rho^R = \frac{f_y}{I_{xx} E}[2(1+\nu) e_{15} + 2\nu e_{31} - e_{33}] y \qquad (3.20)$$

$$\Sigma^R = 0 \qquad (3.21)$$

It is very important to note that, in Eqs. (3.20) and (3.21), the remnant charge is independent of vertical height z. Therefore, electric potential $\varphi = \varphi(x,y) = \varphi(r,\theta)$ (in cylindrical coordinates) is also independent of z (We will drop the superscript $^{(1)}$ for the first order approximation for simplicity from here). Physically, it suggests that the potential is uniform along z direction except for regions very close to the ends of the nanowire.

Noting that $\kappa_{11} = \kappa_{22} = \kappa_\perp$, the solution of Eqs. (3.19), (3.20) and (3.21) is:

$$\varphi = \begin{cases} \frac{1}{8\kappa_\perp}\frac{f_y}{I_{xx}E}[2(1+\nu)e_{15} + 2\nu e_{31} - e_{33}][\frac{\kappa_0 + 3\kappa_\perp}{\kappa_0 + \kappa_\perp}\frac{r}{a} - \frac{r^3}{a^3}]a^3\sin\theta, r < a \\ \frac{1}{8\kappa_\perp}\frac{f_y}{I_{xx}E}[2(1+\nu)e_{15} + 2\nu e_{31} - e_{33}][\frac{2\kappa_\perp}{\kappa_0 + \kappa_\perp}\frac{a}{r}]a^3\sin\theta, r \geq a \end{cases} \tag{3.22}$$

where κ_0 is the permittivity in vacuum. Eq. (3.22) is the potential inside and outside the NW.

From Eq. (3.22), we have the maximum potential at the surface (r = a) of the NW at the tensile (T) side (θ = - 90^o) and the compressive (C) side (θ = 90^o), respectively, being

$$\varphi_{\max}^{(T,C)} = \pm\frac{1}{\pi}\frac{1}{\kappa_0 + \kappa_\perp}\frac{f_y}{E}[e_{33} - 2(1+\nu)e_{15} - 2\nu e_{31}]\frac{1}{a}. \tag{3.23}$$

By elementary elastic theory, under small deflection, the lateral force deflection f_y is related to the maximum deflection of the NW tip $v_{\max} = v(z = l)$ by [10]:

$$v_{\max} = \frac{f_y l^3}{3EI_{xx}} \tag{3.24}$$

Thus the maximum potential at the surface of the NW is:

$$\varphi_{\max}^{(T,C)} = \pm\frac{3}{4(\kappa_0 + \kappa_\perp)}[e_{33} - 2(1+\nu)e_{15} - 2\nu e_{31}]\frac{a^3}{l^3}v_{\max} \tag{3.25}$$

This means that the electrostatic potential is directly related to the aspect ratio of the NW instead of its dimensionality. For a NW with a fixed aspect ratio, the piezoelectric potential is proportional to the maximum deflection at the tip.

3.4 Piezopotential for a transversely deflected nanowire

In the first case, the wire diameter is $d = 50$ nm, length is $l = 600$ nm, and lateral force applied by AFM tip is 80 nN. To further confirm the validity of omitting the higher order terms in our analytical derivation, we performed finite element method (FEM) calculation for a fully coupled electro-mechanical system using eqs.(3.1-3.4) with for a simplified medium of isotropic elastic modulus tensor and with cylindrical geometry. The boundary condition assumed is that the bottom end of the NW is affixed. The electrical boundary condition at the root is that the substrate is perfectly conductive. ZnO was considered as a dielectric medium. Figure 3.1a and 3.1b are respectively the potential distributions calculated by full FEM in the bent NW as viewed from side and in cross-section, clearly presenting the "parallel plate capacitor" model of the piezoelectric potential except at the bottom. As for the nanogenerator and nanopiezotronics, only the potential distribution in the upper body of the NW matters. Using the analytical Eq. (3.22), the calculated potential distribution across the NW cross-section for a lateral

defection of 145 nm when pushed by a force if 80 nN is presented in Fig. 2c, with the two side surfaces having ±0.28 V piezoelectric potential, respectively. Again we emphasize that, in Eq. (3.22), the potential is independent of z_0 except near the top and the bottom.

A similar calculation has been done for a large size NW with $d = 300$ nm, length $l = 2$ μm, and a lateral force of 1000 nN. The value of pushing force is estimated based on the lateral deflection observed experimentally. In analogous to the case shown for the smaller NW in Fig. 2, this large NW give s a potential distribution of ±0.59 V across its cross-section. Again, the analytical solution is within 6% of the FEM full numerical calculation, clearly proves the validity of our analytical solution. Therefore, the perturbation theory we have presented here is an excellent representation for calculating the piezoelectric potential across a NW, and the analytical results given by Eqs. (3.22-3.25) can be applied to quantitatively understanding the experimentally measured results. From the calculation presented above, a 0.3 V is created between the NW and the AFM tip during mechanical bending.

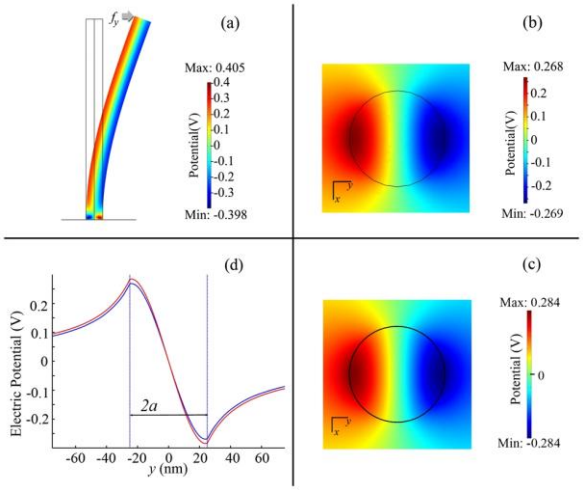

Figure 3.1. Potential distribution for a ZnO nanowire with $d = 50$ nm, $l = 600$ nm at a lateral bending force of 80 nN. (a) and (b) are side and top cross-sectional (at z_0 = 300 nm) output of the piezoelectric potential in the NW given by finite element calculation using fully coupled equations (3.1-3.4), respectively, while (c) is the cross-sectional output of the piezoelectric potential given by analytical equation (3.22). The maximum potential in (b) is smaller than that in (a), because here the potential in the bottom reverse region is larger than that in upper "parallel-plate capacitor" regions. (d) gives a comparison of the line scan profiles from both (b) and (c) (blue is for full FEM, red is for Eq. (3.22)) to show the accuracy of equation (3.22) and the approximations used for deriving it. From [8].

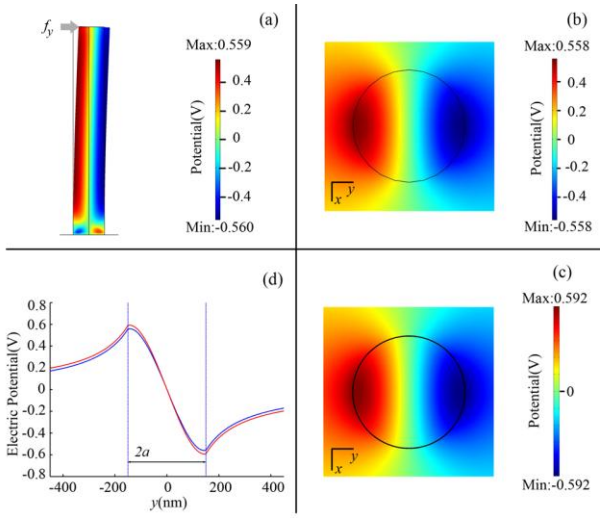

Figure 3.2. Potential distribution for a nanowire with $d = 300$ nm, $l = 2$ μm at a lateral bending force of 1000 nN. (a) and (b) are side and top cross-sectional (at z_0 = 1 μm) output of the piezoelectric potential in the NW given by finite element calculation using fully coupled equations (3.1-3.4), respectively, while (c) is the cross-sectional output of the piezoelectric potential given by analytical equation (3.22). The maximum potential in (b) is almost the same as in (a). (d) gives a comparison of the line scan profiles from both (b) and (c) (blue is for full FEM, red is for Eq. (3.22)) to show the accuracy of equation (3.22) and the approximations used for deriving it. From [8]

3.5 Probing the piezopotential of a transversely deflected nanowire

The piezopotential at the stretched and compressed sides of the PFW have been measured by using a metal tip that is placed either at the tensile side or the compressive side of the NW, while the NW is deflected by air blowing.[11] When a periodic gas flow pulse was applied to a ZnO wire, the wire was bent and a corresponding periodic negative voltage output (Figure 3.3a) was detected by connecting the surface of compressed side of the NW with external measurement circuit. The voltage output detected here was -25 mV. Correspondingly, a periodic positive voltage output (Figure 3.3b) was detected at the stretched side of the wire using a Au coated needle when the ZnO wire was periodically pushed by the Au coated needle. Such measurements were done with the use of a voltage amplifier.

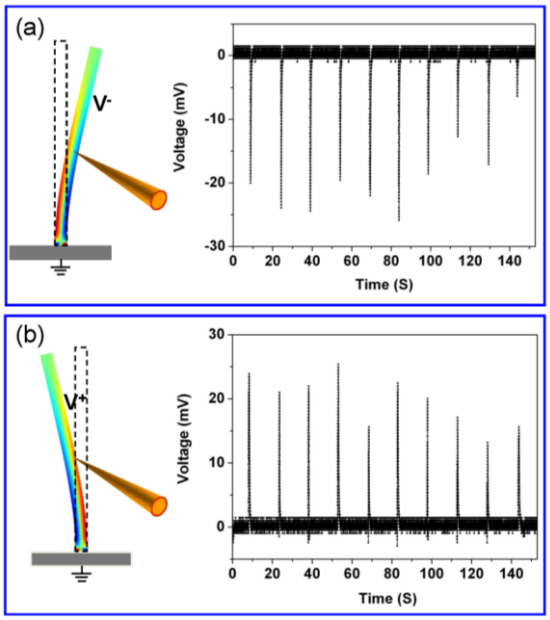

Figure 3.3. Direct measurements of the asymmetric voltage distribution on the tensile and compressive side surfaces of a ZnO wire. (a) By placing a metal tip at the right-hand side and blowing Ar pulses at the left-hand side, negative voltage peaks of ~25 mV were observed once the pulse was on. (b) By quickly pushing and releasing the wire at the right-hand side by a metal tip, a positive voltage peak of ~25 mV was observed for each cycle of the deflection. The frequency of the deflection was once every 15 s.

3.6 Piezopotential for an axial strained nanowire

The main part of a typical two-terminal nanoelectronic device is a hexagonal ZnO nanowire grown along c-axis with its two ends and short segments adjacent to the ends fully embraced by electrodes, where several kinds of forces, including tensile, compression, twisting and combinations of them, act on the nanowire. Our first task is to calculate the piezoelectric potential distribution throughout the nanowire under these forces [12]. In order to simply the system and concentrate on observing how the piezoelectric potential would vary with different applied strain, we assume there is no body force and no free charge in the nanowire by neglecting its conductivity. The fully coupled equations 1-4 can be solved with finite element method (FEM). For simplicity of illustrating the proposed physical model, the charge carriers in ZnO have been ignored, which greatly simplify the numerical approach. Figure 3.4(a) shows a ZnO nanowire without any applied force. The total length of the nanowire is 1200 nm with a 100 nm length of contact domain at each end, and the side length of the hexagonal is 100 nm.

When a stretching force of 85 nN is uniformly acting on the nanowire surfaces surrounded by electrodes in the direction parallel to c-axis, the length of the nanowire would increase for 0.02 nm, which produces a tensile strain of 2×10^{-5}. As shown in Figure 3.4(b), it creates a potential drop of approximately 0.4 V between the two end sides of the nanowire with the +c axis side of higher potential. When the applied force changes to a compressive, the piezoelectric potential reverses with the potential difference remaining 0.4 V but with the –c axis side at a higher potential. As presented in Figure 2(c), the nanowire length decreases for 0.02 nm, revealing a compressive strain of -2×10^{-5}. Note that to produce the same amount of piezoelectric potential, the deformation needed here is much smaller than that in the case of bending a nanowire by a transverse force as we previously demonstrated. Thus the force along the polarization direction (c axis) is easy to produce a high piezoelectric potential.

No matter stretching or compressing, the piezoelectric potential continuously drops from one side of the nanowire to the other, which means that the electron energy continuously increases from the one side to the other. Meanwhile, the Fermi level will be flat all over the nanowire when equilibrium is achieved, since there is no external electrical field. As a result, the electron energy barrier between ZnO and metal electrode will be raised at one side and lowered at the other side, which can be observed experimentally as an asymmetric I-V characteristic. This is the governing principle for understanding the experimental results presented in the following section. As the strain is unavoidable during nanowire device fabrication, we would observe rectifying transport behavior for so many as-fabricated nanowire devices even with two identical electrodes [13].

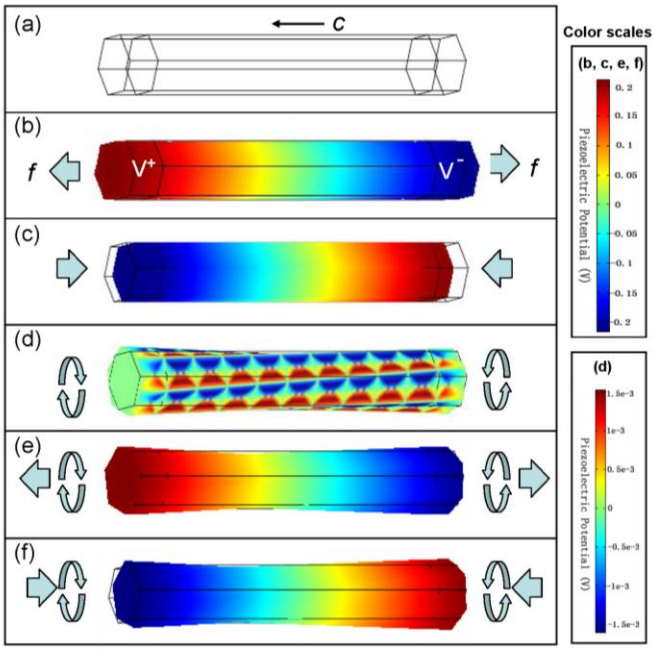

Figure 3.4. Numerical calculation of the piezoelectric potential distribution in a ZnO nanowire without doping. (a) An unstrained ZnO nanowire grown along c-axis with a length of 1200 nm and a hexagonal side length of 100 nm. Two ends of the nanowire are assumed to be surrounded by electrodes for a length of 100 nm. Three-dimensional views of the piezoelectric potential distribution together with deformation shape for the nanowire (b) at a stretching force of 85 nN, (c) at a compressing force of 85 nN, (d) at a twist force pair of 60 nN, (e) at a combination of 85 nN stretching force and 60 nN twist force, (f) at a combination of 8 5nN compressing force and 60 nN twist force. The stretching and compressing forces are supposed to uniformly act on both the end surfaces and side surfaces of the nanowire segments surrounded by electrodes, and the twist force is uniformly applied on the side surfaces of the nanowire segments surrounded by electrodes. The red side is the positive potential side and the blue side is the negative potential side. The potential difference is around 0.4 V. Note the color scale is the same for (b, c, e and f), but (d) has a much smaller scale.

One type of forces that can not be ignored during nanowire manipulation is the twist force. Figure 3.4(d) shows the simulation results when the nanowire has been twisted at its two ends in the opposite direction. There is no electric potential drop along the wire growth direction. Note the magnitude of the created local potential is in the order of mV, much smaller than the case for stretching or compressing. When contacting with electrodes and across the cross-section at the end, the energy barrier between metal and ZnO at one side of the nanowire would be equivalent, thus, a symmetric contact is expected.

For most of the cases in practice, the force is a combination of twist plus tensile, or twist plus compress. As shown in Figure 3.4(e) and figure 3.4(f), there will be a piezoelectric potential drop produced along the wire, while the potential distribution in the cross section of the nanowire is not uniform but with one half higher and the other half lower, similar to the case of pure axial straining.

There are several things to be pointed out here: first, the effect of piezoelectricity on the transport characteristics of metal-ZnO nanowire contains two parts: one is the spontaneous polarization charge effect introduced by the Zn^{2+} and O^{2-} terminating layers at the +c and –c end surfaces; the other is the piezoelectric potential effect. The polarized charges exist at the end surface of the nanowire and can not freely move. They would modulate the local Fermi energy to change the Schottky barrier height

and shape. However, in practice metal-ZnO contacts are not just at the very end surface of nanowire, but also largely at the side surface due to the large contact area of the metal and the nanowire. For most of the time, the contact area in the side surface is much larger than at the end surface. If we only consider the polarization charge effect, electrons can pass by the side surface contact where there is no energy barrier.

Second, the above calculation is based on Lippman theory, since we assume there is no free charge carriers for simplicity and the whole system is isolated. The as-synthesized ZnO nanostructures are typically n-type with a typical donor concentration of 1×10^{17}cm^{-3}. Theoretical calculations based on statistical electron distribution in conduction band show that the free electrons tend to accumulate at the positive potential side of the nanowire at thermal equilibrium. Therefore, the effect of the free carriers is to partially, if not all, screen the positive piezoelectric potential, while no change to the negative piezoelectric potential. In such a case, the calculation results presented in figure 2 can still be adopted for explaining practical experimental results except the magnitude of the positive potential has to be reduced to balance the effect of the free carriers.

Third, strain will not only induce piezoelectric effect in ZnO, but also cause band structure variation. The generated deformation potential can also change the Schottky barrier height: under tensile strain the barrier will be lowered, and under compressive strain the barrier will be raised. However, the variations at two ends of nanowire are identical and in the same tendency, and it cannot change a symmetric I-V curve into a rectifying I-V behavior. This is the piezoresistance effect.

3.7 Equilibrium piezotential in a doped semiconductive nanowire

The Lippman theory can be used to describe bent piezoelectric nanowires when the donor concentration is extremely low, so that the conductivity can be neglected. However, the as-grown ZnO nanowires are typically n-type due to unavoidable point defects. For semiconductor materials with a significant amount of free electrons, the Lippman theory cannot be directly applied, because the free charge carriers are able to distribute all over the material. The statistics of electron/holes must be considered besides the phenomenological thermal dynamics. The main objective of this section is to present a macroscopic-statistical model of piezoelectricity in a laterally bent semiconductive nanowire by considering its moderate conductivity in a normal doping range.

3.7.1 Theoretical Frame

Previous results indicated that, for a ZnO NW with zero free charge carrier density, the tensile surface would show a positive piezoelectric potential, and the compressive side would show a negative potential (In this context, by "piezoelectric potential" we mean that the potential is created by the polarizations of anions and cations in the NW; these charges cannot freely move as long as the strain is preserved.). In order to focus on the core physics by preventing the digression to the less relevant problems about the interface heterojunctions, we assume that the substrate is also made of ZnO. Such a situation occurs for the ZnO nanowires grown on GaN substrates via the VLS method[23], because a thin ZnO film or ZnO walls usually form beneath the nanowires. Our task is to calculate the piezoelectric potential when thermodynamic equilibrium is achieved in the laterally bent nanowires [14].

It is well known that when free electrons/holes are present in a piezoelectric material, the carriers will redistribute due to the electric field established by the polarization. One famous application of such a redistribution effect is in the GaN/AlGaN HEMTs, where electrons are accumulated at the heterojunction to create a 2D Electron Gas (2DEG) [15]. For piezoelectric nanowire applications, the mechanical behavior is more complicated, but the physical pictures are essentially the same. Instead of using a fully coupled constitutive equation, we only write the mechanical equilibrium and the direct piezoelectric effect:

$$\begin{cases} \sigma_p = c_{pq}\varepsilon_q \\ D_i = e_{iq}\varepsilon_q + \kappa_{ik}E_k \end{cases} \tag{3.26}$$

where σ is the stress tensor, ε is the strain, $\vec{E}$ is the electric field, and $\vec{D}$ is the electric displacement. κ_{ik} is the dielectric constant, e_{kp} is the piezoelectric constant, and c_{pq} is the mechanical stiffness tensor. The Voigt-Nye notation[24] is used. Substituting the second equation into the Gauss's law, we get the equation for the electric field:

$$\nabla \cdot \vec{D} = \frac{\partial}{\partial x_i}(e_{iq}\varepsilon_q + \kappa_{ik}E_k) = \rho_e^{(b)} = ep - en + eN_D^+ - eN_A^- \qquad (3.27)$$

where p is the hole concentration in the valance band, n is the electron concentration in the conduction band, N_D^+ is the ionized donor concentration, and N_A^- is the ionized acceptor concentration. Because the as-grown ZnO NWs are usually *n*-typed, we adopt $p = N_A^- = 0$. By introducing

$$\vec{D}^R = e_{kq}\varepsilon_q \hat{i}_k \qquad (3.28.1)$$

as the polarization due to piezoelectricity and

$$\rho^R = -\nabla \cdot \vec{D}^R \qquad (3.28.2)$$

as the corresponding piezoelectric charge, equation 2 can be rewritten for the electric potential φ:

$$\kappa_{ik}\frac{\partial^2}{\partial x_i \partial x_k}\varphi = -(\rho^R - en + eN_D^+) \qquad (3.29)$$

The surface charge due to piezoelectricity is calculated by $\Sigma^R = -\vec{n} \cdot \Delta\vec{D}^R$, where $\Delta\vec{D}^R$ is the change of $\vec{D}^R$ astride the material surface and $\vec{n}$ is the normal to the surface. For simplicity, we have ignored the surface charges introduced by polar surfaces of ZnO.

The redistribution of electrons under thermodynamic equilibrium is given by the Fermi-Dirac statistics:

$$n = N_c F_{1/2}(-\frac{E_c(\vec{x}) - E_F}{kT}) \qquad (3.30.1)$$

$$N_c = 2(\frac{2\pi m_e kT}{h^2})^{\frac{3}{2}} \qquad (3.20.2)$$

where the conduction band edge $E_c(\vec{x})$ is a function of space coordinates. N_c, the effective state density of conduction band, is determined by the effective mass of conduction band electrons m_e and the temperature T. Due to the large strain, the deformation potential might be important. To be specific, the band edge shift ΔE_c is the sum of the electro-static energy part and the deformation potential part:

$$E_c - E_{c_0} = \Delta E_c = -e\varphi + \Delta E_c^{deform} = -e\varphi + a_c\frac{\Delta V}{V} \qquad (3.31)$$

where E_{c_0} is the conduction band edge of a free-standing un-deformed semiconductor material; $\Delta E_c^{deform} = a_c \Delta V / V$ is the band edge shift due to the deformation potential [16], which is proportional to the relative volume change $\Delta V / V$, and a_c is the deformation potential constant. Finally, the activation process of the donors is given by:

$$N_D^+ = N_D \frac{1}{1+2\exp(\frac{E_F - E_D}{kT})} \tag{3.32}$$

where $E_D(\vec{x}) = E_C(\vec{x}) - \Delta E_D$ is the position-dependent donor energy level. The constant ΔE_D is the activation energy of the donors. N_D is the concentration of the donors.

3.7.2 Calculated piezopotential with considering doping

The piezoelectric potential in a bent ZnO nanowire with moderate charger carrier density can be calculated. It should be pointed out that equations (3.29-3.32) are valid only when the system dimension is not too small. For small systems, strong confinement requires quantum mechanical considerations due to discrete bound states. Such as an elaboration in theory is necessary for 2DEG in GaN/AlGaN HEMTs, in which the quantum effect is important. In the following section we will conduct the calculation for nanowires with diameter ~50 nm or larger, where non-quantum mechanical calculation is still acceptable.

The Fermi level E_F is flat all over the bent semiconductor nanowire when thermodynamic equilibrium is assumed. Because the nanowires are assumed to be grown on a substrate whose dimension is much larger than the nanowire, the substrate can be taken as a vast reservoir that pins the Fermi level. In this paper we assume that the substrate is made of the same material as the nanowire itself. For nanowires making direct heterogeneous junctions with the substrate, depletion regions or charge-accumulation regions may form at the bottom junctions, which will not be elaborated in this paper.

Symmetry is used so we only need to solve for the half-space of $x > 0$. Solution in the other half of space can be immediately derived by using the mirror symmetry of $x = 0$ plane. In order to help the convergence, we first linearize equ.(3.30.1) and equ.(3.32) by introducing a extreme case of ultra-high temperature T_{high}. For the convenience of calculations as presented in equ.(3.30.1) and equ. (3.32), we define the following variables:

$$\eta = -\frac{E_c(\vec{x}) - E_F}{kT} \text{ and } \eta_D = \frac{E_F - E_D}{kT} = \eta + \frac{\Delta E_D}{kT} \tag{3.33}$$

When $T = T_{high}$ is large, η and η_D are no longer position-dependent; the problem is thus linearlized for easy solution. As a convergence tool, T_{high} by itself is not required to have realistic physical meaning. Nevertheless, the solutions under high temperature $T = T_{high}$ do evince some meaningful insight in physics. In fact, $\eta \approx \eta_D \approx \ln(\frac{N_D}{N_C})$ when $T = T_{high}$, therefore $N_D^+ = n$ and equ.(3.29) would give an un-screened solution as though there were neither donors nor free charge carriers in ZnO. As the system "cool down" from T_{high} to the realistic temperature, the equations become more and more non-linear. The value of η dictates how degenerate the system is, with $\eta > -3$ being regarded as the highly degenerate case. As we will see later in the results, the problem will involve some degree of degeneracy even when the donor concentration is relatively low. This is analogous to the 2DEG regions in GaN/AlGaN HEMTs [11], where electrons accumulate even when the local doping level is small.

Figure 3.5a shows the equal-potential lines for $N_D = 1\times10^{17} cm^{-3}$ and $T = 300K$ on the cross section plane x = 0, which is right through the axis of the nanowire. Figure 2b gives the equal-potential lines on a cross section perpendicular to the nanowire axis and at a height of $z = 400nm$. The electrostatic calculation is done under a small strain assumption, in which the difference between the Lagrangian reference frame and Eulerian reference frames is neglected. For comparison purpose, the results received under the un-realist temperature of $T = T_{high} = 300{,}000K$ is also plotted in Fig. 2c and Fig. 2d, which correspond to the situation when ZnO were an insulator without any free charge carriers.

The electric potential maximum in the positive side of the nanowire is significantly reduced from ~0.3 V in Fig. 3.5d, which corresponds to an insulator case, to less than 0.05 V in Fig. 3.5b, which considers the moderate doping in ZnO. On the other hand, the potential in the compressed side (negative potential side) is very well preserved. This is consistent with the experimental observation that only negative pulses are observed in an AFM based nanogenerator experiment using n-type ZnO nanowires[7]. It is also consistent with the observation that the output negative potential peak appears only when the AFM tip touches the compressed side of the nanowire. The decrease of positive potential in this model is due to the in-flow of electrons from the substrate where free charges are abundant. When positive polarization charges $\rho^R > 0$ try to create a positive local potential $\varphi > 0$, it would result in a downward bending of the local conduction band. When η gets

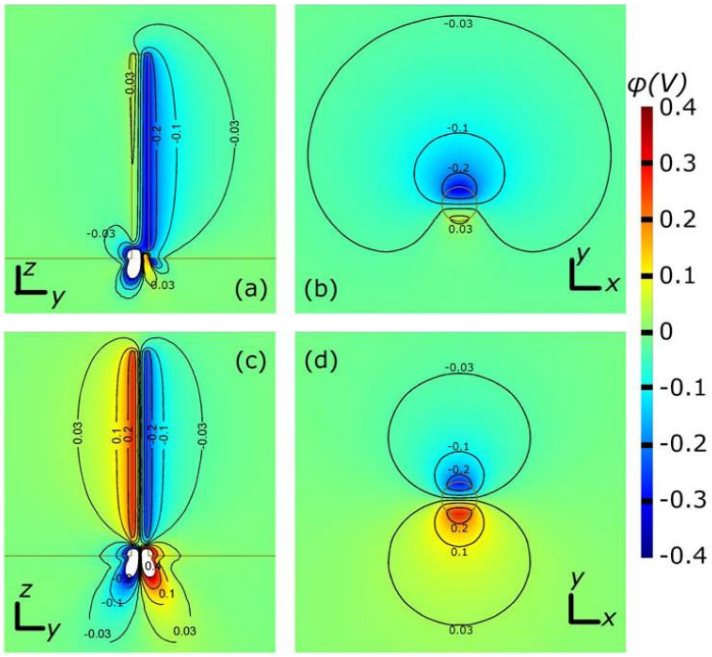

Figure 3.5. Plot of calculated piezoelectric potential φ for $N_D = 1\times10^{17} cm^{-3}$. For easy plot, the bending shape of the nanowire is not presented. Besides the color plot, equi-potential contours for $\varphi = -0.4V$, $-0.2V$, $-0.1V$, $-0.03V$, $0.03V$, $0.1V$, $0.2V$ and $0.4V$ are also superimposed. The dimension of the nanowire is: a=25nm, l=600nm and the external force is f_y=80 nN. (a) Plot of φ for $T = 300K$ at a cross section of $x = 0$. The blank region at the bottom is the region where $\varphi < -0.4V$. The detail in this region is over saturated for display purpose to optimize the color scale in order to show φ in the nanowire. In this paper, we mainly focus on the behavior in the nanowire and will leave the details about the bottom reverse region for future research. (b) Cross section plot of the electric potential for $T = 300K$ at the height $z = 400nm$. Here only half of the space $x > 0$ is calculated using the mirror symmetry of $x = 0$ plane. The plot in $x < 0$ region is derived by a simple reflection of the solution in $x > 0$ region. (c and d) Calculation for an extremely high temperature case of $T = T_{high} = 300000K$ to test the convergence of the result in reference to the result received from nanowires without doping. Again the extreme peaks are over saturated. (c) shows the cross section $x = 0$, (d) is the cross section plot of the electric potential for at the height $z = 400nm$. From [14]

close to or even bigger than zero, a large amount of free electrons would be injected from the substrate reservoir into the nanowire to screen the positive potential.

In the negative potential side (compressed side of the nanowire), however, free charge carriers are depleted due to large negative value of η, leaving only $\rho^R + eN_D^+$ as the net charge in equ. (4). Let us use the analytical equation derived in section 3.3 to evaluate the concentration of ionic polarization charge. Substituting a = 25 nm, l = 600 nm and f_y = 80 nN into $\rho^R = \frac{f_y}{I_{xx}E}[2(1+\nu)e_{15} + 2\nu e_{31} - e_{33}]y$, where $I_{xx} = \frac{\pi}{4}a^4$, one gets the typical piezoelectric polarization charge density $\rho_R^{y=a}/e \sim -8.8\times10^{17}cm^{-3}$ near the wire surface $y = a$, where e is the charge of a single electron. When $N_D = 1\times10^{17}cm^{-3}$, ρ_R cannot be totally screened in the negative side even if all of the electrons are depleted because N_D is much smaller than $\rho_R^{y=a}/e$. For a nanowire with a very high donor concentration $N_D > 10^{18}cm^{-3}$, total neutralization with $\varphi \approx 0$ could occur everywhere. Namely, a NW with a high concentration of free charge carriers is expected to exhibit very small piezoelectric potential. This result agrees to the experimental measurement of a nanogenerator under the illumination of UV light. In reality, the doping level in as-grown un-intentionally doped ZnO nanowires is much smaller than $10^{18}cm^{-3}$.

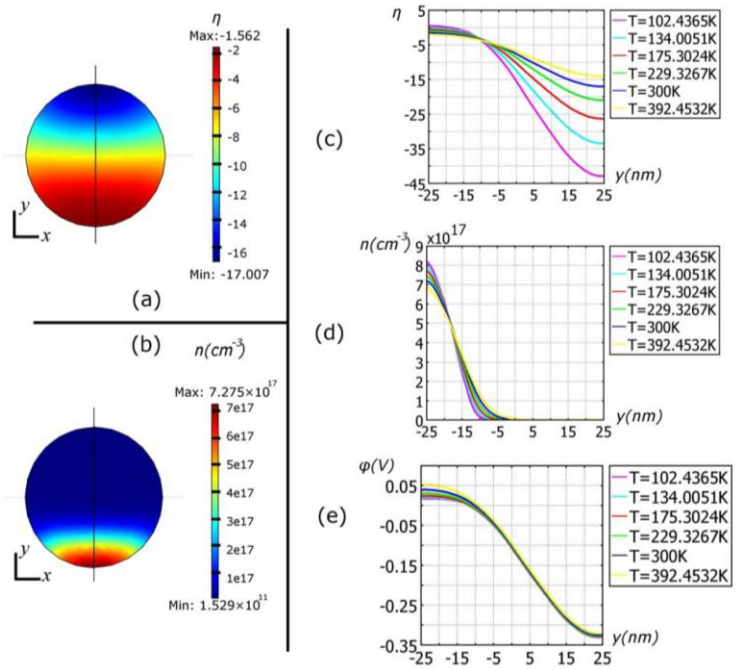

Figure 3.6. (a and b) Cross section color plot of parameters η (a) and local electron density n (b) for $N_D = 1\times10^{17}cm^{-3}$ and $T = 300K$ at the height $z = 400nm$. Here only half of the space $x > 0$ is calculated using the mirror symmetry of $x = 0$ plane. The plot in $x < 0$ region is derived by a simple reflection of the solution in $x > 0$ region. (c-e) Line plot of η, n and φ under different temperatures along the diameter in (a) and (b). The horizontal axis is the *y*-coordinate.

The band edge shift ΔE_c comprises of two parts: electric potential part and the deformation potential part. The Saint-Venant solution for stress in the nanowire is: $\sigma_{zz} = -\frac{f_y}{I_{xx}}y(l-z)$, $\sigma_{xx} = \sigma_{xx} = 0$, therefore,

$$|\Delta E_c^{deform}| = a_c |\Delta V/V| = a_c |Tr(\varepsilon)| = a_c \left|\frac{1-2\nu}{E} Tr(\sigma)\right| = \left| -a_c \frac{1-2\nu}{E} \frac{f_y}{I_{xx}} y(l-z) \right|$$

$$< a_c \frac{1-2\nu}{E} \frac{f_y}{I_{xx}} \cdot a \cdot l = 46meV$$

As a posterior observation, this value is much smaller than the negative side value of $|e\varphi|$, therefore the deformation potential could have been neglected before the calculation if the potential magnitude in the negative side is the main concern. It also indicates that the negative potential observed in experiments [7] should not be due to the deformation potential band-structure shift, but mainly due to piezoelectric effect.

Degeneracy is significant in the screened positive side as seen in the η plot in Fig. 3.6a. The degeneracy in the charge accumulation region is due to the piezoelectric effect but not due to large donor concentration or low temperature. Before deformation, $\eta = \eta_0 = -3.77$ for $N_D = 1\times10^{17} cm^{-3}$ at $T = 300K$; this is below the degeneracy criterion. In order to investigate how temperature affects the free charge carrier distribution and the final electric potential, we plotted n, η and φ for different temperatures (Figs. 3.6c d and e). The variance of n, η and φ is small for temperatures in a range of $100K < T < 400K$. The free carrier concentration is $n \sim 10^{15} cm^{-3}$ in the depletion region and $n \sim \rho_R / e + N_D \sim 10^{18} cm^{-3}$ in the charge accumulation region as seen in Fig. 3.6b. The boundary between the charge accumulation region and the depletion region is quite sharp. We notice that the width of the charge accumulation region is much smaller than the wire diameter a, which implies strong confinement of the conduction band electrons. This strong confinement might result in stronger quantum effect than that seen in the NW's undeformed state.

In order to investigate how the variance of N_D affects the piezoelectric potential, we plot the (a) electric potential φ, (b) parameter η, (c) free electron concentration n and (d) activated donor center concentration N_D^+ for different donor concentrations $0.6\times10^{17} cm^{-3} < N_D < 2.0\times10^{17} cm^{-3}$ under $T = 300K$ in Fig. 3.7. It is seen that the electric potential φ is rather insensitive to the donor concentration in this regime. However, it is expected that φ will be completely neutralized when $N_D > 10^{18} cm^{-3}$, as we have already discussed. In the y<0 region (stretched side of the nanowire), degeneracy is always significant due to large η value (Fig. 3.7b). Therefore, electrons will be accumulated in the y<0 side as seen in figure 4c and depleted in the compressed side of the nanowire (y>0). On the other hand, the donor centers are not well activated in the y<0 side as seen in figure 3.7d, which makes the local electric charge density $\rho^R - en + eN_D^+$ in the y<0 side even smaller.

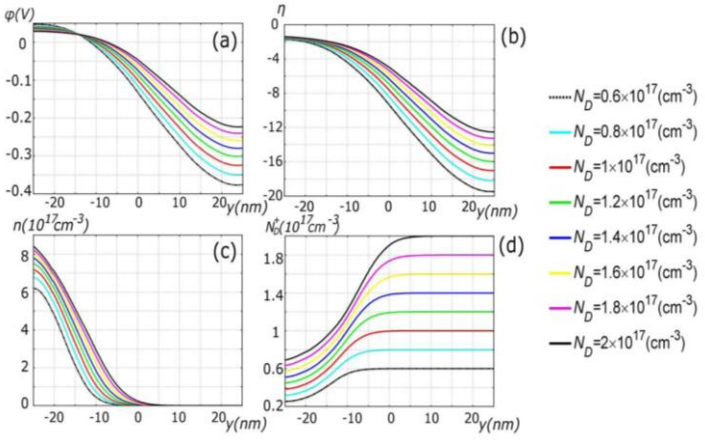

Figure 3.7. (a) Piezoelectric potential φ, (b) parameter η, (c) free electron concentration n and (d) activated donor center concentration N_D^+ for different donor concentrations $0.6\times10^{17} cm^{-3} < N_D < 2.0\times10^{17} cm^{-3}$. The dimension of the nanowire is: a=25nm, l=600nm and the external force is f_y=80nN. $T = 300K$.

3.7.3 Effect of doping concentration

The main objective of this section is to investigate the influence of different parameters on the equilibrium piezoelectric potential distribution in a deformed ZnO semiconductive NW. In particular, we will calculate the electric potential distribution when the thermodynamic equilibrium among free charge carriers is achieved, for NWs under different doping concentrations, different applied forces and different geometric configurations [17].

A ZnO nanowire epitaxially grown along the *c* axis, is laterally bent by a force f_y exerted at the top. An axial symmetric model is chosen in order to simplify the calculations. This means that the equation are solved for the half-space $x > 0$ and the solutions are eventually derived using the mirror symmetry of the $x = 0$ plane.

Figure 3.8 shows the influence of the donor concentration on both the equilibrium piezoelectric potential and the local electron density. The color-plot of the piezoelectric potential in figure 1a, 1b and 1c represents the result of low (0.5×10^{17} cm^{-3}), medium (1×10^{17} cm^{-3}) and high (5×10^{17} cm^{-3}) donor concentrations N_D, respectively. In figures 1d and 1e we plot the electric potential φ and the free electron concentration *n* for different donor concentrations between 0.05×10^{17} cm^{-3} and 5×10^{17} cm^{-3}, under T = 300K. The electric potential φ in the stretched side, showing a positive potential, is less sensitive than the compressed negative side to the increase of donor concentration N_D. The electric potential φ is almost completely screened for $N_D = 5 \times 10^{17}$ cm^{-3}. The reason for the screening of the potential in the compressed side of the nanowire is that free electrons will be depleted in this region, while they will accumulate at the stretched side. Moreover, the decrease of the positive potential is due to the inflow of free electrons from the substrate reservoir, where free charges are abundant. This increase in free electron concentration is clearly evident in figure 3.8e.

Figure 3.9 shows the influence of the applied force to the equilibrium potential distribution and local electron density. All of the other parameters are kept constant: nanowire length 600 nm, radius 25 nm and donor concentration $N_D = 1 \times 10^{17}$ cm^{-3}. The force has been chosen to vary in the range 40

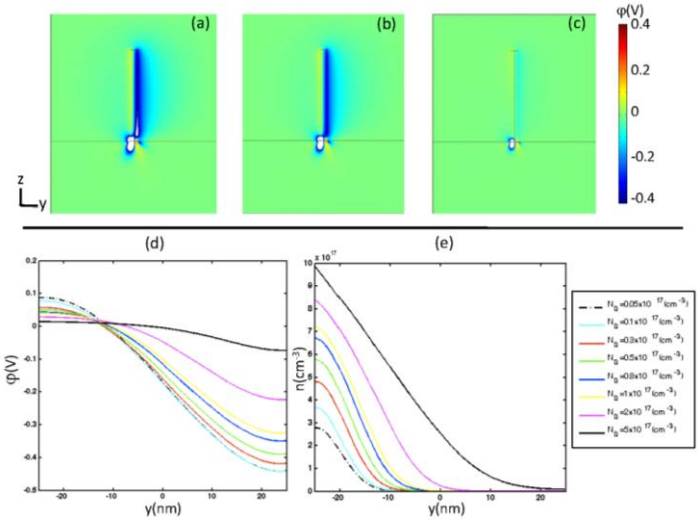

Figure 3.8. Color plot of the calculated piezoelectric potential at a cross section of x = 0, for donor concentrations $N_D = 0.5 \times 10^{17}$ cm^{-3} (a), $N_D = 1 \times 10^{17}$ cm^{-3} (b) and $N_D = 5 \times 10^{17}$ cm^{-3} (c). The dimensions of the nanowire are L = 600 nm and a = 25 nm; the external force is f_y =80 nN. (d) Piezoelectric potential and (e) local electron density for different donor concentrations 0.05×10^{17} cm^{-3} < N_D < 5×10^{17} cm^{-3}, for T = 300 K. The line plot is along the diameter of the nanowire, at z = 400 nm.

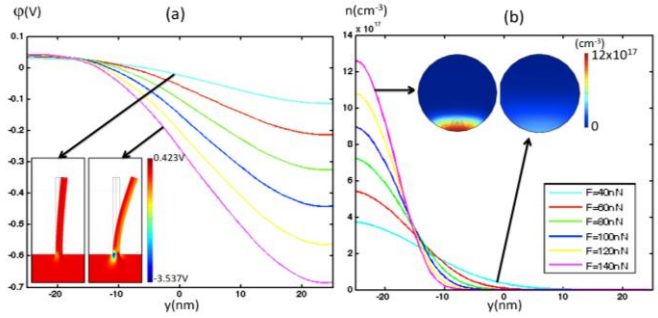

Figure 3.9. (a) Piezoelectric potential and (b) local electron density for different external forces 40 nN < F < 140 nN. (a) also shows the color plot of the calculated potential at a cross section of x = 0 for F = 40 nN and F=140 nN. (b) also shows the color plot of the calculated free electron distribution at a cross section of the nanowire at the height of 400 nm, for F = 40 nN and F = 140 nN. Here only half of the space $x > 0$ is calculated using the mirror symmetry of x) 0 plane. The plot in the $x < 0$ region is derived by a simple reflection of the solution in the $x > 0$ region. From [17].

nN < F < 140 nN. In the calculations, the force has been applied to the top surface of the nanowire in order to avoid punctual deformations. When increasing the applied force, the electric potential (in figure 3.9a) of the compressed side increases, reaching the value of about 0.7 V for the maximum applied force. The free electron concentration (fig. 3.9b) also increases in the stretched side when increasing the force, because of the increase in the polarization charges due to highest strains. Figure 3.9a also shows the color-plots of the electric potential and the scaled deformations for lower and higher applied forces. Figure 3.9b shows the color-plot for the free electron concentration, at the cross-section at z = 400 nm. This last figure is obtained by means of the mirror symmetry of the x = 0 plane.

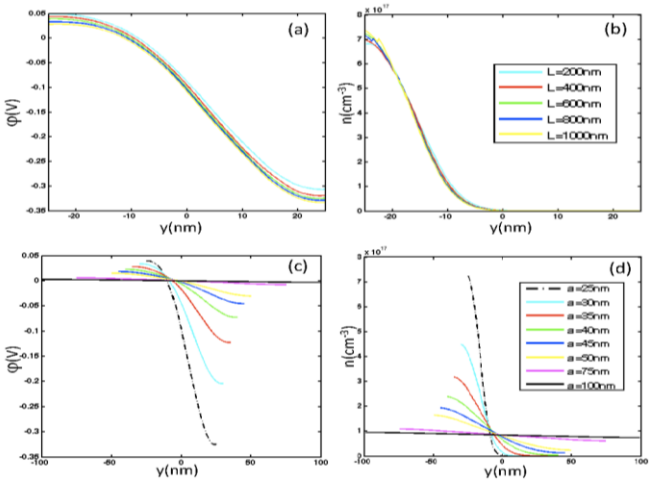

Figure 3.10. (a) Piezoelectric potential and (b) local electron density for different lengths of the nanowire 200 nm < L < 1000 nm. (c) Piezoelectric potential and (d) local electron density for different radius of the nanowire in 25 nm < a < 100 nm. The donor concentration is $N_D = 10^{17}$ cm^{-3}, at T = 300 K; the external force is f_y = 80 nN. The line plot is along the diameter of the nanowire, at z = 400 nm.

The influence of the geometric dimensions of the nanowire on the electric potential and local electron density has also been investigated as shown in figures 3.10 and 3.11. While keeping the radius of the nanowire at 25 nm, the donor concentration at $N_D = 10^{17}$ cm^{-3} and the applied force at 80 nN, the length of the nanowire has been varied in the range 200 nm < L < 1000 nm. Figures 3.9a and 3.9b show that the length of the nanowire does not influence either the electric potential distribution or the free electron density.

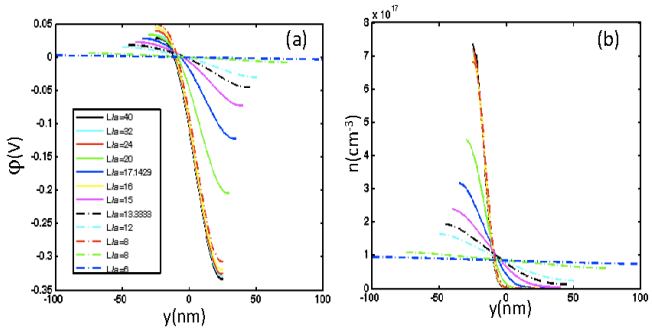

Figure 3.11. Piezoelectric potential and (b) local electron density for different aspect ratio of the nanowire in 6 < L/a < 40. The donor concentration is $N_D = 10^{17}$ cm^{-3}, at T = 300 K; the external force is f_y = 80 nN. The line plot is along the diameter of the nanowire, at z = 400 nm.

When keeping the length of the nanowire constant at 600 nm, the effect of the variation of the radius has been investigated in the range 25 nm < a < 100 nm. The results are shown in figure 3.9c and 3.9d for electric potential and free electron concentration respectively. The increase in the radius decreases both the parameters; the electric potential is almost neutralized for a radius of 100 nm. It has to be noted that the increase of the radius also decreases the magnitude of the strain experienced by the nanowire, as we are keeping the applied force constant.

Figure 10 shows the influence of the aspect ratio L/a, on the electric potential and free electron distribution. It summarizes the results previously described in figures 3.9: the length variation does not affect the variables, while the increase in the radius dimension decreases both of them.

3.7.4 Effect of carrier type

Instead of assuming the n-type doping as for as –synthesized ZnO nanowires, it is possible to receive stable p-type ZnO nanowires. The stability of the p-type doping in nanowires is possibly due to the dislocation free volume and the presence of high concentration of vacancies near the surface of the nanowires. We have calculated the piezoelectric potential in a bent p-type NW taking a finite carrier density into consideration. For a laterally bent ZnO NW without any doping, the stretched side exhibiting positive piezoelectric potential and the compressed side negative piezoelectric potential. With a finite p-type doping, the holes tend to accumulate at the negative piezoelectric potential side. The negative side is thus partially screened by holes while the positive side of the piezoelectric potential preserves. Using the Poisson equation and the statistical Fermi-Dirac distribution of charge carriers, for a typical ZnO NW with diameter 50 nm, length 600 nm, acceptor concentration N_A = 1 x 10^{17} cm^{-3} under a bending force of 80 nN, the piezoelectric potential in the negative side is > -0.05 V and is ~ 0.3 V at the positive side (Fig. 3.12). This means that the piezopotential in p-type nanowire is dominated by the positive piezopotential at then tensile side of surface [18].

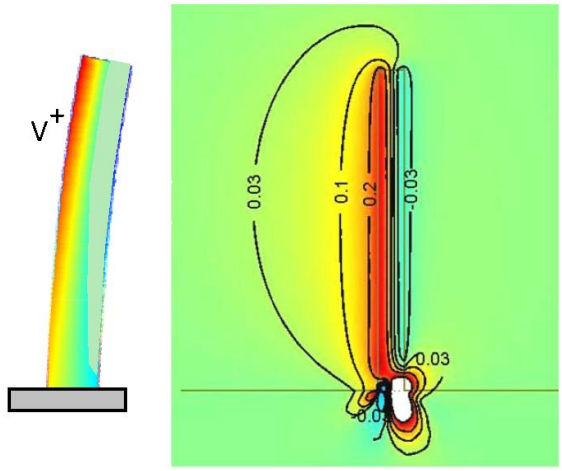

Figure 3.12. Calculated piezoelectric potential distribution in a p-type ZnO nanowire when it is deflected from the left hand side by a transverse force.

References for Chapter 3:

[1] H.J. Xiang, J.L. Yang, J.G. Hou, Q.S. Zhu, *Applied Physics Letters* **89**, 223111 (2006).
[2] Z.C. Tu, X. Hu, *Physical Review B* **74**, 035434 (2006).
[3] A.J. Kulkarni, M.Z. a. F.J.K., *Nanotechnology* **16**, 2749 (2005).
[4] P.J. Michalski, N. Sai, E.J. Mele, *Physical Review Letters* **95**, 116803 (2005).
[5] Z.L. Wang, X.Y. Kong, Y. Ding, P.X. Gao, W.L. Hughes, R.S. Yang, Y.S. Zhang, *Advanced Functional Materials* **14**, (10), 943 (2004).
[6] J.F. Nye, *Physical Properties of Crystals*. Oxford University Press: 1957.
[7] Q.H. Qin, *Fracture Mechanics of Piezoelectric Materials*. WIT Press: Southampton, UK, 2001.
[8] Y.F. Gao, Z.L. Wang, *Nano Lett.* **7**, 2499 (2007).
[9] R.W. Soutas-Little, *Elasticity*. Dover Publications: Mineola, NY, 1999.
[10] L.D, Landau, E.M. Lifshi ät ès, *Theory of elasticity*. Pergamon Press, Addison-Wesley Pub. Co., London, Reading, Mass., 1959.
[11] J. Zhou, P. Fei, Y.F. Gao, Y.D. Gu, J. Liu, G. Bao, Z.L. Wang, *Nano Letters*, 8, 2725 (2008).
[12] Z.Y. Gao, J. Zhou, Y.D. Gu, P. Fei, Y. Hao, G. Bao, Z.L. Wang, *J. Appl. Physics* **105**, 113707 (2009).
[13] C.S. Lao, J. Liu, P.X. Gao, L.Y. Zhang, D. Davidovic, R. Tummala, Z.L. Wang, *Nano Lett.*, **6** 263 (2006).
[14] Y.F. Gao, Z.L. Wang, *Nano Letters* **9**, 1103 (2009).

[15] F. Sacconi, A. Di Carlo, P. Lugli, H. Morkoc, *Ieee Transactions on Electron Devices* **48**, (3), 450 (2001).
[16] W. Shan, W. Walukiewicz, J.W. Ager, K.M. Yu, Y. Zhang, S.S. Mao, R. Kling, C. Kirchner, A. Waag, *Appl Phys Lett.* **86**, (15), 153117 (2005).
[17] G. Mantini, Y.F. Gao, A. D'Amico, C. Falconi, Z.L. Wang[×], *Nano Research* **2**, 624 (2009).
[18] M.P. Lu, J.H. Song, M.Y. Lu, M.T. Chen, Y.F. Gao, L.F. Chen, Z.L. Wang, *Nano Letters* **9**, 1223 (2009).

Chapter 4

The principles of nanogenerators

The concept of the nanogenerator (NG) was first introduced by measuring the piezoelectric properties of ZnO nanowires (NWs) using an atomic force microscope (AFM) [1]. ZnO has a wurtzite structure, in which the Zn cations and O anions form a tetrahedral coordination. The lacking of center symmetry results in piezoelectric effect, utilizing which a mechanical stress/strain can be converted into electrical voltage, and vice versa, owing to the relative displacement of the cations and anions in the crystal. Our first step is to introduce the fundamental principles of nanogenerator.

4.1 Nanogenerators using vertical aligned nanowires

4.1.1 The concept of piezoelectric nanogenerators

As a first step of proof of concept, our study is based on aligned ZnO NWs grown on a conductive solid substrate (Fig. 4.1a). [2, 3, 4] The measurements were performed by AFM using a Si tip coated with Pt film, which has a cone angle of 70°. The rectangular cantilever had a calibrated normal spring constant of 0.76 N/m (see Fig. 4.1c). In the AFM contact mode, a constant normal force of 5 nN was maintained between the tip and sample surface. The tip scanned over the top of the ZnO NW, and the tip's height was adjusted according to the surface morphology and local contacting force (Fig. 4.1b). The thermal vibration of the NWs at room temperature is negligible. For the electric contact at the bottom of the nanowires, silver paste was applied to connect the (large) ZnO film on the substrate surface with the measurement circuit. The output voltage across an outside load of resistance R_L = 500 megohm was continuously monitored as the tip scans over the nanowires (note the defined polarity of the voltage signal). No external voltage was applied in any stage of the experiment.

Experimentally, both the topography (feedback signal from the scanner) and the corresponding output voltage images across the load were recorded simultaneously when the AFM tip was scanned over the aligned NW arrays. In contact mode, as the tip scanned over the vertically aligned NWs, the NWs were bent consecutively. The bending distance was directly recorded in the topography image, from which the maximum bending deflection distance and the elastic modulus of the NW as well as the density of NWs that have been scanned by the tip are directly derived.

In the corresponding voltage output image for each contact

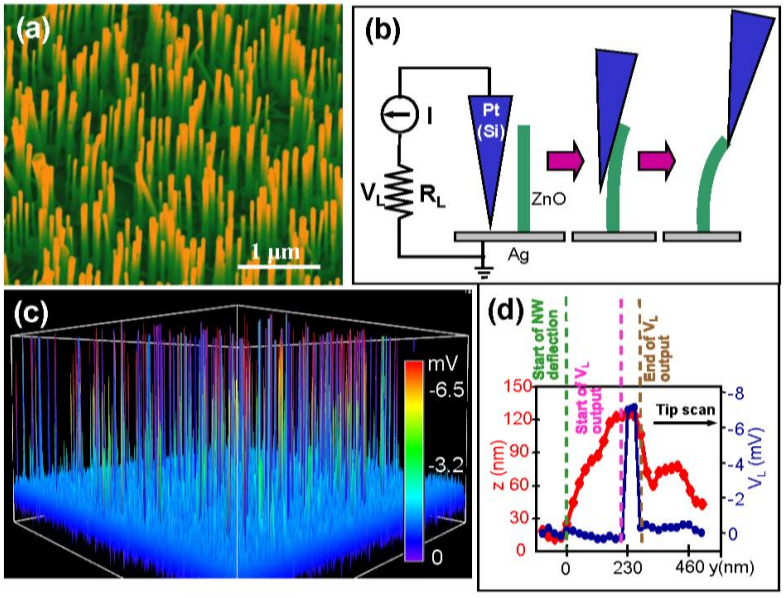

Figure 4.1 (a) Scanning electron microscopy images of aligned ZnO NWs grown on GaN/sapphire substrate. (b) Experimental set up and procedures for generating electricity by deforming a piezoelectric NW using a conductive AFM tip. The AFM scans across the NW arrays in contact mode. (c) Output voltage image of the NW arrays when the AFM tip scans across the NW arrays. (d) An overlap plot of the AFM topological image (red line) and the corresponding generated voltage (blue line) for a single scan of the tip across a NW. A delay in the electricity generation is apparent.

position, many sharp output peaks were observed (Fig. 4.1c). Note the output voltage signal was actually negative in reference to the grounded end. By examining the topological profile of a NW and its corresponding output potential, a delay was observed for the voltage output signal (Fig. 4.1d), which means that there was no electric power output when the tip was first in contact with the NW, but a sharp voltage peak was generated at the moment when the tip was about to leave the contact with NW. This delay is a key signature about the power output process. It is important to note that the voltage V_L presented here was converted from the current flowing through the external load R_L. The NG based on ZnO NWs has the following experimental characteristics:

i) The output potential is a sharp peak that is *negative* in reference to the grounded end of the NW.

ii) No output current is received when the tip first touches the NW and pushes the NW; electrical output is observed only when the tip is almost leaving the NW at the second half of the contact;

iii) The power output occurs only when the tip touches the compressive side of the NW [5];

iv) Output signal is observed only for piezoelectric NWs. No electrical output is received if the NWs are tungsten oxide, carbon nanotubes, silicon, or metal. Friction or contact potential plays no role in the observed output power.

v) The magnitude of the output signal depends sensitively on the size of the NWs [6].

vi) To generate electricity, the contact between the tip and the NW is required to be Schottky, and the contact between the NW and the grounded end is Ohmic.

4.1.2 Schottky barrier at the electrode-nanowire interface

There are two types of contact between a metal and a semiconductor. The most typical one is Ohmic contact, which does not impose a potential barrier at the interface so that the electrons have a symmetric transport at either forward or reversal bias. In such a case, the I-V curve is a linear curve. On the other hand, a potential barrier can be formed at the interface so that the transport of electrons across the interface will not be symmetric. Figure 4.2(a, b) shows the configuration before and after a metal and a n-type semiconductor to form a contact. A potential barrier of $\phi_B = \Phi_M - \chi$, so called Schottky barrier, is formed at the interface, where Φ_M is the workfunction of the metal and χ is the electron affinity. The contact is Ohmic if $\Phi_M < \chi$, and it is Schottky if $\Phi_M > \chi$.

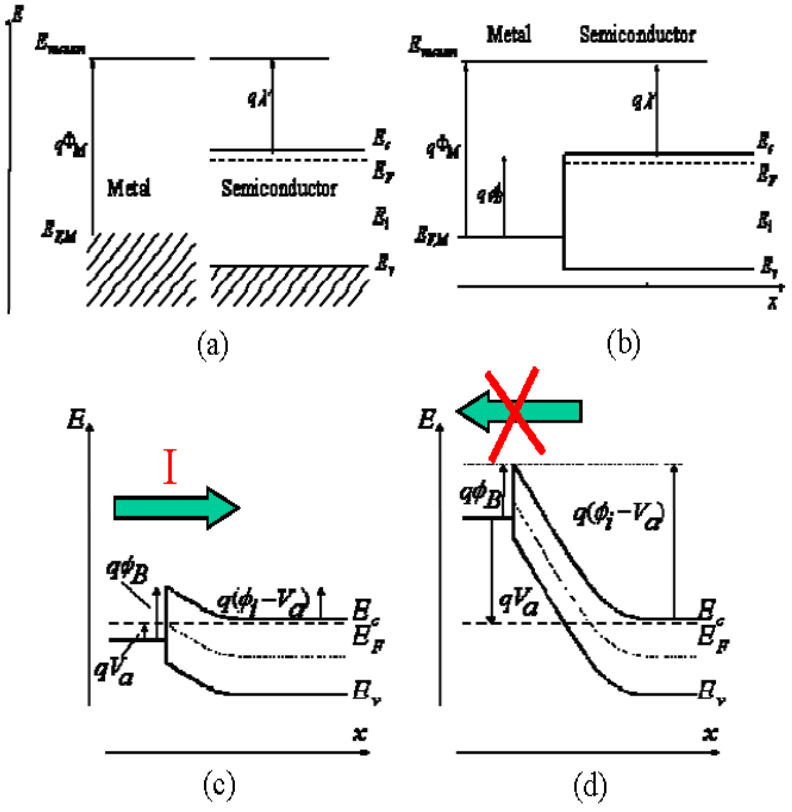

Figure 4.2 (a, b) A metal and an n-type semiconductor before and after making a contact. (c, d) The Schottky contact under forward and reverse bias.

The presence of a Schotty contact at the interface acts as a "diode" (Figure 4.2c,d). At forward bios with the metal has a higher potential, the current can flow through the barrier (e.g., electrons from the semiconductor side to the metal side). At reversal bias with the metal having a lower potential, the electrons cannot overcome the barrier to reach the other side, effectively cutting off the current.

The Schottky contact between the metal contact and ZnO NW is a key factor to the current generation and output process of the nanogenerator. To examine the role played by Schottky barrier in the NG, we used an AFM based manipulation and measurement system as used in our first study for demonstrating the piezoelectric NG (see Fig. 4.3(a)). When a 100 nm thick Pt coated Si tip was used for scanning the NWs in contact mode, voltage peaks were observed (Fig. 4.3(b)), and the output voltage was in the order of ~ - 11 mV (the negative sign means that the current flowed from the grounded end through the external load). By changing the tip to an Al-In (30 nm/30 nm) alloy coated Si tip, the ZnO NWs showed no piezoelectric output (Fig. 4.3(c)). In order to understand the two distinct performances of the two types of scanning tips, we have measured their corresponding I-V characteristics with the ZnO NWs. To ensure the stability of the contact, we used a large electrode that was in contact with a group of NWs, as shown in Fig. 4.3(d). The Pt-ZnO contact clearly presented a Schottky diode (Fig. 4.3(e)), while the Al-In - ZnO was an Ohmic contact. In reference to the piezoelectric output presented in Fig. 4.3(b, c), we conclude that a Schottky contact between the metal electrode and ZnO is a must for a working NG.[7]

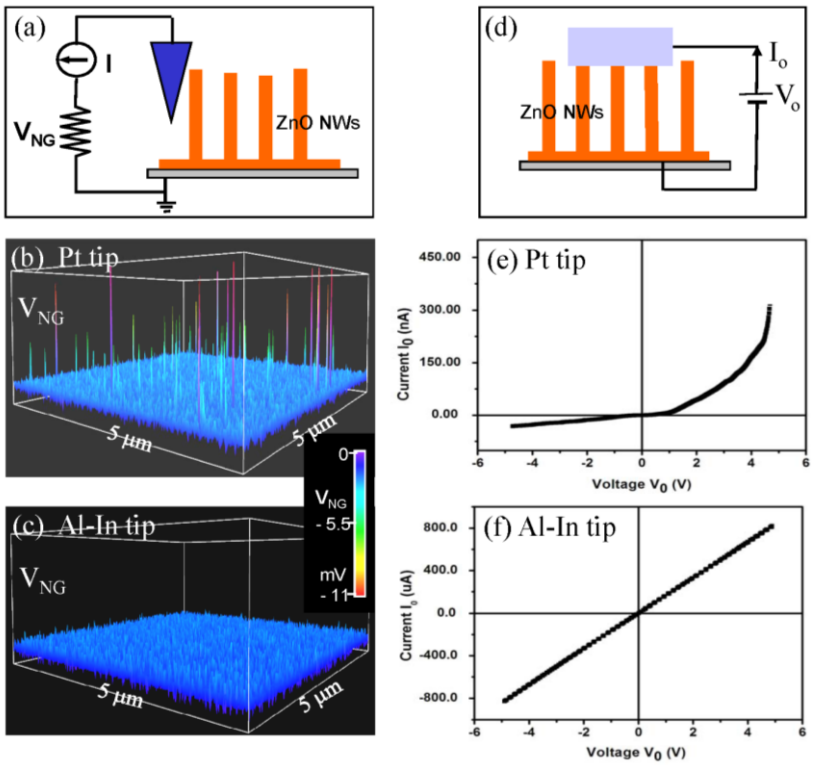

Figure 4.3 (a) AFM based measurement set up for correlating the relationship between the metal-ZnO contact and the NG output. (b) Output potential generated by ZnO NW array when scanned by a Pt coated Si tip. (c) No output potential is generated by ZnO NW array when scanned by an Al-In coated Si tip. (d) Experimental set up for characterizing the I-V transport property of metal-ZnO NW contact. (e) I-V curve of a Pt-ZnO NW contact, showing Schottky diode effect. (f) I-V curve of an alloyed Al/In-ZnO NW contact, showing Ohmic behavior.

4.1.3 The charge generation and output processes

The mechanism for creating, separating, accumulating and outputting the charges through a NW is presented in Fig. 4.4 [1]. For a vertical, straight ZnO NW (Fig. 4.4a), the deflection of the NW by an atomic force microscope (AFM) tip creates a strain field, with the outer surface being stretched and inner surface compressed (Fig. 4.4b). As a result, a piezoelectric potential is build across the NW as well with the stretched side positive and the compressed side negative (Fig. 4.4c) if the electrode at the base of the NW is grounded. The potential is created by the relative displacement of the Zn^{2+} cations with respect to the O^{2-} anions due to piezoelectric effect in the wurtzite crystal structure; thus, these ionic charges cannot

freely move and cannot recombine without releasing the strain (Fig. 4.4c). The potential difference is maintained as long as the deformation is in place and no foreign free charges (such as from the metal contacts) are injected in, which is possible if the doping in the nanowires is rather low. This is the charge creation and separation process.

We now consider the charge accumulation and releasing process. The first step is a charge accumulation process, when the AFM conductive tip that induces the deformation is in contact with the stretched surface of positive potential V^T (Figs. 4.4c and d). The Pt metal tip has a potential of nearly zero, $V_m = 0$, so the metal tip - ZnO interface is negatively biased for $\Delta V = V_m - V^T < 0$. With consideration the n-type semiconductor characteristic of the as-synthesized ZnO NWs, the Pt metal- ZnO semiconductor interface in this case is a reverse-biased Schottky diode (Fig. 4.4d), and little current flows across the interface. The next step is the charge releasing process. When the AFM tip is in contact with the compressed side of the NW (Fig. 4.4e), the metal tip - ZnO interface is positively biased for $\Delta V = V_L = V_m - V^C > 0$. The M-S interface in this case is a positively biased Schottky diode, and it produces a sudden increase in the output electric current. The current is the result of ΔV driven flow of electrons from the semiconductor ZnO NW to the metal tip. The flow of the free electrons from the loop through the NW to the tip will neutralize the ionic charges distributed in the volume of the NW and thus reduce the magnitudes of the potential V^C and V^T.

We have designed a set of experiments to prove the above proposed mechanism. Our experiment was based on mechanical manipulation of a single ZnO wire/belt by an AFM [5]. By selecting a long ZnO wire/belt that was large enough to be seen under an optical microscope, one end of the ZnO wire was affixed on a silicon substrate by silver paste, while the other end was left free. The substrate was intrinsic silicon so its conductivity was rather poor. The wire laid on the substrate but kept a

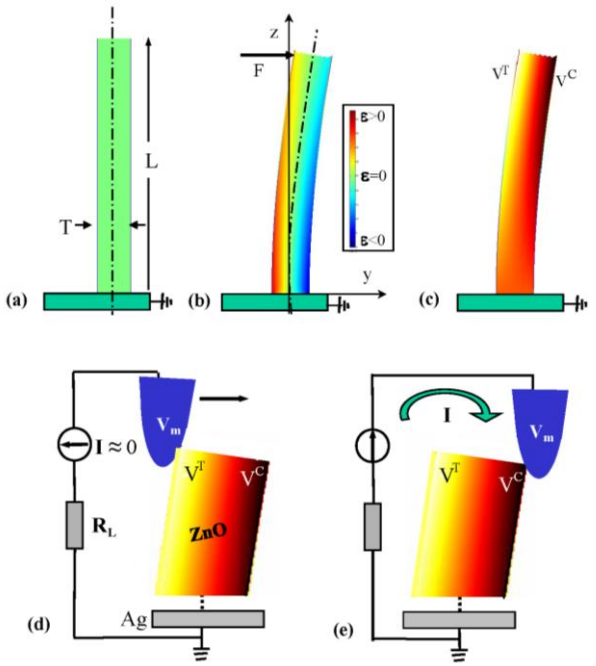

Figure 4.4 Working mechanism for the power generation process of a piezoelectric ZnO wire/belt as a result of coupled piezoelectric and semiconducting properties in conjunction with the Schottky barrier at the AFM tip-semiconductor interface. (a) Schematic definition of a wire/belt. (b) Longitudinal strain $_z$ distribution in the wire/belt after being deflected by an AFM tip from the side. (c) Potential distribution in the wire/belt as a result of piezoelectric effect, with the stretched and compressed side surfaces being positive and negative potentials, respectively. (d, e) Metal and semiconductor contacts between the AFM tip and the semiconductor ZnO wire/belt at two reversed local contact potentials (positive and negative), showing reverse and forward biased Schottky rectifying behavior, respectively. It is this oppositely biased Schottky barrier at the tip-belt interface makes it possible to preserve the piezoelectric charges and later produce the discharge output. The one-way switching role played by the Schottky diode is important for our observation of the piezoelectric output. The process in (d) is to build up and preserve the charges/potential; the process in (e) is to discharge the potential through a flow of electrons from the circuit. The negative output voltage on the load is a result of current flow from the AFM tip through the ZnO belt to the ground.

small distance from the substrate to eliminate the friction with the substrate except at the affixed side (Fig. 4.5a). Both the topography (feed back signal from the scanner) and the corresponding output voltage (*V*) images across a load were recorded simultaneously when the AFM tip was scanned across a wire/belt. The topography image reflects the change in normal force perpendicular to the substrate, which shows a bump only when the tip scans over the wire. The output voltage between the conductive tip and the ground was continuously monitored as the tip scans over the wire/belt. No external voltage was applied in any stage of the experiment. The entire experimental process and the output images were captured by video recording, so that we were able to directly visualize the electric generation process.

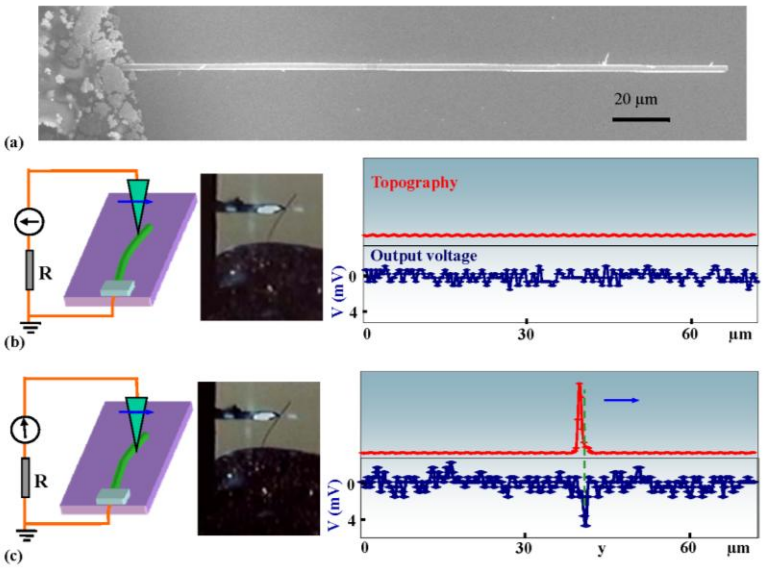

Figure 4.5 In-situ observation of the process for converting mechanical energy into electric energy by a piezoelectric ZnO belt. (a) SEM images of a ZnO belt with one end affixed by silver paste onto a silicon substrate and the other end is free. The belt has a rectangular cross-section. (b, c) Three characteristic snapshots and the corresponding topography (red curve) and output voltage (blue curve) images when the tip scanned across the middle section of the belt. The schematic illustration of the experimental condition is shown at the left-hand side, with the scanning direction of the tip indicated by an arrowhead. In (b), the AFM tip pushed the belt towards the right-hand side but did not go above and across its width, as judged from the topography image, no output voltage was detected. In (c), the AFM tip pushed the belt towards the right-hand side and went above and across its width, as judged from the peak in the topography image, the output voltage image showed a sharp negative peak. There is a delay in the output voltage peak in reference to the normal force image (the peak in the topography image). In (d), for an alternative belt, the AFM tip pushes the belt towards the left but did not go above and across its width, as judged from the topography image, no output voltage was detected beyond noise level although the deflection was large. From [5].

The topography image was directly captured if the tip passed over the belt or not because it was a representation of the normal force received by the cantilever. When the tip pushed the wire but did not go over and across it, as judged by the flat output signal in the topography image (Fig. 4.5b), no voltage output was produced, indicating the stretched side produced no piezoelectric discharge event. Once the tip went over the belt and in touch with the compressed side, as indicated by a peak in the topography image, a sharp voltage output peak is observed (Fig. 4.5c). By analyzing the positions of the peaks observed in the topography image and the output voltage image, we noticed that the discharge occurred after the tip nearly finishing across the wire. This clearly indicates that the compressed side was responsible for producing the negative piezoelectric discharge voltage.

4.1.4 Principle of the nanogenerator for n-type materials

We now consider the nature of the piezoelectric potential. The piezoelectric potential is created by the polarization of ions in the crystal rather than the free-mobile charges. Since the charges associated with the ions are rigid and affixed to the atoms, they cannot freely move. Free carriers in the semiconductor NW may screen the piezoelectric charges, but they cannot completely cancel/deplete the charges. With

the consideration of the Schottky barrier at the interface, the free-electrons cannot across the boundary between the metal and the ZnO, thus, a "dipole" layer is likely to be formed between the accumulated electrons at the metal side and the piezoelectric charges in the ZnO side. This is a distinct difference from the p-n junction in semiconductor physics. Therefore, the piezoelectric potential is still preserved, although a possible reducing in magnitude is possible owing to the finite conductivity of the NW.

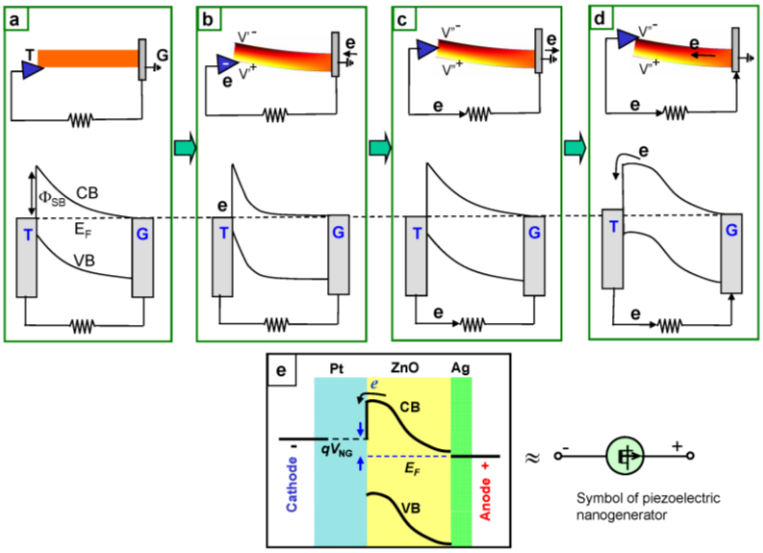

Figure 4.6 Band diagram for understanding the charge outputting and flowing processes in the nanogenerator. (a) Schematic and energy diagram of a NW with one end grounded (G) and the other end to be pushed by a conductive AFM tip (T). A Schottky barrier is at the tip-NW interface. (b) Once being slowly deflected, the asymmetric piezoelectric potential in the NW changes the profile of the conduction band (CB). The local positive piezoelectric potential at the contact area results in a slow-flow of electrons from ground through the load to the tip. The electrons will be accumulated in the tip. (c). When the tip scans across the NW and reach its middle point, a drop in local potential to zero results in a back flow of the accumulated electrons through the load into ground. (d) Once the tip reaches the compressive surface, a local negative piezoelectric potential raises the profile of the conduction band. If the piezoelectric potential is large enough, electrons in the n-type ZnO NW can flow to the tip. This circular motion of the electrons in the circuit is the output current. (e) Energy band diagram for the NG, presenting the output voltage and the role played by the piezoelectric potential. The diagram on the right-hand side is the symbol designed for representing a piezoelectric nanogenerator.

An as-synthesized ZnO NW is generally n-type. The presence of oxygen vacancies and impurities and a large portion of surface atoms (surface states) naturally introduces a moderate conductivity for the NW. These free carriers can partially screen the piezoelectric charges, but they cannot entirely neutralize the charges. Therefore, the piezoelectric potential still preserves, at a reduced magnitude, even with consideration the moderate conductivity of ZnO.

We now present an understanding about the charge releasing process for a NG based on band structure model. The AFM tip (T) has a Schottky contact (barrier height Φ_{SB}) with the NW, while the NW has an Ohmic contact with the grounded side (G) (Fig. 4.6a). When the tip slowly pushes the NW, a positive piezoelectric potential V^+ is created at its tensile surface. As the tips continue to push the NW, electrons slowly flow from the grounded electrode through the external load to reach the tip, but the electrons cannot across the tip-NW interface due to the presence of a reversely biased Schottky barrier at the contact (Fig. 4.6b). In such a case, the accumulated free charges at the tip may affect the piezoelectric potential distribution in the NW owing to the screening effect of the charge carriers. The piezoelectric potential is generated due to the rigid and non-mobile ionic charges in the NW, it cannot be completely depleted by the free carriers. The local newly established potential V'^+ lowers the conduction band (CB) slightly.

When the tip scans in contact mode across the NW and reaches the middle point of the NW (see Fig. 4.6c), the local piezoelectric potential is zero. In such a case, with a sudden drop in local potential, the originally accumulated electrons in the tip back flow through the load to the ground. This is a process

faster than the charge accumulation process presented in Fig. 4.6b. An alternative but the same result case is that the tip temporarily lifts off from the NW, which also leads to the back flow of the accumulated electrons to the ground.

When the tip reaches the compressive side of the NW (Fig. 4.6d), the local potential drops to V"- (negative), which results in the high raising of the conduction band near the tip. If the raise in local potential energy is large enough as determined by the degree of NW bending, the local accumulated n-type carriers in the NW can quickly flow through the contact to the tip, which creates a circular flow of the electrons in the external circuit, thus producing a current. This process is a lot faster than the charge accumulation process, thus, the created transient potential at the external load is large enough to be detected beyond noise level.

The presence of a Schottky at the tip-NW interface is mandatory for a NG, which acts like a "gate" for separating and slowly-accumulating the charges and then fast-releasing the charges. The missing of a "gate" at an Ohmic contact results in no charge accumulation and releasing, thus, no detectable signal will be received.

The next question is how large is the output voltage? This question can be answered by the energy band diagram shown in Fig. 4.6e for the NG. The role played by the piezoelectric potential is to drive the electrons from the ZnO NW to overcome the threshold energy at the metal-ZnO interface into the Pt electrode, but it does not directly determine the magnitude of the output voltage. As more electrons are being "pumped' into the Pt electrode, the local Fermi surface in raised. Therefore, the output voltage is the difference between the Fermi energies for Pt and the bottom electrode Ag.

It must be pointed out that, although the total amount of charges Q generated by a single NW is small (~1000-10,000 electrons), a fast release of these electrons can produce a significantly large measurable electric current/voltage pulse, because $V_L \approx R_L Q/\Delta t$, where Δt is the time interval for the charge releasing process. A conventional calculation of output voltage by the capacitance C of the NWs and system, $V = Q/C$, applies only to static process! The voltage predicted by this calculation is usually far less than the magnitude of the pulse observed experimentally.

As a summary of the charge flowing processes presented in Fig. 4.6, the first process is a forward and back flow of the electrons through the load from the ground to the tip; the second process is a piezoelectric potential driven circular flow of the electrons through the NW. The two processes generate the constructive currents flowing in the same direction, resulting in a negative voltage at the load in reference to the grounded electrode. This is an important characteristic. The output current can be significantly large if the charge releasing process is fast. In the case of the AFM tip contact, the second process is likely the dominant process. The entire process of energy generation process can be summarized into one sentence: the piezoelectric potential driven flow of external electrons is the power output process of the nanogenerator.

4.2 Nanogenerator for p-type materials

4.2.1 Characteristic of output signals

It is known that an as-grown ZnO NW is typically n-type. The piezoelectric output measured using an AFM usually gives a negative output potential, and the potential is observed when the tip contacts the compressed side of the NW. We have recently measured the electricity generation of p-type ZnO nanowires, and the results are shown in Figs. 4.7a and b [8]. In contrast to the result received for n-type ZnO nanowires, the output voltage at the external load is always positive in reference to the grounded nanowire root. To confirm this result, we used the same AFM tip and under identical experimental conditions at almost at the same time, we measured the electricity generation of n-type ZnO nanowire, and the results are shown in Figs. 4.7d and e, clearly showing negative output voltage. More importantly, in reference to the morphological image of the nanowire, the output voltage peak occurs at the first half of the contact between the tip and the nanowire for the p-type nanowire (Fig. 4.7b), while it occurs at the last

half of the contact between the tip and the nanowire for the n-type nanowire (Fig. 4.7f). This distinct difference is directly related to the mechanism of the nanogenerator.

As for the p-type of nanowires, the Fermi level is located more close to the valence band edge. The metal-semiconductor is forward biased if the semiconductor has a higher potential, otherwise the junction is reversely biased. When the tip is in contact with the nanowire, as shown in Fig. 4.7c, the negative piezoelectric charges created at the compressed side of the nanowire is partially screened by the positively charged holes. Once the magnitude of the positive piezoelectric potential at the stretched side exceeds a value that can either drive the p-type carriers or the electrons in the metal tip across the junction, a positive output voltage would be observed at the external load. This event occurs at the first half of the contact between the metal tip and the nanowire.

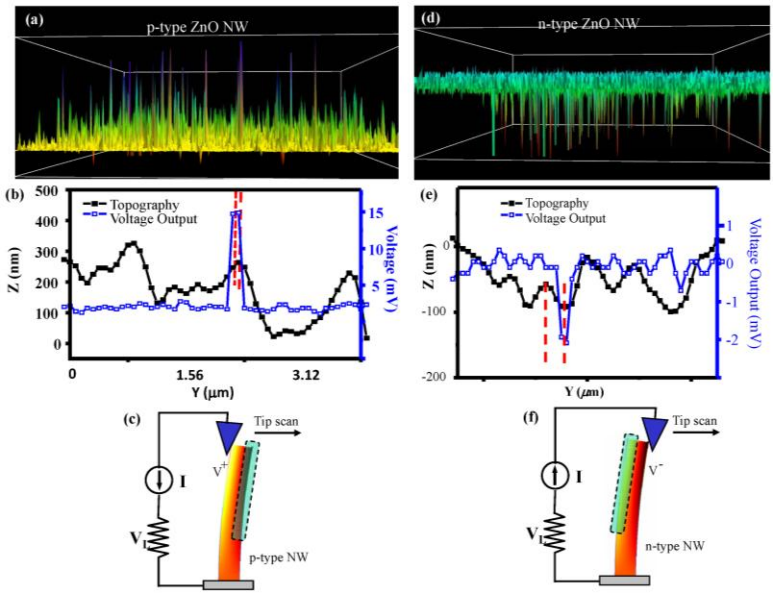

Figure 4.7 A comparison of nanogenerators based on n-type and p-type ZnO nanowires. (a) 3D voltage output profile across the n-type ZnO nanowire array when an AFM tip was scanned in contact mode for generating electricity, and (b) a corresponding comparison between the topological scan and output voltage scan, showing the negative output voltage was generated when the tip reached the compressed side of the nanowire. (c) The mechanism for the n-type nanowire nanogenerator. (d) 3D voltage output profile across the p-type ZnO nanowire array when an AFM tip was scanned in contact mode for generating electricity, and (e) a corresponding comparison between the topological scan and output voltage scan, showing the negative output voltage was generated when the tip reached the stretching side of the nanowire. (c) The mechanism for the p-type nanowire nanogenerator.

As for the n-type of nanowires, the metal-semiconductor is forward biased if the metal has a higher potential, otherwise the junction is reversely biased. When the tip is in contact with the nanowire, as shown in Fig. 4.7, the positive piezoelectric charges created at the stretched side of the nanowire is partially screened by the electrons. A potential different is established between the tip and the nanowire once the tip is in contact with the compressed side of the nanowire, which has negative piezoelectric potential. This piezoelectric potential at the compressed side drives the electrons to flow across the junction, resulting in a negative voltage at the external load. This event occurs at the last half of the contact between the metal tip and the nanowire.

4.2.2 Criteria for identification of p- and n-type nanowires

For ZnO films, the *n*- or *p*-type conductivity of the sample is determined in two ways: measurements of Hall Effect and Seebeck effect, which are well established techniques and convenient as it is easy to fabricate the electrodes for thin film. However, due to low dimensionality, it is hard to carry out such measurements for ZnO News. Up to now, the transport measurement of single NW based field effect transistor (FET) is being applied to identify the carrier type ZnO NWs. FET is widely applied to investigate the electronic properties of a single semiconductor NW.

We have proposed a new criterion for identifying the carrier type of individual ZnO NWs based on the piezoelectric output of a NW when it is mechanically deformed by a conductive AFM tip in contact mode [9]. The *p*-type/*n*-type shell/core NWs give positive piezoelectric outputs, while the *n*-type NWs produce negative piezoelectric outputs. Importantly, the results are reproducible and reliable for three sets of samples. This finding, together with the previous results on phosphorus-doped *p*-type ZnO NWs, firmly establishes a simple technique for quickly identifying the conductivity type of ZnO NWs without damaging the sample.

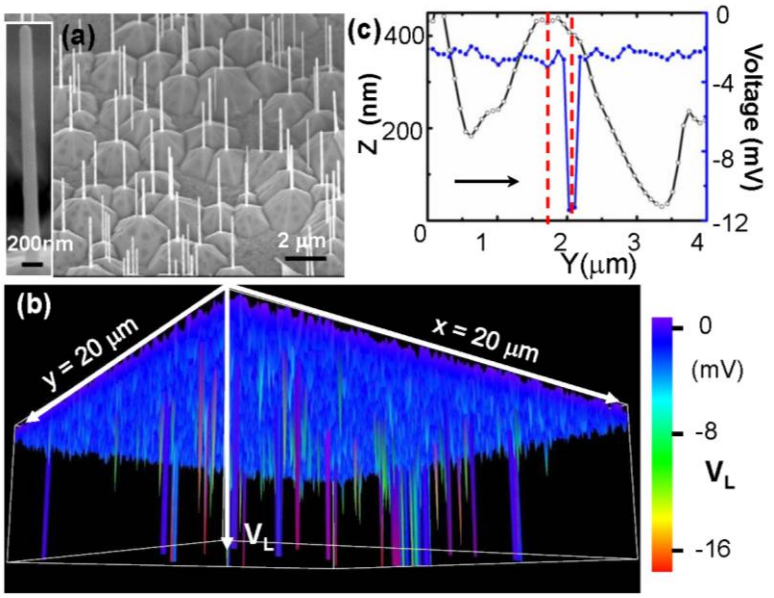

Figure 4.8 (a) SEM image of the as-synthesized ZnO NWs array by pulsed laser deposition; the inset shows a single NW, the diameter of which is around ~150 nm. (b) Three dimensional plot of output voltage of as-synthesized *n*-type ZnO NWs. (c) A typical line scan profile from the AFM topography (black) and the corresponding output voltage (blue).

The vertically aligned *n*-type ZnO NWs were synthesized on silicon substrates by pulsed laser deposition (PLD). Detailed synthesis process will be systematically reported elsewhere. Nitrogen-doped *p*-type shell layer was deposited by plasma-free MOCVD, using diethyl zinc as the zinc source and a mixture of O_2 (13 sccm) and NO (13 sccm) as oxygen and N doping source. The growth temperature was fixed at 400 °C and the deposition thickness was 300-400 nm.

Figure 4.8(a) shows a SEM image of the as-grown NWs array by PLD and the inset displays a single NW. The as-synthesized NWs have typical diameters of ~100-150 nm. Figure 4.8(b) shows the corresponding three-dimensional (3D) voltage output image after scanning an area of 20μm×20μm over the *n*-type ZnO NW array. The *n*-type ZnO NWs produce negative voltage outputs when bent by a Pt-coated AFM tip. A typical profile of voltage output is shown in figure. 4.8(c), revealing that the negative voltages are produced when the AFM tip touches the compressed side the NWs, as indicated by the delay of the voltage peak in reference to the peak in the morphological profile. This delay is a unique characteristic of *n*-type ZnO NW.

In the second step, using the PLD grown NW arrays as template, a thin layer (300-400 nm) of N-doped *p*-type ZnO was uniformly deposited on the surface of the NW array by plasma-free MOCVD [22]. The electronic properties of the *p*-type film grown on the glass substrate, which was grown under the exactly same conditions as the *p*-type shell layer was deposited on ZnO NWs, were characterized by Hall-effect measurements.

Figure 4.9(a) shows a SEM image of the NWs after depositing the *p*-type layer. The *n*/*p* core/shell NWs have typical diameters ~400 nm, as shown in the inset of figure. 4.9(a). The uniform and much larger diameter of the *n*/*p* core/shell NWs compared with the as-synthesized NWs demonstrate that the *p*-layer has been successfully grown epitaxially on the *n*-type NWs (This was also confirmed by electron diffraction pattern, not shown here). After scanning an area of 20μm×20μm over the *n*/*p* core/shell ZnO structures under the contact mode by using the conductive AFM, the 3D voltage output image is produced as shown in Figure 4.9(b). The *n*/*p* core/shell NWs produce positive outputs throughout the entire scan range. Detailed analysis shows that the voltage peak is ahead of the peak in morphological image in reference to the scan direction of the tip, as indicated in figure 4.9(c). Figure 4.9(d) gives more evidences that all of the positive voltage peaks are produced when the AFM tips contact the stretched side of the corresponding NWs. It was found that the piezoelectric response differences between the *n* and *n*/*p* core/shell NWs can be reproducibly observed for an extended period of time.

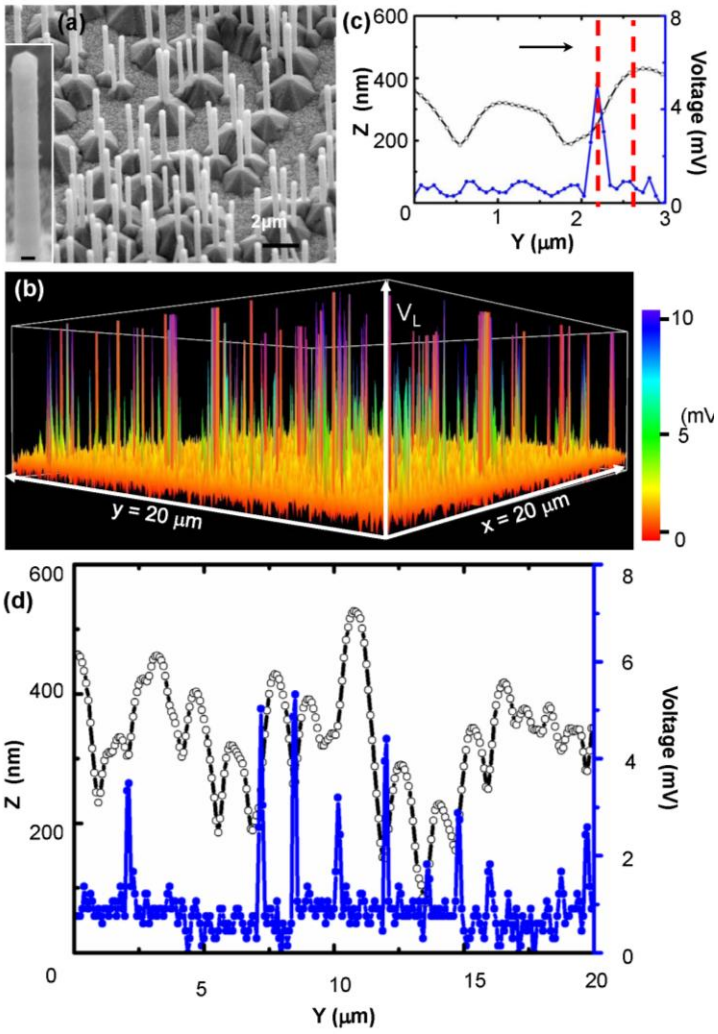

Figure 4.9 (a) SEM image of *n*/*p* core/shell ZnO NWs array. Inset, a single NW, the diameter of which is ~400 nm. (b) Three dimensional plot of output voltages of *n*/*p* core/shell ZnO NWs. (c) A typical line scan profile from the AFM topography (black) and the corresponding output voltage image (blue). (d) A 20 μm line scan profile from the AFM topography (black) and the corresponding output voltage (blue) image; the voltage peaks were produced when the AFM tip contacted the stretched side of the NWs.

4.3 Nanogenerator based on other wurtzite structured nanowires

Besides ZnO, nanowires of GaN [10], InN [11], CdS [12] in the wurtzite family have been used for electricity generation. In output of GaN and InN are particularly encouraging; one nanowire can give an output voltage of about 1 V (Fig. 4.10). The mechanism for the charge output process is entirely consistent with that of ZnO. We anticipate to have high output NG fabricated if we can grow high quality aligned GaN nanowire arrays.

4.4 Nanogenerator based on laterally bonded nanowires

In this section, an alternating-current (AC) generator is demonstrated based on cyclic stretching-releasing of a piezoelectric fine-wire (PFW) (microwire, nanowire), which is firmly contacted at two ends with metal electrodes, laterally bonded and packaged on a flexible substrate [13]. When the PFW is stretched as driven by substrate bending, a piezoelectric-potential-drop is created along the PFW. A Schottky barrier formed at least at one end-contact of the PFW serves as a "gate" that prevents the flow of

electrons in the external circuit through the PFW so that the piezoelectric potential is preserved. The PFW acts as a "capacitor" and "charge pump", which drives the back and forth flow of the electrons in the external circuit to achieve a charging and discharging process when the PFW is stretched and released, respectively. A repeated stretching-releasing of a single PFW with 0.05-0.1% strain creates an AC output at a voltage up to ~50 mV. The energy conversion efficiency of the PFW is up to 6.8%. The output is scalable by a serial connection of multiple AC generators. The reported work demonstrates a robust, no sliding-contact and packageable nanowire technology in polymer films for harvesting low-frequency energy from vibration, air flow/wind and mechanical deformation. The flexible AC generators are feasible and practical to be implanted in muscles, embedded in cloths, built in surface layers, and placed in shoe pads.

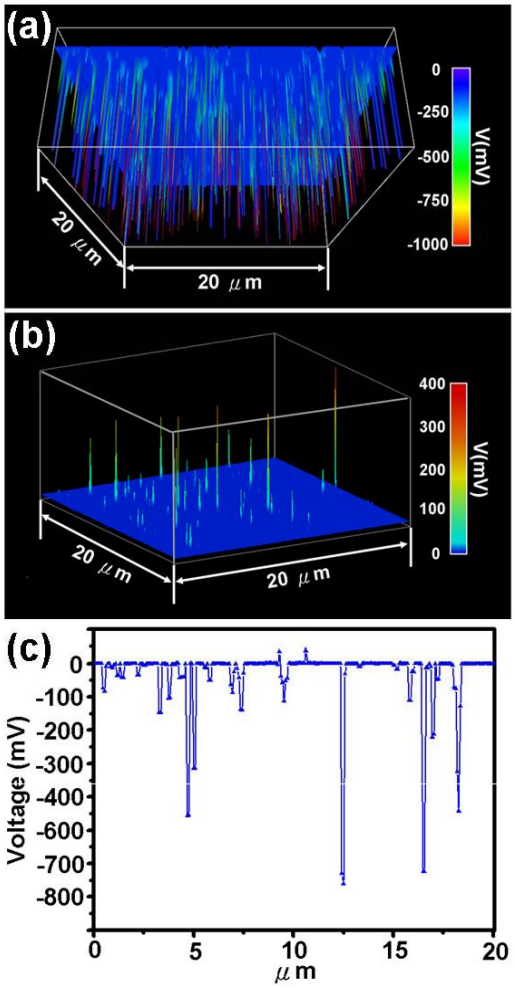

Figure 4.10 AFM measurement of piezoelectric output from as-grown InN nanowires. The 3D plots and a line scan plot of the output signal, showing an output voltage of up to - 1 V.

4.4.1 Basic design

The generator was fabricated by bonding a ZnO PFW laterally on a Kapton polyimide film (Fig. 4.11a) [13]. The ZnO PFWs were synthesized by a physical vapor deposition method, and they typically have diameters of 3-5 μm and lengths 200-300 μm. We chosen long PFWs because they were easy to be manipulate, but the same process applies to nanowires. Silver paste was applied at both ends of the ZnO PFW to fix its two ends tightly on a flexible substrate. A current/voltage measurement meter was connected to two ends of the PFW without introducing any external power source in the circuit.

To measure the electric energy generated by the PFW when subjected to mechanical deformation, a periodic mechanical bending was introduced to the substrate using a motor driven mechanical arm. The final bent radius of the substrate was ~2 cm, which is much larger than the length of the PFW. In addition, the thickness of the Kapton film was much larger than the diameter of the PFW. As a result, the bending of the substrate film induced a tensile strain of 0.05 – 0.1% in the PFW attached to its outer surface (Fig. 4.11b). Due to the piezoelectric property of ZnO, a piezoelectric potential field was created along the PFW, which drove the flow of electrons in the external circuit (or interconnects). When the substrate was periodically bent and released, the PFW was periodically stretched and released, resulting in an alternating current. Generators based on multiple PFWs are integrated to raise the output voltage (Fig. 4.11c). The entire structure has been packaged inside a thin layer of insulating wax or flexible polymer to maintain its physical stability during the deformation of the substrate (Fig. 4.11c).

4.4.2 Output measurements

Before and after a single wire generator (SWG) was tested for generating electricity, its transport property was characterized to understand its performance and signal output. For a working SWG that was effective for producing output power, the I-V characteristic always showed a Schottky behavior. This is the most outstanding characteristic of a good SWG. To properly represent the location of the Schottky barrier in the schematic diagram, a diode symbol is introduced at the left-hand side for notation purpose, in reference to which the sign of the output signal is defined. For the discussions hereafter, we define the side that has the Schottky diode as the positive side of the SWG.

The short-circuit current (I_{sc}) and open-circuit voltage (V_{oc}) were measured to characterize the performance of an SWG. To verify that the measured signal was generated by an SWG rather than the measurement system, a "switching-polarity" test (see Chapter 5) was applied to all of our measurements (Fig. 4.11e). When the current meter was forward connected to an SWG, which meant that the positive and negative probes were connected to the positive and negative electrodes of the SWG, respectively, a positive voltage/current pulse was received for each fast stretching (FS) of the polymer substrate (Fig. 4.12a), and a corresponding negative pulse was created when the substrate was fast released (FR). By FS and FR, we meant that the angular bending rate of the substrate was ~260 ?sec at a radius of 2 cm. The output voltage/current for each cycle of FS and FR is a pair of positive and negative peaks, respectively. The output voltage is 20 – 50 mV and output current is 400 – 750 pA for a single PFW of ~ 4 μm in diameter and ~ 200 μm in length. Although the heights of the current peaks for the FS and FR appear differently,

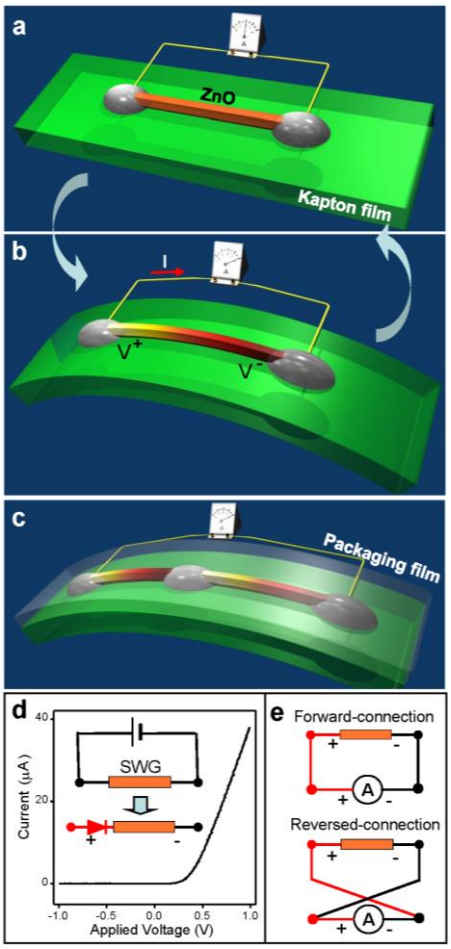

Figure 4.11 Design of a piezoelectric fine-wire generator on a flexible substrate. (a) The PFW lays on a polymer Kapton film substrate, and its two ends are tightly bonded to the substrate and outlet interconnects. The entire PFW and the interconnects can be totally covered by a layer of insulating flexible polymer or wax for packaging purpose (not shown here for clarity). (b) Mechanical bending of the substrate creates tensile strain and corresponding piezoelectric potential in the PFW, which drives the flow of the electrons through the external load. (c) Packaging of the generators made of multiple fine-wires inside a thin and flexible polymer film, showing its integration with soft materials to improve mechanical stability and environmental adaptability. (d) I-V characteristic of a SWG that is effective for producing output power, showing a typical Schottky diode characteristic with a forward-bias threshold voltage of ~0.3 V. In our study, the end-contact of the SWG that has the Schottky behavior is defined to be positive, where a diode symbol is introduced to represent its presence at the interface (lower diagram). (e) Definition of the switching-polarity test adopted for all of the measurements.

possibly because of different straining rate, the areas under the peaks remain the same (Table 4.1); and the total charges transported in the two processes remain almost the same (within 5% in difference). For each straining process, the total electrons transported were ~ 10^8.

Table 4.1. Total charge generated when the SWG was fast stretched and fast released by integrating the area of the peak in the I-t curve shown in Fig. 4.12a. The negative sign means the charges flow in an opposite direction.

Peaks of output current	Total generated charge when fast stretched ($C \times 10^{-11}$)	Total generated charge when fast released ($C \times 10^{-11}$)
First	1.49	-1.88
Second	1.73	-1.87
Third	1.76	-1.86
Fourth	1.74	-1.94
Fifth	1.85	-1.72
Sixth	1.67	-1.92
Seventh	1.86	-1.77
Eighth	1.90	-1.87
Ninth	1.90	-1.69
Tenth	1.79	-1.85
Average	1.77	-1.84

When the current meter was reversely connected (see Fig. 4.11e), which meant that the positive and negative probes were connected to negative and positive electrodes of the SWG, respectively, the observed voltage and current shown in Fig. 4.12b were a reversal of that displayed in Fig. 4.12a. The inverted output signals confirmed that the power was indeed generated by the SWG.

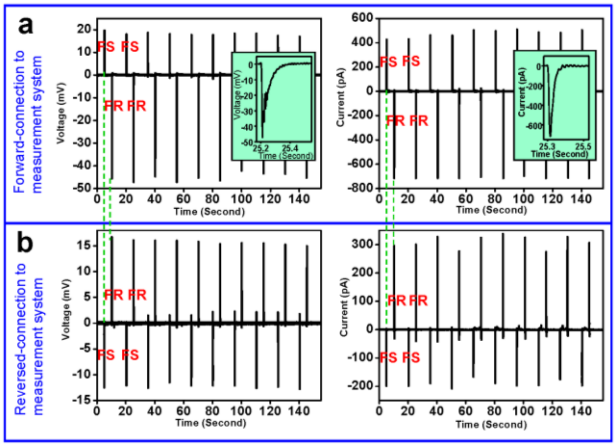

Figure 4.12. Open-circuit voltage and short-circuit current output of a single wire generator and their stability. (a, b) Generated alternating voltage and current of a SWG when repeatedly fast-stretched (FS) and fast-released (FR), showing the reversal in signal output when the SWG being forwardly- and reversely-connected to the electrical measurement system, respectively. This polarity-switching test is a criterion for ruling out possible system artifacts. The insets in (a) and (b) are an enlarged output voltage and current peak, respectively. The area under the I-t curve is the total transported charges.

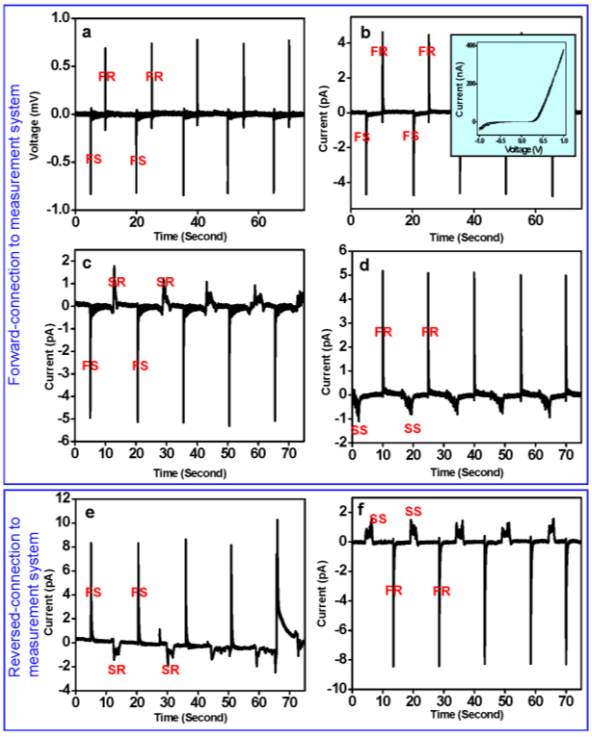

Figure 4.13. Open-circuit voltage and short-circuit current output of a single wire generator that shows opposite sign of output signal in comparison to that shown in Fig. 4.12. (a, b) Generated alternating voltage and current of a SWG when repeatedly fast-stretched (FS) and fast-released (FR). (c, d) Electric current generated when the PFW was fast stretched but slowly released (SR), or slowly stretched (SS) but fast released, showing a drastic reduce in the magnitude of the output current peak but with an increased width. The total transported charge in each process remained the same. (e, f) Analogous to the current output shown in (c, d) but with the SWG reversely connected in polarity with the measurement system, showing the reversal of the output signal.

The magnitude of the generated electricity depends on the rate at which the strain deformation is introduced. A FS and FR of a SWG produced alternating voltage/current output (Figs. 4.13a, b), while a FS but a slow release (SR) or a slow stretch (SS) but a FR produced strong electric output only when the deformation action was fast (Figs. 4.13c, d). By SS and SR we mean that the angular bending rate was ~ 7 ?sec for a radius of 2 cm. By reversing the connection polarity, the output signal reversed (Fig. 4.13e, f), unambiguously proves that the signal was generated by the SWG. Either a slow stretching or slow releasing generated a broad but smaller amplitude output signal [14], but the areas under the signal peaks for both FS and SR or SS and FR remain almost the same (within 4%, see Tables 4.2 and 4.3), indicating that the total released charges were the same for a fixed final strain regardless of the straining rate and straining process. Therefore, the total charges transported in the stretching and releasing processes were conservative, and the SWG had little leakage current.

Table 4.2: Total charge generated when the PFW was slowly stretched and fast released by integrating the area of the peak in the I-t curves given in Fig.4.13c. The negative sign means the charge flow in opposite direction.

Peaks of output current	Total generated charge when slowly released ($C \times 10^{-13}$)	Total generated charge when fast stretched ($C \times 10^{-13}$)
First	8.02	-6.75
Second	6.95	-7.39
Third	7.49	-7.47
Fourth	7.39	-7.55
Fifth	8.97	-8.21
Average	7.76	-7.48

Table 4.3: Total charge generated when the PFW was slowly stretched and fast released by integrating the area of the peak in the I-t curves given in Fig. 4.13f. The negative sign means the charge flow in opposite direction.

Peaks of output current	Total generated charge when slowly stretched ($C \times 10^{-13}$)	Total generated charge when fast released ($C \times 10^{-13}$)
First	14.9	-16.44
Second	15.44	-16.81
Third	16.695	-15.90
Fourth	17.795	-15.53
Fifth	17.89	-14.48
Average	16.54	-15.83

4.4.3 Principle of the nanogenerator

The working principle of the SWG is proposed based on the band structure of the system with the presence of a Schottky barrier and the creation of an inner piezoelectric field in the PFW under tensile strain [13]. The ZnO PFWs used in our experiments are oriented along c-axis. It is known that the (0001) and $(000\bar{1})$ facets of ZnO are terminated with Zn and oxygen, respectively. A non-symmetric Schottky contact usually appears at one end in transport measurement. An energy band diagram is shown in Fig. 4.14a for a ZnO PFW in contacting with metal electrodes of Fermi level E_F, with a Schottky barrier of height Φ_{SB} at the left–hand (L) side and Ohmic contact at the right-hand (R) side. The Schottky barrier is

represented by a diode symbol. In the first step, once subjecting to tensile strain, a piezoelectric field is created in the PFW (Fig. 4.14b), which is the result of ionic charges that are associated with the polarization of atoms in the crystal and cannot freely move. The piezoelectric charges remain in the PFW for at least a few seconds or even much longer without "depletion" by the free carriers as long as the strain is preserved. In the first case, we assume that the piezoelectric potential is positive V^+ at the Schottky barrier side and is negative V^- at the Ohmic side (assuming $V^+ > V^-$). In such a case, the conduction band and Fermi level of the electrode at the R side is raised for $\Delta E_p = e(V^+ - V^-)$ in reference to that of the L electrode. Thus, electrons will flow from the R side electrode to the L side through an external load R_L because the resistance across the Schottky barrier is very high when the local voltage is less than the forward threshold voltage of the diode (~ 0.3 eV) even at positive bias. The electrons accumulate at the interfacial region between the L electrode and ZnO PFW due to the presence of the Schottky barrier. This process continues until the potential created by the accumulated electrons balance the piezoelectric potential, thus, the Fermi levels of the two electrodes reach a new equilibrium (Fig. 4.14c). This is the process of generating the first positive output current/voltage peak in Fig. 4.14e.

In the second step, when the polymer substrate is released, the tensile strain in the PFW is released as well. An immediate disappearance of the piezoelectric potential lowers the Fermi surface of the R electrode by ΔE_p, accompanying to which the electrons originally accumulated at the interfacial region between the L electrode and the PFW flew back through the external circuit to the R electrode due to the presence of the Schottky barrier at the interface (Fig. 4.14d). This process ends when the Fermi levels at the two electrodes are at equilibrium and the system returns to the original status as shown in Fig. 4.14a. This is the process of generating the negative output current/voltage peak presented in Fig. 4.14e. The total electrons transported in the two steps are the same regardless the straining process, provided there is no current leakage (see Tables 4.1-4.3). A repeat of the last two steps produces an alternating output.

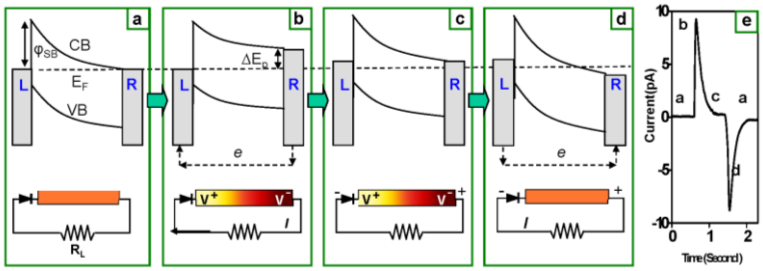

Figure 4.14. Charge generation and outputting mechanism of an alternating-current single wire generator illustrated by energy band diagram. (a) Energy band diagram of a ZnO PFW contacted with two metal electrodes, where CB and VB are the conduction band and valence band of ZnO PFW, respectively. The low diagram is a sketch of the realistic measurement circuit, where a small load resistor R_L is introduced, which is much smaller than the resistance of the PFW and/or the contacts. (b, c, and d) Energy band diagrams of the SWG when the PFW is tensile stretched, re-reaches equilibrium, and then released, respectively, showing the generation of a pair of positive and negative voltage/current peaks (see text) for a case in which the piezoelectric potential of the PFW is assumed higher at the side next to the Schottky barrier, while the other side with Ohmic contact has a lower piezoelectric potential. (e) An experimentally measured output current from a SWG, in which the output regions corresponding to the processes shown in (a-d) are indicated by the corresponding labels a-d. (f, g, h) Energy band diagrams of a SWG when the PFW is tensile stretched, re-reaches equilibrium, and then released, respectively, showing the generation of a pair of negative and positive voltage/current peaks for an alternative case in which the piezoelectric potential of the PFW is lower at the side next to the Schottky barrier, while the other side with Ohmic contact has a higher piezoelectric potential.

In an alternative case, we assume that the piezoelectric potential at the Schottky barrier side is negative V^- and at the Ohmic side is positive V^+. The Fermi level of the L electrode is thus raised by ΔE_p in comparison to that of the R

electrode (Fig. 4.14f). Thus, the electrons flow from the L electrode through the external load R_L to the R electrode because of the presence of the Schottky barrier at the interface. The free electrons may enter the PFWs and screen the piezoelectric charges but cannot neutralize/deplete the piezoelectric charges, because they are rigid charges affixed to atoms and cannot freely move. To represent the decrease in magnitude in potential as a result of possible screening effect, the local effective potential is denoted by V_1^- and V_1^+. The positive charges accumulated at the L electrode are affixed to the atoms and cannot freely move (see Fig. 4.14g). It is thus possible to have some residual charges left at the electrode. The process continues until an electric potential due to the free moving electrons is created across the PFW to balance the piezoelectric potential and the Fermi levels at the two electrodes reach a new equilibrium (Fig. 4.14g). This is the process of creating a negative voltage/current peak when the PFW was stretched.

In the next step, once the strain is released, the piezoelectric potential disappears, and the free charges used to screen the piezoelectric charges are free to move. At this moment, the Fermi level of the R electrode is higher than that of the L electrode, resulting in a simultaneous back flow of the electrons from the R electrode through the external circuit to the L electrode because of much lower resistance than the PFW and the contacts. This process ends when the Fermi levels of the two sides reach equilibrium, which is the starting configuration shown in Fig. 4.14a. This is the process of generating a positive voltage/current output peak when the PFW was released.

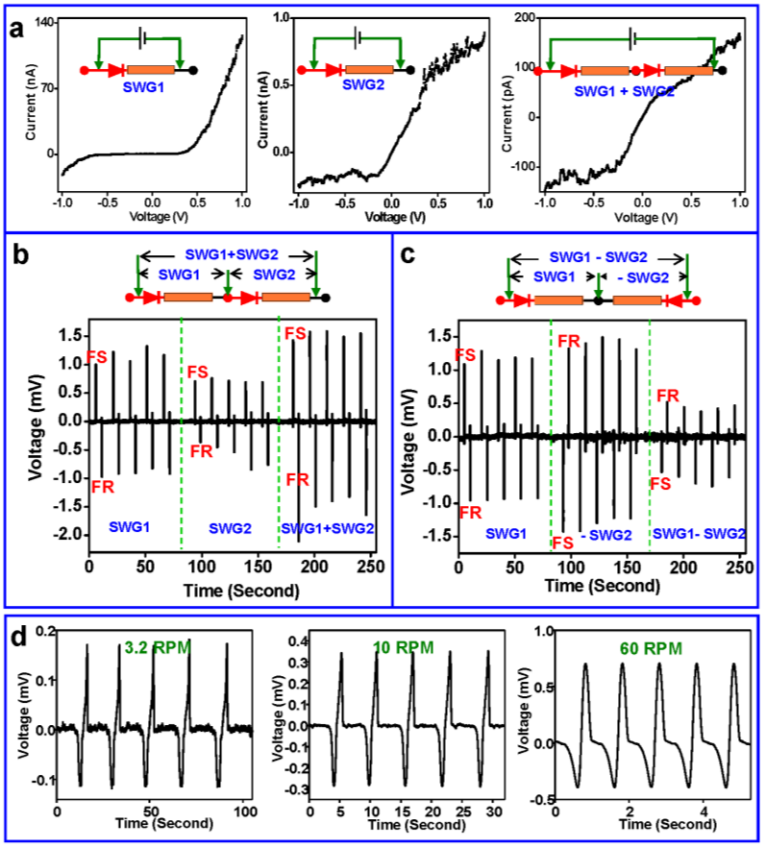

Figure 4.15. Serial connection of two SWGs to show their potential for scaling up the output power. (a) I-V characteristics of the two individual SWGs and their resultant transport property after connected in serial, using which we can identify the polarity of the generators. The Schottky behavior is the key for outputting electricity. (b) Voltage output of the two individual SWGs and that after they were connected constructively in serial, showing a linear summation of the output voltages. The output signal was measured under the same experimental conditions except by outputting the signals at different points of contacts, as shown schematically at the top. (c) Voltage output of the two individual SWGs and that after they were connected destructively in serial, showing the linear subtraction of the output voltages. The linear superposition of the output signals for the SWGs is a key criterion for ruling out possible system artifacts. (d) An increase in straining rate leads to an increase in output voltage. At a 60 RPM, the shape of the output voltage is close to sinusoidal.

4.4.4 Linear connections

The output power of the generators was enhanced by connecting them in serial or parallel for raising output voltage or current. Before connecting two SWGs in serial, the polarity of the

Schottky barriers at the ends was determined by I-V measurement, as shown in Figs. 4a and b, so that the two were connected in the correct polarity and sequence. By connecting the two in serial, the corresponding I-V characteristic still showed a Schottky behavior. The measured voltage is approximately a sum of the two SWGs (Fig. 4.15b). By reversely connecting the two SWGs in serial, the output voltage is the difference of the two (Fig. 4.15c). This linear superposition characteristic together with the reversal of the output signal after reversing the polarity of connections are the necessary and sufficient conditions to confirm the true signals generated by the SWGs (see Chapter 5).

Finally, increasing the straining rate drastically improved the magnitude of the output electricity both in voltage and current (Fig. 4.15d). At a bending frequency of 60 rpm, the output voltage is close to sinusoidal (Fig. 4.15d), e.g. alternating current.

4.4.5 Power conversion efficiency

The efficiency of the SWG has been estimated (Fig. 4.16) [13]. Assume the Kapton substrate was bent with a radius of R. The thickness of Kapton substrate is h. The ZnO fine wire has a length of L and diameter of D. Because $R >> h$ and $h >> D$, the strain of ZnO nanowire is approximately equal to the strain of the outer surface of Kapton film, $\varepsilon \approx h/2R$ (Fig. 4.16a). The thickness of the Kapton substrate is 50 μm, and the radius R is between 2.0-3.0 cm. According to above formula and the value of h and R, the strain of ZnO fine wires is ε = 0.05%-0.1%. The total mechanical deformation energy stored in the PFW after stretching is $W_m = ½\ EA(L - L_0)^2/L_0$, where E is the elastic modulus of the PFW, L_0 and L are its original and final length after straining, respectively, and A is its cross-section. The total electric energy generated is $W_e = \int VI\ dt$ (Figs. 4.16, b, c). The ZnO fine wire in this report has a diameter D about 4 μm, *L0* about 200 μm, E about 30-50 GPa, and ε about 0.05%. The energy conversion efficiency of the PFW itself, excluding the substrate film, is up to 6.8%.

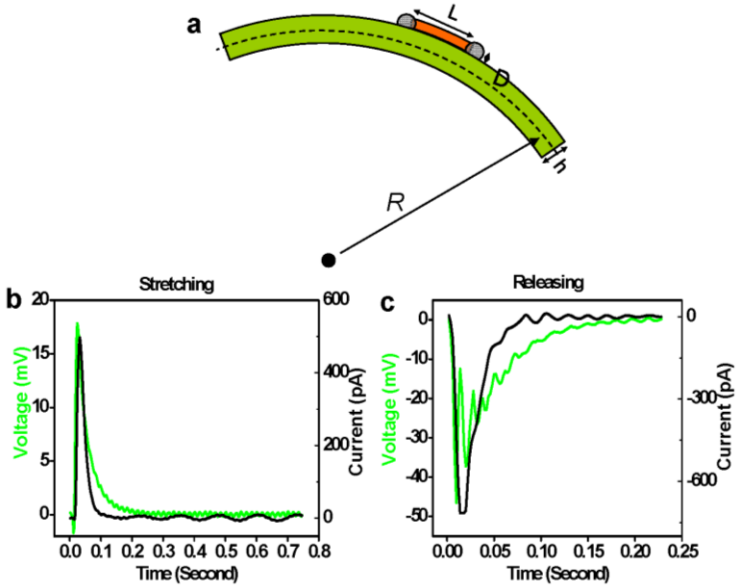

Figure 4.16. Calculation of the energy conversion efficiency of the piezoelectric wire. (a) Building up of tensile strain in the piezoelectric wire when the substrate film was bent. (b, c) Output current and voltage when a SWG was stretched and released.

4.4.6 Harvesting biomechanical energies

4.4.6.1 In-vitro case

A living species has abundant sources of mechanical energy, such as walking, breathing, and heart beating. A wide range of fluctuation in frequency and intensity is a challenging issue. This issue seriously retarded the progress of energy harvesting using traditional techniques. Our approach provides a new technology for harvesting mechanical energy from irregular motion with a magnitude at very gentle level without adding any appreciable burden.

The first example of the biomechanical energy harvesting was a SWG driven by a human finger [14]. The NW in the SWG was 100-800 nm in diameter and 100-500 μm in length. A flexible polymer layer over the entire SWG improved its robustness and adaptability. The SWG was affixed at the joint position at the top of an index finger, as shown in the inset in Figure 4.17a. The tapping of the finger induced the deformation of the ZnO NW in the SWG with a strain rate about 4-8 $\times 10^{-3}$ s^{-1} and a maximum strain of ~0.2%. As discussed earlier, the strain results in a piezoelectric polarization along the NW and thus a potential difference between the two ends, which drove the flow of the electrons in the external circuit. Such physical motion is a very gentle and slow motion.

The measured open-circuit voltage and closed-circuit current are presented in Figure 4.17a and b respectively. The periodic peaks are corresponding to the periodic tapping of the finger. Figure 4.17a shows that the voltage output is up to 25 mV while the current from Figure 5b can be more than 150 pA from a single SWG device.

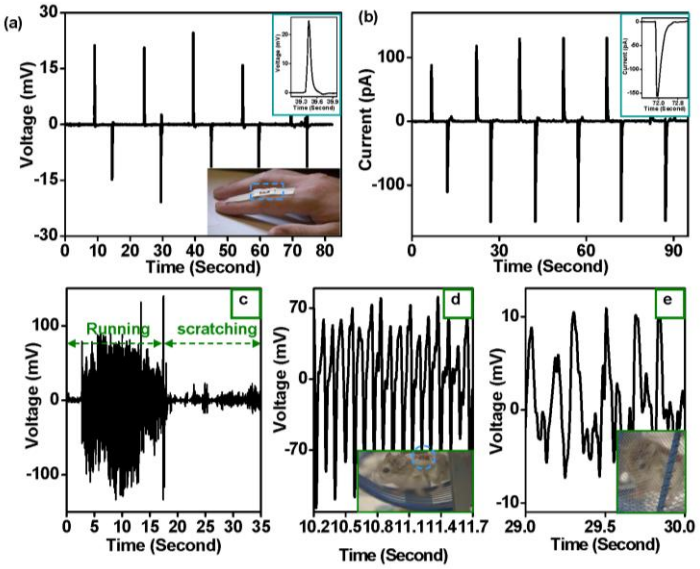

Figure 4.17. Energy harvesting from biosystem with the nanogenerator. (a) Open-circuit voltage and (b) short-circuit current output from a single wire generator fixed at the top of the index, as shown in the inset. (c) open-circuit voltage output from a nanogenerator fixed to the jacket worn by a hamster while it's running or scratching. (d) and (e) are enlarged voltage output corresponding to the running hamster and scratching hamster respectively. Insets in (d) and (e) are corresponding snapshots of the hamster with the nanogenerator on its back

In addition to the human finger, a living hamster has also been demonstrated to produce electricity with a SWG. The hamster adopted in this experiment belongs to the Campbell's dwarf type, which can produce both regular and irregular motion, like running or scratching. A special jacket has been made for the hamster to wear such that the hamster could move freely in a round cage and drive the SWG on the jacket at the same time. We measured the electric output signal from the SWG without disturbing the movement of the hamster, as shown in Figure 4.17c-e. Varied motion, running or scratching, of the hamster provided mechanical energy with distinct pattern and energy intensity to the SWG. As expected, the output electricity from the SWG changed as well. The enlarged voltage output signal in Figure 4.17d from a running hamster shows a clearly periodic pattern with the magnitude about 50-100 mV and the frequency of ~10-11 Hz. This periodicity agrees well with the running steps of the hamster. The much higher signal than the SWG on the human finger is due to the much faster strain rate of the running hamster. In comparison, the voltage output from a scratching hamster, as shown in Figure 4.17d, was quite irregular with lowered magnitude due to the irregular movement and less intense activity of the hamster. The closed-circuit current measurement revealed similar phenomena. A running hamster produced a periodic alternating current up to ~0.5 nA and a scratching hamster produced a lower irregular current.

4.4.6.2 In-vivo case

In in-vivo case, due to the presence of bio-fluid under the in-vivo working condition, the entire device was packaged with a flexible polymer to isolate it from the surroundings medium and to improve its robustness [15]. The output of the SWG is typically less than 50 mV and 500 pA in most cases. An effective SWG must exhibit Schottky behavior at one end before and after measurement. The output voltage and current of a SWG should meet the switching polarity test. For easy notation and reference, we define the side of a SWG with Schottky contact as the positive side. When the positive and negative probes of the measurement system are connected to the positive and negative sides of the SWG, respectively, the configuration is described as forward connection. The configuration with the two probes switched over is defined as reverse connection. Both configurations have to be tested. The magnitude of the signal from different connecting configurations may differ due to the influence of a small bias current of the measurement system. So the magnitude of the true signal is an average of those under forward and reverse connections.

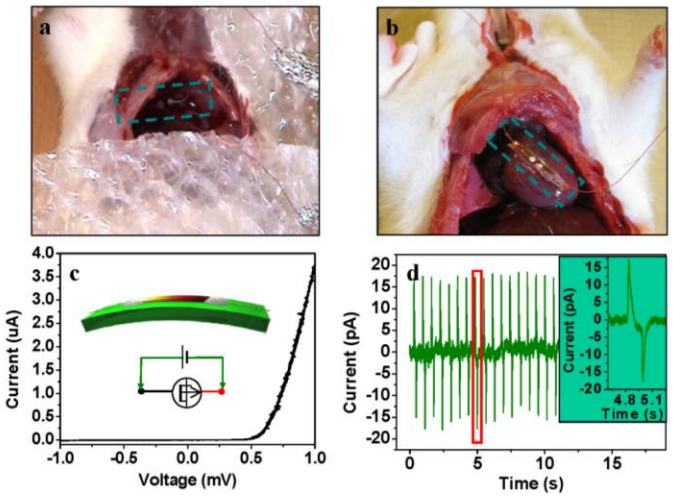

Figure 4.18. Energy harvesting from the breath and heart beat of a live rat using a SWG. A SWG attached to a live rat's diaphragm (a) and its heart (b), which drives the SWG to periodically bend and produce AC power output. (c) I-V characteristic of the SWG. The inset illustrates the schematic of the SWG and its connection configuration in reference to the measurement system. (d) Typical current output recorded from a SGW under in-vivo condition [from (a)].

A group of experiments is to convert the mechanical deformation due to the periodic expansion and contraction of the diaphragm of a rat into electricity (Fig. 4.18). The adult rats SD (Hsd: Sprague Dawley, male, 200-224g) were used for the experiment. The anesthesia procedure of the rat started with the intake of isoflurance gas (1-3% in pure medical grade oxygen), followed by the injection of Ketamine cocktail (intraperitoneal, ketamine 50-90mg/kg, xylazine 5mg/kg) and buprenorphine (intraperitoneal, 0.03mg/kg) for anesthesia induction and maintenance, respectively. The tracheotomy was first operated; and a tracheal intubation was connected to a respirator, which provided artificial respiration and sustained the life of the rat through the entire experiment. Then the rat's abdominal cavity was opened to make the ventral-side of the diaphragm reachable for implanting a SWG (Fig. 4.18). Part of the liver was cut off after proper ligation for easy observation and operation.

The reported flexible generator has demonstrated the following innovations in comparison to the nanogenerator based on vertically aligned nanowire arrays. First, the PFW is firmly bonded to a polymer substrate, thus there is no sliding/scrubbing/frictioning between the electrode and the nanowire. The stability and robustness of the generator has been largely improved from the basic working principle to technology design. Second, the entire generator system is covered by flexible polymer so that it can be packaged/built inside soft materials. This allows it to be used in fluid and under hash conditions where liquid/water/gas infiltration is possible. It is possible to raise the output power by rationally connecting individual generators in serial; it is possible to integrate thousands of such generators inside a common substrate to form a flexible power sheet/film (see Chapter 7). Third, the new design eliminates the complication of maintaining a small gap (50-100 nm) between the top zigzag electrode and the NW arrays during packaging, making it much easy and low cost for practical manufacturing. Finally, the generator established here could be extended to piezoelectric nanowires/microwires made of $Pb(Zr,Ti)O_3$, for example, which have a large piezoelectric coefficient. The flexible generators are feasible and practical to

be implanted in muscles, embedded in cloths, built in surface layers, and placed in shoe pads. The demonstrated principle and design establish a new fundamental methodology and technology for scavenging mechanical energy from the environment for applications in biomedical science, environmental monitoring, defense technology and personal electronics.

References for Chapter 4:

[1] Z.L. Wang, J.H. Song, *Science* **312**, 242 (2006).
[2] X.D. Wang, J.H. Song , P. Li , J.H. Ryou , R.D. Dupuis , C.J. Summers and Z.L. Wang, *J. Am. Chem. Soc*. **127**, 7920 (2005).
[3] Z.L. Wang, *J. Nanoscience and Nanotechnology* **8**, 27 (2008).
[4] X.D. Wang, J.H. Song and Z.L. Wang, *J. Materials Chemistry* **17**, 711 (2007).
[5] J.H. Song, J. Zhou, Z.L. Wang, *Nano Letters* **6**, 1656 (2006).
[6] P.X. Gao, J.H. Song, J. Liu and Z.L. Wang, *Adv. Materials* **19**, 67 (2007).
[7] J. Liu, P. Fei, J.H. Song, X.D. Wang, C.S. Lao, R. Tummala, Z.L. Wang, *Nano Letters* **8**, 328 (2008).
[8] M.P. Lu, J.H. Song, M.Y. Lu, T.C. Chen, L.J. Chen, Z.L. Wang, *Nano Letter*, submitted.
[9] S. S. Lin, J. H. Song, Y. F. Lu, Z. L. Wang*, *Nanotechnology* **20**, 365703 (2009).
[10] C.T. Huang, J.H. Song, W.F. Lee, Y. Ding, Z.Y. Gao, Y. Hao, L.J. Chen, Z.L. Wang, *J. Am. Chem. Soc*. **132**, 4766 (2010).
[11] C.T. Huang, J.H. Song, C.M. Tsai, W.F. Lee, D.H. Lien, Z.Y. Gao, Y. Hao, L.J. Chen, and Z.L. Wang, *Adv. Mater*. **36**, 4008-4013 (2010).
[12] Y.F. Lin, J.H. Song, D. Yong, S.Y. Lu, Z.L. Wang, *Adv. Materials* **20**, 3127 (2008).
[13] R.S. Yang, Y. Qin, L.M. Dai, Z.L. Wang, *Nature Nanotechnology* **4**, 34 (2009).
[14] R.S. Yang, Y. Qin, C. Li, G. Zhu, Z.L. Wang, *Nano Lett.* **9**, 1201 (2009).
[15] Z. Li, G. Zhu, R.S. Yang, A.C. Wang, Z.L. Wang, *Adv. Mater.* **22**, 2534 (2010).

Chapter 5

Characterization of Nanogenerator Outputs

Owing to the anisotropic property and small output signals of the piezoelectric nanogenerators (NGs) and the influence of the measurement system and environment, identification of the true signal generated by the NG is critical. The output of the SWG may be affected by the measurement system, change in capacitance of the microwire and electric circuit during mechanical deformation, and the coupling of the SWG with the measurement system, it is thus easy to observe false signals. To differentiate the electric power that is generated by the SWG from possible artifacts, we have developed three criteria consisting of 11 tests to rule out artifacts [1, 2]. The generator must satisfy not only the Schottky behavior test (1) and switching polarity tests (2), but also a linear superposition of current and voltage for 8 configurations as well. A true signal (current and voltage) generated from a generator must pass each and all of the tests. Those criteria and configurations are applicable to all types of nanogenerators and can serve as standard tests for general purpose.

5.1 Output current

For the short-circuit current measurement, we first measured the forward connection, in which the positive probe and negative probe of the measurement system are connected to the positive and negative ends of the generator, respectively. Figures 5.1a and b show the results for SWG A and SWG B. The inserts give the connection configurations. The positive peaks correspond to the stretching states of the PFW when the underneath substrate is bent inward. When the substrate is released, the PFW returns to free state, resulting in a negative electric peak. The mechanism about the creation of the signal has been reported elsewhere.

In order to identify if the signal is the true electricity output due to piezoelectric property of the ZnO fine wire, we did the switching-polarity test, in which the positive and negative probes of the current meter are connected to the negative and positive ends of the SWG, respectively. The result is given in Fig 5.1c and d. The output signal is reversal of that presented in Figs. 5.1a and b. Stretching of the PFW produces a negative pulse, and a positive pulse is generated when released. The satisfaction of the switching-polarity test rules out the possible error from the system capacitor change. The change of contact resistance might produce a signal when the SWG is deformed, but such signal will not change its sign from positive to negative when the connection is reversed. Additionally, we also notice the magnitude difference between the signals with forward connection and with the reverse connection. The non-symmetric output of the SWG prior and after switching the polarity is likely caused by the measurement system that has a bias current. If this bias current adds up to the current generated by the SWG at forward connection configuration, it will be subtracted from the generated current at reversely connected configuration. The true signal generated by the SWG is an average of the magnitudes observed under forward and reverse connection configurations

Due to the presence of Schottky at one end of the SWG, the switching-polarity test is not sufficient to rule out some of the artifacts. The linear superposition is thus applied. We did the current measurement

when two SWGs were connected in parallel to examine the liner superposition of currents. Since there is a Schottky contact at one end of the SWG, we need to pay attention to their connection direction. Figure 5.1e presents the result when two SWGs are in the same direction, in which output current is enhanced and approximately equal to the sum of signal from Fig. 5.1a and Fig. 5.1b. In comparison, when two SWGs were connected in reversed directions as shown in Fig. 5.1f, the output current is decreased and approximately equal to the sum of the signals. As a result, a linear superposition of current is satisfied for the two SWGs. In addition, the parallel connection of the two SWGs also satisfy switching-polarity test.

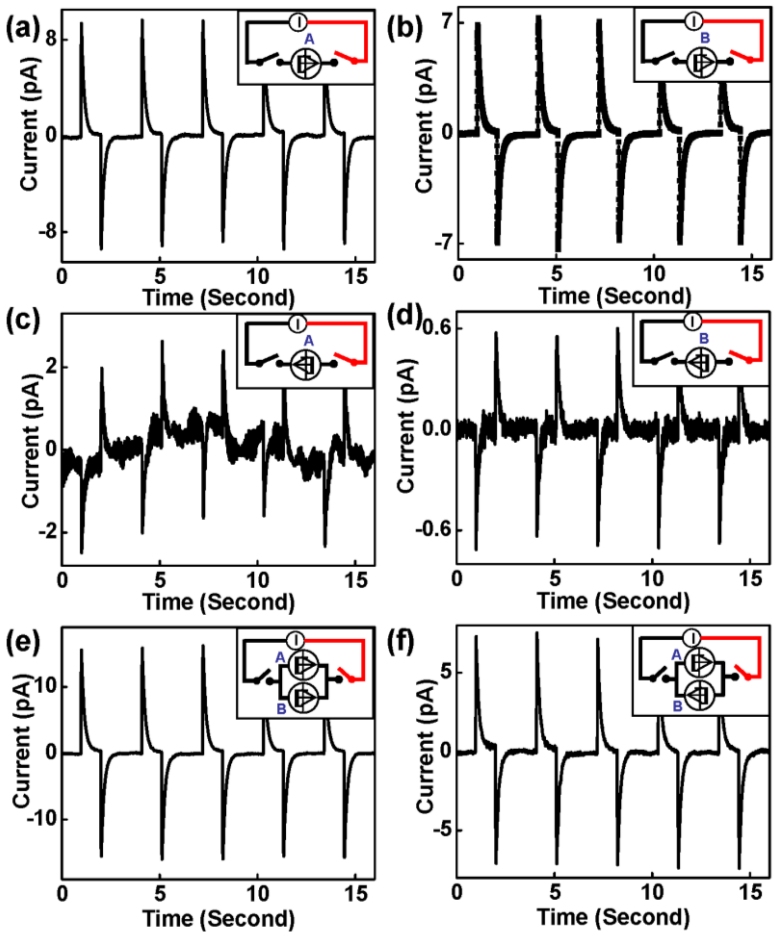

Figure 5.1 (a) and (b) Short-circuit current power output from SWG A and SWG B, respectively, under forward connection. (c) and (d) Short-circuit current power output from SWG A and SWG B, respectively, under reverse connection. (e) and (f) Parallel connection of SWG A and SWG B demonstrates SWG's ability to "add up" or "cancel out". All insets illustrate the connection configuration of the two SWGs in reference to the measurement system.

5.2 Output voltage

The voltage output of the SWGs is present in Figure 5.2. SWG A and SWG B generate a positive voltage signal when the PFWs are stretched and a negative signal when the PFWs are release, as shown in Figs. 5.2a and b. The switching-polarity is also satisfied for output voltage, as shown in Figs. 5.2c and d. In order to testify the signal and further characterize the generator, it is necessary to measure the voltage when the two SWGs are in serial, as shown in Figs. 5.2e and f. When two SWGs are connected in the same direction, the final output is apparently increased. In comparison, when two SWGs are connected in opposite directions, the final output is reduced. As a result, the superposition of voltage is also satisfied for those two SWGs. Further more, the SWGs connected in serials also satisfy switching-polarity test.

By taking the average value from the output signals when the SWGs are bent, the output current and

voltage for Figs. 5.1 and 5.2 are tabulated in Table 5.1. In order to simplify the discussion, we define V_A^+ and I_A^+ as the voltage and current measured from SWG A under forward connection, and V_A^- and I_A^- when reversely connected. The same definitions apply to SWG B. In an ideal case, we should have $V_A^- = -V_A^+$ and $I_A^- = -I_A^+$. However, with consideration the contribution from the bias current from the measurement system, the measured voltage/current may not have the same magnitude. In any case, a true electricity output from an SWG must change its sign when the SWG is reversely connected. The first two rows in Table 5.1 fully support that the SWG A and SWG B satisfy the first criteria of switching-polarity test for both output current and voltage.

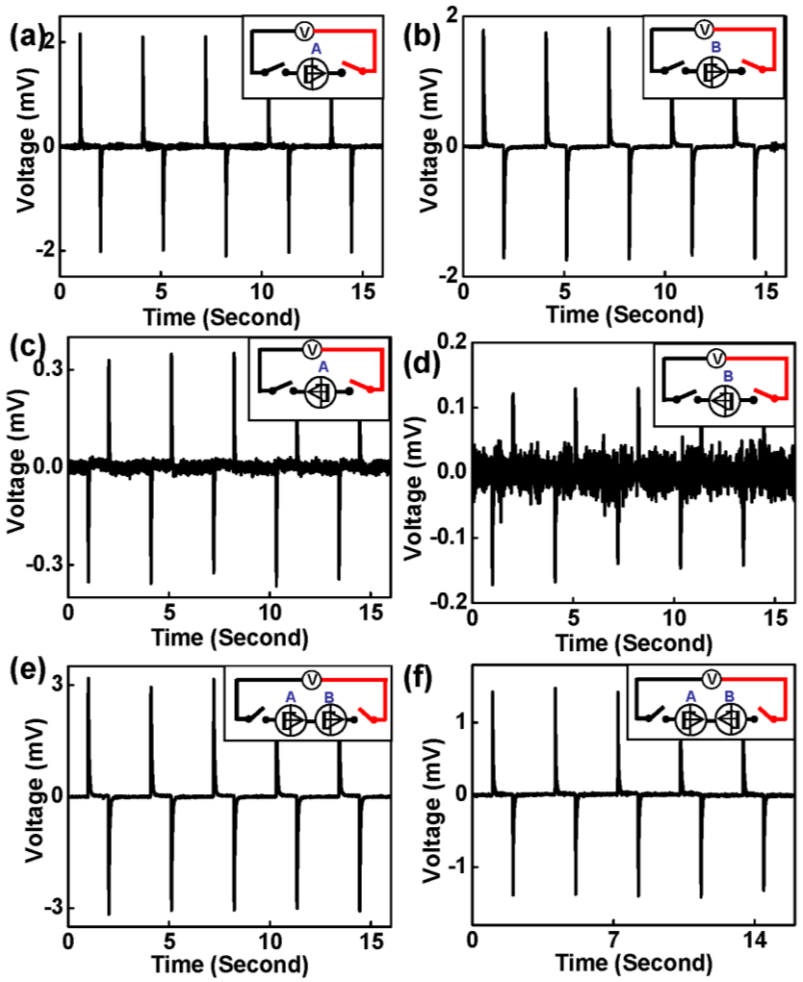

Figure 5.2 (a) and (b) Open-circuit voltage output from SWG A and SWG B, respectively, under forward connection. (c) and (d) Open-circuit voltage power output from SWG A and SWG B, respectively, under reversal connection. (e) and (f) Serial connection of SWG A and SWG B demonstrates the "add up" or "cancel out" effect. All insets illustrate the connection configurations of the SWGs in reference to the measurement system.

Table 5.1: Summary of current and voltage output when the SWG A and B were connected under various configurations illustrated in Figs. 5.1 and 5.2.

	Current (pA)		Voltage (mV)	
	Forward Connection	**Reverse Connection**	**Forward Connection**	**Reverse Connection**
SWG A	9.54	-2.42	2.13	-0.36
SWG B	7.31	-0.7	1.81	-0.15
SWG A+SWG B	16.2	-3.76	3.18	-0.37
SWG A -SWG B	7.33	4.65	1.46	1.5

The last two rows in Table 5.1 demonstrate the second criteria of linear superposition of current and voltage under 8 connection configurations. When the SWG A and B are connected in parallel, as shown in the insets in Figure 5.1e and f, the measured currents (last two rows in Current columns) obey the following requirements:

$$I^{+}_{A+B} = I^{+}_{A} + I^{+}_{B}$$
$$I^{-}_{A+B} = I^{-}_{A} + I^{-}_{B}$$
$$I^{+}_{A-B} = I^{+}_{A} + I^{-}_{B}$$
$$I^{-}_{A-B} = I^{-}_{A} + I^{+}_{B}$$

When the SWG A and B are connected in series, as shown in the insets in Fig. 5.2e and f, the measured voltage (last rows in Voltage columns) obey the following requirements:

$$V^{+}_{A+B} = V^{+}_{A} + V^{+}_{B}$$
$$V^{-}_{A+B} = V^{-}_{A} + V^{-}_{B}$$
$$V^{+}_{A-B} = V^{+}_{A} + V^{-}_{B}$$
$$V^{-}_{A-B} = V^{-}_{A} + V^{+}_{B}$$

5.3 Summary

In summary, we have developed two criteria, switching-polarity tests and linear superposition tests of current and voltage under 10 configurations, for identification of the electricity output from nanogenerators. Those two criteria can explicitly exclude the common system errors and serve as the standards to guide the characterization of different piezoelectric nanogenerators. This study is of considerable importance for further investigation and scale-up of nanogenerators towards practical applications.

References for Chapter 5:

[1] R.S. Yang, Y. Qin, C. Li, L.M. Dai and Z.L. Wang, *Appl. Phys. Letts.* **94**, 022905 (2009).

[2] R.S. Yang, Y. Qin, L.M. Dai, Z.L. Wang, *Nature Nanotechnology* **4**, 34-39 (2009).

Chapter 6

High output nanogenerators – vertical nanowire arrays

Although the principles presented in Chapter 4 are applicable for energy harvesting [1], the output power using a single nanowire is rather small. Innovative approaches must be developed in order to scale up the approach so that a significant amount of power can be acquired. In this chapter, we present the two approaches developed by using vertically aligned nanowire arrays.

6.1 Ultrasonic wave driven nanogenerator

As for the AFM tip based mechanical agitation, we must make an innovative design to drastically improve the performance of the NG in following aspects. First, we must eliminate the use of AFM for making the mechanical deformation of the NWs so that the power generation can be achieved by an adaptable, mobile and cost-effective approach over a larger scale. Secondly, all of the NWs are required to generate electricity simultaneously and continuously, and all the electricity can be effectively collected and output. Finally, the energy to be converted into electricity has to be provided in a form of wave/vibration from the environment at even low frequency such as a few Hz. We have developed an innovative approach that has addressed these challenges [2].

6.1.1 Why zigzag electrode?

Figure 6.1a and b show the mechanism of the power output when an AFM tip triggers a piezoelectric nanowire, as presented in Chapter 4. To replace the role play by AFM tip in deflecting the NW, we first examined an "inverted V-shape" (i-V) electrode. Once the i-V electrode moves downward as driven by an external excitation, a NW would be deflected towards left-hand side, for example. At the first contact point, a positive potential is created due to the local tensile strain (Fig. 6.1c). In such a case, the piezoelectric potential is preserved since the local contact is a reversely biased Schottky barrier that does not permit the flow of charges. When the electrode further pushes the NW until it bends enough to reach the other side of the i-V electrode (Fig. 6.1d), the local contact is a forward biased Schottky barrier, thus, the local potential drop drives the flow of electrons. Therefore, we can replace the AFM tip by an i-V electrode. The i-V electrode can be extrapolated into a zigzag electrode (Fig. 6.1e), which is made of Si coated with Pt. The Pt coating is not only for enhancing the conductivity of the electrode but also for creating a Schottky contact at the interface with ZnO. In practice, the coating metal can be any conductive alloy

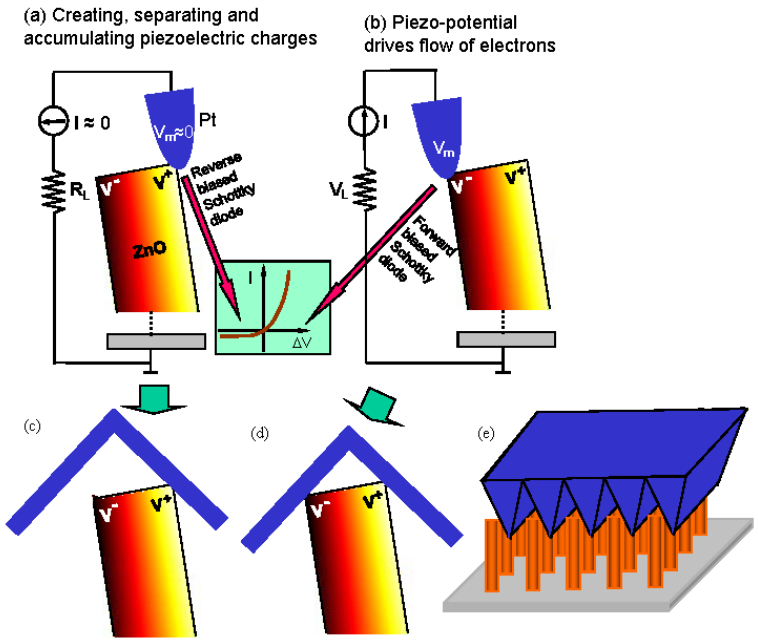

Figure 6.1 (a, b) The current generation process of a piezoelectric nanowire under the deformation of an AFM tip. (c-d) The idea for introducing the zigzag electrode following the mechanism shown in in (a, b) for capturing the electricity generated by millions of nanowires.

as long as it can form a Schottky barrier with ZnO. The zigzag electrode acts as an array of parallel AFM tips. The electrode was placed and manipulated above the NW arrays at a controlled distance. The electricity produced by the relative deflection/displacement between the NWs and the electrode via either bending or vibration is expected to be output simultaneously and continuously.

6.1.2 Working mechanism

Figure 6.2a-c show four possible configurations of contact between a NW and the zigzag electrode. NWs I and II are being deflected towards left- and right-hand side, respectively, by the electrode. Regardless their deflection directions, the currents produced by the NW I and II constructively add up. NW III is chosen to elaborate the vibration induced by an ultrasonic wave. As shown in Fig. 6.2c, when the compressive side of NW III is in contact with the electrode, the same discharge process as for NW I occurs, resulting in the flow of current from the electrode into the NW. NW IV, short in height, is in compressive strain by the electrode without bending. In such a case, the piezoelectric voltage created at the top of the NW is negative. Thus, across the electrode–ZnO interface, a positively biased Schottky barrier is formed; hence, the electrons can freely flow across the interface. As a result, electrons flow from the NW into the top zigzag electrode as the deformation occurs. This discharging process, if significant, may also contribute to the measured current. The output current is a sum of those NWs that actively contributing output power, but the voltage of the NG is determined by a single NW because all of the NWs are "in parallel".

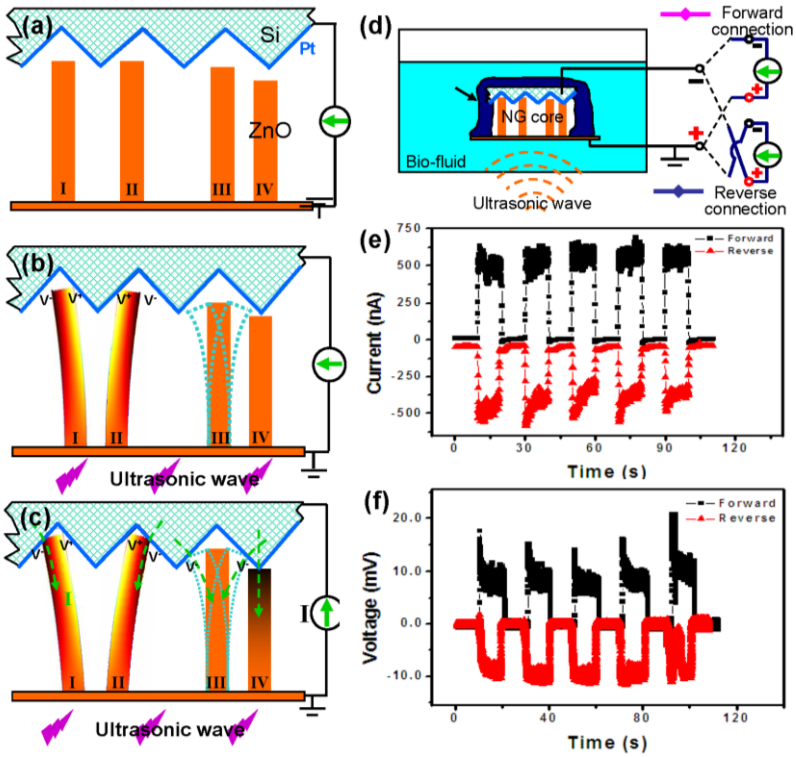

Figure 6.2. The mechanism of the nanogenerator driven by ultrasonic wave. (a) Schematic illustration of the zigzag electrode and the four types of representing configurations of the NWs. (b) The piezoelectric potential created across the NW I and II under the push/deflection of the electrode as driven by the ultrasonic wave, but without flow of current due to the reversely biased Schottky barrier at the electrode-NW interface. The NW III is in vibration under the stimulation of the ultrasonic wave. The NW IV is in compressive strain without bending. (c) Once the NWs touches the surface of the adjacent teeth, the Schottky barrier at the electrode-NW interface is forward biased, piezoelectric discharge occurs, resulting in the observation of current flow in the external circuit. (d) Schematic of a NG that operates in bio-fluid and the two types of connections used to characterize the performance of the NG. The pink and blue curves represent signals from forward connected current/voltage (I/V) meter and reversely connected I/V meter, respectively. (e, f) The short circuit current and open circuit voltage measured by the two types of connections when the ultrasonic wave was periodically turned on and off.

6.1.3 Output at 50 KHz

The packaged NG was placed in the water bath to measure the closed circuit current and open circuit voltage. The ultrasonic wave of frequency 41 kHz was periodically turned on every other 15 seconds. Fig. 6.2e shows the

closed circuit current when the ultrasonic wave was turned on and off. The data clearly indicate that the current output was originated from the NG as a result of ultrasonic wave excitation, as the output coincided with the working cycle of the ultrasonic wave generator. A similar pattern in the open circuit voltage output was also observed, as shown in Fig. 6.2f. Both the current and voltage outputs exhibit high levels for this type of NG, with a current ~500 nA and voltage ~10 mV. Considering the effective area of the NG (6 mm^2), it is equivalent to a current generation density of ~8.3 $\mu A/cm^2$. A power generation density of ~83 nW/cm^2 is reported.

It must be pointed out that the operation of the NG does not rely on mechanical resonance as required by some of the energy harvesting technologies, instead it is based on mechanical deflection. Such a design allows the NG to work in a wide range of frequencies, from few Hz, kHz and even to MHz. This large adaptability greatly expands the application of the NG for harvesting various mechanical energies.

6.2 Integrated nanotip-to-nanowire approach

As presented in the earlier section, the zigzag electrode acts as an array of parallel integrated tips for simultaneously creating, collecting and outputting electricity from all of the active NWs. In this design, the non-uniform heights and random distribution of the NWs on substrate, however, may prevent a large fraction of NWs from contributing to the energy conversion process; the packaging technology is of critical importance to keep the gap distance between the zigzag electrode and the NW arrays just right so that it is large enough to allow the NWs to be freely bent/deflected, but small enough to ensure an intimate contact between the NWs and the electrode. In this section, we present a new approach to NG that is composed of integrated, paired nanobrushes made of pyramid-shaped metal coated ZnO nanotip (NTP) arrays and hexagonal-prism shaped ZnO NW arrays [3 , 4], which were synthesized using chemical approach at < 100 ^oC on the two

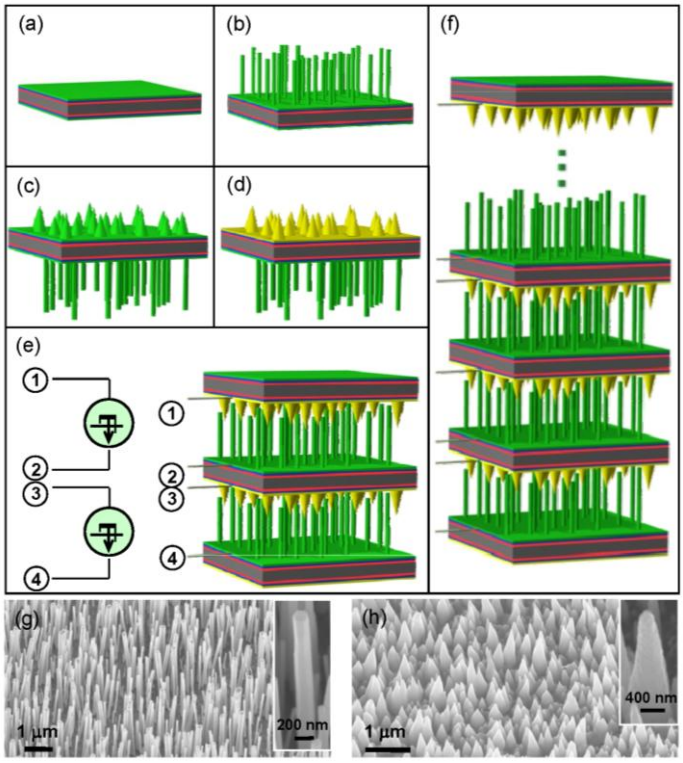

Figure 6.3. Design and fabrication procedures of the multilayered NGs and rational growth of ZnO NW and NTP arrays. (a) The as-fabricated substrate after coating with the $Zn(CH_3COO)_2$ seed layer. (b) Growth of hexagonal prism shaped NW arrays by wet chemical method on one side. (c) Growth of pyramid shaped NTP arrays on the other side. (d) Coating the NTP arrays with Au layer by magnetron plasma sputter. (e) Two layered NG made by stacking three layers of the wafer structures shown in (d), with the Au coated NTP arrays facing and interpenetrating the bare NW arrays. The right-hand side is the designed symbol for representing the NGs. (f) A multilayered three-dimensional NG integrated by stacking multiple layers of wafer structures. (g) 60° tilt view scanning electron microscopy (SEM) image of the hexagonal prism shaped ZnO NW arrays grown by chemical approach. (h) 60° tilted view SEM image of the pyramid shaped ZnO NTP arrays grown by chemical approach. Inset SEM images are high magnification views of a single NW and NTP.

surfaces of a common substrate, respectively. By stacking one piece of such structure in close proximity over another to form a layer-by-layer matched brush architecture, direct current is generated by exciting the architecture using ultrasonic waves. A four-layer integrated NG is demonstrated to generate an output power density of 0.11 $\mu W/cm^2$ at a voltage of 62 mV.

6.2.1 Fabrication method

The NGs were first fabricated by rationally growing ZnO arrays of controlled orientation and shape on a double-side polished Si wafer. The wafer was coated with 100 nm thick Al_2O_3 film on both sides by atomic layer deposition, which served as an insulating layer to ensure independent operations of the NGs to be built in the adjacent layers. Then the wafer was deposited with a 20 nm thick Cr layer by direct current magnetron plasma sputtering on both the top and bottom surfaces except the side surface. Following that, a 50 nm thick ZnO layer was deposited by radio frequency magnetron sputtering onto the Cr layers at the top and bottom surfaces except side surfaces. The Cr layer served not only as an adhesion to bind the Al_2O_3 layer and the ZnO layer together, but also as a common electrode for collecting the charges to be transported through each and every active NW/NTP.

The aligned ZnO arrays were grown via chemical methods on both sides of the Si wafer with a slight modification to achieve rationally desired morphologies. The wafer was rinsed by 4 ℃ 0.5 mmol/L $Zn(CH_3COO)_2$ in ethanol solution on both sides, and then baked at 350 ℃ for 15 minutes to form a layer of (0001) textured ZnO seeds, which leads to the growth of ZnO NWs and NTPs. The density of the ZnO seeds could be varied by using different concentrations of the $Zn(CH_3COO)_2$ ethanol solution. The morphology of the ZnO arrays could be manipulated by using different growth temperatures for different lengths of time. Generally speaking, at a low growth temperature and long growth time, NWs were formed (Figure 6.3b,g), while at a relatively high growth temperature and short growth time, NTPs were grown (Figure 6.3c,h). The morphology controlled growth of ZnO NW/NTP arrays on different sides of the Si wafer was achieved by floating the substrate on the nutrient solution surface, which is composed of 5 mM 1-to-1 ratio of $Zn(NO_3)_2$ and hexamethylenetetramine, during the growth so that we could apply different growth conditions (the nutrient solution was heated up to 100 ℃ for 24 hours for growing the pyramid shaped NTPs or 70 ℃ for 48 hours for growing the hexagonal prism shaped NWs) independently for either side. Finally, the side with NTPs was coated uniformly with 100 nm thick Au by magnetron plasma sputtering to form a metal tip array.

A NG was made by stacking together two pieces of the grown wafer structures, with the Au coated NTPs partially interpenetrating into the NWs as illustrated in Figure 6.3e; and in the same way, a multilayered NG was integrated by stacking multiple layers of such structures layer-by-layer (Figure 6.3f). The Au coated NTPs acted like an array of AFM tips, slightly interpenetrating into the spacing between the NWs underneath, just like two face to face brushes with a small degree of interdigitative overlap at the ends. Such a design does not have a strict requirement on the height uniformity of the NWs, nor needs to maintain a specific gap distance between the layers, rendering it to be much easier to control the packaging of the layers. Each layer was insulated from adjacent layers by the Al_2O_3 thin film. After making connection to output wires, the entire architecture was sealed and packaged by epoxy resin to prevent infiltration of any liquid. In the current generating process, the positive electrode was the side with bare ZnO NW arrays and the negative electrode was the side with Au coated ZnO NTP arrays.

6.2.2 Working mechanism

Several effects could be involved in the energy generation process: triboelectric, pyroelectric and piezoelectric. The contribution from triboelectric was ruled out by our direct in-situ AFM observation of power generation from a single nanowire under optical imaging and our measurements carried out using nanowires of WO_3, Si and carbon nanotubes. As for the pyroelectric effect, the temperature in the ultrasonic wave chamber (~one gallon) was fairly uniform and there was surely no significant temperature gradient across the nanogenerator that had a size of a few millimeters.

The energy conversion process can be understood from the change in local band structure induced by the piezoelectric potential, which is asymmetric across the NW with the stretched side positive and the compressed side negative. Since Au has a work function of 4.8 eV, which is larger than the electron affinity of ZnO (4.5 eV), a Schottky contact (barrier height of Φ_{SB}) at the interface is formed (Figure 6.4a). The Schottky barrier exists as soon as the NTP is in contact with the NW, When a NTP slowly pushes a NW, a strain field is created across the NW width, with its outer surface in tensile and its inner surface in compressive strain. This asymmetric strain produces an asymmetric piezoelectric potential across its width, with V^- (negative) at the compressive surface and V^+ (positive) at the stretched surface[3,12]. It is important to note that the piezoelectric potential is created by the ions in the crystal when the NW is subject to mechanical deformation, which cannot move freely; they may be partially screened by free carriers in the NW but cannot be completely neutralized or depleted.[13] This means that the piezoelectric potential still preserves even with consideration of the existence of moderate free charge carriers in ZnO NW. When a NTP is in contact with the stretched surface of the NW, which has a higher local potential than the NTP, a reversely biased Schottky barrier (Φ_{SB}) blocks the flow of electrons through the interface (Figure 6.4b). Because the piezo-potential is built up very fast inside the NW [13] as the NTP is

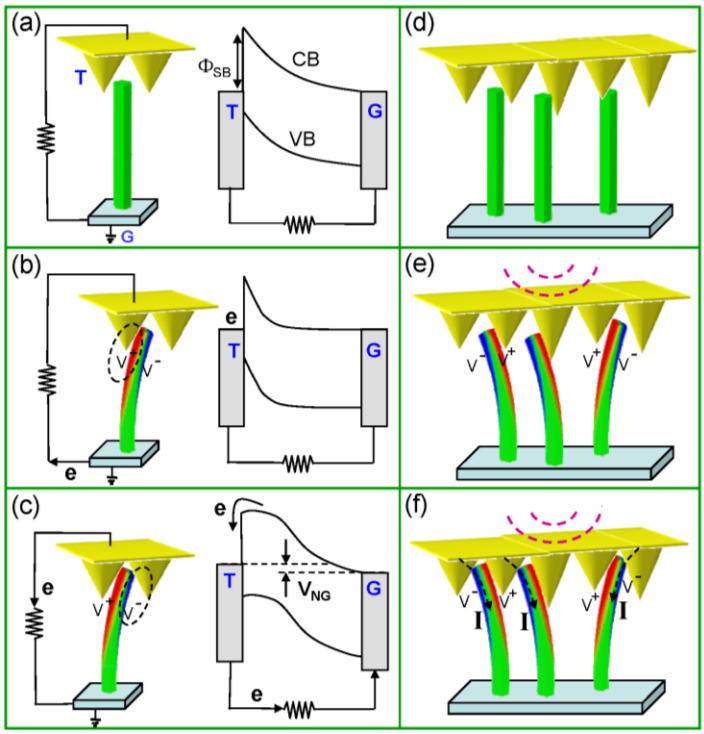

Figure 6.4. Physical principle of a single layered NG. by considering band diagrams taken from the left/right boundaries of the NW. (a) Schematic diagram of the NG and the corresponding electron energy band diagram, where "T" is the Au-NTP, and "G" is the grounded NW. (b) Under the excitation of ultrasonic wave, there is a relative movement (in both vertical or lateral directions) between the NTP and the NW, and as a result the NW is bent with the contact surface being stretched. The corresponding local piezoelectric potential (positive) creates a reversely biased Schottky barrier. This diagram represents the equilibrium status of the contact between the NTP and NW. (c) When the relative movement of the NTP and NW is strong enough, the NW is bent enough to touch another adjacent NTP with its compressive side. Then, the local piezoelectric potential (negative) sets the Schottky barrier to be forward biased and drives the flow of electrons from the NW into the NTP. If we consider the statistical contribution of thousands of electrons from many NWs, a steady current is formed. This diagram represents the equilibrium status of the energy diagram as many NWs participating the energy generation. (d) Schematic diagram of multiple NW and NTP contacts with slight variation in heights and lateral distribution. (e) Disregard the NWs being deflected to left-hand or right-hand, the first contacting surfaces with the tips are tensile surfaces with a positive piezoelectric potential. (f) Electric currents created by the driving force of the piezoelectric potential when the compressive surfaces of the NWs contact the surfaces of adjacent tips. The contacts can be simultaneous or with a slight delay, but the created transient currents all flow in the same direction, which is from NTPs to NWs.

pushing the NW, at every moment during the pushing process, the whole system is in an equilibrium state. In other words, if we take a snapshot of every moment of the process, for example Figure 6.4b, the system is in equilibrium. This is because the flow speed of charges is a lot faster than the scanning speed of the tip. As the degree of NWs' bending increases, its compressive side may reach the surface of an adjacent NTP, thus, the local piezoelectric potential V^- (negative) in the NW results in a local shape modification of the conduction band of the NW near the NTP (Figure 6.4c). The piezoelectric potential extends through almost the entire length of the NW according to theoretical calculation, and its most important modification to the band shape is at near the Schottky contact region because of the high-raise of the local band. If the raise in local potential energy is large enough as determined by the degree of NW bending, the accumulated local n-type carriers in the NW can quickly flow through the contact into the NTP, which creates a circular flow of the electrons in the external circuit, e.g., the output current. In terms of a single pair of NTP and NW, this process is transient. But if we focus on the statistical contributions from thousands of NTP/NW pairs, this process is in a steady state, with a stable and continuous current output. The role played by the Schottky barrier is to prevent the flow of electrons from the NTP into the NW, which is a key structure for preserving the piezoelectric potential and releasing the free electrons from the NW into the NTP. The role played by the piezoelectric potential is to drive the electrons from the ZnO NW to overcome the threshold energy at the Au-ZnO interface and flow into the Au NTP. The piezoelectric potential does not directly determine the magnitude of the output voltage.

For the ultrasonic wave driven nanogenerator, there were thousands to millions of NWs that contribute to the electric output in a random phase. Although each NW is considered to be in an unequilibrium/trasient state, but the statistical average of thousands of them can be considered as in a steady state with a stable and continuous output, which is similar to the process in solar cells, in which a single photon can only crease one or a few electrons that can form an electric pulse, but a continuous current can be formed if thousands of photons strike the cell in random phase. This concept is applied to understanding the output voltage of the NG. As shown in Fig. 6.4c, as more electrons are pumped into the Au NTP, the local Fermi surface is raised by the accumulated electrons with considering the statistical contribution from all of the NWs, as discussed above. Therefore, the theoretical output voltage is dictated by the difference between the Fermi energies of the Au-NTP on the top and the ZnO-NW at the bottom, as illustrate by V_{NG} in Figure 6.4c. In practice, one has to consider the contact resistance, system capacitance and possible current leakage, all of which would lower the voltage output to be measured.

As the NGs was subjected to ultrasonic wave excitation in a water bath, the ultrasonic wave would cause a vertical or lateral vibration of the Si wafers and/or vibration of the ZnO NWs, resulting in a relative bending/deflection of the NWs as enforced by the Au coated NTPs (Figure 6.3e). The degree of bending/deflection depends on the intensity of ultrasonic wave. So the variation of ultrasonic wave will cause the change of the output signals, which has been studies by our group and will be published elsewhere. The NTPs were significantly thicker and stiffer than the NWs (Figure 6.3g, h). Regardless the NWs being deflected to left-hand or right-hand, the currents generated by all of them add up constructively as determined by the Schottky barrier and the uniaxial growth of the NWs (Figures 6.3e and f), although the output voltage is determined by the performance of individual NW. A constant and steady direct output current is observed as long as the ultrasonic wave is on.

6.2.3 Enhancing performance

The layer-by-layer integrated NGs show enhanced output current and voltage [3]. By connecting two individual layers of NG in parallel, e.g., connecting electrodes ① with ③ and electrodes ② with ④ in Figure 6.3e, the output current was a sum of the two NGs. As shown in Figure 6.5a, a single layer of NG L1 gave ~13 nA of short circuit output current, and the other layer of NG L2 gave ~10 nA under the same conditions. After connecting them in parallel, the output current increased to an average of 22 nA (Figure 6.5a, red curve). The total output current was just 3 nA (Figure 6.5a, purple curve), which was the difference of their individual output currents. As shown in Figure 6.5a, the output signal for the L1+L2 case is a lot "unstable" than the L1-L2 case. This is due to the fact that the L1+L2 case double amplifies the instability introduced by the intensity and frequency of the ultrasonic wave source, while the L1-L2 case impairs the instability.

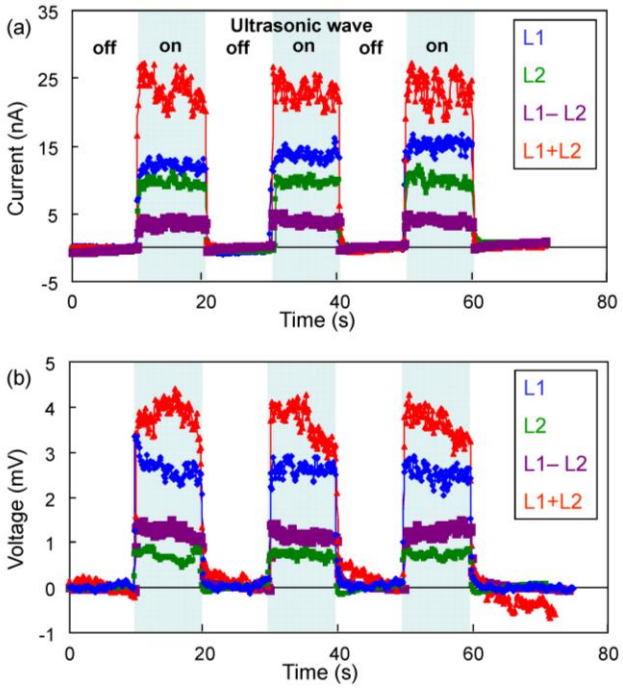

Figure 6.5. Output current and voltage signals by connecting two single-layered NGs in parallel and anti-parallel, and serial and anti-serial, illustrating the 3D integration of the NGs for raising output power. (a) Short circuit current output measured from the NGs when connected in parallel and anti-parallel. (b) Open circuit voltage output measured from the NGs when connected in serial and anti-serial. The regions when the ultrasonic wave was on and off are indicated. The surface area of each NG was 6 mm^2.

In a similar way, by connecting two layers of NGs in serial, e.g., connecting electrodes ② with ③ in Figure 1e, the output voltage was the sum of the output voltages from the two individual layers. As presented in Figure 6.5b, L1 gave an output voltage of approximate 2.6 mV, while L2 gave about 0.8 mV. When those two layers of NG were connected in serial and tested under the same condition, the output voltage was around 3.5 mV on average (Figure 6.5b, red curve), which was the sum of their individual outputs. Furthermore, if we put the two layers in anti-serial, e.g, connecting electrodes ② with ④ in Figure 1e, the output voltage was just 1.5 mV (Figure 6.5b, purple curve), which was the difference of their individual output voltages.

Integration of multilayers of NG has great potential for raising the output voltage. Once the output voltage is high enough to operate an electronic device, such as a diode, the outputting electric energy from the NGs can be stored for future use. To demonstrate the technological feasibility of the approach, we have connected several NGs in serial. As shown in Figure 6.6a, four individual layers of NGs, L3, L4, L5 and L6 with 11 mV, 14 mV, 16 mV and 20 mV open circuit output voltages, respectively, were connected in serial. The resultant total output voltage was ~62 mV as expected. The corresponding short circuit output current was around 105 nA (Figure 6.6b). The I-V curves of NGs L3, L4, L5 and L6 are presented in Figure S3. Each of them shows typical Schottky characteristics. It appears that the ultrasonic wave of 41 kHz can penetrate rather deep so that the damping effect is not a major problem. The maximum power output of the four-layer integrated NG is 6.5 nW for a surface area of 6 mm^2. A power density of 0.11 $\mu W/cm^2$ was achieved.

6.3 Integrated nanogenerators with firmly contacted ends

We report an innovative and much improved approach toward high power output alternating-current (AC) NG (AC-NG) based on vertically aligned ZnO NW arrays that are in solid bond/contact at the two ends with the electrodes [5 , 6]. A periodic, low-frequency, uniaxial straining onto the ZnO NWs by an external mechanical impact via the top electrode creates a piezoelectric potential along the NWs, which results in an alternative electrical output, if there is a Schottky contact at least at one end. A three layer integration of such AC-NGs enhances the output voltage up to 0.243 V and a peak power density of ~2.7 mW/cm^3. The integration of an AC-NG with a ZnO NW based pH or UV nanosensor has demonstrated the "self-powered" nanosystem that is built up solely using ZnO NWs, which shows its potential to work as an independent, reliable and sustainable unit at environments where a dynamic compressive stress/straining is available, such as in shoe pads, automobile tires and underneath of carpet/floor.

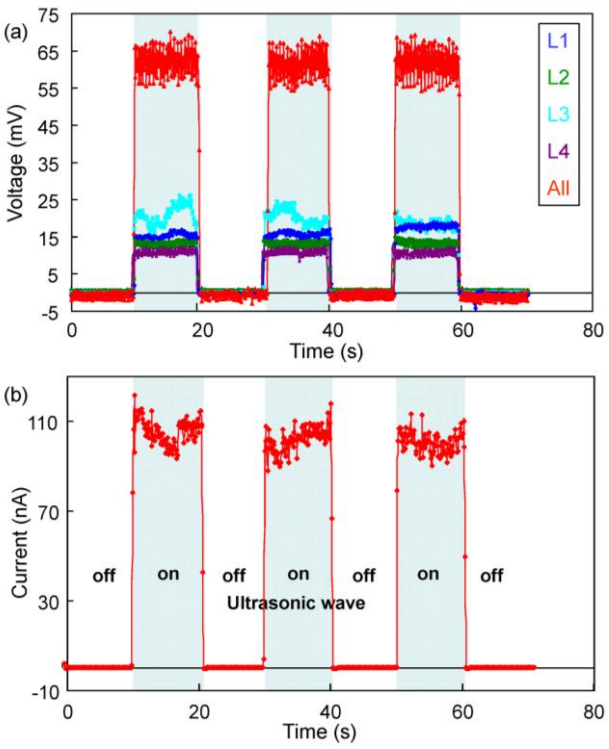

Figure 6.6. Open circuit voltage and short circuit current output measured from serially connected four-layer integrated NG. (a) Open circuit voltage output measured from each individual layers and the serially connected four-layer integrated NG. (b) Short circuit current output measured from the serially connected four-layer integrated NG. The regions when the ultrasonic wave was on and off are indicated. The surface area of the NG was 6 mm^2.

6.3.1 Structure design

The key to the self-powered nanosystem is the fabrication of NG that gives high output voltage/power. The fabrication flow chart of the three-dimensionally integrated and packaged AC-NGs is illustrated in Fig. 6.7. The vertically aligned ZnO NW arrays were grown on an Au coated flat surface by wet chemical method (Section A in supporting online material (SOM)). Briefly, we first deposited Ti and Au thin films consecutively onto a Si wafer by magnetron sputtering (Fig. 6.7A(a)), on which ZnO NWs of ~300 nm in tip diameter and ~4 μm in length were grown at a temperature less than 100 ^{o}C (Fig. 6.7A(b), Fig. 6.7B(a)). The density and length of the ZnO NWs could be adjusted properly by tuning corresponding chemical reaction parameters (*13*). After the growth of ZnO NWs, a layer of polymethyl-methacrylate (PMMA) was spun coated onto the NWs to entirely fill up the space between the NWs (Fig. 6.7A(c), Fig. 6.7B(b)). The ZnO NWs were fully wrapped up by the PMMA film from the top to the bottom. This process largely improved the stability and mechanical robustness of the entire structure and prevented possible short circuit contact between the substrate and the top electrode. To expose the tips of the NWs out of the PMMA film, oxygen plasma etching was performed at a radio frequency power of 10 W for 20 mins, to etch off the PMMA film on the top (Fig. 6.7A(d), Fig. 6.7B(c)) and left behind fresh and clean tips of the ZnO NWs and a roughed surface texture of the PMMA film as well (Fig. 6.7B(c) inset). Then a piece of Si wafer coated with 300 nm thick Pt film was placed in direct contact with the ZnO NWs (Fig. 6.7A(e)), where a Schottky contact was created at the interface. Electrical connection leads were made before the entire structure was encapsulated and packaged with a soft material. The measurement was done in a Faraday cage using a linear motor stimulator for generating the mechanical strain at an impact speed of 0.1 m/s.

6.3.2 Working principle

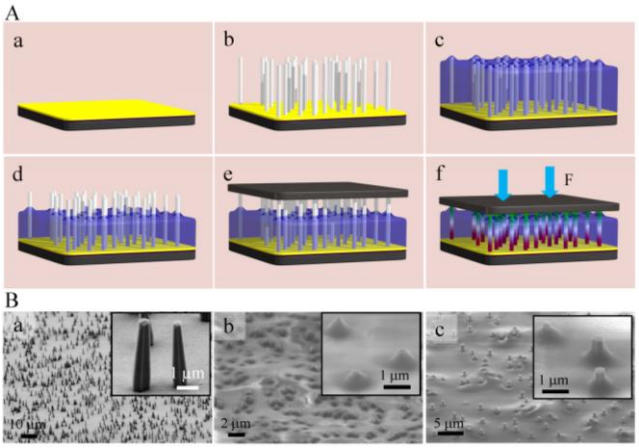

Figure 6.7. (A) Fabrication flow chart of an AC-NG. (a) On an Au coated Si wafer, (b) ZnO NW arrays are grown by low-temperature hydrothermal decomposition. (c) PMMA spin coating covers both the bottom part and tip part of the NW arrays. (d) After oxygen plasma etching, the tips of the NWs are exposed fresh and clean but the main body and bottoms of the NWs are still fully enclosed, which greatly improves the robustness of the structure. (e) A Pt coated flat electrode is placed on the top of the NWs to form a firm Schottky contact. When an uniaxial stress is applied at the top electrode, the NWs are readily compressed, the straining of the crystallographically aligned NWs generates a macroscopic piezoelectric potential along the *c*-axis growing direction of the NWs. (B) SEM images of the (a) as-grown ZnO NW arrays on the substrate, (b) after spin coating with PMMA, and (c) after oxygen plasma etching.

The working principle of the AC-NG is the coupling of piezoelectric and semiconducting properties of ZnO NW. Studies by several groups have shown that Wurtzite structured NWs grow uniaxially parallel to the c-axis [7 , 8 , 9]. The crystallographic alignment of the NWs means the piezoelectric alignment in response of the NWs to the external stress. Under uniaxial straining, a separation of the static ionic charge centers in the tetrahedrally coordinated Zn-O units results in a piezoelectric potential gradient along the c-axis of the NW (Fig. 6.7A(f)). Since the NWs are grown on the substrate with their c-axis aligned in parallel, the created piezoelectric potentials along each NW have the same tendency of distribution so that they have an enhanced macroscopic behavior. When an uniaxial stress is applied onto the top electrode, the NWs are under uniaxial compression, with negative piezoelectric potential at the tip for instance, which is the Schottky contact side, and positive piezoelectric potential at the bottom, which is the Ohmic contact side. To simplify the analysis and discussion here, we assume that there is no shear strain component and only pure compression in the axial direction for each and every single NW. The negative piezoelectric potential raises up the conduction band and the Fermi level at the tip side of the NWs relative to the bottom side. Thus electrons would flow from the tip side to the bottom side through the external circuit. The Schottky barrier at the tip side, however, obstructs the electrons from transporting through the interface. Therefore, these electrons are blocked and accumulated around the bottom side of the NWs. The Fermi level at the bottom side is consequently raised up by the accumulated electrons until the piezoelectric potential is fully "screened" and the Fermi levels of the two sides reach a new equilibrium again. During this process, the flow of electrons via the external circuit is detected as a current pulse. As the external force is removed from the top electrode and the compressive strain is released from the NWs, the piezoelectric potential inside diminishes. And then those electrons accumulated at the bottom side undoubtedly flow back via the external circuit if leakage is negligible, which creates a current pulse in the opposite direction.

During the entire process, the role played by the Schottky barrier is similar to an insulating gate oxide layer that is thin enough to allow the effective interaction of the piezoelectric field in the NWs with the free mobile electrons, but prevents those mobile charges in the external circuit from going through the NW-metal contact interface. The piezoelectric potential acts as a "charging pump" that drives the electrons to flow. By the same token, the same process occurs if the Schottky barrier is at the bottom side or both sides of the NWs. The presence of a Schottky contact at least at one end of the NWs is essential for the operation of the AC-NG.

6.3.3 Enhanced output

The output voltage and current could be greatly enhanced by linearly integrating a number of AC-NGs together. Three AC-NGs of individual output voltage of 80, 90, and 96 mV, respectively, were connected in serial; the output voltage was 0.243 V (Fig. 6.8A), which was nearly the numerical sum of those of the three individuals. Likewise, the three AC-NGs of individual output current density of 6.0, 3.9 and 8.9 nA/cm^2, respectively, were connected in parallel; the output current density was 18.0 nA/cm^2 (Fig. 6.8B), which was approximately the numerical sum of those of the three individuals.

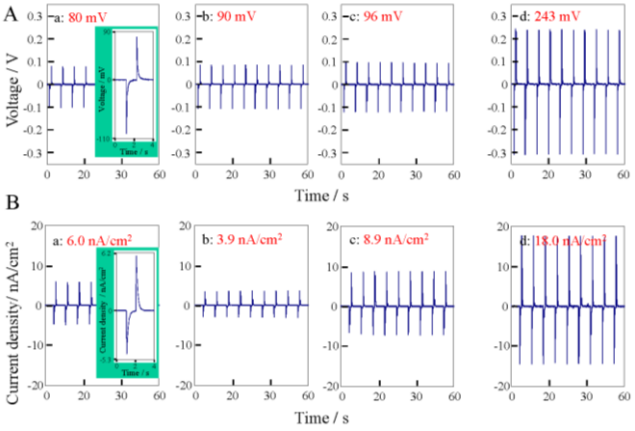

Figure 6.8. (A) Enhancing the output voltage of the AC-NGs by integrating them in serial. Individual AC-NG produces output voltage of (a) 80 mV, (b) 90 mV, and (c) 96 mV, respectively. (d) When the three AC-NGs are connected in serial, the voltage increases to 243 mV. (B) Linear superposition for output current when the AC-NGs are connected in parallel. Individual AC-NG produces output current density of (a) 6.0 nA/cm^2 (b) 3.9 nA/cm^2, and (c) 8.9 nA/cm^2, respectively. (d) When the three AC-NGs are connected in parallel, the output current density increases to 18.0 nA/cm^2. Insets in A(a) and B(a) are enlarged views of a single pulse.

The maximum power density of the AC-NG can be estimated using the peak values of the output voltage and current. From Fig. 6.8A(c) and Fig. 6.8B(c), the size of the AC-NG was ~4 mm^2, outputting V = 96 mV and I = 0.355 nA. The average diameter of the NW D = 400 nm, length L = 4 μm, and the total number of NWs grown in the NG was ~75,000 (area density 1.9x10^6/cm^2). By conservatively assuming that 1/3 of all of the NWs were actively generating electricity in a perfectly synchronized process, the power density was estimated to be 2.7 mW/cm^3, which is 6-11 times of that generated by a PZT cantilever (*23*, *24*).

6.3.4 Self-powering a nanosensor

The AC-NG has been integrated with a single NW based nanosensor to demonstrate a self-powered nanosystem [5]. An AC-NG was connected to a ZnO NW based pH sensor (*27*), or UV sensor (*28*), and the voltage across the nanosensor was monitored (Section B in SOM). A pH sensor was built using a single ZnO NW that was coated with a 10 nm Si_3N_4 layer, which was thin enough for the electrostatic interaction between the surface adsorbed charges and the carriers in the NW. By powering the pH sensor using an AC-NG that generated an output voltage of ~ 40 mV, a clear sensitivity to local pH change was observed (Fig. 6.9A). When the buffer solution was basic (high pH value), the surface of the nanosensor was dominated by $-O^-$ groups. Those negatively charged groups resulted in depletion regions at the surface of the n-type ZnO NW, which increased the resistance of the ZnO NW. Thus, the voltage drop on the ZnO NW was relatively high. As the buffer solution was changed from basic to acidic (from high pH value to low pH value), the surface of the nanosensor was gradually changed from $-O^-$ to $-OH_2^+$ groups. Therefore, the depletion regions at the ZnO NW surface diminished, which would lower the resistance of the ZnO NW. As we changed the pH value of the testing buffer solution from 10.01, 9.18, 7.01, 6.86, then to 4.01 (with pH accuracy of ±0.01, HANNA Instruments), the voltage drop on the pH sensor changed accordingly (Fig. 6.9A).

Our newly designed AC-NGs are of great mechanical stability and robustness, and it is feasible for layer-by-layer three-dimensional integration for applications where a dynamic compressive stress/straining is available, such as in shoe pads, automobile tires and underneath of carpet/floor.

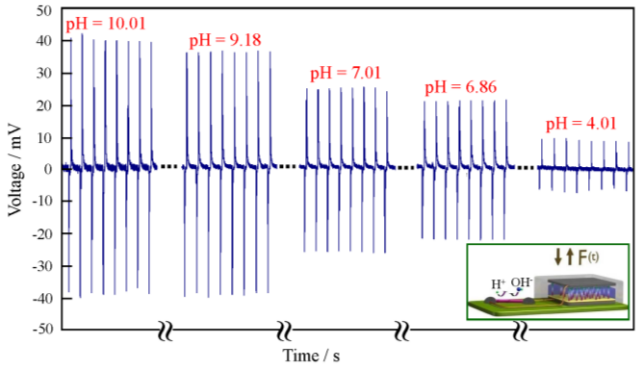

Figure 6.9. Integration of an AC-NG (4 mm^2 in size) with nanosensors to demonstrate the solely NW-based "self-powered" nanosystem. The mechanical impacts are applied at a frequency of 0.16 Hz, and each cycle produces a pair of positive-negative output voltage/current signal. The voltage drop across a single ZnO NW based pH sensor that is powered by an AC-NG with an output voltage of ~ 40 mV, showing a stepwise dropping of the voltage across the nanosensor as a function of its local pH value. The ZnO NW was covered with a thin layer of Si_3N_4 and the testing was carried out within one hour so that the etching effect from the solution was negligible.

References for Chapter 6:

[1] Z.L. Wang, J.H. Song, *Science* **312**, 242 (2006).
[2] X. D. Wang, J. H. Song, J. Liu, Z. L. Wang, *Science* **316**, 102 (2007).
[3] S. Xu, Y. G. Wei, J. Liu, R. Yang, Z. L. Wang, *Nano Lett.* **8**, 4027 (2008).
[4] Y. Qin, X.D. Wang, Z.L. Wang, *Nature* **451**, 809 (2008).
[5] Xu, S.; Qin, Y.; Xu, C.; Wei, Y.; Yang, R.; Wang, Z. L. *Nature Nanotech.* **5**, 367 (2010).
[6] D. Choi, M.Y. Choi, W.M. Choi, H.J. Shin, H.K. Park, J.S. Seo, J. Park, S.J. Chae, Y.H. Lee, S.W. Kim, J.Y. Choi, S.Y. Lee, J.M. Kim, *Adv. Mater*. **22**, 2187 (2010).
[7] S. Y. Bae, H. W. Seo, D. S. Han, M. S. Park, W. S. Jang, C. W. Na, J. Park, C. S. Park, *J. Cryst. Growth* **258**, 296 (2003).
[8] J. Jasinski, D. Zhang, J. Parra, V. Katkanant, V.J. Leppert, *Appl. Phys. Lett.* **92**, 093104 (2008).
[9] C. Liu, Z. Hu, Q. Wu, X.Z. Wang, Y. Chen, H. Sang, J.M. Zhu, S.Z. Deng, N.S. Xu, *J. Am. Chem. Soc*. **127**, 1318 (2005).

Chapter 7

High output nanogenerators – lateral nanowire arrays

The design of a single nanowire based AC-NG in Chapter 4 uses a piezoelectric wire that is firmly contacted at its two ends with metal electrodes, laterally bonded and packaged on a flexible substrate, the bending of which can be driven by mechanical agitation present in our living environment. The single wire generator demonstrates a robust approach for harvesting low-frequency energy generated by in-vitro human or animal motion. However, the output power of a single nanowire based nanogenerator (NG) is rather limited. As for practical applications, it is essential to scale up the design of the AC-NGs so that we can integrate the contributions made by millions of nanowires in order to enhance the output power [1**,** 2**,**3**,**4]. To present the design of the integrated NGs, we first illustrate the principle of the AC-NG using a single NW. Since the diameter of the NW is much smaller than the thickness of the substrate film, the NW is subjected to a pure tensile strain when the substrate is stretched, and a piezoelectric-potential-drop is created along the NW, with the positive c-axis of the crystal orientation pointing toward a higher piezopotential side. A Schottky barrier formed at least at one end-contact of the NW serves as a "gate" that prevents the flow of electrons across the NW-metal interface, so that the electrons are accumulated adjacent to the contact. This is the charging process. When the substrate is released from straining, the strain in the NW is released and the corresponding piezopotential disappears as well. The accumulated electrons will back flow through the external load. This is the charge releasing process. The piezopotential in the NW serves as a "charging pump" that drives the back and forth flows of the electrons in the external circuit in responding to the straining and releasing of the NW. If we can synchronize the charging and discharging processes of many NWs, the generated AC voltages can be added up constructively, resulting in a high output.

7.1 Lateral integrated nanogenerator (LING) [5]

Several factors have to be considered to constructively integrate the outputs of many single-wire based NGs. First, the metal contacts at the two ends of the nanowire arrays should be non-symmetric to produce a Schottky contact at one side and an Ohmic contact at the other side (Fig. 7.1b). This is required following the mechanism introduced above. Second, the contacts at the two ends of the NWs are required to be robust, which is achieved by fully enclosing the ends of the NWs with the deposited metal so that the mechanical deformation can be more effectively transmitted from the electrodes to the NWs. Third, all of the ZnO NWs should have the same crystallographic orientation to ensure the polarities of the piezoelectric potentials generated in all of the NWs are aligned. Since a ZnO NW grows in parallel to *c*-axis for a general case, and with consideration its anisotropic wurtzite structure and its polarization along the c-axis [6**,**7**,**8**]**, the NWs need to be rationally grown directly on the substrate rather than by chemical assembly, the latter usually gives orientation alignment but not crystallographic polarity alignment. The polarity aligned

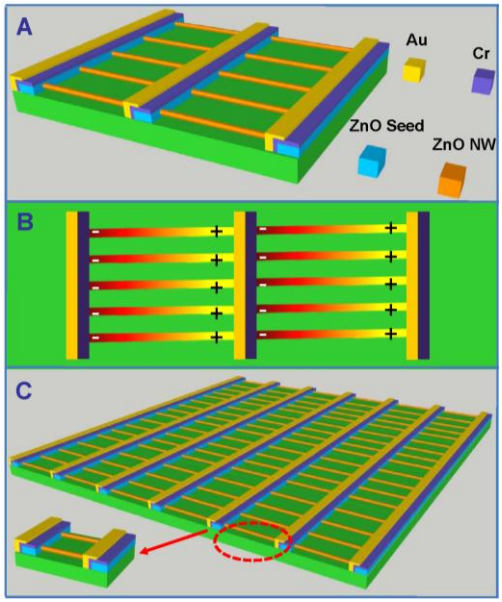

Figure 7.1. Design of a lateral-nanowire integrated nanogenerator (LING) array. (a) Schematics of the LING structure, where Au and Cr are used to create Schottky and Ohmic contacts, respectively, at the two ends. (b) The working mechanism of the LING when it is subjected to a mechanical deformation. The "+, -" signs indicate the polarity of the local piezoelectric potential created in NWs. (c) Schematics of a LING array made of many rows of nanowires.

NWs create a macroscopic piezoelectric potential; in contrast, a randomly c-axis oriented NWs may result in cancellation of the generated electric currents. Finally, all of the ZnO NWs must be stretched and released in a synchronized manner, so that the polarities of the piezoelectric potential generated by all of the NWs are in the same direction at the same time (Fig. 7.1c), resulting in the maximized output voltage.

7.1.1 Device fabrication

The detailed fabrication of the LING was accomplished following a five step procedures (Figure 7.2a). In the first step, patterned ZnO stripes covered with Cr layer on the top were fabricated as the seed layer. A Kapton film with a thickness of 125 μm was cleaned with acetone, isopropyl alcohol and ethanol using ultrasonic, which was used as the substrate. A photoresist was span coated onto this film at a speed of 3000 RPM for 40s. Then the film was baked at 110 ℃ for 10 minutes. The film was first patterned using mask aligner. Then, 300 nm ZnO and 5 nm Cr layers were deposited. Finally, after developing and lifting off, the stripe-shape ZnO pattern with a top layer of Cr was fabricated (Fig. 7.2a(1)). The second step was to deposit Cr only at one side of the ZnO stripe but with the other side exposed. We span coat the entire structure by a layer of photoresist, then used a masker to cover only one side of the ZnO strip by controlling its offset position. Optical lithography followed by developing exposed only one side of the strips. Then, a layer of Cr (10 nm) was sputtered. A lift-off produced the structure shown in Fig. 7.2a(2). In the third step, the growth of ZnO NW arrays as shown in Fig. 7.2a(3) was carried out using solution chemistry at 80 ℃. After 12 hour aging in the solution, the film surface turned into white, indicating that they were covered by ZnO NW arrays. At last, they were rinsed with deionized water for several times and baked at 100 ℃ for 1 hour. Figure 2b shows a typical scanning electron microscopy (SEM) image of a horizontally grown ZnO NW arrays. Most of the ZnO NWs were grown horizontally with one end fixed onto the seed layer. The length of the NWs is about 5 microns and the diameter is around several hundred nanometers. The length of the NWs was controlled by refreshing the aging solution and increasing the aging time so that they reached the other electrode (Fig. 7.2e). In the fourth step, patterned Au electrodes were fabricated using a masking technique, and the Au was deposited only at the side where the Cr layer was present (Fig. 7.2a(4)). The thickness of the Au layer was controlled to ensure a good connection between the NWs and

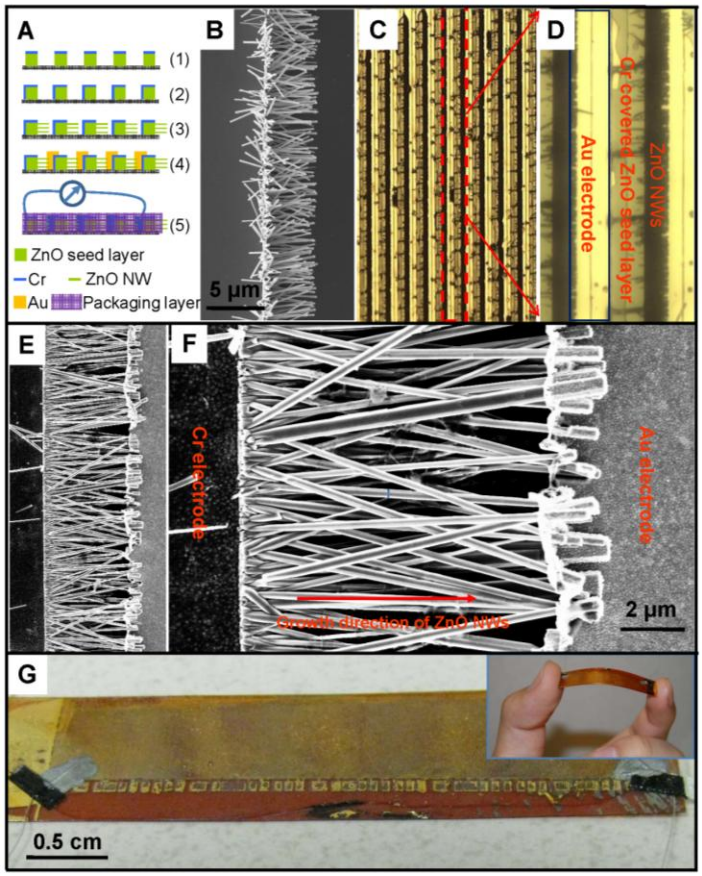

Figure 7.2. Fabrication process and structure characterization of the LING. (a) Schematics for the rational growth of orientation aligned NW arrays parallel to the substrate surface (see the experimental section for details). (b) SEM image of a row of laterally grown ZnO NW array. (c) and (d) Optical microscopy images of the LING structure using many rows of NW arrays. (e) and (f) SEM images of a single row LING structure. (g) An low-magnification optical image of the LING and a demonstration of its flexibility (inset).

the electrodes (Fig. 7.2f). Finally, the entire structure can be packaged using insulative soft polymer, such as a photoresist (MicroChem PMMA 950K A2) (Fig. 7.2a(5)). This packaging layer fixed the ZnO NWs firmly onto the substrate and made the NWs to be synchronized in mechanical stretching or releasing with the outer surface of the Kapton film. Figures 2c and 2d are optical microscopy images of the fabricated LING. The ZnO NW arrays are connected with each other end-to-end by patterned electrodes. Figures 7.2e and 7.2f show the SEM images of the as-fabricated LING structure. A fully packaged, large-size LING is presented in Fig. 2g, and its flexibility is demonstrated as shown in the inset.

The following experimental procedures were rationally designed to fabricate the laterally-integrated NG (LING) to meet all of the required conditions, as presented in Fig. 7.1. The first step is to grow crystallographically aligned NW arrays using chemical approach at < 100 ^{o}C (Fig. 2a) [9]. An array of stripes of ZnO seed layers were first deposited on a polymer substrate. After covering one side and the top side of the seed stripes with Cr that prevented the local growth, ZnO NWs were grown directly from the exposed seed layer at the other side using chemical approach along the direction almost parallel to the substrate (Fig. 7.2b). The lengths of the NWs were controlled by growth time to close in touch with the other side of the electrode. Then, a gold (Au) layer was deposited using an aligned mask technique to connect the tips of the ZnO NWs with the Au electrode (Figs. 7.2c and d). The work function of Au is higher than the electron affinity energy of ZnO, which usually leads to a Schottky connection between ZnO NWs and Au electrode. An Ohmic contact was formed between ZnO and Cr at the other end. By depositing a thick Au film, the tip ends of the NWs were fully enclosed and bonded with Au electrode so that the NWs could be robust for mechanical deformation without loose contacts (Figs. 7.2e and f). Mechanical stretching of the substrate produced tensile strain in the NWs, which created a macroscopic piezoelectric potential along the NWs owing to the crystallographic alignment of the NWs. The multi rows of NGs were integrated to form a flexible sheet (Fig. 7.2g).

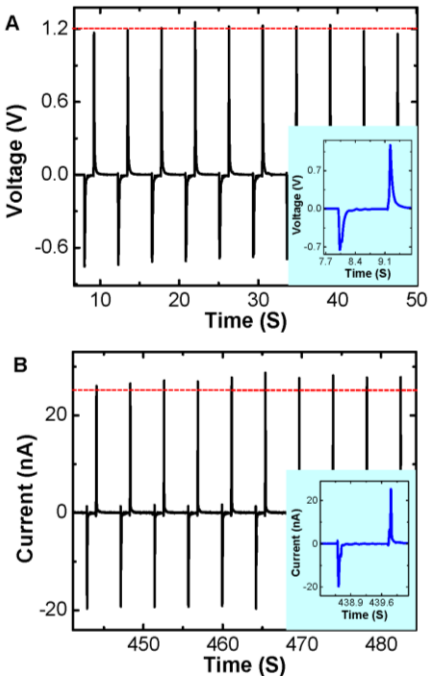

Figure 7.3. The performance of a laterally-integrated nanogenerator. (a) Open-circuit output voltage, and corresponding (b) short-circuit output current measured from a LING structure that is made of 700 rows of NW arrays. The maximum output voltage peak reaches 1.26 V. The insets are output voltage and current in one cycle of mechanical deformation. The LING is periodically deformed at a straining rate of 2.13%/s to a maximum strain of 0.19%.

7.1.2 Output measurements

To measure the energy harvesting performance of the LING, a periodic external force was used to deform the Kapton substrate so that the NWs experienced a cycling stretching-releasing deformation process. Since the thickness of the Kapton substrate was much thicker than the diameter of the NWs, a push to the substrate at its middle section by a mechanical motor resulted in a stretch at its outer surface, which produced a pure tensile strain across the rows of the NGs built on the top. Such strain was calculated based on the curvature of the bending and the thickness of the substrate film (see Supplementary online Materials (SOM)). In our experiments, we pushed the Kapton substrate at a relatively fast straining rate, but hold it at the position for one second before releasing. Then wait for two seconds before pushing again. The degree to which the LING can be deformed is determined by the robustness of its structure.

Integrating more ZnO NWs, improving the interconnection between electrodes and ZnO NWs and increasing the strain as well as straining rate are very important for enhancing output voltage and current of the LING. Figure 7.3 shows the output voltage and current of a LING that has demonstrated an average

output voltage of ~1.2 V at a straining rate of 2.13%/s and strain of 0.19%. The LING was composed of 700 rows of NWs and each row contained about ~20,000 NWs. When the Kapton film was mechanically deformed, a positive voltage pulse of 1.2 V and a current pulse of 26 nA were measured (Figure 7.3a and 7.3b). Note, the magnitudes of the current/voltage peaks were slightly different when the LING was stretched and released because of the difference in straining rate in the two processes; the stretching was driven by an external force, while the releasing was natural. The inserted figures are the V_{oc} and I_{sc} output for one cycle of deformation. The stretching of the ZnO NWs generated a piezoelectric potential along ZnO NW at the Au contact side, which drove the electrons in external circuit to flow from low potential side to high potential side and accumulated at the contact interface. After one second, the NG was released, which led to the disappearance of the piezoelectric potential, correspondingly the accumulated electrons flowed back in the opposite direction. The average output voltage peaks were greater than 1.2 V (indicated by the red dashed line in Figure 7.3a) and the maximum voltage reached 1.26 V. The result demonstrates the potential of scale up the output voltage by a serial integration of many rows of NWs. Most of the output current peaks were greater than 25 nA (indicated by the red dashed line in Figure 3b) and the maximum current peak was 28.8 nA. By assuming that 1/3 of the NWs that were actively contributing to the current output, the average current generated by one NW was estimated to be 4.3 pA, which was compatible to the output current of ~10 pA when a NW was triggered by an AFM tip. If we excluded the area occupied by the electrodes, a peak output power density of ~70 nW/cm^2 was obtained.

The LING structure has been demonstrated to largely enhance the total output voltage of the NGs by lateral integration. This is a major landmark progress toward the applications of the NGs. The limited output current is likely due to the following reasons. First, the orientation alignment of the as-grown lateral-NWs was not perfect and many of them were sticking out a little bit away from the electrode, so that only a fraction of them were in contact to the Au electrode. Among the NWs that were in contact, only a fraction of them were actively outputting electricity, so called active NWs, while the inactive NWs made no contribution to the output current but served as a capacitance to reduce the output voltage.[10] Second, the bonding between Au and ZnO was not very tight, which might become loose during repeated mechanical stretching. This may prevent applying a large strain to the NWs. We only applied a maximum strain of 0.19% in our experiments. Theoretical simulation indicates that the maximum tensile strain that a ZnO NW can hold before fracture is 6%.[11] Lastly, the inner resistance of the entire integrated sheet was 1-10 MΩ, which reduced the total output current.

7.2 Flexible high-output nanogenerator [12]

In this section, we report here a simple and effective approach, named scalable sweeping-printing-method, for fabricating flexible high-output nanogenerator (HONG) that can effectively harvesting mechanical energy for driving a small commercial electronic component. The HONG consists of two main steps. In the first step, the vertically-aligned ZnO nanowires (NWs) are transferred to a receiving substrate to form horizontally-aligned arrays. Then, parallel stripe type of electrodes are deposited to connect all of the NWs together. Using a single layer of Hong structure, an open-circuit voltage of up to 2.03 *V* and a peak output power density of ~11 mW/cm^3 have been achieved. The generated electric energy was effectively stored by utilizing capacitors, and it was successfully used to light up a commercial light-emitting diode (LED), which is a landmark progress toward building self-powered devices by harvesting energy from the environment. This research opens up the path for practical applications of nanowire based piezoelectric nanogeneragtors for self-powered nanosystems.

7.2.1 Principle and fabrication

The mechanism of converting mechanical energy by a single ZnO NW that is laterally bonded to a substrate has been discussed in details in Chapter 4. Owing to much smaller diameter of the NW compared to the substrate thickness, outward bending of the substrate induces a uniaxial tensile strain in the NW. Due to the piezoelectric property of the ZnO NW, the stress results in a piezoelectric field along the length, which causes a transient charge flow in the external circuit. The Schottky contact at the bonded ends can regulate the charge flow. As a result, the bending and releasing of the single-wire-NG gives rise to an alternating flow of the charges in the external circuit. In this work, the power output has been scaled up with the integration of hundreds of thousands of horizontally-aligned NWs, which was made by a scalable sweeping-printing-method that is simple, cost-effective and highly efficient.

The method consists of two main steps. In the first step, the vertically-aligned NWs are transferred to a receiving substrate to form horizontally-aligned arrays. The major components of the transfer setup are two stages (Fig. 7.4a). Stage 1 has a flat surface that faces downwards and holds the vertically-aligned NWs; stage 2 has a curved surface and holds the receiving substrate. Polydimethylsiloxane (PDMS) film on the surface of stage 2 is used as a cushion layer to support the receiving substrate and enhances the alignment of the transferred NWs. The radius of the curved surface of stage 2 equals the length of the rod supporting the stage, which is free to move in circular motion. In the second step, electrodes are deposited to connect all of the NWs together.

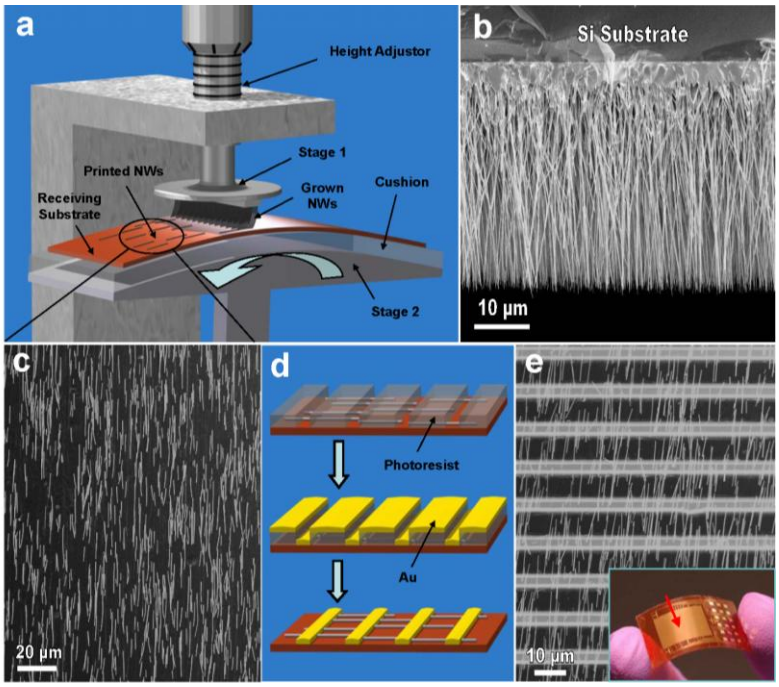

Figure 7.4. Fabrication process and structure characterization of the HONG. a, Experimental setup for transferring vertically grown ZnO NWs to a flexible substrate to make horizontally aligned ZnO NW arrays with crystallographic alignment. b, SEM image of as-grown vertically aligned ZnO NWs by physical vapor method on Si substrate. c, SEM image of the as-transferred horizontal ZnO NWs on a flexible substrate. d, Process of fabricating Au electrodes on horizontal ZnO NW arrays, which includes photolithography, metallization, and lift-off. e, SEM image of ZnO NW arrays bonded by Au electrodes. Inset: demonstration of an as-fabricated HONG. The arrowhead indicates the effective working area of the HONG.

Vertically-aligned ZnO NWs on Si substrates were synthesized using physical vapor deposition method. The dense and uniform NWs have the length of ~50 μm, diameter of ~200 *nm*, and growth direction along *c*-axis (Fig. 7.4b). The same growth direction of NWs guarantees the alignment of the piezoelectric potentials in all of the NWs and a successful scaling up of the output, which will be elaborated later. A small piece of Si substrate with grown ZnO NWs was mounted onto stage 1 (Fig. 7.4a) and a piece of Kapton® film with the thickness of 125 μm was attached to stage 2 (Fig. 7.4a). The distance between the receiving substrate and NWs was precisely controlled to form a loose contact between the two. The receiving substrate then counterclockwise swept across the vertical NWs arrays, which were detached from Si substrate and aligned on the receiving substrate along the direction of sweeping due to the applied shear force (Fig. 7.4a). The as-transferred NWs are presented in Fig. 7.5c, with an estimated

average density of 1.1×10^6 cm^{-2}. The length variation is probably due to the fact that not all of the NWs were broken off at the roots.

Next, the evenly spaced electrode pattern over the aligned NWs was first defined using photolithography and then followed by sputtering 300 *nm* thick Au film (Fig. 7.4d). After the lifting off the photoresist, 600 rows of stripe-shaped Au electrodes with 10 μm spacing were fabricated on top of the horizontal NW arrays (Fig. 7.4e). Au electrodes form Schottky contacts with the ZnO NWs, which are mandatory for a working NG. Approximately 3.0×10^5 NWs in an effective working area of 1 cm^2, as pointed by an arrowhead in Fig. 7.4d (inset), are in contact with electrodes at both ends. Finally, a PDMS packaging over the entire structure can further enhance mechanical robustness and protect the device from invasive chemicals.

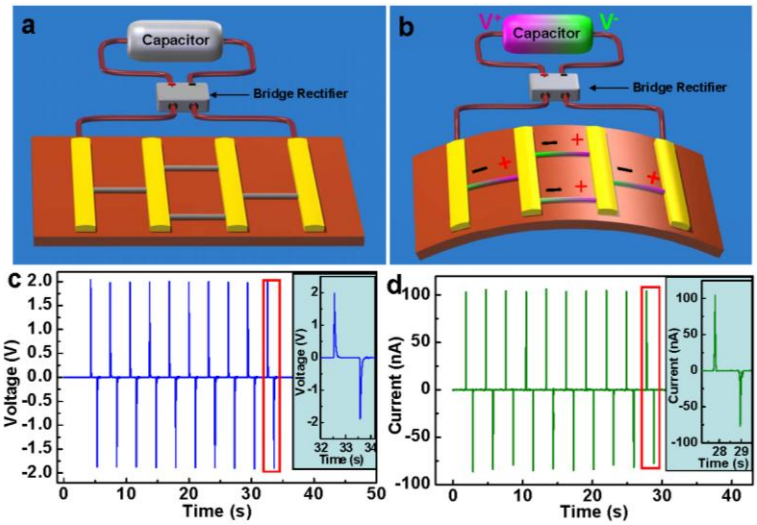

Figure 7.5. Working principle and output measurement of the HONG. a, Schematic diagram of HONG's structure without mechanical deformation, in which gold is used to form Schottky contacts with the ZnO NW arrays. b, Demonstration of the output scaling-up when mechanical deformation is induced, where the "+/-" signs indicate the polarity of the local piezoelectric potential created in the NWs. c, Open circuit voltage measurement of the HONG. d, Short circuit current measurement of the HONG. The measurement is performed at a strain of 0.1% and strain rate of 5% s^{-1}, with the deformation frequency of 0.33 *Hz*. The insets are the enlarged view of the boxed area for one cycle of deformation.

The working principle of the HONG is illustrated by the schematic diagrams in Fig. 7.5a, b. NWs connected in parallel collectively contribute to the current output; and NWs in different rows connected in serial constructively improve the voltage output. It is worth noting that, the same growth direction of all NWs and the sweeping printing method ensure that the crystallographic orientations of the horizontal NWs are aligned along the sweeping direction. Consequently, the polarity of the induced piezopotential is also aligned, leading to a macroscopic potential contributed constructively by all of the NWs (Fig. 7.5b).

7.2.2 Output measurements

In order to investigate the performance of the HONG, a linear motor was used to periodically deform the HONG in a cyclic stretching-releasing agitation (0.33 *Hz*). The open-circuit voltage (V_{oc}) and the short-circuit current (I_{sc}) were measured with caution to rule out possible artifacts[19]. At a strain of 0.1% and strain rate of 5% s^{-1}, peak voltage and current reached up to 2.03 *V* and 107 *nA*, respectively. Assuming that all of the integrated NWs actively contribute to the output, the current generated by a single NW is averaged to be ~200 *pA*; and the voltage from each row is ~3.3 *mV* in average. Considering the size of the working area of the nanogenerator (1 cm^2) (Fig. 7.4e, inset), a peak output power density of ~0.22 $\mu W/cm^2$ has been achieved, which is over twentyfold increase compared to our latest report based on a more complex design. For nanowires with the diameter of ~200 *nm*, the power volume density is ~11 mW/cm^3.

Further scaling up the power output is expected to be technically feasible. If NWs can be uniformly and densely packed as a monolayer over the entire working area, and all can actively contribute to the

output, the maximum power area density is expected to reach ~22 $\mu W/cm^2$. The power volume density is anticipated to be improved up to ~1.1 W/cm^3. With 20 layers of such NW arrays stacked together, the power area density would be boosted up to ~0.44 mW/cm^2.

The performance of the HONG is affected by strain and strain rate. For a given strain rate (5% s^{-1}), an increase in strain leads to a larger output (Fig. 7.6a, b). Likewise, at a constant strain (0.1%), the output is proportional to the strain rate (Fig. 7.6c, d). Beyond a certain strain and strain rate, saturation of the magnitude occurs, probably due to the converse piezoelectric effect, which is the strain created by the piezopotential and it is opposite to the externally induced strain. It is noticed that 0.1% strain is sufficient to induce effective output, which is much smaller than the 6% fracture strain of the ZnO NW predicted theoretically [6].

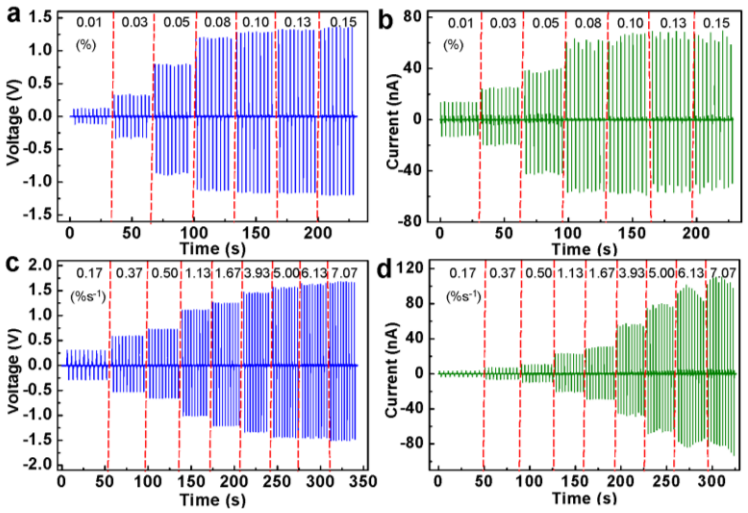

Figure 7.6. Performance characterization of the HONG with increasing strain and strain rate. a, Open circuit voltage measurement of the HONG with increasing strain at a given strain rate of 5% s^{-1}. b, Short circuit current measurement of the HONG with increasing strain at a given strain rate of 5% s^{-1}. c, Open circuit voltage measurement of the HONG with increasing strain rate at a constant strain of 0.1%. d, Short circuit current measurement of the HONG with increasing strain rate at a constant strain of 0.1%. For all measurements, the mechanical deformation frequency is fixed at 0.33 *Hz*.

7.2.3 Storage of generated energy

Storing the generated energy and driving functional devices are extremely important steps towards practical applications of the nanogenerator. In this work, they were accomplished by using a charging-discharging circuit with two consecutive steps (Fig. 7.7). The circuit function is determined by the status of a switch (Fig. 7.7a inset). The switch is at position A for energy storage achieved by charging capacitors. Upon charging completion, the switch is switched to position B for energy releasing to power a functional device, such as a light emitting diode.

It is the key for a successful and effect energy storage to take full advantage of the alternating output. As a result, an integrated full wave rectifying bridge was connected between a HONG and capacitors. The output of the HONG measured after the bridge exhibits only positive signals (Fig. 7.7a). Full wave rectification achieved by the bridge ensures energy storage at an enhanced efficiency, although the rectified signal (as pointed by an arrowhead in Fig. 7.7a) has appreciably reduced magnitude due to the reverse current leakage of the diodes in the bridge; and this reducing effect is rather notable at small output current. In order to facilitate the charging process, the output frequency of the HONG was tuned up to 3 *Hz* by reducing the periodicity of the mechanical deformation. Ten capacitors were connected in parallel such that they were simultaneously charged, and the voltage across a single capacitor finally reached 0.37 *V*.

An effective energy generation efficiency is defined as the ratio between the energy stored by the capacitors and the strain energy input to all of the active NWs, and it takes into account the performance of the electronic components in the circuit. The total electrical energy stored by the capacitor can be calculated as $W_{stored}=CU^2n/2=1.37$ *J*, where *C* is the capacitance of a single capacitor, *U* is voltage across

the capacitor, n is the number of capacitors. Since the dominant strain in the ZnO NWs is tensile strain, with shear strain safely neglected, the totally strain energy can be estimated as $W_{strain}=\pi D^2 L_0 E\varepsilon^2 f t n_0/8= 30J$, where D is the diameter of the NW (200 nm), L_0 is its original length (10 μm) which is fixed by the electrode spacing, E is the Young's modulus (30 GPa), ε is the strain of NWs (0.1%), f is the frequency of deformation (3 Hz), t is the total charging time (7200 s), and n_0 is the number of integrated NWs (300,000) [13]. Therefore, the effective energy generation efficiency is estimated to be ~4.6%. This value is naturally lower than the energy conversion efficiency of a single nano/micro wire (~7%), which is defined as the ratio between the generated electric energy ($W_{generated} = \int VIdt$, where V is the voltage, and I is the current) and the mechanical input strain energy. This is mainly attributed to the energy dissipation on rectifying bridge and capacitors, as elaborated in the supplementary materials.

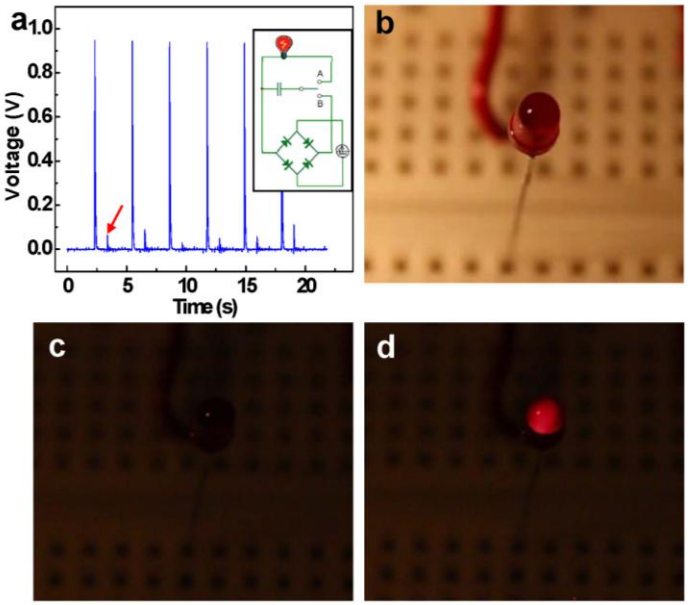

Figure 7.7. Application of the electric energy generated by the HONG to drive a commercial light emitting diode. a, The electric output measured after a full wave rectifying bridge. Signals of negative signs are reversed, as pointed by the arrowhead. Inset: Schematic of the charging-discharging circuit for storing and releasing the energy generated by the HONG, respectively. b, Image of a commercial LED, which is incorporated into the circuit. c, Image of the LED in dim background before it was lit up. d, Image of the LED in dim background at the moment when it was lit up by the energy generated from

7.3 Powering a light emitting diode

Upon finishing charging, the capacitors were reconfigured from parallel connection to series connection, leading to a total voltage source of 3.7 V. The stored electricity was used to drive a commercial red LED (Fig. 7.7b), which has an emission spectrum centered at 635 nm. The turn-on voltage and forward-biased resistance are 1.7 V and 450 Ω, respectively. The discharging process was triggered, leading to a maximum discharging current of 4.5 mA and the LED was lit up. The emitted light lasted 0.1 s-0.2 s and was clearly captured in dim background (Fig. 7.7c, d, video in supplementary information). During the whole charging-discharging process, no other power sources were involved. The entire circuit is essentially a complete self-powered system, which consists of three components: an energy harvester (the HONG), storage units (capacitors), and a functional device (the LED).

In summary, we have successfully fabricated high-output flexible nanogenerators using a sweeping-printing method. We managed to transfer vertically grown ZnO NWs to a flexible substrate and achieved horizontally aligned NW arrays that have crystallographic alignment, based on which an innovatively designed HONG was fabricated. The electrical output of the HONG reached a peak voltage of 2.03 V and current of 107 nA, with a peak power density of ~11 mW/cm^3, which is 12-22 times of that from PZT based cantilever energy harvester. An effective energy generation efficiency of 4.6% was demonstrated. The electric energy generated by the HONG was effectively stored by capacitors and used to light up a commercial LED. Furthermore, by optimizing the density of the NWs on the substrate and with the use of multi-layer integration, a peak output power density of ~0.44 mW/cm^2 and volume density of 1.1 W/cm^3 are redicted. This is a key step that is likely to bring nanogenerator based self-powering technology into people's daily life, with potential applications in mobile electronics, health monitoring, environmental inspection, cargo shipping tracking system, infrastructure monitoring and even defense technology.

References for Chapter 7

[1] C. Chang, V.H. Tran, J. Wang, Y. Fuh, L. Lin, *Nano Lett*. **10,** 726 (2010).
[2] Y. Qi, N. T. Jafferis, K. Lyons, Jr., C. M. Lee, H. Ahmad, and M.C. McAlpine, *Nano Lett.*, **10**, 524 (2010).
[3] M.Y. Choi, D. Choi, M.J. Kim, I. Kim, K.H. Kim, J.Y. Choi, S.Y. Lee, J.M. Kim and S.W. Kim, Adv. Mater., **21**, 2185 (2009).
[4] S.N. Cha, J.S. Seo, S.M. Kim, H.J. Kim, Y.J. Park, S.W. Kim, J.M. Kim, Adv. Mater. **22**, 4726 (2010).
[5] S. Xu, Y. Qin, C. Xu, Y.G. Wei, R.S Yang, Z.L. Wang Nature Nanotechnology, **5**, 366 (2010).
[6] J. Jasinski, D. Zhang, J. Parra, V. Katkanant, V. V.J. Leppert, *Appl. Phys. Lett.* **92**, (2008).
[7] S.Y. Bae *et al.*, *J. Crys. Grow.* **258**, 296 (2003).
[8] S.H. Lee *et al.*, *Nano Lett.* **8**, 2419 (2008).
[9] Y. Qin, R.S. Yang, Z.L. Wang, *J. Phys. Chem. C* **112**, 18734 (2008).
[**10**] J. Liu, P.X. Gao, W.J. Mai, C.S. Lao, Z.L. Wang, *Appl. Phys. Lett.* **89**, 063125 (2006).
[11] R, Agrawal, B. Peng, H.D. Espinosa, *Nano Lett.* ***9,*** 4177 (2009).
[12] G. Zhu, R.S. Yang, S.H. Wang, Z.L. Wang, Nano Letters, **10**, 3151 (2010).

Chapter 8

High output nanogenerators – non-contact nanowires

In this Chapter, we present a simple, cost-effective, robust and scalable approach for fabricating a nanogenerator that gives an output power strong enough to continuously drive a commercial liquid crystal display (LCD) [1]. Utilizing the conical shape of the as-grown ZnO nanowires, a nanogenerator is fabricated by simply dispersing them onto a flat polymer film to form a rational "composite" structure. It is suggested that the geometry induced unipolar-assembly of the conical-nanowires in such a composite structure results in a macroscopic piezoelectric potential across its thickness by introducing a mechanical deformation, which may be responsible for driving the flow of the inductive charges between the top and bottom electrodes. A compressive strain of 0.11% at a straining rate of 3.67% s^{-1} produces an output voltage up to 2 V (equivalent open circuit voltage of 3.3 V). This is a practical and versatile technology with the potential for powering small size personal electronics.

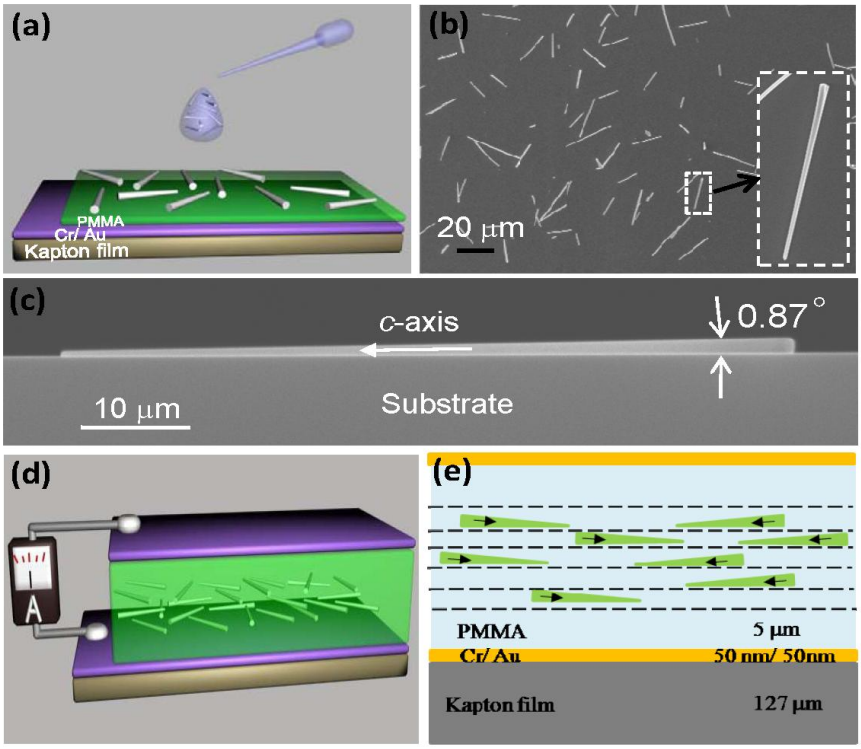

Figure 8.1. Fabrication of the nanogenerator. (a) Schematic diagram showing the fabrication process of the nanogenerator. (b) SEM image showing the CNWs were fairly uniformly distributed on the substrate surface with their lateral orientations in random; the insert enlarged image showing the conical shape of the nanowire. (c) Cross-section view SEM image of a conical nanowire laying on a flat substrate. The bottom side surface of the nanowire tightly attached to the substrate, and the conical angle of the nanowire was 0.87˚. The white arrowhead indicates that the *c*-axis of the nanowire is pointing downward into the substrate. (d) Schematic image of the fabricated device structure. (e) Schematic diagram showing the principle idea for the design and the suggested working principle of the structure (see text).

8.1 Basic design

The basic structure of the NG is two metal films sandwiched composite, which is made of unipolar-assembly of conical-nanowires infiltrated with PMMA [1]. First, a Cr/Au (50 nm/50 nm) metal layer was deposited on a Kapton film

(127 μm in thickness, Dupont™ 500HN) by electron beam evaporation; on the metal film a layer of PMMA (~2 μm in thickness) was spun coated on. The deviation in flatness of the PMMA film was better than 1 nm as measured by atomic force microscopy imaging. The NWs used in our experiments were grown on a solid substrate via vapor deposition process with lengths over 30 μm. The NWs have a conical shape due to the fastest growth along the *c*-axis and a much slower growth rate in the basal plane. The conical shape has been proven vitally important for the NG presented here, which is to be elaborated next. Then, the conial nanowires (CNWs) together with the substrate were soaked into ethanol; applying an ultrasonic wave effectively chopped off the CNWs from the substrate, forming a freely suspended CNW solution. By dispersing a droplet of the CNW solution onto the PMMA film, the CNWs were fairly uniformly distributed on the substrate surface with their lateral orientations in random (Figs. 8.1a, b). The area density of the CNWs on the substrate was low (1400 ~ 1500 nanowires per mm^2) to avoid overlapping and aggregations among the CNWs. The spin-coating of a thin PMMA layer (~100 nm) and dropping-on of the ZnO CNW solution were carried out alternately to form a rationally designed "composite" structure. When five cycles of PMMA and ZnO CNWs were deposited alternatively, another thicker PMMA layer (~ 2 μm) was deposited, on which a Cr/Au (50 nm/ 50 nm) metal film was deposited to serve as an electrode (Fig. 8.1d, e). For electricity generation, the as-fabricated NG was attached to a flexible polystyrene substrate (~1 mm in thickness) and an external force strained the assembled structure from the back of the substrate. Therefore, the NG experienced a compressive strain when mechanically agitated, thus the CNWs were under compressive strain as assumed in following calculations.

8.2 Working mechanism

The working principle of the assembled NG is suggested to be resulted from the unipolar-assembly of the conical-nanowires [1]. The CNWs laid down with random lateral orientation (Fig. 8.1b), while the bottom side surfaces were tightly attached to the flat surface of the substrate (Fig. 8.1c). With considering the [0001] growth direction of the ZnO CNW, which represents the polar direction of a NW, the conical shape of the nanowires results in a constructive alignment in their projected polar directions for all of the nanowires in the direction perpendicular to the substrate and pointing downward into the substrate, as shonw in Fig. 8.1e, in which the dashed line indicate one cycle of CNWs deposition. The conical shape nanowires and their corresponding *c*-axes are represented by arrowheads, which are the symmetry axes of the nanowires. Owing to the geometrical shape, the component of the c-axis of each nanowire in the normal direction of the substrate is c $sin(\alpha/2)$, where α is the conical angle of the CNW. This projected component of all of the CNWs along the vertical direction constructively adds up, which is the source of pizoelectric polarization across the thickness of the composite structure for creating the piezopotential. The unipolar-assembly is probably the key for producing a macroscopic piezoelectric potential in the direction normal to the substrate.

We now calculated the potential generated across the top and bottom electrodes using a simple model as shown in Fig. 8.2a. The entire structure was taken as a free standing beam with its one end being fixed and a periodical transverse force being applied at its top edge. The voltage drop across the top and bottom electrodes was calculated. In case of our experiments, the ZnO conical nanowire grows along the c-axis. When the CNWs were drop on the substrate, the CNWs had a random orientation in parallel to the substrate. When an external strain was created along the z-axis in parallel to the substrate (see the

coordinate system in Fig. 8.1), statistically, we had 50% of the CNWs whose c-axis projections in parallel to z are along +z axis, while the other half were along –z axis. To represent this type of configuration in our calculation in a simplified model, we chosen a pair of CNWs who have opposite c-axis orientations on the substrate in parallel to z-axis. Since the density of the CNWs was low, so that the coupling between the CNWs was rather weak, we placed them in anti-parallel in the unit cell designed for the calculation, as shown in Fig. 1e.

By considering the density of the as-deposited CNWs on the substrate, each pair of CNWs had a volume on average to occupy. If we considering the random orientation of the CNWs on the substrate and their projected length along the z-axis, a factor of 2 / p was multiplied to the real density to account of this equivalent effect. Therefore, an effective volume to be occupied by a pair of CNWs on average is represented by a rectangular box, as shown in Fig. 1f, with a width of 50 μm and height 5μm. The radius, length and semi-conical angle of a CNW were 500 nm, 45 μm and 0.4^0, respectively. The externally applied shear stress was 40 MPa (equivalent to a total force of F = 0.01 N applied on the top edge). Such an applied force produces a compressive strain of 0.12% at the fixed end of the CNW, in comparable to the experimental condition.The material constants used in the calculation were: anisotropic elastic constants of ZnO: c_{11}=207 GPa, c_{12}=117.7 GPa, c_{13}=106.1 GPa, c_{33}=209.5 GPa, c_{44}=44.8 GPa, c_{55}=44.6 GPa , piezoelectric constants e_{15}=-0.45 C/m^2, e_{31}=-0.51 C/m^2 and e_{33}=1.22 C/m^2. The ZnO relative dielectric constants were $k_{\perp}$=7.77 and $k_{//}$=8.91. The PMMA Young's modulus, Poisson ratio and the relative dielectric constants were E=3 GPa, v=0.4 and k=3.0, respectively. All of the calculations were carried out using COMSOL package.

In Fig. 1(e), the left-hand side of the structure is affixed and the right-hand side is free, on which the vertical shear stress is applied at the top end surface. The top and bottom surfaces are electrodes so that the top and bottom surface are equal potential planes. The bottom surface electrode is grounded. In open circuit case, the total charges on the top and bottom surface must be zero.

Our model is a capacitor-like plate structure with ZnO CNWs and PMMA as the composited "dielectric" media. By fixing one end of the plate and applying a transverse mechanical force (Fig. 8.2a), the mechanical deformation of the plate structure was calculated first. Under such a deformation configuration, the distribution of the piezoelectric field in the CNWs was obtained[21] by assuming a paired-CNW model to be discussed next. We purposely placed the CNWs in the region that was under compressive strain was to reflect the experimental situation in which the entire NG was under compressive strain with the consideration of backside substrate utilized for the measurements. Lastly, the distribution of the inductive charges in the electrode plates at the top and bottom surfaces were calculated with considering the proper boundary conditions, from which the electric potential difference between the two plates was obtained. Our calculation ignored the coupling between the piezoelectric field and the inductive charges in the electric plates under the first order approximation. The ZnO CNWs were assumed to be intrinsic without doping. To correctly represent the random distribution of the CNWs on the PMMA film surface, two CNWs with opposite *c*-axes were chosen for the simulation, as shown in the model in Fig. 8.2b. The establishment of the induced electric potential difference across the two plate electrodes is the driving force for the flow of electrons in the external load. Although the magnitude of the potential difference depends slightly on the relative depth of the CNWs in the NG due to

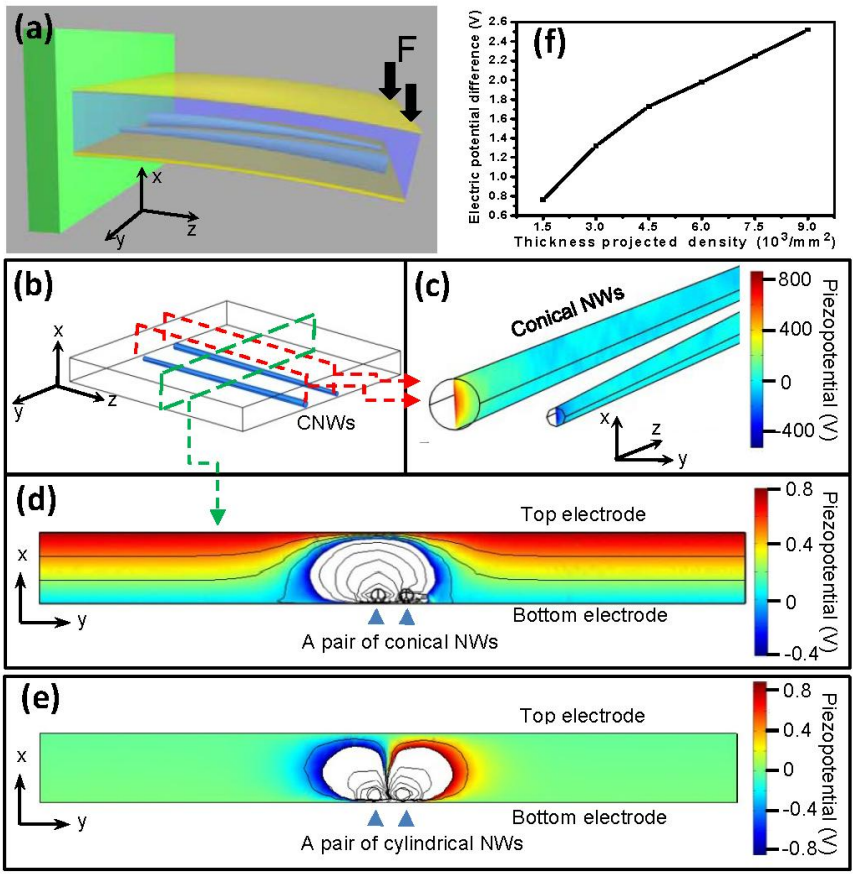

Figure 8.2. (a) Schematic model showing the set up for measuring the energy conversion. The polystyrene substrate used to hold the NG at its upper side, where the force F is applied, is not shown here for clarity of presentation. The CNWs are under compressive strain during the deformation. (b) The unit cell and model used for calculating the potential distribution across the top and bottom electrodes of the NG with the presence of a pair of CNWs, where the corresponding cross-sections at which the potential distributions were exhibited are indicated by dashed lines, and the results are shown in (c, d), respectively. Owing to the large magnitude variation in the potential distribution across the cross-section, we use both color grade and equal potential lines to present the local potential. The blank region close to the CNWs is the region where the calculated piezopotential is smaller than -0.4 V, beyond the range selected for the color plotting In order to show the detail in this region, we only used equal potential lines to present it. The CNWs were positioned close to the bottom of the unit cell in (b) to ensure that they were under compressive strain once a transverse force was applied in order to match the experimental case. (e) We also calculated the potential induced by perfect cylindrical NWs (e.g., zero conical angle). The result indicated that there was no potential difference being generated at the two electrodes. Presented is the cross-section output of the calculated piezopotential similar to Fig. 8.2d. (f) Calculated potential difference between the top and bottom electrodes of a nanogenerator as a function of the thickness projected conical nanowire density. The distance between the top and bottom electrode was kept constant (5 μm). The density required for a uniform, fully packed, monolayer coverage of the substrate is ~90,000/mm^2.

variation in local strain, the physical picture presented remains valid. Once the applied stress is withdrawn, the strain in the CNWs is released and so is the piezoelectric field, the inductive charges in the electrode plates have to flow back. This is the process of producing an AC output current [2].

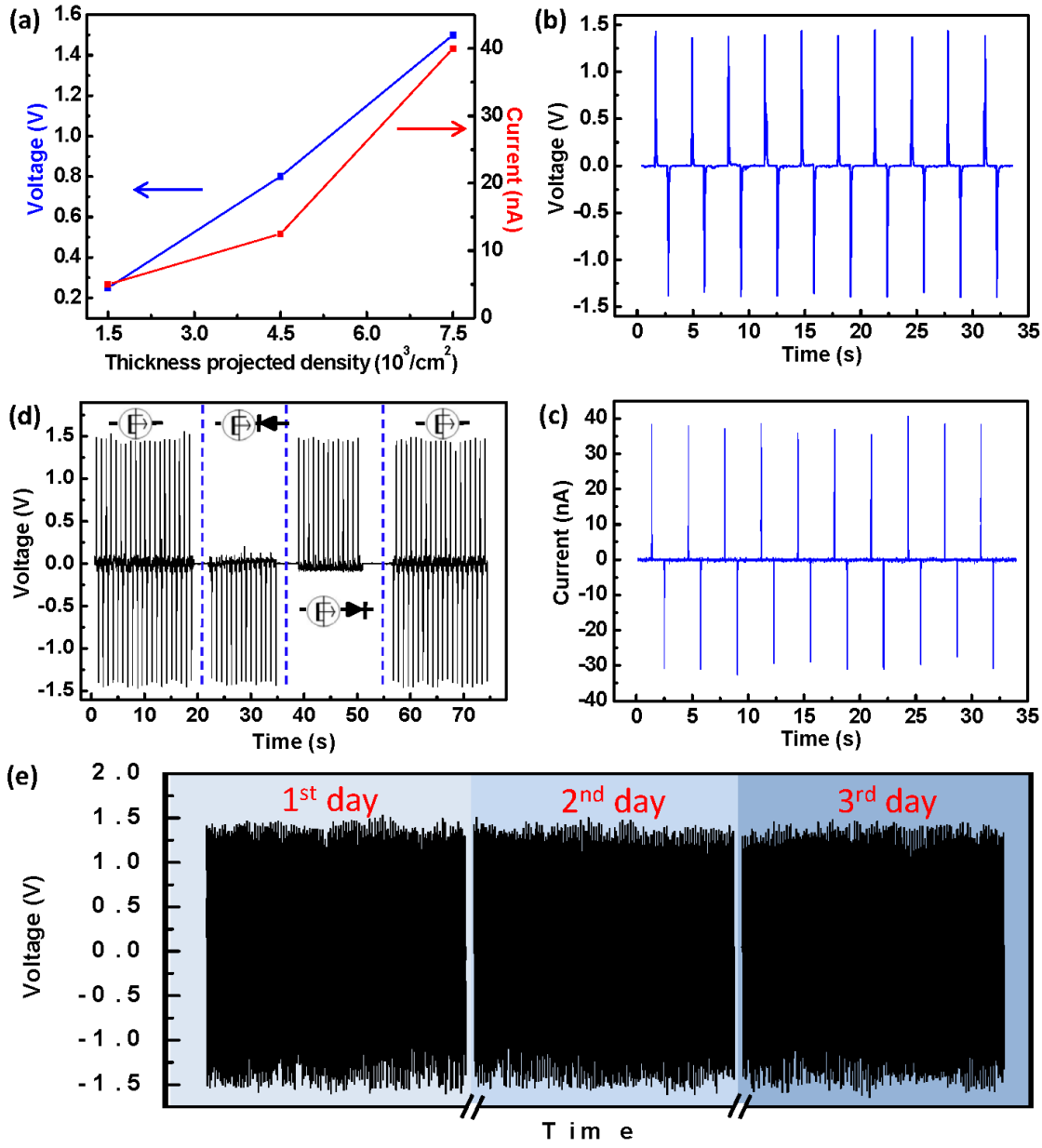

Figure 8.3. The performance of a packaged nanogenerator. (a) The measured output of a NG as a function of the thickness projected CNWs density. (b) The measured output voltage and (c) output current of a nanogenerator made of CNWs with a thickness projected density of 7000-7500/mm^2. (d) Output voltage of the nanogenerator before and after applying a diode to rectify the generated current. (e) The nanogenerator was tested for three days to examine its stability. The nanogenerator was continuously run for 3 hours at a frequency of 1.64 Hz for each day.

For easy visualization of the calculated potential, the orientation relationship between the realistic model for the measurement (Fig. 8.2a) and the representing cross-sections (Fig. 8.2b) at which the distribution of the potential were exhibited (Fig. 8.2c and 8.2d) can be correlated by the (x, y, z) coordinate as indicated in the corresponding figures. The piezopotential inside the CNWs is rather high so

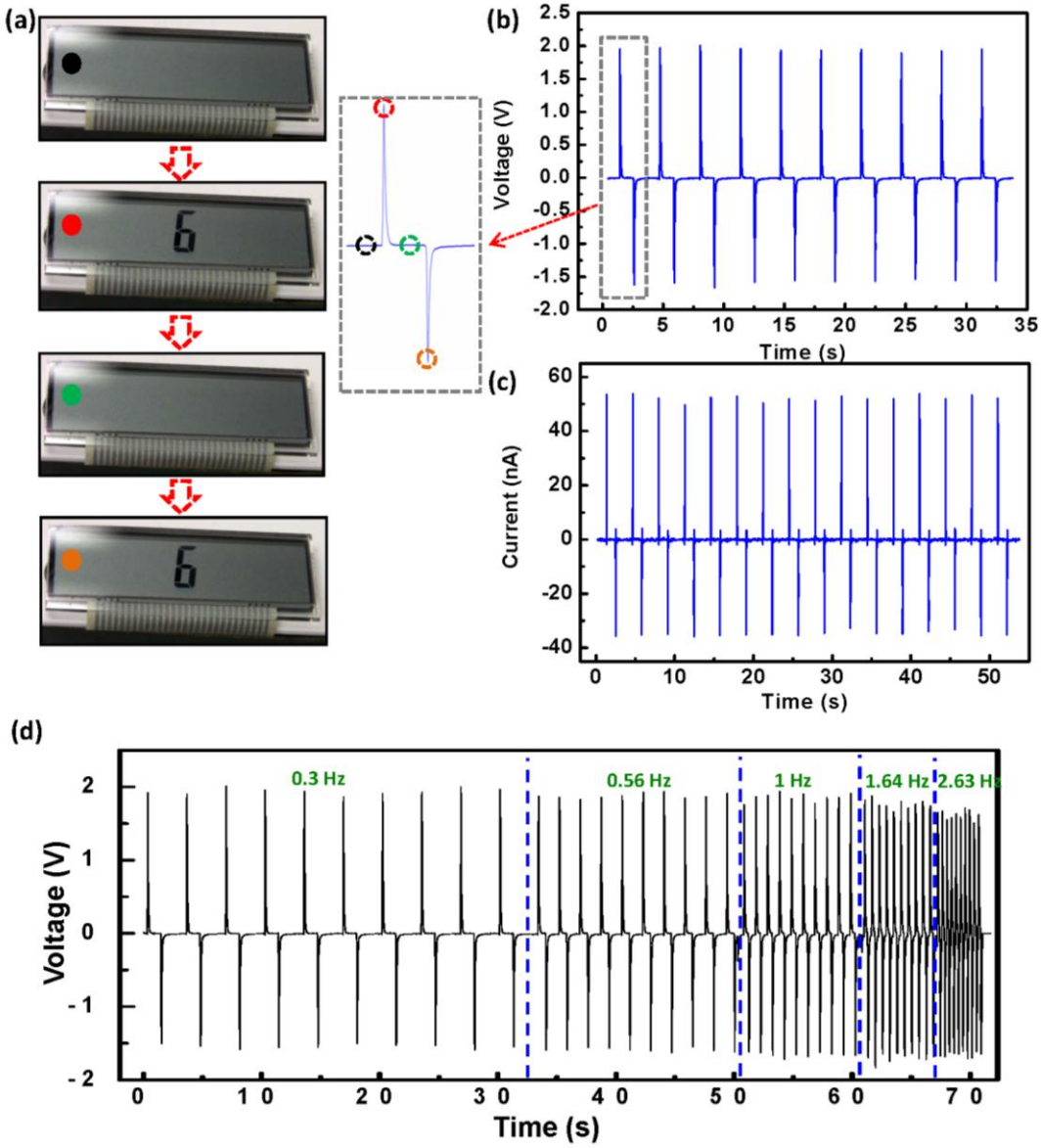

Figure 8.4. Driving a commercial LCD by a nanogenerator. (a) Four snapshots taken from a full cycle driving of a LCD by the NG at a frequency of 0.3 Hz. (b) and (c) are the measured output voltage and output current of the NG. The right-hand part of (a) is an enlarged single cycle of the NG output. We use the dotted circle marked in different colors to show the LCD blinking in corresponding to each AC output peak of the NG. The LCD was taken from a calculator; only a small segment of the entire display area was powered by the NG. (d) The output of the NG with the increase in driving frequency, showing its good stability.

that it is plotted separately in Fig. 8.2c. Owing to the conical shape of the nanowires and the opposite *c*-axis, the piezopotential inside the two CNWs are opposite in sign under compressive strain, but with a small separation in the charge centers in the direction normal to the substrate surface, which is the fundamental mechanism for creating the inductive charges at the top and bottom electrodes. By adjusting the display scale of the piezopotential in the space outside of the CNWs, a 0.8 V inductive potential difference across the two electrodes is clearly shown (Fig. 8.2d), which is generated by an applied compressive strain of 0.12% at the fixed end of the CNW (maximum strain). This is the driving force for the AC nanogenerator. As a verification of the conical shape of the NW being the key of the piezopotential in our design, a calculation for cylindrical nanowires with zero conical angle showed that there is no potential difference across the two electrodes (Fig. 8.2e). Our calculation also predicts that the voltage across the top and bottom electrodes is approximately proportional to the thickness projected density of CNWs if the total deposition is less than a monolayer (Fig.8. 2f).

8.3 General output

We firstly tested the nanogenerator with only one cycle of ZnO CNW deposition in corresponding to an area density of 1400-1500 CNWs /mm^2. Note the deposition density of the CNWs was rather low in comparison to a uniform and fully packed monolayer of CNWs of density ~ 90,000/mm^2. The measured output voltage was ~ 0.25 V, and the output current was ~5 nA when strained to 0.11% at a straining rate of 3.67% s^{-1}. The output of the NG is approximately linearly proportional to the thickness-projected density of the CNWs (Fig. 8.3a), in agreement with the theoretical prediction (Fig.8. 2f). After increasing the cycles of deposition of CNWs to 5, in corresponding to a thickness projected density of 7000-7500 CNWs / mm^2, the output voltage was raised to 1.5 V and the current to 30 – 40 nA (Figs. 8.3b and c). The output current can be rectified using a diode (Fig. 8.3d) and stored for later use. The device showed good stability after three days of testing (Fig. 8.3e).

8.4 Driving of conventional electronic device

The output power of the NG is sufficient to drive a LCD screen. An LCD is a non-polar device that can be driven directly by an AC power as long as its output potential exceeds a threshold value. The LCD screen used for the test was taken from a Sharp calculator; a proper connection combination was chosen to get an output of number "6" at the front panel; the lighting area had a size about the same as that of the NG. The LCD screen was directly connected to a NG without involvement of any external sources or measurement meters. Figure 8.4a is a series of snapshots taken for a full cycle driving of a LCD by the NG at a frequency of 0.3 Hz, showing the LCD blinking corresponding to each AC output peak of the NG. The output was measured to be 2 V in voltage (equivalent to an open circuit voltage of 3.3 V) and 50 nA in current (Figs. 8.4b and c). Thus, the LCD screen blinked when a periodical mechanical deformation of strain 0.11% at a straining rate of 3.67% s^{-1} was applied to the NG. The output of the NG was not affected significantly by an increase in the driving frequency (Fig. 8.4d), and the power output at each peak was able to drive the LCD.

The NG can continuously lighten a LCD. An LCD screen is a capacitive device that can release the input charges within a period of time, during which it continuous lights up if the electric field generated by the remaining stored charges is above the threshold. This is possible if the LCD discharging time is longer than the time interval between two consecutive mechanical straining actions, and its charging time is shorter than the response time of a human eye. Figures 8.5a and b show the performance of an NG with an output voltage of 1.5 V and current of 300 nA. The equivalent inner resistance of this NG was ~ 5.3 MΩ, and the maximum output power was calculated to be ~118 nW. When the LCD screen was powered by the NG, it showed a continuous lighting up status (Fig. 8.5c). From the video we can see that the screen was blinking at first, then, part of the segments was lightened continuously. Finally, after several cycles, it reached an equilibrium lighting status for the full character. This means that our nanogenerator can produce enough power for continuous driving of a LCD.

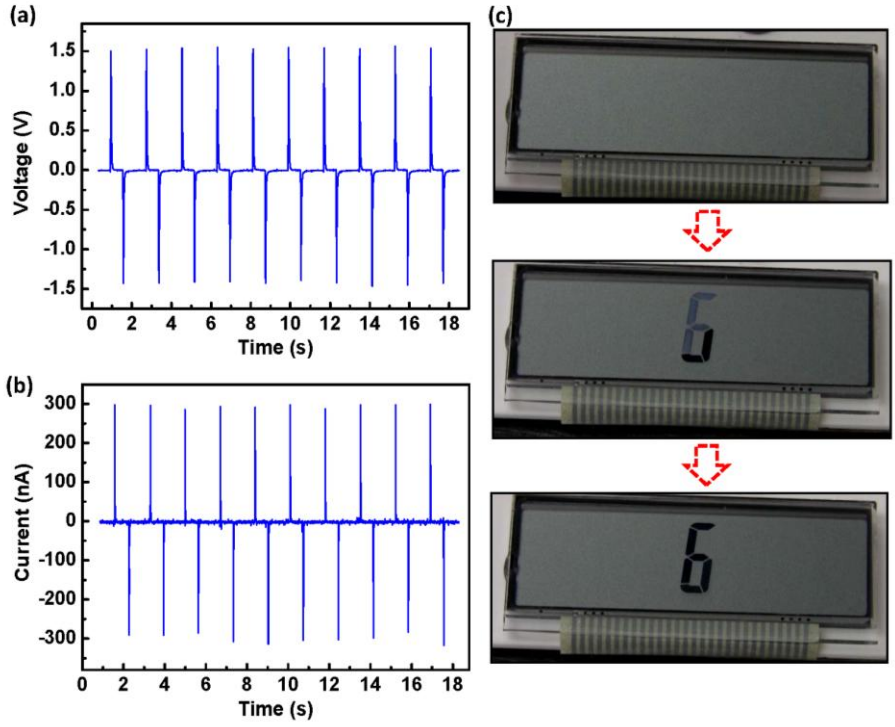

Figure 8.5. Continuous driving of a commercial LCD by a nanogenerator at a mechanical straining frequency of 0.56 Hz. (a, b) The measured output voltage and current of the NG, with peak voltage of 1.5 V and current of 300 nA. (c) Three snapshots taken from the LCD when the NG was periodically strained at a frequency of 0.56 Hz, showing that part of the character "6" was lightened up and then all of the segments were continuous lightened up afterward.

8.5 Summary

There are several advantages for using nanowires than thin films for energy harvesting. First, the growth of single crystal ZnO thin film needs to be done at a high temperature (typically > 400 ^{o}C),[25-27] which limits the choice of substrates especially for flexible electronics. By using nanowires, although they need to be grown at relatively high temperature, transferring the nanowires from the growth substrate to any other substrate is an easy and simple process using our "dropping-on" technique (see Fig. 1a). Second, the composited structure of ZnO and PMMA is much more flexible than ZnO thin films. In order to test the flexibility of a ZnO thin film, we sputtered a 100 nm thick ZnO film on a Kapton substrate that was

covered with PMMA. Figure S11 shows the SEM images of ZnO film before and after being stressed to 0.1% compressive strain. We can see that there are lots of crack lines in the film perpendicular to the bending direction. While for the composite structure of ZnO nanowires and PMMA, there was no crack after being strained to the same degree for several days.

In comparison to our previously demonstrated approaches,[13, 16] our new method has the following unique advantages. First, the CNWs are fully enclosed by polymer without direct contacting with the electrodes. This non-contact design is likely to offer a robust nanogenerator with high stability. Secondly, from the fabrication process presented in Figs. 1 and S1, the fabrication procedures for the NG are simple and cost effective. Finally, the approach has the potential for scale up, and it is likely to be adaptable for industrial mass production.

In summary, utilizing the conical shape of the ZnO nanowires, a nanogenerator is fabricated by simply dispersing them onto a flat PMMA film to form a rational "composite" structure. The flat PMMA surface may lead to a projected *c*-axis unipolar-assembly of the conical-nanowires in the direction perpendicular to the substrate, which produces a macroscopic piezoelectric potential across the thickness of the structure by mechanical deformation. It is suggested that the observed AC current the dynamic flow of inductive charges between the top and bottom surface electrodes of the structure once subjecting to dynamic mechanical straining. For a nanogenerator with a thickness projected nanowire density of $7000/mm^2$ and physical size of 1.5 x 2 cm^2, compressive strain of 0.11% at a straining rate of 3.67% s^{-1} produces an output voltage up to 2 V (equivalent open circuit voltage of 3.3V), which has been shown to continuously drive a commercial liquid crystal display (LCD). Importantly, the size of the NG used for driving the LCD had a size that was comparable to the size of the lighting area, so that it could be integrated at the back of the LCD, indicating its possibility for live-driving of a flexible display. Our nanogenerator is a simple, cost-effective and scalable technology for small personal electronics and self-powered system.

References for Chapter 8

[1] Y.F. Hu, Y. Zhang, C. Xu, G. Zhu and Z.L. Wang, *Nano Letters* **10**, 5025 (2010).

[2] R.S., Yang, Y. Qin, L.M. Dai, Z.L. Wang, *Nature Nanotech.* **4**, 34 (2009).

Chapter 9

Fiber based nanogenerators

Nanogenerators can be fabricated on a range of substrates, from polymer, semiconductor to metal, and from flat substrate to even fiber based substrate, because ZnO nanowires can be grown at low temperature on any substrate and any shape substrate via a solution growth. In this chapter, we focus on the nanogenerators fabricated around a fiber that can be as fine as a hair [1].

9. 1 Microfiber- Nanowire Hybrid Structure

9.1.1 Fabrication of the structure

The ZnO NWs were grown radially around Kevlar 129 fibers through a hydrothermal approach. The as-grown ZnO NWs were then chemically bonded to the fiber surface as well as to each other by coating with tetraethoxysilane (TEOS). The double-fiber NG was assembled by entangling a fiber covered with as-grown NWs around the other fiber covered with Au coated NWs. By holding the two ends of a fiber, and slide the other fiber back and forth, a relative brushing motion between the two fibers produces output current due to a coupled piezoelectric-semiconducting properties. Short circuit current and open circuit voltage were recorded when the two fibers were slide with respect to each other.

The fibers used in our experiments were Kevlar 129 fibers of 14.9 μm in diameter. First, the fibers were cleaned in acetone then ethanol under sonication for 5 minutes each. A 100 nm-thick ZnO seed layer was uniformly coated around the fiber using magnetron sputtering. ZnO NWs were then grown radially on the fiber surface via a hydrothermal approach by immersing the fibers in the reactant solution at 80 ℃. The reactant solution was prepared by dissolving 0.1878 g of $Zn(NO_3)_2 \cdot 6H_2O$ and 0.0881 g of hexamethylenetetramine (HMTA) in 250 mL deionized water at room temperature. The concentration of each in the solution was 0.025 mol/L. After 12-hour aging in the solution, the fibers turned into white, indicating that they were covered by dense ZnO NWs. Finally, they were rinsed with deionized water for several times and baked at 150 ℃ for 1 hour. The as-synthesized ZnO NW-coated fibers were immersed in 99.9% tetraethoxysilane (TEOS) for 2-3 minutes. Because the as-deposited ZnO seed layer usually has some cracks due to its incompatibility with the fiber, capillary force can attract TEOS flew through the cracks to reach the interface between the ZnO seed layer and the fiber as well as the roots of the NWs. Thus, two layers of TEOS above and below the ZnO seed layer were formed.

A typical scanning electron microscopy (SEM) image of a ZnO NW-covered Kevlar fiber is shown in Fig. 9.1a. Along the entire length of the fiber, ZnO NWs grew radially and exhibited a very uniform coverage and well preserved cylindrical shape. Some splits on the NW arrays can be identified (Fig. 9.1b), which were produced owing to the growth induced surface tension in the seeding layer. All of the ZnO NWs are single crystalline and have a hexagonal cross-section with a diameter in the range of ~50-200 nm and a typical length of ~3.5 μm. Their top and side surfaces are smooth and clean, indicating that they are able to form reliable metal-semiconductor junctions needed for the NG. The space between the NWs is of the order of a few hundreds nanometers, which is large enough for them to be bent for generating the piezoelectric potential [2]. The NWs' tips are separated from each other due to their small tilting angles ($< \pm 10°$), but their bottom ends are tightly connected (inset of Fig. 9.1b). As a result, a continuous ZnO film at the NWs' roots served as a common electrode for signal output. Previous experiments showed that AFM manipulation of a solution grown ZnO NW can give up-to 45 mV output voltage [3].

To maintain the high flexibility of the fiber after growing a crystalline film and NWs, a surface coating strategy was introduced to improve the mechanical performance of the fiber and the binding of NWs. As shown in Fig. 1c, two layers of tetraethoxysilane (TEOS) were infiltrated above and below the ZnO seed layer as a binding agent. The Si-O bonds in TEOS are highly reactive with the OH^- groups on the ZnO surface, and its organic chains firmly bind to the body of the aromatic polyamide fiber. As a result, the ZnO seed layer and the fiber core were tightly bound with each other by a thin layer of TEOS. Furthermore, since TEOS could easily form cross linked chains, the NWs were firmly bundled and bound together at their roots and fixed on the ZnO seeding layer, successfully preventing the NWs from scratching/stripping off during mechanical brushing/sliding. Even when the fiber was looped into a circle of ~1 mm in diameter, no cracks, loose pieces or peel-offs were observed in the ZnO NW coating layer (Fig. 9.1d). At the bending area, the radial aligning morphology of the ZnO NWs was also very well preserved (Fig. 9.1e), clearly demonstrating its toughness for mechanical deformations and bending.

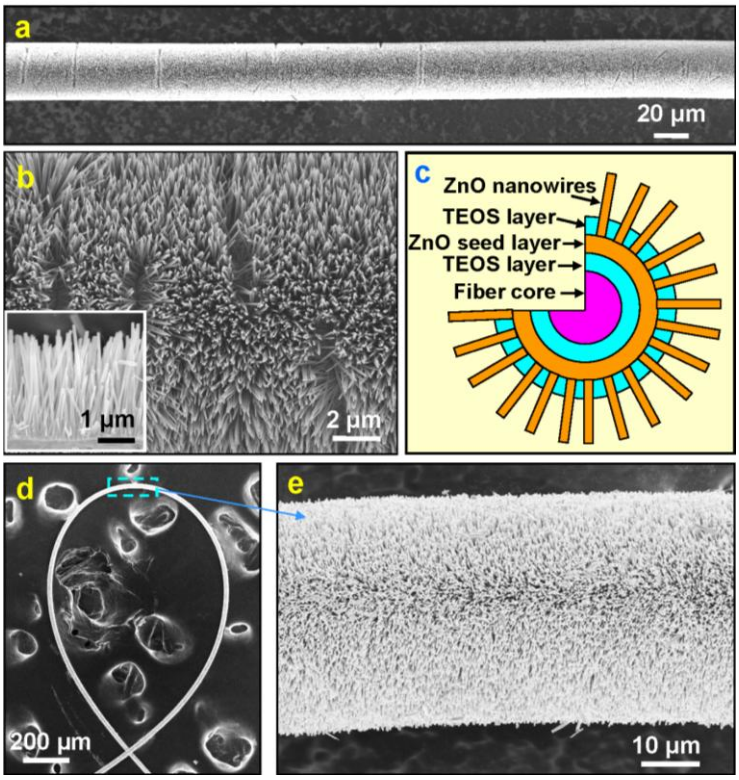

Figure 9.1. ZnO NW coated Kevlar fibers. a, SEM image of a Kevlar fiber covered with ZnO NW arrays along the radial direction. b, Higher magnification SEM image and a cross-section image (inset) of the fiber, showing the distribution of NWs. c, Schematic showing the cross-section structure of the TEOS enhanced fiber designed for improving its mechanical performance. d, SEM image of a looped fiber showing the flexibility and strong binding of the NW layer. e, Enlarged section of the looped fiber showing the distribution of the ZnO NWs at the bending area [1].

9.1.2 Fabrication of the fiber generator

A typical double-fiber NG was assembled using two 3 cm-long ZnO NW coated fibers, one coated with Au and one as-grown. The Au layer was coated by a DC sputtering system. During the sputtering, the fiber was fixed on the stage at one end and its body was left freestanding. Therefore, a fairly uniform Au coating was achieved along entire fiber by rotating the sample stage. Generally, the thickness of the Au coating was 300±20 nm, which was read by a quartz thickness monitor equipped inside the sputtering system. In assembling the double-fiber NG, both ends of the as-grown ZnO NW fiber were fixed on a glass substrate with one end grounded and electrically connected to an external measurement circuit as the NG's output anode. One end of the gold coated fiber was attached to a small spring, which was affixed to the substrate; while the other end was attached to a pulling string so that it can freely move back and forth. The gold coated fiber was electrically connected to the external circuit as the NG's output cathode. The effective length of the fiber NG was 4-5 mm and typically contained nine cycles, where each cycle was ~500 μm in length.

The double-fiber NG was fixed on a stationary stage with the movable gold-coated fiber attached to a pulling bar. The pulling bar was driven by a speed control motor with an extrusion on its spin axis, which

transferred its rotary motion into a back-forth motion of the pulling bar at a chosen frequency. Under each round, the gold coated fiber first moved to the pulling direction when the pulling bar was lifted up; then was retracted back to its original position by the spring attached to the other end. The back-and-forth brushing movement between the two fibers was thus achieved at a controlled frequency.

In order to demonstrate the power generation ability of the ZnO NW covered fibers, a double-fiber model system was designed as shown in Fig. 9.2a. Two fibers, one coated with a 300 nm thick gold layer and the other as-grown, were entangled to form the core for power generation. The relative brushing between the two fibers was simulated by pulling/releasing the string using an external rotor with a controlled frequency. The gold coated fiber was connected to the external circuit as the NG's output cathode. The pulling force ensured a good contact between the two fibers, as shown by an optical microscopy image in Fig. 9.2b.

In this design, the gold coated ZnO NWs acted as an array of scanning metal tips that deflected the ZnO NWs rooted at the other fiber; a coupled piezoelectric and semiconducting property resulted in the charge creation and accumulation and charge release process. The gold coating completely covered the ZnO NWs and formed a continuous layer along the entire fiber. The successful coating was confirmed by its metallic I-V characteristic (Fig. S1). Once the two fibers were firmly entangled together, some of the gold coated NWs interdigitatively penetrated slightly into the spaces between the uncoated NWs rooted at the other fiber, as shown by the interface image in Fig. 2c. Thus, when there was a relative sliding/deflection between them, the bending of the uncoated ZnO NWs produced a piezoelectric potential across their width, and the Au coated NWs acted as the "zigzag" electrode as for the DC nanogenerator[Error! Bookmark not defined.] for collecting and transporting the charges.

9.1.3 Working mechanism

Figures 9.2d to illustrate the charge generation mechanism of the fiber NG. Analogous to the case of deflecting a NW by an AFM tip, when the top fiber moves to the right-hand side, for example, the gold coated NWs bend the uncoated ZnO NWs to right-hand side (for simplicity of description, we assume that the Au coated NWs are much stiffer and suffer little bending). Piezoelectric potential is thus generated across the uncoated NW due to its piezoelectric effect, with the stretched surface positive (V^+) and the compressed surface negative (V^-) [4]. The positive potential side has a reversely biased Schottky contact with Au and thus prevents the flow of current, while the negative potential side has a forward biased Schottky contact with the Au and it allows the current to flow from the Au to the NW. Since the density of the NWs is high (see Fig. 9.1b), it is very likely that a bent NW rooted at the uncoated fiber touches the backside of another gold coated NW after subjecting to bending (such as NW I in Fig. 9.2e). In this case, the negative potential surface of the ZnO NW contacts the gold layer, so the Schottky barrier at the interface is forward biased, resulting in a current flowing from the gold layer into the ZnO NW. Then, when the top fiber keeps moving further towards the right-hand side (Fig. 9.2f), the gold coated NWs scan across the ZnO NWs' tip and reach their negatively charged side (NW I and II in Fig. 9.2f). Therefore, more current will be released through the forward biased Schottky barrier (Fig. 9.2f). This means that the currents from all of the NWs will add up constructively regardless the NW being deflected to which direction even in the same cycle of pulling. The output voltage is defined by the characteristic of one NW, and the sign of the voltage does not change in responding to the deflection configuration of the NW due to the rectifying effect of the Schottky barrier at the Au-ZnO interface. The same effect is expected if the top fiber is driven to retract toward the left-hand-side. Due to the similar mechanical property of the top and bottom NWs, the gold coated NWs could also be possibly bent by the NWs rooted at the uncoated fiber, but this does not affect the mechanism presented in Fig. 9.2. For the Au coated fiber, all of the NWs are completely covered by a thick gold layer, and they can be considered as an equal potential electrode connected to the external measurement circuit. Thus, the role played by the ZnO NWs was only a template for supporting the Au coating and no piezoelectric charges will be preserved inside the gold coated NWs.

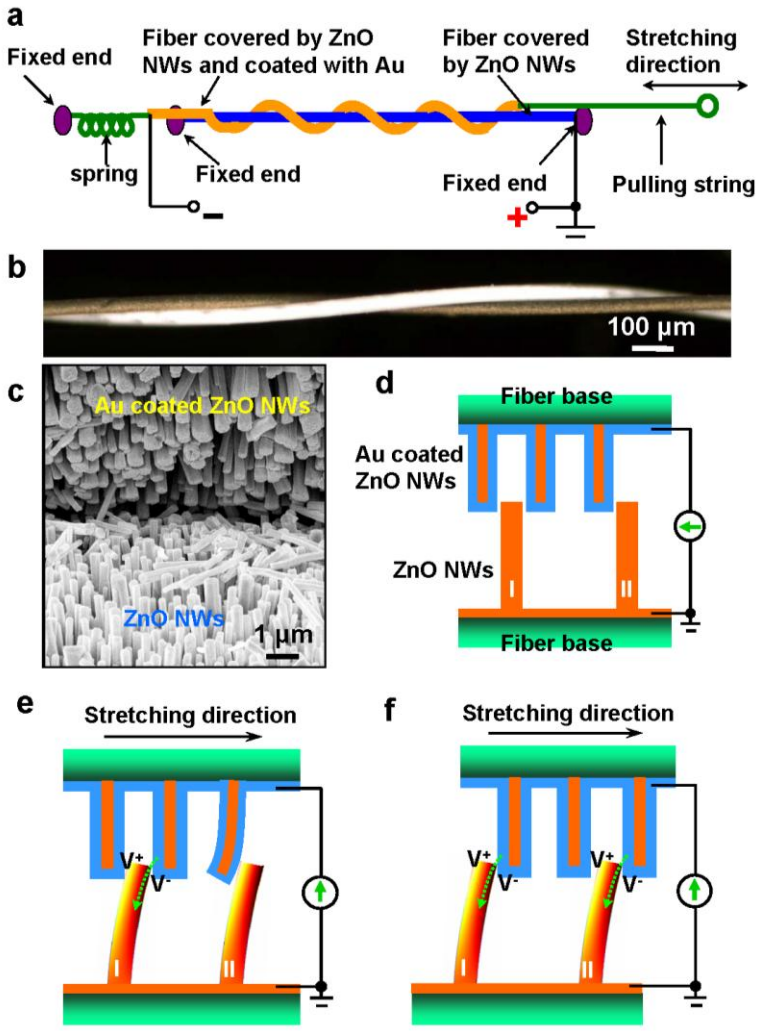

Figure 9.2. The design and mechanism of the fiber based nanogenerator as driven by a low-frequency, external vibration/friction/pulling force. a, Schematic experimental set up of the fiber based nanogenerator. b, An optical micrograph of a pair of entangled fibers, one of which is coated with Au (in darker contrast). c, SEM image at the "teeth-to-teeth" interface of two fibers covered by NWs, with the top one coated with Au. The Au coated NWs at the top serve as the conductive "tips" that deflect/bend the NWs at the bottom. d, Schematic illustration of the teeth-to-teeth joining between the two fibers covered by NWs. e, The piezoelectric potential created across the NW I and II under the pulling of the top fiber by an external force. The side with positive piezoelectric potential does not allow the flow of current owing to the existence of a reversely biased Schottky barrier. Once the NW is pushed to bend far enough to reach the other Au coated NW, electrons in the external circuit will be driven to flow through the uncoated NW due to the forward biased Schottky barrier at the interface. f, When the top fiber is further pulled, the Au coated NWs may scrub across the uncoated NWs. Once at the last moment that the two types of NWs are in the final contact, the interface is a forward biased Schootky, resulting in further output of electric current, as indicated by arrowheads. The output current is a sum of all contributed by all of the NWs, while the output voltage is determined by one NW [1].

9.1.4 Output measurements

The short-circuit current (I_{sc}) and open-circuit voltage (V_{oc}) were measured to characterize the performance of the fiber NGs. The pulling and releasing of the Au coated fiber was accomplished by a motor at a controlled frequency. The resulting current signals detected at 80 rpm (round per minute; 60 rpm = 1 Hz) are shown in Fig. 9.3a. A "switching polarity" testing method was applied during the entire measurement for ruling out system artifacts. When the current meter was forward connected to the NG, which means that the positive and negative probes were connected to the positive and negative electrodes of the NG as defined in Fig. 9.2a, respectively, ~ 4 pA positive current pulses were detected at each pulling-releasing cycle (blue curve in Fig. 9.3a). Negative current pulses with the same amplitude were received (pink curve in Fig. 9.3a) when the current meter was reversely connected, which means the positive and negative probes connected to negative and positive electrodes of the NG, respectively. The small output current (~4 pA) is attributed mainly to the large loss in the fiber due to extremely large inner resistance ($R_i \approx 250$ MΩ). The large resistance of the fiber based nanogenerator is likely due to the cracks in the ZnO seed layer that is directly adjacent to the fiber because of the structural incompatibility and large difference in thermal expansion coefficients. Reducing R_i of the fiber NG is an effective way to improve its power output efficiency, which is to be demonstrated in Fig. 4b. The inverted output current signals confirmed that the current was indeed originated from the fiber NG. The shapes of the positive and negative current pulse are enlarged and shown in Fig. 9.3c and d, respectively, from which, a double-peak feature is clearly observed for each cycle of pulling the fiber.

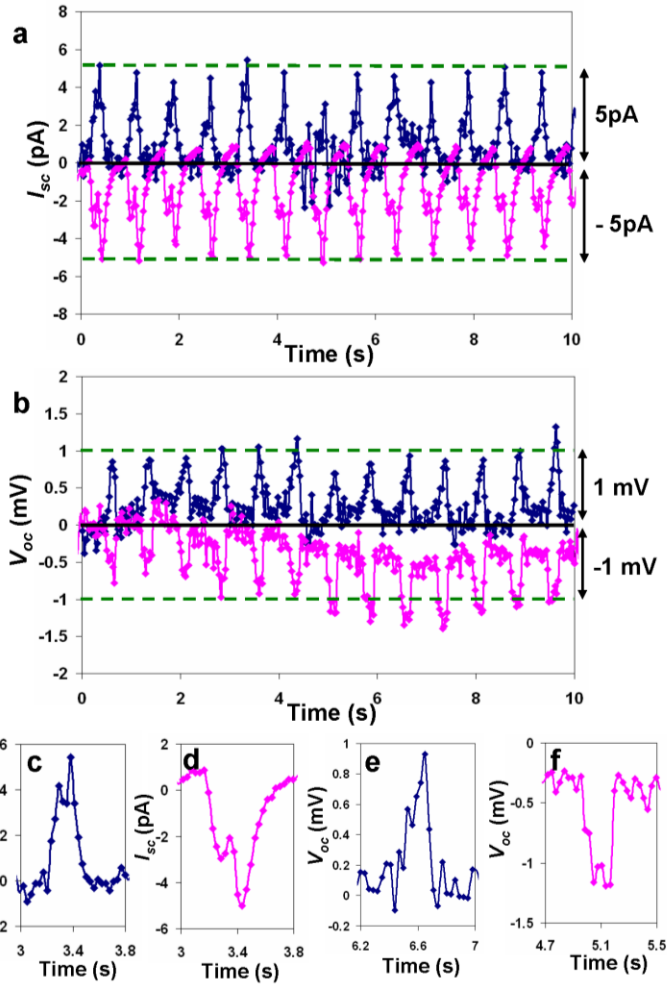

Figure 9.3. Electric output of a double-fiber NG. a, The short-circuit output current (I_{sc}) and b, open-circuit output voltage (V_{oc}) of a double-fiber NG measured by applying an external pulling force at a frequency of 80 rpm. When the measurement circuit was forward connected to the NG, which means that the positive and negative probes were connected to the positive and negative output electrodes of the NG, respectively, the output signals are represented by a pink curve. By reversing the polarity of the connection of the NG output electrodes, the output signals are presented in a blue curve. c, d, Magnified output current and e, f, output voltage for a single cycle of the fiber pulling. The background introduced by the measurement circuit was removed in the displayed plots.

Open-circuit voltage was

also measured by the switching polarity method. Corresponding positive and negative voltage signals were received while the voltage meter was forward and reversely connected to the fiber NG, respectively (Fig. 9.3b). The amplitude of the voltage signal in this case was ~1-3 mV (also see Fig. S4). Same as for the current signal, double-peak feature was also observed in both positive and negative voltage signals, as shown in Fig. 9.3e and f.

The double peaks in the output signal (Fig. 9.3c-f) are related to the cycle motion of the fiber. When the fiber was pulled to the right-hand-side during stretching and then retracted back by the spring when releasing, the mechanism illustrated in Fig. 9.2 remained the same. Although the two moving directions were opposite, the currents generated flowed in the same direction, and a ~0.2s delay one with respect to the other produced double peaks in the resultant output current and voltage. This is a general phenomenon that existed in every output pulse regardless of its polarity. A slight difference in the magnitude of the double peaks may be related to the speed at which the fiber was pulled and retracted.

9.1.5 Improving performance

After demonstrating the electricity generation principle, a few approaches were investigated to increase the output power and prototype integration. To simulate a practical fabric made of yarns, a single yarn made of 6 fibers were tested, among which three were covered with NWs and coated with Au and three were only NWs. All of the gold-coated fibers were movable in the testing (Fig. 9.4b). At a frequency of 80 rpm, an average current of ~ 0.2 nA was achieved (Fig. 9.4a), which is ~30-50 times larger than the output signal from a signal fiber NG's due to the largely increased surface contact area among fibers. Apparently, the width of each pulse was broadened due to the unsynchronized movement and a relative delay in outputting current among the fibers.

Reducing the inner resistance of the fiber and the NWs was found to be effective for enhancing the output current. By depositing a conductive layer directly onto the fiber before depositing the ZnO seeds, the inner resistance of the NG was reduced from ~ 1 GΩ to ~ 1 kΩ, thus, the output current I_{SC} of a double-fiber NG was increased from ~ 4 pA to ~ 4 nA (Fig. 9.4c). The current I_{SC} is approximately inversely proportional to the inner resistance of the NG (inset in Fig. 9.4c). This study shows an effective approach for increasing the output current. In addition, by connecting NGs in serial and parallel, the

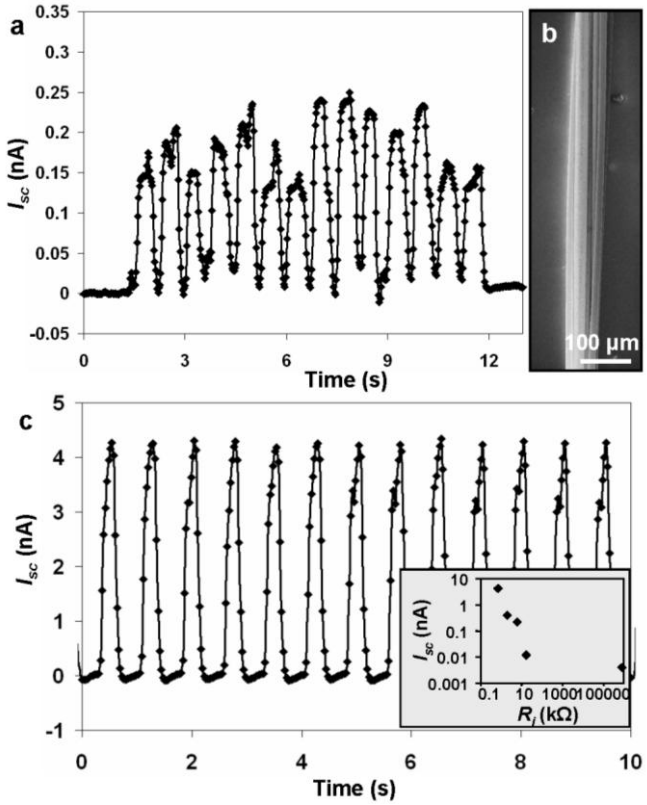

Figure 9.4. Output improvements. a, The short-circuit output current (I_{sc}) of the multi-fiber NG operated at 80 rpm. A broadening in the output current peaks is observed due to the unsynchronized movement among the fibers. b, SEM image of the multi-fiber NG that was composed of three gold-coated fibers and three ZnO NW covered fibers. This shows the possibility of using a bundle of NWs as a yarn for enhancing the output current. c, Enhancement of output current by reducing the inner resistance of the nanogenerator. By coating the surface of the fiber first with a conductive layer, then depositing ZnO seeds, the inner resistance of the nanogenerator was reduced by orders of magnitude. The background introduced by the measurement circuit was removed in the displayed plots.

output voltage and current, respectively, can be increased as well.

9.1.6 Summary

The textile-fiber based nanogenerator has demonstrated the following innovative advances in comparison to the DC nanogenerators reported previously. First, using ZnO NWs grown on fibers, it is possible to fabricate flexible, foldable, wearable and robust power source in any shape (such as "power shirt"). Second, the output electricity can be dramatically enhanced using a bundle of fibers as a yarn, which is the basic unit for fabrics. The optimum output power density from textile fabrics can be estimated based on the data we have received, and an output density of 4-20 mW per square meter of fabric is expected (see online Supplementary Materials). Thirdly, the nanogenerator operates at low-frequency in the range of conventional mechanical vibration, foot steps and heart beating, greatly expanding the application range of nanogenerators. Finally, since the ZnO NW arrays were grown using chemical synthesis at 80 ^{o}C on a substrate with any curvature and materials nature, the fields to which the nanogenerators can be applied to and integrated with have been greatly expanded. The near term goal is to optimize the structure and design for improving the efficiency and total output power.

9.2 Pressure driven flexible fiber nanogenerators

Air pressure is a very common physical parameter that affects our daily life in many ways. Air/liquid flow induces dynamic pressure change, which can drive a lot of things. How to use the energy induced by air pressure/flow is important for today's energy technology. Fluctuation in air pressure is a rather irregular phenomenon with a large degree change in amplitude and frequency, which makes it rather difficult to be harvested directly using the conventional technologies. Take the piezoelectric cantilever approach as an example, it has the maximum energy harvesting efficiency if the external mechanical stimulating frequency matches the resonance frequency of the cantilever. If the stimulating frequency is low, the required size of the resonator has to be large, which can only harvest the energy if the magnitude of the applied force is strong enough. If the applied frequency is high, the size of the resonator is required to be small, but the high frequency mechanical signals are not as popular as the low frequency agitations in our living environment, especially in biological systems, such as breathing and heart beating.

In this section, we presented a new approach for fabricating flexible fiber nanogenerator (FNG) that can be used for smart shirt, flexible electronics and medical applications [5]. The FNG is based on carbon fibers that are covered cylindrically by textured ZnO thin films. Once subjects to uni-compression by applying a pressure, the cylindrical ZnO thin film is under a compressive strain, resulting in a macroscopic piezopotential across its inner and exterior surfaces owing to the textured structure of the film, which is the driving force for generating the electric current in the external load. Using such a structure, an output peak voltage of 3.2 V and the average current density of 0.15 μAcm^{-2} have been demonstrated. The FNG relies on air pressure, so that it can work in a non-contact mode in cases of rotating tire, flowing air/liquid and even in blood vessel. The pressure driven FNG in a syringe shows its potential to harvest energy in a blood vessel, gas pipe and oil pipe, as long as there is a fluctuation in pressure (or turbulence). The heart pulse driven FNG can serve as ultrasensitive sensor for monitoring human heart behavior, which may possibly be applied to medical diagnostics as sensors and measurement tools.

9.2.1 Growth of radial textured ZnO thin film on fibers

Our design of the FNG is based on radial textured ZnO thin film grown around carbon fibers (Fig. 9.5a). In principle, any conductive fiber can be used for this purpose. The fiber used not only as flexible soft substrate to grow ZnO thin film at high temperature but also acts as an electrode for charge transport. The key point of our method is that our technique produces textured film that is made of densely packed nanowires with [0001] orientations, which is around the fiber to form a radially textured, cylindrical, shelled structure. The density of the NWs can be controlled by experimental condition without using ZnO seeds.

The source materials used for the growth of ZnO film on carbon fiber were ZnO powder (Alfa Aesar, 99.9%, 200 mesh), activated carbon particles (Alfa Aesar, steam activated, acid washed) with equal ratio in mass, which were placed at the center of a tube furnace with a quartz tube to keep the carbon fiber and flow guide of the gas. The carbon fibers (1K, T600, Tsinghua Univ.) were freely suspended in the tube on the way of carrier gas， which was location at the ~10 cm from the end of the tube. The carrier gas was made of oxygen and nitrogen gas (99.9% , Georgia Tech) at a ratio of 1:4 at a flow rate of 40 sccm. The growth temperature was 960℃.

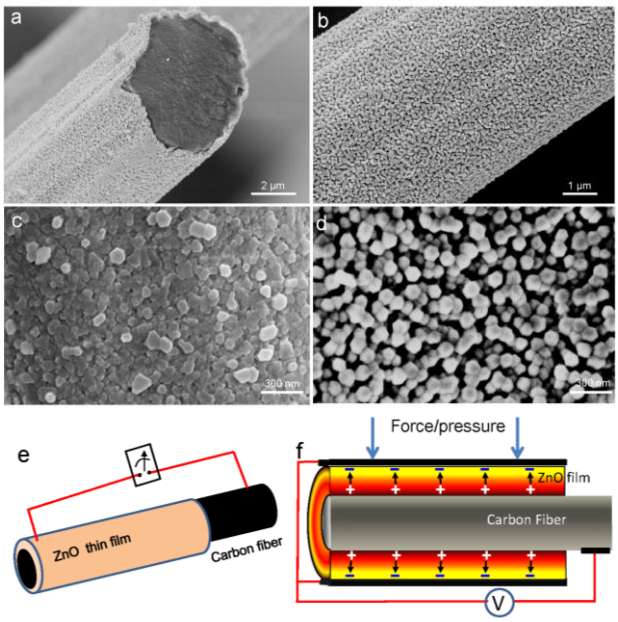

Figure 9.5. Textured ZnO thin films grown around a carbon fiber. (a, b), Low magnification SEM image of the ZnO/fiber structure. (c), A ZnO film made of dense packed ZnO nanorods with a uniaxial direction of *c*-axis. (d), A ZnO film made of sparely aligned ZnO nanorods their *c*-axes closely in parallel. (e), Structural of the fiber nanogenerator based ZnO thin film coated carbon fiber. Schematic of the nanogenerator. (f), Working principle of the fiber nanogenerator, where the '+/−' signs indicate the polarity of the local piezoelectric potential created on the inner and outer surfaces of the ZnO thin film [5].

The growth of the ZnO thin film that cylindrically covering the surface of a carbon fiber was carried out using a physical vapor deposition method (Fig. 9.5b). The as grown thin film is composed of nearly parallel aligned ZnO nanorods to form a textured film (~ 250 nm in thickness) with the normal direction along [0001]. This can be clearly seen in the SEM image presented in Fig. 9.5c, in which the densely packed ZnO nanorods are clearly seen with hexagonal flat tops. These nanorods can have random orientation in the film plan, but a good alignment in the normal direction so that the entire film has a uni-polar structure along the *c*-axis. The distribution of the nanorods around the fiber can be clearly seen if the density of the nanorods is not high (Fig. 9.5d). Our previous study using X-ray diffraction study shows that ZnO tends to form epitaxial thin films on literately on any surfaces, such as polymer and silicon. This provides a unique advantage not only to accommodate the curvature as defined by the shape of the substrate that is the fiber, but also provides a uni-polar structure for piezoelectric applications.

9.2.2 The working principle of the fiber nanogenerator

For the fabrication of the fiber nanogenerator (FNG), the ZnO thin film at one side of carbon fiber was etched off locally by NaOH solution to expose the fiber electrode for making contact. The other electrode of the FNG was contacted to the top surface of the ZnO thin film using a silver tape/paste (Fig. 9.5e). As shown in Fig. 9.5 and our previous study [6], wurtzite structured ZnO nanorods form a densely packed and polar-direction aligned thin film, with the polar direction pointing radial outward. The FNG was constructed by aligning the ZnO coated carbon fibers in parallel, with an electrode connected to the carbon fibers and one electrode connected to the top surface of the ZnO film. A plastic substrate was used to support the aligned fibers, and all of the fibers were fixed to the substrate.

The working principle of the FNG is as follows. For simplicity, the textured film can be treated as a "single-crystal" for the purpose of FNG. When the film is compressively strained under the applied external pressure through air/liquid, a separation between the static ionic charge centers in the tetrahedrally coordinated Zn-O units results in a piezoelectric potential gradient along the *c*-axis. The

textured structure of the thin film results in a macroscopic piezoelectric potential across the thickness of the film (Fig. 9.5f). If the c-axis is pointing outward of the fiber substrate, the negative side of the piezopotential is the external surface of the film, which raises up the conduction band and the Fermi level at the electrode[16], forcing the electrons to flow from this side to the other electrode through the external load due to the existence of the Schottky barrier at the interface until equilibrium is reached. As the external force is removed and the compressive strain is released, the piezoelectric potential inside the film diminishes. The electrons accumulated at the other electrode flow back via the external circuit, creating an electric pulse in the opposite direction. The role of the Schottky barrier is to prevent those mobile charges from passing through the film-metal interface. The piezoelectric potential acts as a 'charging pump' that drives the electrons to flow [7]. A cycled strained induced in the film by the externally applied pressure results in an AC output. The key role played by the fiber is to effectively use the pressure from all directions.

Experimentally, a linear motor was used to periodically deform the FNG in a cyclic stretching-releasing agitation. The short-circuit current (I_{sc}) and open-circuit voltage (V_{oc}) were measured to characterize its performance. When the current meters was forward connected to the FNG, a positive current pulse was recorded during fast stretching of the substrate (see SI), and a corresponding negative pulse for fast release (where 'fast' means an angular bending rate of ~260° sec^{-1} at a radius of 2 cm for the substrate). For a FNG made of 150 carbon fibers of ~10 μm in diameter and ~ 20 mm in length each, the maximum output voltage received was 2.0~2.2 V and the output current was 60~120 nA. Although the heights of the current peaks for the stretch and release appear differently, possibly because of different straining rates, the areas under the peaks remain about the same to within 5%. Similar experiments have been done when the FNG was under compressive strain.

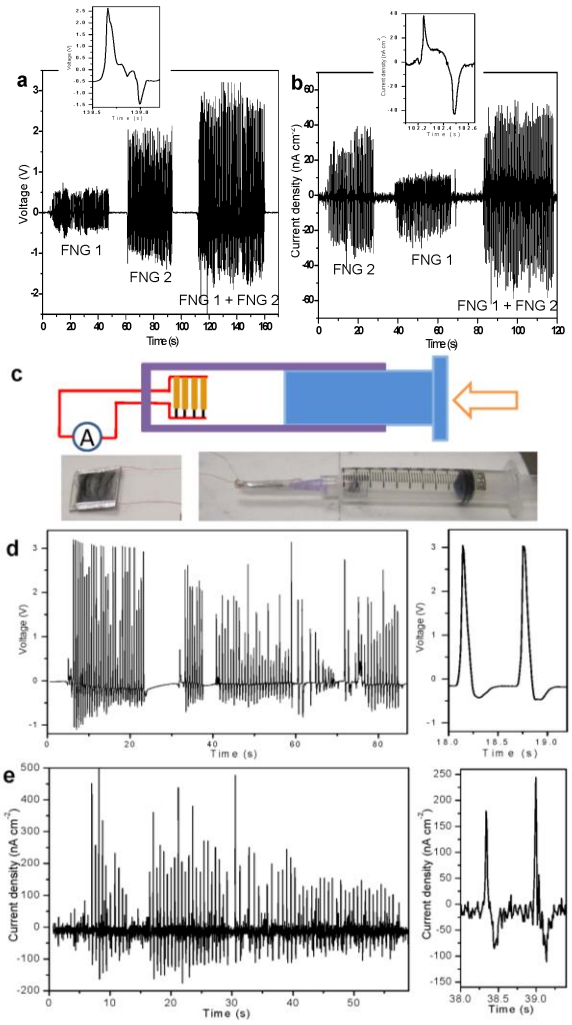

Figure 9.6. Two normal good working FNG for a 'linear superposition' test of outputs current density (a) and voltage (b), The output voltage of the two FNGs (FNG1+FNG2) was the sum of the FNG1 and FNG2 when they are connected in serial. The output current density also added up when the two FNGs were connected in parallel. In insets are the details of the output signals.
Integration and performance of an air pressure driven fiber nanogenerator. (c) Schematics for the air pressure driven FNG when it is placed inside a syringe. The variation in the air pressure is created by the piston of the syringe. Open-circuit output voltage (d) and short-circuit output current (e) measured for a FNG structure comprising of 100 carbon fibers. The maximum output voltage peak reaches 3.2 V. The insets at the right-hand side are one cycle of the output voltage and current [5].

9.2.3 Air pressure driven fiber nanogenerator

Since air pressure can act on every part of an object that is exposed without a specific direction, we packaged the ZnO film coated carbon fibers loosely on a flexible substrate, as shown in Fig. 9.6c following the connection as shown in Fig. 9.5e. A uni-radial compression by the air pressure around the fiber creates a piezoelectric potential as shown in Fig. 9.5f. A dynamic variation in pressure creates a compression-release process to the cylindrical shape ZnO film; the corresponding generated piezoelectric potential drives the back and forth flows of the electrons in the external load in responding to the fluctuation in air pressure.

By placing the FNG inside a syringe (Fig. 9.6c) and applying a periodic pressure through the compression of the piston, an AC output was received (Fig. 9.6d). The generated electricity output is not quite symmetric because the pressure and rate the pressure was applied were different when compressing and releasing the piston. The output peak voltage reached up to 3.2 V and the average current density reached 0.15 μAcm^{-2}. The surface area was calculated as the area of the working carbon fibers in the nanogenerator. The output was significantly higher than our previous reports possibly because that there was no packaging material to cover the FNG so that the pressure acted directly onto the ZnO film without being damped by the packaging material or substrate.

9.2.4 Exhalation driven fiber nanogenerator/sensor

Gentle air flow has the following characteristics. First, the direction of the air flow varies unpredictably. Second, the force of the air flow acting on a small device is rather weak so that it may not drive a generator if the stiffness and damping of the packaging material are too high. Lastly, the frequency of the air flow also varies. To enhance the effectiveness of the gentle breeze in driving the FNG, we used carbon fibers that are long and flexible enough to respond to the air breeze, as shown in the inset in Fig. 3a. A ring shape FNG was fixed on a glass substrate. One electrode was connected to carbon fibers and the other one was joined to the ZnO film. When blowing the FNG by a gentle exhalation, the breezing wind made the FNG to change shape and vibrate, resulting in electricity output (Fig. 9.7). Repeated exhalation resulted in an AC output. The average output voltage was 1.5 mV and the average output current was 0.5 nA. The low output is possibly due to the low strain created in the film by exhalation. Such low output may not be useful for energy harvesting, but it can be used as a breathing sensor in biomedical and health care application.

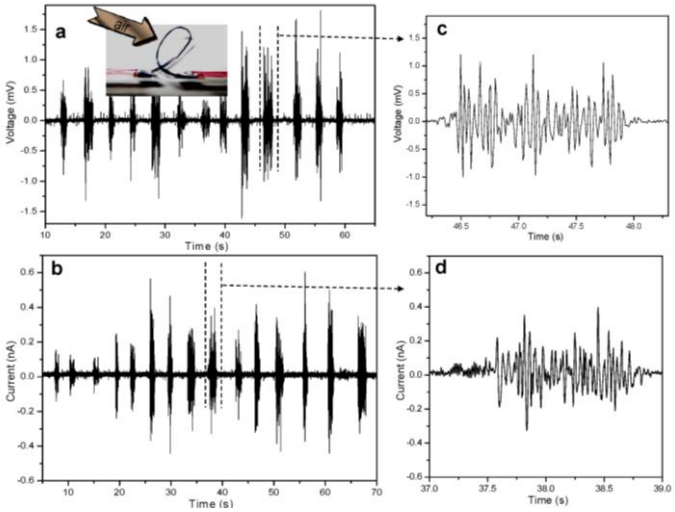

Figure 9.7. Performance of an air flow driven fiber nanogenerator. Inset in (a) is a loop shape FNG fixed to a glass substrate, which was made of 50 carbon fibers. When breezing the air by exhalation, the open-circuit output voltage (a, b) and short-circuit output current (c, d) for the FNG are received [5].

9.2.5 Wrist pulse driven nanogenerator as pressure sensor

The pulse pressure (PP) is one of the output signals of a human heart system, which is a complex time–dependent and non-linear signal reflecting the fluctuation of one's motion and health situation[8]. A quantitative measurement of pulse signal provides important information for medical monitoring especially in medical diagnostics [9]. The origins of PP are complex because it is adequately described by cardiac output and total peripheral resistance. In the literatures [10], PP is increasingly being recognized as a risk factor for cardiovascular, and also for other diseases. Our first experiment is to use the pulse at the wrist of a human to drive a FNG. A FNG made using relatively long fibers of ~4 cm was attached to the wrist with cloth athletic tape. The FNG was placed over the pulse point as schematic shown in Figure 9.8a. In order to get the in-situ original blood pressure signal, a medical applicable blood pressure gauge was affixed on the top of the FNG. The output of the FNG was recorded in responding to the heart beating behavior. Figures 9.8a, b and c show three different output patterns of heart beat as measured by the output current of the FNG. These curves contain information about the dynamics of the heart beating. An application of data analysis technique can derive some specifics about possible health condition of a person. Traditional pulse feeling method in Chinese medicine takes twenty-eight pulses as mostly clinical pulse condition [11]. The normal pulse pressure wave should be like Fig. 9.8b. A young person has a smooth pulse as shown in Fig. 9.8c. An older person would have the pulses like the ones shown in Fig. 9.8d.

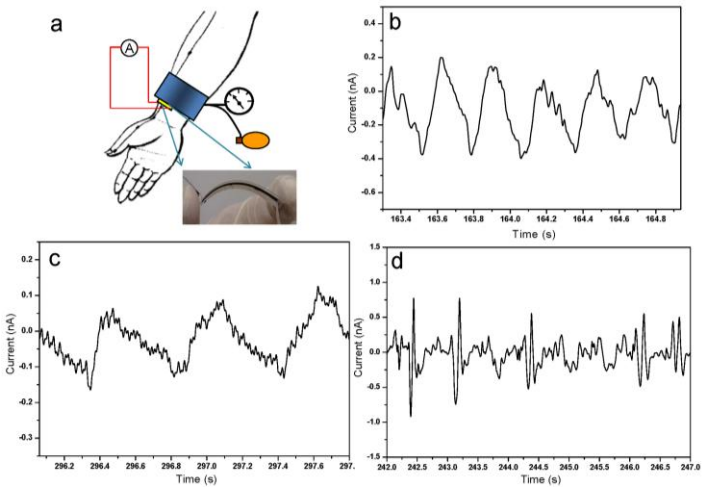

Figure 9.8. Heart pulse driven fiber nanogenerator for energy harvesting or strain sensor. (a), Schematics of the experimental set up. (b, c, d) Three typical heart pulse generated electric current outputs from a FNG, which not only demonstrate the energy conversion from small physical motion, but also as bio-strain-sensor.

9.2.6 Summary

We presented a new approach for fabricating flexible fiber based nanogenerator that can be used for smart shirt and flexible electronics. The NG is based on carbon fibers that are covered cylindrically by a textured ZnO thin film. Once subjects to uni-compression by applying a pressure, the cylindrical ZnO thin film is under a compressive strain, resulting in a macroscopic piezopotential across its inner and exterior surfaces, which is the driving force for generating the electric current in the external load. Using such a structure, an output peak voltage of 3.2 V and the average current density 0.15 μA cm^{-2} had been demonstrated.

The demonstrated NG has a number of advantages over the NGs based on vertically or laterally aliened nanowire arrays. First, the NG uses flexible fibers so that it has the potential to be integrated with fabric for smart clothes. Second, the NG does not need to be protected by a thick polymer layer, which usually damps the magnitude of the mechanical triggering, thus, the output voltage is substantially high. Lastly, the design relies on air pressure, so that it can work in a non-contact mode on all of the available surface area, which can also be as three-dimensional sensor in the cases of rotating tire, flowing air/liquid and even in blood vessel. The pressure driven NG in a syringe shows its potential to harvest energy in a blood vessel, gas pipe and oil pipe, as long as there is a fluctuation in pressure (or turbulence). The energy generated can be used to monitor the status and operation of the fluid/gas. The heart pulse driven NG can serve as ultrasensitive sensor for monitoring the human heart behavior, which may possibly serve for medical diagnostics.

References for Chapter 9

[1] Y. Qin, X. D. Wang, Z. L. Wang, *Nature* **451**, 809 (2008)
[2] Y.F. Gao, Z.L. Wang, *Nano Lett.* **7**, 2499 (2007).
[3] P.X. Gao, J.H. Song, J. Liu, Z.L. Wang, *Adv. Mater.* **19**, 67 (2007).
[4] Z.L. Wang, J.H. Song, *Science* **312**, 242 (2006).
[5] Z.T. Li, Z.L. Wang, *Adv. Mater.* 23, 84 (2011).
[6] J. Hong, J. Bae, Z.L. Wang, R. Snyder, *Nanotechnology* **20**, 085609 (2009).
[7] R. Yang, Y. Qin, L. Dai, Z.L. Wang. *Nat.Nanotechnol.* **4**, 34 (2009).
[8] A.M. Dart, B.A. Kingwell, *J. Am. Coll.Cardiol.* **37**, 0735 (2001).
[9] J.J. Shu, Y. Sun, *Complement. Ther. Med.* **15**, 190 (2007).
[10] A. Mahmud, J. Feely, *Hypertension* **41**, 183 (2003).
[11] M.F.ORourke, A. Pauca, X.J. Jiang, *Br. J. Clin. Pharmacol*. **51**, 507 (2001).

Chapter 10

Hybrid cells for harvesting multi-types of energies

Our living environment has an abundance of energies in the forms of light, thermal, mechanical (such as vibration, sonic wave, wind and hydraulic), magnetic, chemical and biological. Harvesting these types of energies is of critical importance for long-term energy needs and sustainable development of the world. Over the years, rationally designed materials and technologies have been developed for converting solar and mechanical energies into electricity. Photovoltaic relies on approaches such as inorganic pn junctions [1], organic thin films [2, 3] and organic-inorganic heterojunctions [4, 5]. Mechanical energy generators have been designed based on principles of electromagnetic induction and piezoelectric effect [6, 7]. These existing approaches are developed as independent technologies and entities that are designed based on drastically different physical principles and diverse engineering approaches to uniquely harvest a particularly type of energy. A solar cell works only under sufficient light illumination; a mechanical energy generator is applicable if there is significant mechanical movement/vibration. Innovative approaches have to be developed for conjunctional harvesting of multiple types of energies using an integrated structure/material so that the energy resources can be effectively and complimentary utilized whenever and wherever one or all of them are available. This chapter is to introduce a few approaches that we have developed for simultaneously harvesting solar, mechanical and chemical energies.

At a small scale, the development of a wireless self-powered system [8] that harvests its operating energy from the environment is of great importance and an attractive proposition for sensing, personal electronic, and defense technologies. Recently, harvesting multiple type energies using a single device has been a new trend in energy technologies. The first multimode energy harvester has been demonstrated for simultaneously harvesting solar and mechanical energies [9]. Recently, the hybrid cell has been developed for concurrently harvesting biochemical and mechanical energies for in-vivo applications [10]. This multimode energy harvester has the potential of fully utilize the energy in the environment under which the devices will be operating.

10.1 Hybrid cell for harvesting solar and mechanical energy

`The first prototype of the nanowire-based hybrid cell demonstrated to harvest both solar and mechanical energies is using dye sensitized solar cell (DSSC) [11, 12] and piezoelectric nanogenerator [13]. Using aligned ZnO nanowire arrays grown on surfaces of a flat substrate, a dye-sensitized solar cell is integrated with a piezoelectric nanogenerator. The former harvests solar energy irradiating on the top, and the latter harvests ultrasonic wave energy from the surrounding. The two energy harvesting approaches can work simultaneously or individually, and they can be integrated in parallel and serial for raising the output current and voltage, respectively, as well as power.

In this section, we report an innovative approach that convolutes a solid state dye sensitized solar cell and an ultrasonic wave driven piezoelectric nanogenerator into a single compacted structure for concurrently harvesting solar and mechanical energies. The structure is fabricated based on vertical ZnO nanowire arrays with the introduction of solid electrolyte and metal coating. Under a light illumination of a simulated sun emission (100 mW/cm^2), the optimum power is enhanced by 6% after incooperating the contribution made by the nanogenerator. This research sets the platform toward multi-mode energy harvesting as practical power sources.

10.1.1 Structure design

The design of the compacted hybrid cell (CHC) was to convolute the roles played by the nanowire arrays to simultaneously perform their functionalities in a nanogenerator and a DSSC [14]. The main frame structure is made of two sets of ZnO nanowire arrays that are placed teeth-to-teeth (Figure. 10.1a),

as previously demonstrated for the fiber based nanogenerator (see Chapter 9). The DSSC follows the template offered by the nanowire arrays at the top, which is finally coated with a layer of metal for serving as the electrode for the nanogenerator, and the nanowire array at the bottom acts as piezoelectric structure for converting mechanical energy into electricity. The solar illuminates the device from the top, and the ultrasonic wave[16] is applied from the bottom.

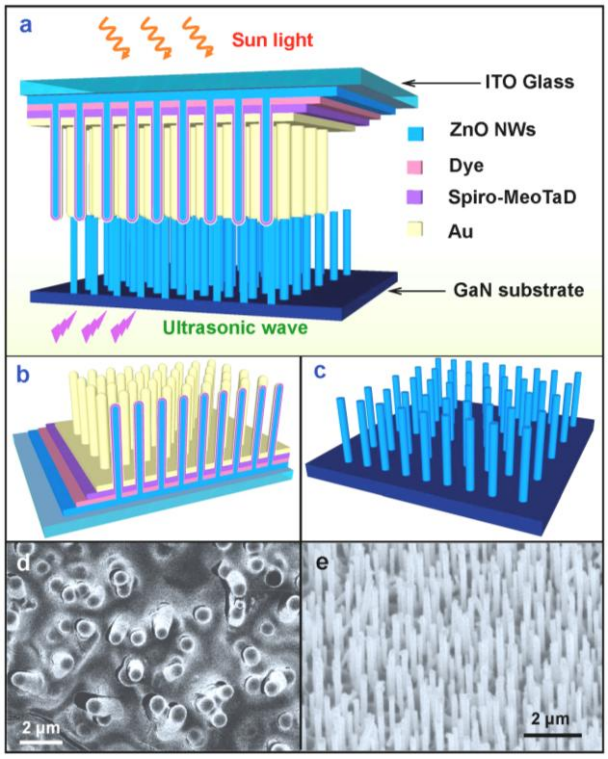

Figure 10.1. Design of the compacted hybrid cell (CHC) structure composed of dye sensitized solar cell (SC) and nanogenerator (NG) (A) Schematic illustration of a CHC, which is shined by sunlight from the top and excited by ultrasonic wave from the bottom. The ITO layer on the DSSC part and GaN substrate are defined as the cathode and anode of the CHC, respectively. (B) Schematic illustration of a solid state DSSC. (C) Schematic illustration of a vertical aligned ZnO nanowire array grown on GaN substrate. (D) Top view SEM image of the DSSC. (E) SEM image of the ZnO nanowire array through the high temperature vapor deposition method for the NG [14].

To fabricate the solid state DSSC, the vertically aligned ZnO nanowires (NWs) were grown on an ITO-coated glass substrate (CB-40IN-0107, 4-8Ω, Delta Technologies, Ltd.) through a hydrothermal method. The substrate was first cleaned by standard acetone/ethanol/IPA/Di water sonication and a thin film of ZnO with 200 nm thickness was deposited by magnetron RF sputter. Then, the ZnO NWs were synthesized by floating the substrate on the nutrient solution surface, which is composed of 5 mM 1 to 1 ration of $Zn(NO_3)_2$ and hexamethylenetetramine at 80℃ for 24h. After rinsed with Acetone, the NWs were immersed in a 0.5mmol L^{-1}sensitized solution of $(Bu_4N)_2Ru(dcbpyH)_2(NCS)_2$ (N719 dye) in ethanol for 1h for dye loading. Then an amorphous organic hole-transport material 2,2',7,7' –tetrakis(N,N-di-p-methoxyphenyl-amine) 9,9' –spirobifluorene (OMeTAD) was spun on the dye-sensitized ZnO NWs with a 2000rpm for 60s and baked at 100℃ to get rid of the organic solution. As shown schematically in Figure 10.1b, a cone shape surface was thus created. A continuous gold (Au) thin film (60 nm in thickness) coating resulted in the formation of a cone shape electrode as required for the NG to be described next. Figure 10.1d shows the scanning electron microscopy (SEM) imaging of cone shape surface in which the space between the cones was 1-2 μm in width.

For NG fabrication, ZnO NWs (Figure 10.1c) used for the NG were grown on a GaN (0001) surface using the high-temperature vapor deposition process to achieve uniform polarity. The nanowires were ~2-3 μm in length and the interspacing between the nanowires was 400-700 nm. By stacking the two sets of nanowire arrays interdigitatively face-to-face, the Au-coated cone shape electrode on the top served as the "zig-zag" electrode for mechanically triggering the nanowires located at the bottom (Figure 10.1a). This is a functional nanogenerator to be driven by ultrasonic wave.

The "convolution" of the DSSC and NG in serial to form a CHC is presented in Figure 10.2a. Here ITO serves as the cathode while silver (Ag) paste in contact with GaN serves as the anode in this

configuration. After connecting to output wires, the entire CHC was sealed and packaged by epoxy resin to prevent infiltration of any liquid except the window of DSSC.

10.1.2. Working principle

The working principle of the CHC is presented by the electron energy band diagram (Figure 10.2b). The electrons were promoted by piezoelectric potential and photovoltaic potential consecutively through the two devices [9, 14]. The maximum output voltage achievable is the difference between Fermi level of the ZnO NWs in the DSSC ($E_{F,\ ZnO\text{-}SC}$) and that of the ZnO NWs in the NG ($E_{F,\ ZnO\text{-}NG}$). It's a summation of the output voltages of the NG and DSSC. In the NG section, the gap between the Fermi level of the ZnO NWs ($E_{F,\ ZnO\text{-}NG}$) and that of the Au determined the maximum voltage output of the NG (V_{NG}). The Au-ZnO junction forms a Schottky contact[24] because Au has a work function of 4.8 eV that is greater than the electron affinity of ZnO (4.5eV), which serves as a "gate" that blocks the back flow of electrons. When the Au electrode slowly pushed a NW like an AFM tip[1], a strain field was created across the NW width, with the outer surface in tensile strain and the inner surface in compressive strain. The piezoelectric potential at the compressive side of the nanowire sets the Schottky contact as forward biased and drives the electrons to across the Au-ZnO junction. Through an electron-transfer process, these charge carriers continue transport in the solid state electrolyte into the DSSC. In the DSSC section of Figure 10.2b, the maximum voltage output (V_{SC}) is dictated by the difference between the ZnO's Fermi level ($E_{F,\ ZnO\text{-}SC}$) and the electrochemical potential of the electrolyte. Visible-light absorption by the dye sensitizer excites electron transfer to the conduction band of ZnO. The electron injection from the excited sensitizer into ZnO is followed by regeneration of the dye sensitizer by the electron from OMeTAD. The electrons in the conduction-band of ZnO and the holes in the electrolyte are separated and subsequently transported to the contact electrodes.

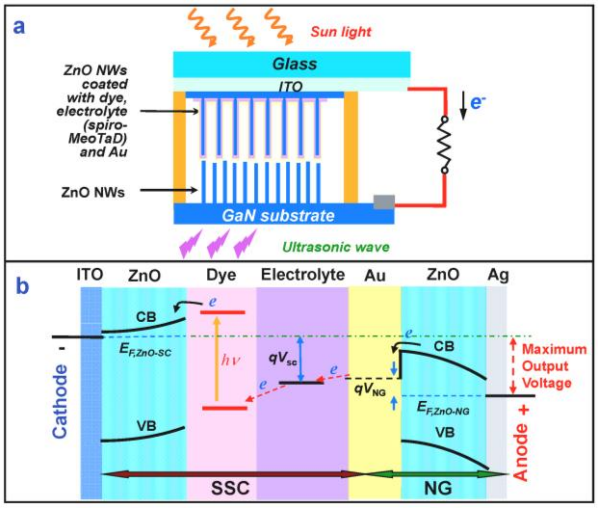

Figure 10.2. Design and physical principle of the CHC. (A) Schematic structure of a CHC. (B) Electron energy band diagram of the CHC, showing that the maximum output voltage is a sum of those produced by DSSC and NG. The abbreviations are: conduction band (CB), valence band (VB), and Fermi level (E_F) [9, 14].

10.1.3. Characterization of output

Both DSSC and NG units of the CHC can work independently and conjunctionally. The CHC was characterized by affixing it on the water surface in an ultrasonic generator cavity with the transparent DSSC side facing sunlight source and the NG side in direct contact the water underneath, where an ultrasonic generator with a frequency of ~41 kHz was applied from the bottom side (Figure 10.1a). J-V curves were recorded for the CHC, DSSC and NG, respectively. The short circuit current was measured by serially connecting the CHC to a DS345 30MHz synthesized function generator (Stanford Research Systems) with a resistance of 50 Ω sweeping from -1 to 1V as an external load. The current signal was using a DL 1211 preamplifier (DL instruments). All of the signals were converted through a BNC-2120 analogue-to-digital converter (National Instruments) and recorded by a computer. The photovoltaic performance of the DSSC for CHC was first characterized under simulated sunlight illumination (AM 1.5G simulated sun light 300 W model 91160, Newport) without applying ultrasonic wave. The open circuit voltage (U_{OC}-SC) was 0.42 V and the short circuit current density (J_{SC}-SC) was 0.25 $mAcm^{-2}$

(Figure 10.3a). The fill factor of the DSSC reached 30.6% corresponding to an overall energy conversion efficiency of 0.03%, which is comparable to that of the ZnO based solid state DSSC.

The NG was characterized by introducing ultrasonic waves through the water media without sunlight illumination; the corresponding J-V curve showed that the U_{OC}-NG was ~0.019 V and the I_{NG} was ~0.3 pA cm^{-2} (the left inset of Figure 10.3a). A J – V curve of the NG (Figure 10.4a) was recorded when the sunlight was turned on and off. The corresponding Uoc-NG showed no change, indicating that there was no contribution from the SC to the NG when only NG was being characterized. Furthermore, An I-V curve of the NG was also recorded at near-zero-point region when the device was in dark condition without applying ultrasonic waves. As shown in Figure 10.4b, the curve passed right across the zero point. The data prove that the DSSC and NG units in the CHC can work independently when only one type of energy source is available. ZnO based solid state DSSC was purposely chosen because the output of the DSSC is comparable to that of NG. But it can be largely improved by using TiO_2 based solid state DSSC.

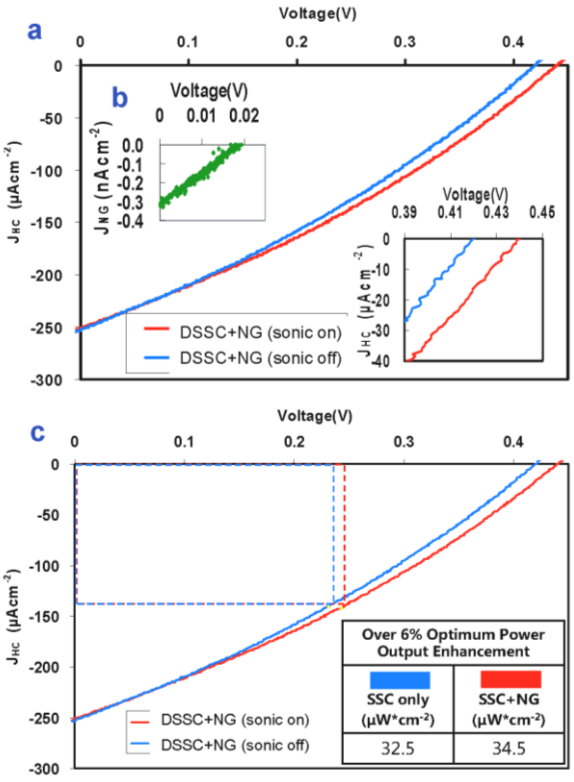

Figure 10.3. Performance of the CHC. (A) A comparison of J-V characteristics of a CHC when illuminated by simulated sunlight with (red curve) and without (blue curve) turning on the ultrasonic wave excitation. Inset is an expanded output of the open circuit voltage U_{OC} points around the axial cross point, showing the increment of U_{OC} for ~19 mV after turning on ultrasonic waves. (B) J-V characteristic of the NG when subjected to ultrasonic wave's excitation but with sunlight off. (C) A comparison in power output J-V characteristics of a CHC. The rectangle area is the optimal power output for the CHC.

To demonstrate the technological feasibility of the CHC for simultaneously harvesting of solar and mechanical energies, we measured the J-V curve on CHC under different condition. When the full sunlight source was on and the ultrasonic wave source was off, the CHC exhibited a U_{OC} of 0.415 V and J_{SC} of 252 μAcm^{-2} (blue curve in Figure 10.3a). When both the ultrasonic wave and sunlight were turned on, the U_{OC} reached 0.433 V, while the J_{SC} remained at 252 μAcm^{-2} (red curve in Figure 10.3a). The output voltage of the CHC showed a 19 mV difference when turning on and off the ultrasonic wave, as shown by the expanded plot of U_{OC} in the right-hand inset of Figure 10.3a, which is just the output voltage of the NG when the sunlight was off (Figure 10.3b).

In order to further confirm that the increase of U_{OC} is truly coming from the NG unit, another set of J-V characteristic was measured between the cathode and anode of DSSC unit without including the NG unit in the measurement circuit. The performance of the CHC was shown in the J-V curves (Figure 10.4a) with the NG performance in Figure 10.4b. By turning on and off the ultrasonic waves, the J-V curves exhibited almost an identical trace (Figure 5c). Particularly, the U_{OC}-SC remained at the same point, as shown by the expanded plot of U_{OC} in the inset of Figure 10.4c.

To visually see the optimum power output from the J-V curve, the product of current density and voltage was calculated. The area of the rectangle was representing the optimum output power density. By

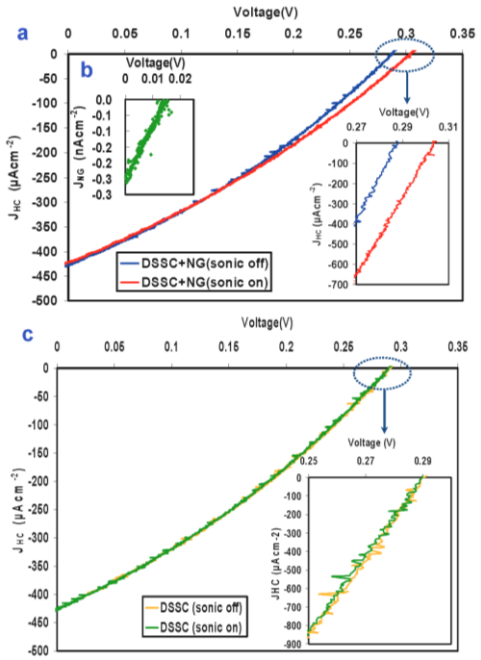

Figure 10.4. Controlled performance of the CHC. (A) J-V characteristics of another CHC when a simulated sunlight was illuminating onto the SC side and the ultrasonic wave was turned on (red curve) and off (blue curve). (B) J-V characteristic of the NG component when subjected to ultrasonic wave excitation but with sunlight off. (C) J-V characteristic of the DSSC, without including the NG unit in the measurement circuit, when illuminated by a simulated sunlight with (green curve) and without (orange curve) turning on ultrasonic waves. Inset is an expanded plot around the U_{OC} points, showing there is almost no change in U_{OC} by turning on ultrasonic waves. The open circuit voltage U_{OC} point was not affected by the ultrasonic wave, simply ruling out the contribution made by the fluctuation in NG resistance to the performance of the SC.

comparing the area difference, we can tell that the CHC enhances the energy harvesting performance than either one of the devices. When only the DSSC component was in operation and under the one full sunlight illumination, the optimum output power density (blue rectangle) was found to be 32.5 μWcm^{-2} at J_{SC} = 140 μAcm^{-2} and U_{OC} = 0.231 V. When both DSSC and NG were simultaneously operating in serial connection, the corresponding output power density was 34.5 μWcm^{-2} at J_{SC} = 141 μAcm^{-2} and U_{OC} = 0.243 V (red rectangle). An increment (ΔP_{HC}) of 2 μWcm^{-2} in power density was thus achieved after turning the ultrasonic wave on, which was over 6% enhancement in optimum power. Therefore, in addition to the open circuit voltage, the CHC successfully added up the total power outputs from both SC and NG.

10.2. Hybrid cell for concurrently harvesting biomechanical and biochemical Energy

Energy harvested from the environment will likely be sufficient for powering nanodevices used for periodic operation, owing to their extremely low power consumption and small sizes. For example, an implantable device that wirelessly communicates the local glucose concentration for diabetes management; or the local temperature for infection monitoring after surgery; or a pressure difference to indicate blockage of fluid flow in the central nervous system and/or blood clotting; can all be foreseen as potential applications that need implantable energy sources. Powering such devices could be accomplished by concurrently harvesting energy from multiple sources within the human body, including mechanical and biochemical energy to augment or even replace batteries. However, powering implantable nanodevices for biosensing using energy scavenging/harvesting technology is rather challenging because the only available energy *in-vivo* is mechanical, biochemical, and possibly electromagnetic energy, whereas thermal energy cannot be harvested due to lack of an adequate temperature gradient, and solar energy is not available for devices implanted inside the body.

In this section, we present a hybrid energy scavenging device for potential *in-vivo* applications. The hybrid device consists of a piezoelectric poly(vinylidene fluoride) nanofiber nanogenerator for harvesting mechanical energy, such as from breathing or from the beat of a heart, and a flexible enzymatic biofuel cell for harvesting the biochemical (glucose/O_2) energy in biofluid, which are the two types of energy available *in-vivo*. The two energy harvesting approaches can work simultaneously or individually, thereby boosting output and lifetime. Using the hybrid device, we demonstrate a 'self-powered' nanosystem by powering a ZnO nanowire UV light sensor.

10.2.1 PVDF based nanogenerator

The NG based on a single ZnO nanowire that is laterally bonded onto a polymer substrate was first demonstrated by our group.[5] Based on a similar mechanism and design, a NG using a single piezoelectric poly(vinylidene fluoride) (PVDF) nanofiber (NF) was reported recently [15]. In our hybrid design we use PVDF nanofibers as the working component for the mechanical energy harvester. Cheng et. al. used near-field electrospinning to synthesize the single PVDF NFs, where the high electric field used to draw the NF was suggested to naturally align the dipoles along the NF long axis. We used conventional electrospinning with the two electrode technique[13] to synthesize and pattern an array of aligned NFs, followed by a post, in-plane poling process (Figure 10.5a-d). PVDF powder (MW 534,000) was purchased from Sigma-Aldrich and used as received. 1.5 g PVDF was dissolved in a mixture of 3 mL DMF (VWR) and 7 mL Acetone (VWR), and heated at 60 °C for 30 min so that the solution is homogeneous. The transparent viscous solution is transferred into a Hamilton 1 mL syringe for electrospinning. A Chemyx Fusion 200 syringe pump and Betran DC High Voltage power supply was used, a voltage of 12 kV was applied to the syringe needle and a feed rate of 50 μL/min was used. The electrospun fibers were collected onto two grounded copper pieces with a 2 cm gap, placed 15 cm away from the needle, and the fibers were electrostatically aligned across the electrode gap.

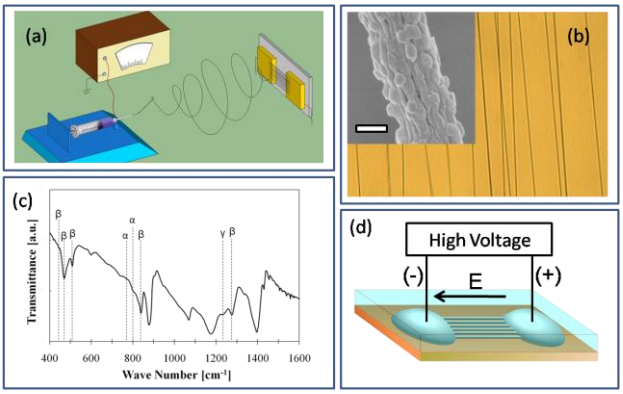

Figure 10.5. (a) Schematic of the electrospinning process to obtain aligned PVDF NFs. (b) Optical image of aligned PVDF NFs on Kapton film and high resolution SEM of NF surface morphology shown in the inset (400 nm). (c) FTIR transmission spectrum of PVDF NFs. (d) Schematic of the high field in-plane poling of PVDF NFs.

A scanning electron microscopy (SEM) image (Figure 10.5b inset) reveals the textured morphology on the NF surface, presumably resulting from the formation of small crystallites. Fourier Transform Infrared Spectroscopy (FTIR) was used to characterize the crystal phases present in the PVDF NFs. The FTIR transmission spectrum of the as-spun PVDF nanofibers is presented in Figure 10.7c. A mixture of the polar β phase and the non-polar α and γ phases was indexed[14]. The random dipole orientation of the polar β phase was oriented by encasing the device in PDMS and performing high-field (~ 0.2 MV/cm) in-plane poling (Figure 10.5d) for ~ 15 min.

The working principle of the PVDF NG is based on the insulating property of the PVDF NF and the creation of an inner piezoelectric field during applied tensile strain. As the device is deformed under alternating compressive and tensile force (Figure 10.6c-d), the NF acts like a “capacitor” and “charge pump”, which drives a flow of electrons back and forth through the external circuit. This charging and discharging process results in an a.c. power source.

For fabricating the nanogenerator, a 1 cm × 2 cm × 30 μm Kapton@Dupont thin film was used as the supporting substrate. To form two electrodes a 50 nm thick layer of Au was deposited onto the Kapton substrate, leaving a 1 mm uncoated gap in the middle by using a mask. The electrospun fibers were carefully transferred across the Au electrodes and electrically bonded using silver paint (Ted Pella). A 0.5 mm layer of PDMS was deposited over the device for dielectric protection and biocompatibility. The final device was dipped into paraffin oil, and 20 kV was applied between the two electrodes for 15 minutes. After poling, the electrodes were shorted for over 12 hrs.

The strain rate dependence on the open-loop voltage and short-circuit current produced by a PVDF NG undergoing cyclic mechanical loading is presented in Figure 10.6a-b. The induced strain was fixed at ~ 0.05 % and applied over 0.06 s, 0.04 s, and 0.03 s. By increasing the strain rate over this range, the open loop voltage increased from 15 mV to 20 mV and the short circuit current increased from 0.2 nA to 0.3 nA, which is consistent with piezoelectric theory.[15] The output voltage is dictated by individual nanowire, while the output current is the sum of those from all of the active nanowires. The output of the PVDF NG could be improved by replacing PDMS with a material having a higher break-down voltage, so that higher poling fields could be applied to obtain a greater remnant polarization.[16,17] In addition, hundreds of NFs could potentially be integrated together and connected in series and/or parallel to further improve the power output.

10.2.2 Harvesting Biochemical Energy by Biofuel Cell

An enzymatic BFC was used to convert the chemical energy of glucose and oxygen in biofluid into electricity [16]. The BFC configuration used in this study is illustrated in Figure 10.7c. The electrodes were patterned onto Kapton film and coated with multi-wall carbon nanotubes (MWCNTs), followed by immobilization of glucose oxidase (GOx) and laccase to form the anode and cathode, respectively (see Experimental Methods for details). In addition to immobilizing the enzymes onto the electrodes, it has been shown that CNTs help promote the electron transfer between the enzymes and the electrodes [17, 18, 19]. The operating principle of the BFC is illustrated in Figure 10.7d. When the device is in contact with a biofluid that contains glucose (such as blood), the corresponding chemical processes occurring at the two electrodes is [20]: glucose is electro oxidized to gluconolactone at the anode: $Glucose \xrightarrow{GOx} Gluconolactone + 2H^+ + 2e^-$, and dissolved O_2 is electro reduced to water at the cathode:

$$\frac{1}{2}O_2 + 2H^+ + 2e^- \xrightarrow{Laccase} H_2O.$$

Glucose oxidase (GOx, from Aspergillus niger, type X-S) and laccase powder (from Trametes versicolor) were purchased from Sigma-Aldrich, multi-wall carbon nanotubes from Hanhwa Nanotech (diameter 3~9nm, purity>95%) and phosphate buffer solution (PBS, pH 7.0) from Fluka. All chemicals were used as received. Carbon nanotubes were dissolved in ethanol and sonicated for 1 h to form 2 g/L dispersion. A 4 g/L solution of GOx in phosphate buffer solution and a 4 g/L solution of laccase in phosphate buffer solution was prepared. The Kapton film with Au electrodes was prepared as described and then bleached and rinsed with deionized water before use. 2 μL of CNT dispersion was deposited onto both electrodes, and was rinsed with deionized water after drying. 2μL GOx solution was then deposited onto one of the CNT/Au electrodes to form the anode and 2 μL of laccase solution was deposited onto the other to form the cathode. The device was then stored under 4 °C for at least 4 hrs before use. Prior to use, the electrodes were rinsed in

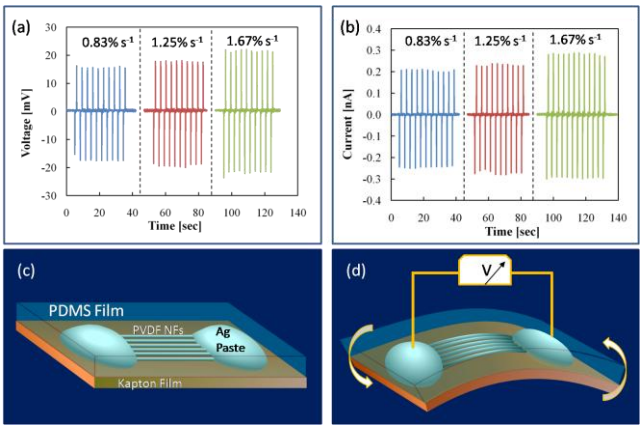

Figure 10.6. Open-loop voltage (a) and short-circuit current of a PVDF NG as a function of strain rate with a maximum strain of ~ 0.05 %. (c) The PVDF NF lies on a Kapton substrate, with both ends bonded with silver paste and the entire device encapsulated with PDMS. (d) Mechanical bending of the substrate creates tensile strain and a corresponding piezoelectric field along the fiber that drives the electrons through an external load back and forth following the cycled mechanical action.

pure PBS.

The open-loop voltage and short-circuit current produced by the BFC operating in Phosphate Buffer Solution (PBS, pH 7.0) with glucose concentrations of 0.5 mM, 5 mM, and 50 mM is presented in Figures 10.7a-b. Both the current and the voltage were found to increase with increasing glucose concentration. Human blood has a glucose concentration that fluctuates between ~ 4 to 6 mM and has a pH of 7.35-7.45.[9] At 5 mM the open loop voltage was found to be 50 mV and a short-circuit current of 11 nA. The power density of the BFC depends on load matching and was found to have a maximum at ~ 10 MΩ with a corresponding power density of ~ 2.2 nW/cm^2 and a current density of ~ 58 nA/cm^2 (see Supporting Information).

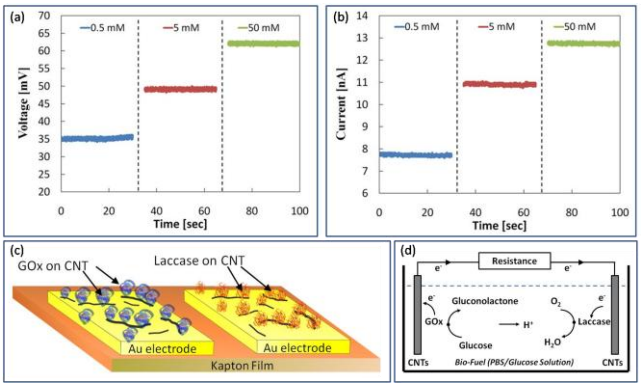

Figure 10.7. Open-loop voltage (a) and short-circuit current (b) of the BFC as a function of glucose concentration in PBS solution. (c) Schematic illustration of the fabricated BFC device. (d) Simplified schematic of the BFC operating mechanism.

The highest theoretical voltage that may be obtained from a GOx/laccase based BFC is dictated by thermodynamics and is ~ 1 V.[9] To obtain this voltage various factors need to be optimized, but the most important one is the enzyme surface interactions. By cross-linking or "wiring" the immobilized redox enzymes to a redox hydrogel, the output of the BFC can be further optimized in the future.[21-23] In addition, multiple BFCs could be integrated together to boost power output.

10.2.3. Hybrid Biochemical and Biomechanical Nanogenerator

The independent and integrated operation of the PVDF NG, the BFC, and the hybrid BFC-NG, is presented in Figure 10.8a-c [21]. To integrate the AC voltage of the PVDF NG with the DC voltage of the BFC, a simple RC high pass filter (Figure 10.8b) was used, which effectively blocks the DC voltage of the BFC in one direction while passing the AC voltage of the NG. By integrating the two devices, the peak voltage was nearly doubled from ~ 50 mV to ~ 95 mV. Furthermore, the PDMS packaging of the PVDF NG allows for operation inside biofluid and *in-vivo* environments. In addition, using a flexible Kapton film substrate for the BFC permits the devices to be integrated back-to-back as conceptually illustrated in Figure 10.8d. It is important to point out that our goal here is not to maximize the output of BFC, instead we keep the output of the BFC to be in a reasonable range so that the hybridization of the BFC and NG can be clearly illustrated.

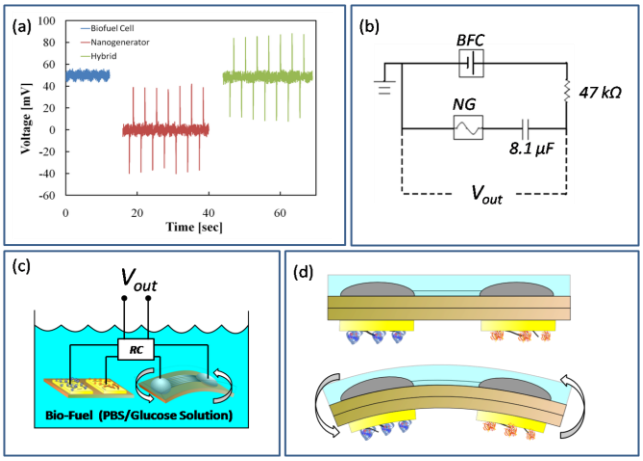

Figure 10.8. (a) Open-loop voltage of the independent and combined operation of the BFC and PVDF NG. (b) Circuit diagram used for integrated of the hybrid BFC-NG device. Note, with considering the inner resistance of the NG, the time required to charge the capacitor is much longer than the period at which the strain was applied to the NG, so that the output V is a sum of those from BFC and NG. (c) Schematic of hybrid device integration. (d) Conceptual design of a BFC-NG hybrid device.

The power output of the hybrid nanogenerator is the sum of the BFC and NG. The voltage output of the BFC is V_{BFC} and the output voltage of the ac NG is $\pm V_{NG}$. Considering the infinitely large resistance of the PVDF nanofiber, the output voltage of the NG component is $\pm V_{NG}$ even with the presence of a load. The inner resistance of the BFC is rather low since it is dictated by electron transfer between the active center of the enzymes and the CNT electrodes. In such a case, the voltage applied to an external load R is $V_{BFC} \pm V_{NG}$, which gives an output power of $(V_{BFC} \pm V_{NG})^2/R$. The average peak output power for each cycle of the mechanical action is $[(V_{BFC} + V_{NG})^2/R + (V_{BFC} - V_{NG})^2/R]/2 = (V_{BFC})^2/R + (V_{NG})^2/R$. In addition, methods can eventually be developed for rectification of the a.c. NG output to obtain a d.c. signal and integration with the d.c. output of the BFC to give an overall enhanced d.c. output.

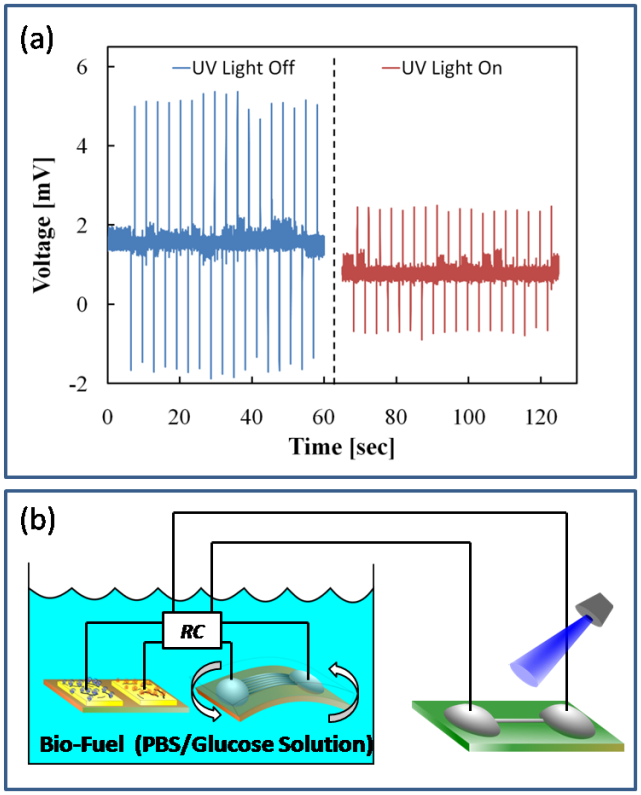

Figure 10.9 Integration of the hybrid BFC-NG device with a UV nanosensor to demonstrate 'self-powered' nanosystem (a) Voltage drop across the ZnO NW UV light sensor when UV light is off and on. For illustration purposes, only stabilized signals are displayed. (b) Schematic illustration of the self-powered hybrid nanosystem.

10.2.4. Powering a nanosensor by hybrid cell

The hybrid BFC-NG was also used to drive the operation of a ZnO nanowire based UV light sensor (Figure 10.9b). When there was no UV light, the resistance of the ZnO nanowire was ~ 7 MΩ (see Supporting Information) and the corresponding peak voltage drop on the nanosensor was ~ 5 mV, as shown in Figure 10.9a. Upon irradiation with UV light, the nanowire resistance dropped to ~ 800 kΩ and the peak voltage drop across the nanowire device was reduced to ~ 2.5 mV. This demonstrates the potential of a fully 'self-powered' nanosystem for *in-vivo* applications.

References for Chapter 10

[1] W.G. Pfann, W.J. Van Roosbroeck, *Appl. Phys.* **25**, 1422 (1954).
[2] G. Yu, J. Gao, J.C. Hummelen, F. Wudl, A.J. Heeger, *Science* **270**, 1789 (1995).
[3] J.J.M. Halls, C.A. Walsh, N.C. Greenham, E.A. Marseglia, R.H. Friend, S.C. Moratti, A.B. Holmes, *Nature* **376**, 498 (1995).
[4] B. O'Regan, M.A. Gr ätzel, *Nature* **353**, 737 (1991).
[5] W.U. Huynh, J.J. Dittmer, A.P. Alivisatos, *Science* **295,** 2425 (2002).
[6] J.A. Paradiso, T. Starner, *IEEE Perv. Comp.* **4**, 18 (2005).
[7] Z.L. Wang, J.H. Song, *Science* **312**, 242 (2006).
[8] Z.L. Wang, *Sci. Am.* **298**, 82 (2008).

[9] C. Xu, X.D. Wang, Z.L. Wang, *JACS* **131**, 5866 (2009).
[10] B.J. Hansen, Y. Liu, R.S. Yang, Z.L. Wang, *ACS Nano*, 2010, Online.
[11] B. Oregan, M. Gratzel, *Nature* **353**, 737 (1991).
[12] M. Law, L.E. Greene, J.C. Johnson, R. Saykally, P.D. Yang, *Nat. Mater.* **4**, 455 (2005).
[13] X.D. Wang, J.H. Song, J. Liu, Z.L. Wang, *Science* **316**, 102 (2007).
[14] C. Xu, Z.L. Wang*, *Adv. Mater.* **23**, 873 (2011).
[15] C. Chang, V.H. Tran, J. Wang, Y. Fuh, L. Lin, *Nano Letters* **10**, 726 (2010).
[16] C. Pan, H. Wu, C. Wang, B. Wang, L. Zhang, Z. Cheng, P. Hu, W. Pan, Z. Zhou, X. Yang, J. Zhu, *Adv. Mat.* **20**, 1644 (2008).
[17] A. Guiseppi-Elie, C. Lei, R.H. Baughman, *Nanotechnology* **13**, 559 (2002).
[18] J.H.T. Luong, S. Hrapovic, D. Wang, F. Bensebaa, B. Simard, *Electroanalysis* **16**, 132 (2004).
[19] C. Cai, J. Chen, *Analytical Biochemistry* **332**, 75 (2004).
[20] A. Heller, *PCCP* **6**, 209 (2004).
[21] B.J. Hansen^{+}, Y. Liu^{+}, R.S. Yang, Z.L. Wang, *ACS Nano*, **4**, 3647 (2010).

Chapter 11

Self-powered sensors and systems

The emerging development of nanotechnology today moves from inventing individual components to the integrated system that can perform one or more designed function by integrating a group of nanodevices with modern microelectronics technologies. A general integrated system is a package of components such as sensors, transducers, data processor, control unit, and communication system. As the size of the devices shrinks to the nano or micro scale, the power consumption also drops to a much lower level. Take a commercial Bluetooth headset as an example, its power consumption is just around several microwatts (data transmission rate ~500 kbits/s; power consumption 10 nW/bit). The power consumption of a nanodevice would be even smaller. At such a low power consumption level, it is entirely possible to drive the devices by scavenging energy from the sources in the environment such as gentle airflow, vibration, sonic wave, solar, chemical, and/or thermal energy.

We have been developing this "self-powered nanotechnology" since 2005, aiming at building a self-powered system that operates independently, sustainably and wirelessly by itself without using a battery [1, 2]. Self-powered systems will play a very important role in the independent, sustainable, maintenance-free operations of implantable biosensors, remote and mobile environmental sensors, nanorobotics, micro-electromechanical systems, and even portable/wearable personal electronics [3]. Mechanical energy in our living environment, for example, is abundant but irregular energy with variable frequency (mostly low frequencies) and magnitude, such as airflow, noises, human activity, which largely limits the application of the traditional resonator based energy harvester that works at specific frequencies. A rational design is required to tolerate the variable environment. The NG using the piezoelectric effect of ZnO nanowires applies to such purposes.

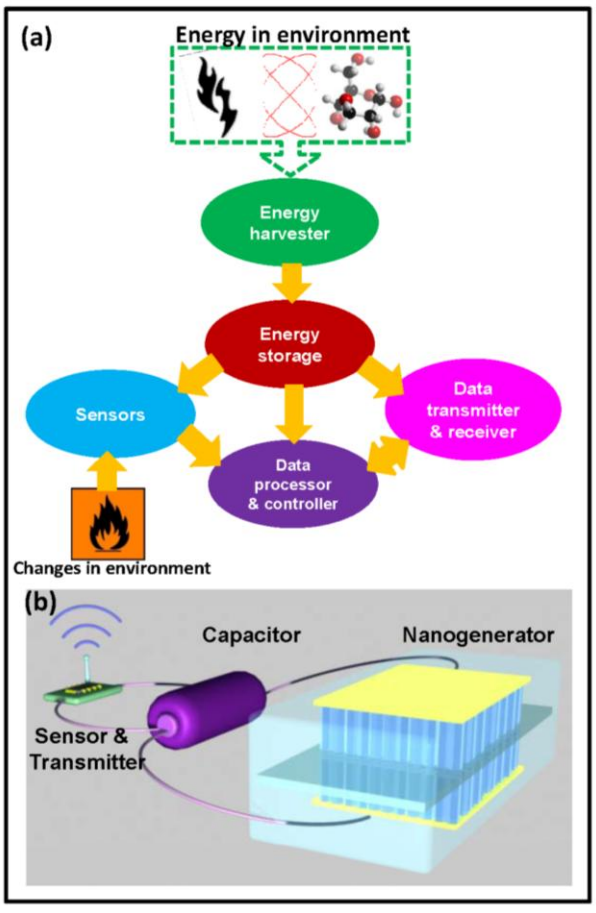

Figure 11.1. Schematic diagram of the integrated self-powered system. (a) An integrated system can be divided into five modules: energy harvester, energy storage, sensors, data processor & controller, and data transmitter & receiver. (b) The prototype of an integrated self-powered system by using a nanogenerator as the energy harvester.

11.1 Concept of self-powered system

An integrated self-powered system can be simply depicted in Figure 11.1a [4]. The power source in this system includes the energy harvesting and storage modules. The harvester scavenges some kind of energy (solar, thermal, mechanical and/or chemical) from the environment and stores it in the energy storage module. Thus the collected power is used to drive the other parts of the system. The sensors detect the changes in the environment, while the data processor & controller analyze the information. Then, the signal is sent out by the data transmitter, and simultaneously the response is received. In this paper, we demonstrate a

prototype self-powered system that is made of a NG for harvesting mechanical energy, a low-loss full-wave bridge rectifier, a capacitor for storing the energy, an infrared photodetector and a wireless data transmitter (as shown schematically in Fig. 11.1b). The successful operation of this system is the first proof of utilizing a NG for a self–powered wireless sensor network.

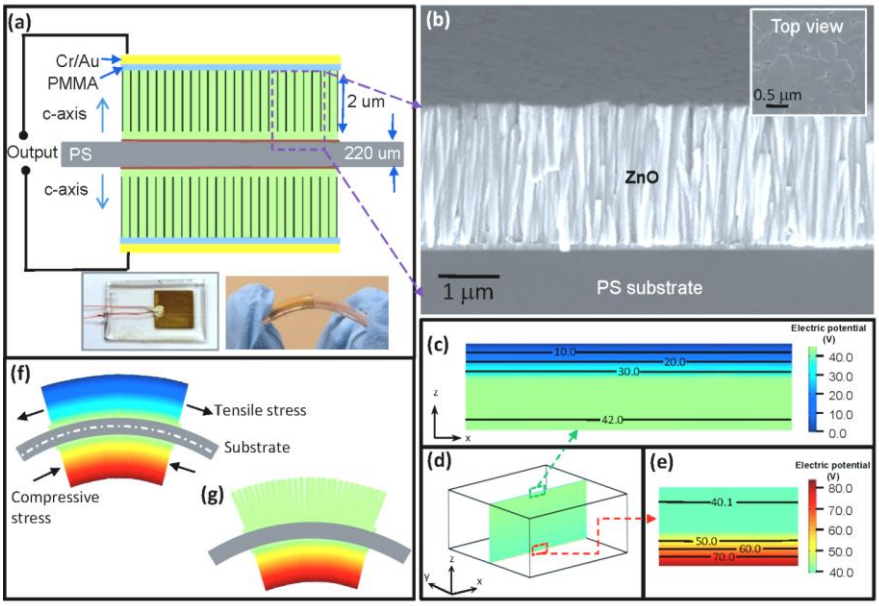

Figure 11.2. Nanogenerator fabrication and its working mechanism. (a) Fabrication process of the nanogenerator. The lower right parts are photos of a fabricated nanogenerator after packaging. The bending of the nanogenerator shows its good mechanical flexibility. (b) Cross section SEM image of the as-grown nanowire textured film on the substrate. The insert is the top view of the nanowire film. (d) The model for the simulation of the nanogenerator working mechanism. It was a triple-layer rectangular box, containing the flexible substrate and the ZnO films on the top and bottom surface. The calculated local potentials across the top electrode and bottom electrode are displayed in (c) and (e), respectively. (f) Distribution of the piezopotential in the designed structure if the ZnO NWs form a densily packed solid film that behaves like a continuous medium. The white dashed line in the substrate indicates the strain neutral plane. (g) Distribution of piezopotential in the designed structure if the ZnO NWs form a densily packed film but with a possibility of small gaps or inter-wire sliding, so that the NWs on the stretched side of the substrate may contribute nothing to the output voltage, while the NWs on the compressed side always creates a piezopotential drop.

The NG relies on the piezoelectric potential generated in the nanowire as it is being dynamically strained under an extremely small force; a transient flow of electrons in an external load as driven by the piezopotential to balance the Fermi levels at the two contacts is the fundamental mechanism of the NG. The power generated by a NG may not be sufficient to continuously drive a device, but an accumulation of charges generated over a period of time is sufficient to drive the device to work for a few seconds. This is very suitable for applications in the fields of sensing, infrastructure monitoring and sensor networks. A common characteristic for these applications is that there are so many sensors in the system, and each sensor is expected to work independently and wirelessly, but all of them will be linked through a network/internet. Each sensor is not required to work continuously and simultaneously, instead, it will have a "blinking" working mode with a standby status and active status. The standby mode is normally longer, while the active mode is shorter. The energy scavenged and stored during the standby status can be used to drive it in the active mode. This means that these sensors periodically sample from their working environment and transmit data within a fraction of second. We can use the NG to harvest energy from the environment and store most of the energy when the sensor is in the standby mode. Then the collected energy will be used to trigger the sensor, process and transmit the data in the active mode.

11.2. The design of nanogenerator

The NG used in the integrated system is a free-standing cantilever beam made of a five-layer structure using densely packed ZnO nanowire textured films [4]. The NG was fabricated on a flexible polyester (PS) substrate (Dura-Lar™, 220 μm in thickness), as shown in Figure 11.2a. First, a 5 nm thick Cr adhesion layer followed by a 50 nm thick ZnO seed layer were deposited at the selected rectangular region of 1 cm × 1 cm on the top and bottom surfaces of the substrate. The ZnO seed layer is for growing densely packed ZnO nanowires via a wet chemical method.[22, 23] The nutrient solution we used in the chemical growth process of ZnO densely packed nanowires textured films was an equal molar aqueous solution of $Zn(NO_3)_2$ $6H_2O$ and hexamethylenetetramine (HMTA), and the concentration was 0.1 M. The nanowire films at the top and bottom surfaces were grown sequentially by placing the substrate at the top of the nutrient solution with one face down. Because of the surface tension, the substrate floated on the solution surface. Growth of ZnO nanowires was carried out in a mechanical convection oven (model Yamato DKN400, Santa Clara, CA) at 95˚C for 5 hours. Figure 11.2b is a scanning electron microscope (SEM) image of the as-grown ZnO nanowires on the substrate. The dimensions of the nanowires were about 150 nm in diameter and 2 μm in length. From the cross section view, we can see that the ZnO nanowires were grown vertically from the substrate, with a high packing density, and the bottoms of these nanowires were bonded through the ZnO seed layer. The insert of Figure 11.2b is the top view of the as-grown ZnO nanowires. Tweezers were used to scratch the top surfaces of these nanowires to establish that the top surfaces of these nanowires were also bonded together tightly in a uniform film. Therefore, the entire ZnO structure could be regarded as a textured film[24] that consisted of fully packed ZnO nanowire arrays between two parallel ZnO films. According to the growth mechanism, the c-axes for these nanowires were their growth direction, as shown in Figure 11.2a. Then, a thin layer of polymethyl methacrylate (PMMA) (MicroChem 950k A11) was spin coated on both surfaces of the substrate at the speed of 3000 rpm, followed by a Cr/ Au layer deposition on the central rectangular area serving as the electrode of the NG. Finally, the whole device was fully packaged with polydimethylsiloxane (PDMS) to enhance the mechanical robustness and flexibility. The lower right corner of Figure 11.2a is a photo of a fabricated device. The size of the effective working area of the NG was 1 cm×1 cm. Two leads were connected to the top and bottom electrodes, respectively. It must be pointed out that the processing temperature was rather low (< 100 ^{o}C) so that the entire process is adaptable for flexible electronics.

We first calculated the distribution of piezopotential in the nanowire films in order to present its working mechanism. The entire structure of the NG was modeled as a cantilever beam with textured nanowire films on a common substrate. The films on the top and bottom surfaces had uniaxial texturing of [0001], respectively. We calculated the electric potential difference across the top and bottom electrodes when the entire structure was bent. Considering that the ZnO nanowire arrays grown on the substrate were close-packed with top and bottom ends bonded, they were represented by a thin film to simplify the calculation. The device was represented by a rectangular box with a dimension of 500 μm × 500 μm × 224 μm, as shown in Figure 11.2d. It is a triple-layer structure, including two single crystal ZnO thin films (2 μm thick each) on the top and bottom surface of a polymer substrate (220 μm in thickness) (Note the thickness of the electrodes were 100 nm, so they were ignored in the calculation). The material's constants of ZnO used in the calculation are the same as in Ref. 25. The Young's modulus, Poisson ratio and the relative dielectric constants of the polymer substrate were E = 5 GPa, v = 0.33 and k = 3.2, respectively. All of the calculations were carried out by using the COMSOL package. The distribution of the piezoelectric potential was calculated by modeling the device structure as a cantilever beam with its one end being fixed (y = 0 plane in Figure 11.2d) and a periodical transverse force being applied on its top edge at the other end (y = 500 μm plane in Figure 11.2d). The strain distribution in the cantilever was non-uniform. The mean strain in the beam applied in parallel to the substrate along the y-axis (see Fig. 11.2d) was of 0.2%. To represent the metal electrodes in the NG, the top and bottom surfaces of the structure were set as equal potential planes with the bottom one grounded. In the open circuit case, the total charge on the top and bottom surface must be zero. ZnO films were assumed to be

intrinsic without doping. The piezoelectric potential has a large magnitude variation in the ZnO films. For easy visualization of the calculated potential, the local potential across the top (Fig. 11.2c) and bottom (Fig. 11.2e) electrodes of the NG under strain was present, also the potential inside the device is plotted in Fig. 11.2d. From our calculation results, an 83.8 V inductive potential difference across the two electrodes was predicted. Such a potential drop across the top and bottom electrodes is the driving force for the transient flow of electrons in the external load.

There are two scenarios if we consider the fact that the ZnO film is made of densely packed NWs. When the NG is bent, considering the neutral plane of strain is at the central of the substrate, as indicated by white dashed line in Fig. 11.2f, the NW film on the stretched surface of the substrate is subject to a tensile stress, while the one on the compressed surface is under compressive stress. First, if the bonding between the NWs is very strong to form a solid film with considering that the growth direction of the NWs is along c-axis (polar direction for ZnO), a tensile stress perpendicular to the NWs results in a compressive strain along the c-axis direction, thus, creating a piezopotential drop from the roots of the NWs to their top-ends, as shown in Fig. 11.2f. At the same time, a corresponding compressive stress is applied to the NWs on the bottom surface of the substrate, resulting in a tensile strain along the c-axis, thus, the top-ends of the NWs have a higher piezopotential than their roots. Therefore, the piezopotential drops in the top and bottom ZnO films have the same polarity, and they add up constructively. This piezopotential distribution will introduce induced charges in the top and bottom electrodes, and consequently generating the output voltage.

Secondly, in a case that the bonding between the NWs is very weak with the possibility of inter-wire sliding/gaps, no piezoelectric potential would be produced by the film on the top surface of the substrate that is under tensile stress. But, considering the NWs are fully packed and can be squeezed between each other, a piezopotential drop is still created with some degradation by the film at the substrate bottom surface that is subject to a compressive stress (see Fig. 11.2g). Therefore, a potential drop is also expected between the top and bottom electrodes, but with its magnitude drops less than half in comparison to that in the first case. The actual bonding condition among nanowires should be between the two cases discussed above. Also, it is known that the as-grown ZnO nanowires have n-type doping, which can significantly screen the higher piezopotenital side, but leave the lower piezopotential side almost unchanged.[26] Thus, the observed output voltage of the NG will be smaller than the theoretically calculated value due to the reasons list above.

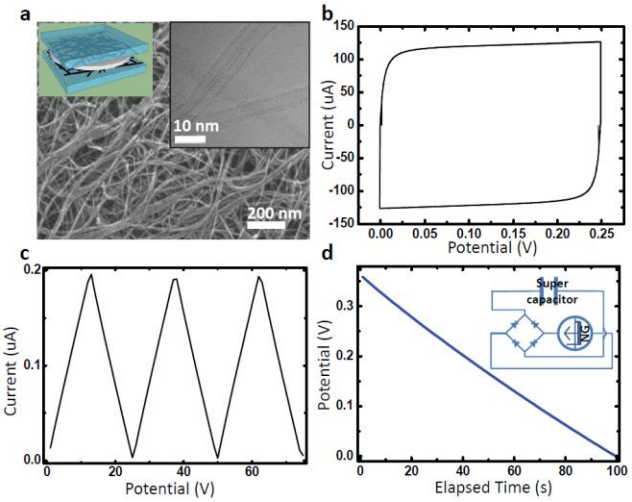

Figure 11.3. Characteristics of multi-walled carbon nanotube based super-capacitor and storage test using nanogenerator. (a) Schematic diagram and SEM/TEM images of carbon nanotube network based super-capacitor. (b) Cyclic voltammetry of a fabricated super-capacitor. The scan range was between 0 and 250 mV with scan rates of 100 mVs^{-1}. (c) Galvanostatic charge-discharge graph of the super-capacitor. (d) Discharging graph of super-capacitor, which was charged by ten-layer integrated nanogenerators for ~1 h.

11.3. Charge storage by supercapacitor

Integration of NGs with energy storage device such as a super-capacitor can be a prototype of a power cell for periodically acetifying sensing devices [5]. During hibernation of the sensor, generated electricity from the NG is able to be stored in super-capacitor. When the sensor needs to be operated, stored energy in super-capacitor/capacitor will supply electric power for detection of environmental polluters. To achieve this, we first fabricated super-capacitor based on multi-walled CNT (MWNT) coated ITO electrodes and PVA/H_3PO_4 electrolyte. Direct spray coating method was applied to make uniformly dispersed MWNT layers on ITO glass substrates (Figure 11.3a). MWNT coated ITO glass substrates served as working and counter electrodes for super-capacitor. PVA/H_3PO_4 polymer like solution was used as electrolyte. Right upper inset in Figure 11.3a shows schematic diagram depicting the structure of super-capacitor fabricated in here. The electrochemical properties of the capacitors in PVA/H_3PO_4 electrolyte solution were investigated using a potentiostat/galvanostat (Princeton Applied Research VersaStat 3F). Figure 11.3b exhibits cyclic voltammetry that shows our device has a good electrochemical stability and the capacitance. The scan range was between 0 and 250 mV with scan rates of 100 mVs^{-1}. The galvanostatic charge–discharge measurement was also conducted to characterize the electrochemical performance of the MWNT-based super-capacitor (Figure 11.3c). To store the generated charge from NGs, a super-capacitor and 10-layer-integrated NGs were connected with rectifying bridge (inset in Figure 11.3d). The generated AC outputs from NGs were rectified into direct-current (DC) signals, which directly resulted in charging process in a super-capacitor.

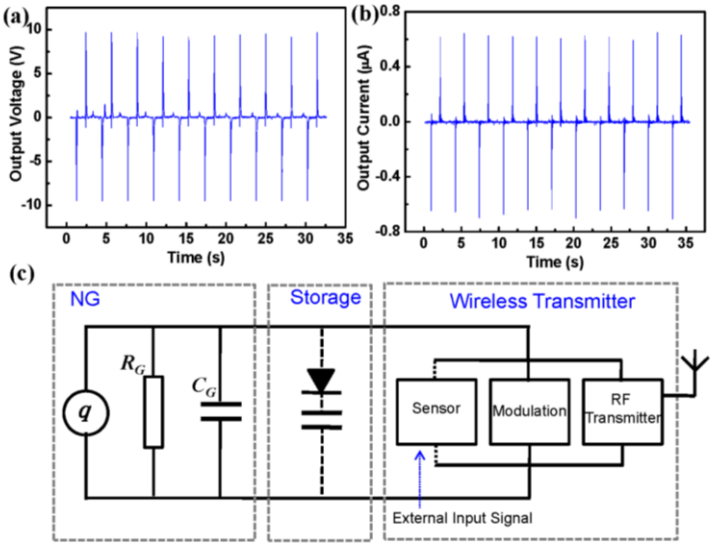

Figure 11.4. Performance of a nanogenerator and design of an integrated system. (a) Output voltage and (b) output current of a typical nanogenerator. The voltage reached 10 V and the current exceeded 0.6 μA. (c) Schematic diagram of the designed self-powered system. For the wireless transmitter part, a phototransistor was used as the sensor to detect the light from an LED. The signal detected by the sensor was transmitted wirelessly by a single transistor RF transmitter.

11.4. Self-powered photon sensor and system

To prove the possibility of wireless data transmission, we used a single transistor radio frequency (RF) transmitter to send out the detected electric signal [4]. The oscillation frequency was tuned to be around 90 MHz, and a commercial portable AM/FM radio (CX-39, Coby) was used to receive the transmitted signal. First, we only tested the transmitting part of the circuit. When the transmitter was triggered by the stored energy harvested by the NG, there was a disturbing noise received by the radio (View the video in the supporting information). Due to the low power consumption (< 1 mW) of the transmitter, the energy generated and stored during three straining cycles of the NG was enough to transmit the signal. The maximum transmission distance for our setup was over 5 meters as limited by the quality of the receiver.

Then a phototransistor in a slotted optical switch (OPB 825, OPTEK Technology.) was added to the system as the photon detecting sensor to demonstrate that the self-powered system can work independently and wirelessly. The optical switch consisted of an infrared light emitting diode (LED) and a NPN silicon phototransistor mounted in a low-cost black plastic housing on opposite sides of a 4 mm wide slot. The LED was triggered by a synthesized function generator (DS345, Stanford Research System) with a programmed voltage sequence to work as an external input light source, shining onto the phototransistor. The signal of the photocurrent generated by the phototransistor was periodically sent out using the energy stored in the capacitor. Due to the larger power consumption of the phototransistor (100 mW), it required the energy harvested for 1000 strain cycles of the NG (the performance of this NG was shown in Figure 11.4a) to simultaneously power the phototransistor and the transmitter (Note, the driving time was 20-25 ms). Each time when it was triggered, the signal received by the phototransistor modulated the transmitting signal, and the information was received by the radio, and the demodulated signal was recorded from the headphone jack. The voltage sequence used to trigger the LED is shown in Figure 11.4b. Each cycle included an on (16 ms)/off (5 ms)/on (5 ms)/off (10ms) status sequence. Figure 11.4c is the signal demodulated by the radio. The radio was tuned to work at a frequency avoiding the commercial radio signals around 90 MHz. When the phototransistor and the transmitter were triggered, there was a pulse detected beyond the noise background. If we enlarged this pulse, it contained a segment of the information that had the same waveform envelope as the triggering voltage sequence of the LED, as shown in Figure 11.4d in comparing with Figure 11.4c. This indicates that the wireless data transmission have been achieved by using this self-powered system.

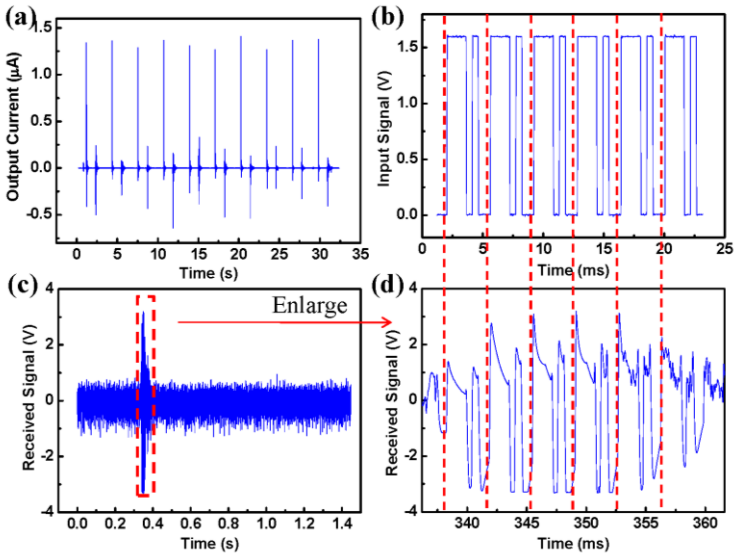

Figure 11.5. Wireless data transmission. (a) Performance of the nanogenerator used in our wireless data transmission test. (b) The voltage sequence used to trigger the LED, which represented waveform envelope of the input signal. (c) Recorded signal from the headphone jack of the radio, which is detected and transmitted by our integrated self-powered system. (d) Enlargement of the pulse in (c). It shows a segment with the same waveform envelope as the initial excitation input signal. The red dashed lines show the corresponding time sequence in (b) and (d).

For our NG structure, there are three factors that are important to the power output performance: the length of the nanowires, the thickness of the substrate and the magnitude of the NG distortion. From the practical point of view, there are two modes to trigger the NG depending on the form of the mechanical energy scavenged by the NGs in the environment. For cases where the NGs are triggered at a constant stress, such as air flow, the calculated results show that the piezopotential between the two electrodes increases as the length of the nanowires is increased or the thickness of the substrate is decreased. When the applied strain is fixed, such as when the NG is driven by the vibrations of a bridge where the trigger source is rigid, the piezopotential changes in the opposite sense compared to the former case. Thus, by adjusting the two competing factors, the thickness of the substrate and the length of the nanowire arrays, the device can be optimized to maximize its power harvesting efficiency to specific working situations according to the character of the scavenged energy in the environment. Increasing strain can also

significantly enhance the output voltage. In adition, ZnO is a biocompatible and environmentally friendly material. The nanowire films can be grown at very low temperature (< 100 ^{o}C) on any kind of substrate and any shape of substrate. These merits are critical for its industrial applications in flexible/stretchable electronics and many areas.

11. 5. Self-powered environmental sensor system

It is more desirable to have a sensor system that is not only wireless, mobile and extremely small, but also self-powered and sustainable. To achieve those requirements, we have fabricated a self-powered environmental sensor, which can detect Hg^{2+} ion and indicate its concentration via intensity of LED. A single-walled CNT (SWNT) based FET and ZnO NW array were served as a Hg^{2+} sensor and an energy harvesting part, respectively. SWNT network based sensor array were fabricated in 4-inch wafer by using chemical patterning method reported before [17, 21-22]. Figure 11.6a shows a photograph image of fabricated sensor array on 4-inch SiO_2 wafer. SWNT network based FETs can be in either *enhancement mode* or *depletion mode* since network was composed of metallic and semiconducting SWNTs. In our sensor fabrication, density of SWNT networks was intended to be relatively low (Figure 11.6b) because networks with low density tend to be in *enhancement mode* [23]. Firstly, drain-source current of a sensor was monitored in various concentration of Hg^{2+} ions in water-droplet to characterize sensing process. Figure 11.6c and inset show measured drain-source current and resistance of a sensor in different concentration of Hg^{2+} ions in water droplet. Initially, least current (< 10^{-8} A) was only observed as we chose a SWNT FET in *enhancement mode*. When the concentration of solution reached about ~10 nM which is the allowable limit of Hg^{2+} ions in drinking water set by most government environmental protection agencies, a noticeable change of resistance was appeared (see the inset in Figure 11.6c). Sequential injections of Hg^{2+} ion leaded discreet changes of resistance on a sensor. Working principle of our sensor is the difference of standard potential between SWNTs (E^{0}_{SWNT} = 0.5-0.8 V versus NHE) and Hg^{2+} ions (E^{0}_{Hg2+} = 0.8535 V versus NHE) [24-26].

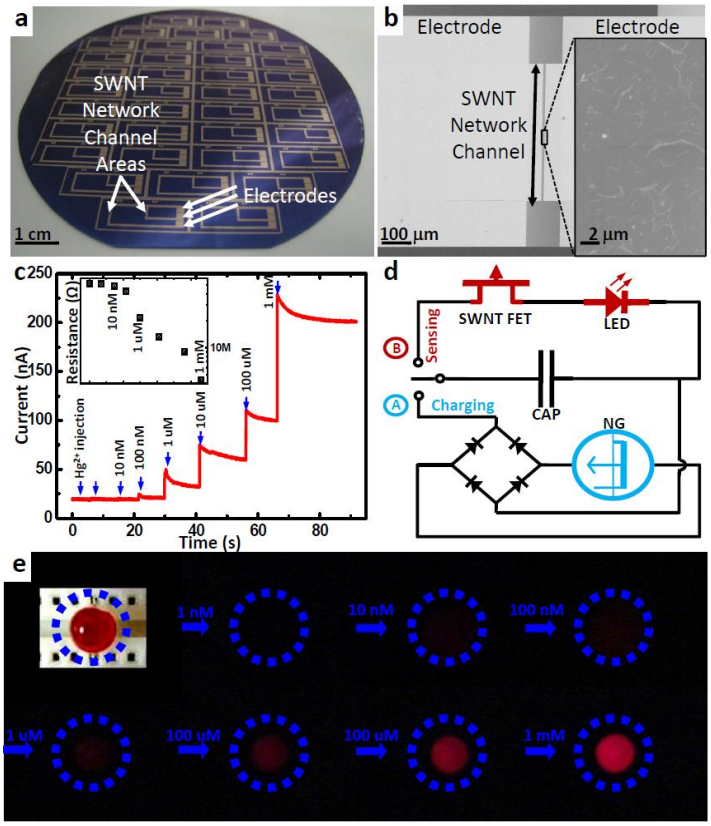

Figure 11.6. Characteristics of self-powered Hg^{2+} sensor driven by nanogenerators. (a) Optic image of fabricated sensor array on 4 inch silicon wafer. (b) SEM image of single-walled carbon nanotube network in a sensor. (c) Sensing behaviour of our fabricated sensor with various concentrations of Hg^{2+} ions in water solution. The inset shows the plot of resistance depending on mercury ion injection. (d) Circuit diagram depicting our self-powered sensor composed of nanogenerator, rectifying bridge, capacitor, Hg^{2+} detector and light emitting diode with (a) *charging* and (b) *sensing* process selecting switch.(e) Optic images of a laser emitting diode representing intensity changes owing to resistance changes in the detector depending on the concentration of Hg^{2+} ions in water solution. All measurements were conducted with energy stored by nanogenerators.

By integrating NGs with Hg^{2+} sensor, we could build a self-powered environmental sensing device. Figure 11.6d shows circuit diagram. Light emitting diode was attached on the circuit to serve as an indicator for Hg^{2+} detection. To accomplish self-powered sensing of environmental polluters with NGs, a circuit was designed with two independent loops. In energy harvesting process, a circuit was connected in the loop 'A' (Figure 11.6d) with NGs and rectifying diode bridge to store generated charges into the capacitor (1000 uF, Nichicon). After sufficient charging process, connection was changed to the loop 'B' in Figure 11.6d, thus it was ready to detect Hg^{2+} ions and light up an LED with a certain intensity depending on the concentration of polluters in water droplet. As a proof of concept, we demonstrated an environmental sensor circuit fully powered by NGs which also can give us the result of detection simultaneously without any supporting equipments. Figure 11.6e shows photograph images of an LED that was lit up under each concentration of Hg^{2+} ions in water droplet. In this experiment, six capacitors were charged individually for ~1 h using 10-layer integrated NGs (10Hz, 1.2 cm peak-to-peak vibration distance, Labworks Inc.). Charged capacitors were connected in series to supply sufficient voltage (~3 V) for operation of a SWNT FET-based sensor and LED all together. There was no external electric power source in our system. Hg^{2+} ions were injected on water droplet in sequential steps from 1 nM to 1 mM. All detection procedure was conducted in ~30 sec to observe intensity changes of LED under constant power from capacitors. To minimize any power dissipation during sequential detection procedures, observation started from low concentration to high concentration. In lower concentration of Hg^{2+} ions in water droplet, only least power (V^2/R) was expected to be used for the sensing operation due to relatively high resistance in a circuit (see also Figure 11.6c inset and d). As shown after the third image of Figure 11.6e, noticeable LED light was appeared from the concentration of 10 nM and getting brighter gradually till those of 1 mM. Note that this detection experiment was conducted only utilizing our sensing circuit powered by NGs without any auxiliary equipment such as voltage or current signal amplifiers. In addition, the LED can be replaced by an RF unit so that the signal can be detected wirelessly over a longer distance. In the future, our system can be a prototype for environmental sensors which are stand-alone, self-powering and self-indicating.

In summary, by storing the energy generated by the NG, we have demonstrated a self-powered system that can work independently and wirelessly. The system was composed of a NG, rectification circuit, and capacitor for energy storage, sensor, and RF data transmitter. Wireless signals sent out by the system were detected by a commercial radio at a distance of 5-10 meters. This study proves the feasibility of using ZnO nanowire NGs for building self-powered systems with capability of long distance data transmission, clearly proving its potential application in wireless biosensing, environmental infrastructure monitoring, sensor networks, personal electronics and even national security.

References for Chapter 11

[1] Z. L. Wang, J. Song, *Science* **312**, 242 (2006).

[2] Z. L. Wang, *Sci. Am.* **298**, 82 (2008).

[3] P. Glynne-Jones, N.M. White, *Sensor Review* **21**, 91 (2001).

E. Katz, A.F. Bückmann, I. Willner, *J. Am. Chem. Soc.* **123**, 10752 (2001).

M. Goldfarb, E.J. Barth, M.A. Gogola, J.A. Wehrmeyer, *Mechatronics, IEEE/ASME Transactions on* **8**, 254 (2003).

E.P. James, M.J. Tudor, S.P. Beeby, N.R. Harris, P. Glynne-Jones, J.N. Ross, N.M. White, *Sensors and Actuators A* **110**, 171 (2004).

S.P. Beeby, M.J. Tudor, N.M. White, *Measurement Science & Technology* **17**, R175 (2006).

D. Dondi, A. Bertacchini, D. Brunelli, L. Larcher, L. Benini, *Industrial Electronics, IEEE Transactions on* **55**, 2759 (2008).

T.H. Owen, S. Kestermann, R. Torah, S.P. Beeby, *Sensor Review* **29**, 38 (2009).

[4] Y.F. Hu, Y. Zhang, C. Xu, L. Lin, R.L. Snyder, Z.L. Wang, *Nano Letters.* **11** (6), 2572 (2011).
[5] M.B. Lee, J.H. Bae, J.H. Lee, C.S. Lee, S.H. Hong, Z.L. Wang, *Energy & Environmental Science*, DOI: 10.1039/c1ee01558c.

Appendix

Published journal articles by Wang's group on Nanogenerators and Piezotronics (2006-2011)

2011

[1] Joonho Bae, Young Jun Park, Minbaek Lee, Young Jin Choi, Churl Seung Lee, Jong Min Kim, Zhong Lin Wang* "Single-fibre-based hybridization of energy converters and storage units using graphene as electrodes", Adv. Mater.

[2] Minbaek Lee, Joonho Bae, Joohyung Lee, Churl-Seung Lee, Seunghun Hong and Zhong Lin Wang,"Self-powered environmental sensor system driven by nanogenerators " *Energy Environ. Sci.*

[3] Wenzhuo Wu and Zhong Lin Wang "Piezotronic Nanowire-Based Resistive Switches As Programmable Electromechanical Memories " Nano Lett., Online

[4] "Polar Charges Induced Electric Hysteresis of ZnO Nano/Microwire for Fast Data Storage "Jinhui Song, Yan Zhang, Chen Xu, Wenzuo Wu, and Zhong Lin Wang, Nano Lett.

[5] Youfan Hu, Yan Zhang, Chen Xu, Long Lin, Robert L. Snyder, and Zhong Lin Wang, "Self-Powered System with Wireless Data Transmission " Nano Lett

[6] Yan Zhang, Ying Liu, Z.L. Wang* "Fundamental Theory of Piezotronics", Adv.Mater.

[7] Longyan Yuan, Yuting Tao, Jian Chen, Junjie Dai, Ting Song, Mingyue Ruan, Zongwei Ma, Li Gong, Kang Liu, Xianghui Zhang, Xuejiao Hu, Jun Zhou* and Zhong Lin Wang* "Carbon Nanoparticles on Carbon Fabric as Flexible Higher Performance Field Emitters", Adv. Func. Materials.

[8] AifangYu, Hongyu Li, Haoying Tang, Tengjiao Liu, Peng Jiang，Zhong Lin Wang "Vertically Integrated Nanogenerator Based on ZnO Nanowire Arrays", P hys. Status Solidi RRL **5** (2011) 162–164.

[9] Chen Xu and Zhong Lin Wang* "Compacted hybrid cell made by nanowire convoluted structure for harvesting solar and mechanical energies", Adv. Mater. 23 (2011) 873-877.

[10] Joonho Bae, Min Kyu Song, Young Jun Park, Jong Min Kim*, Meilin Liu, Zhong Lin Wang*" Fiber supercapacitors made of nanowire-fiber hybrid structure for wearable/stretchable energy storage", Angew. Chem. 123 (2011) 1721-1725.

[11] M. Riaz, J.H. Song, O. Nur, Z. L.Wang and M. Willander* **"**Experimental and finite element method calculation of piezoelectric power generation from ZnO nanowire arrays grown on different substrates using high and low temperature methods ", Adv. Functional Materials. 21 (2011) 623-628.

[12] Zetang Li and Zhong Lin Wang* "Air/liquid pressure and heartbeat driven flexible fiber nanogenerators as micro-nano-power source or diagnostic sensors", Adv. Mater. 23, (2011) 84-89.

2010

[13] Caofeng Pan, Ying Fang, Ahamd Mashkoor, Zhixiang Luo, Jianbo Xie, Lihua Wu, Zhong Lin Wang, Jing Zhu* "Generating Electricity from Biofluid with a Nanowire-Based Biofuel Cell for Self-Powered Nanodevices", Adv. Materials. 22 (2010) 5388-5392.

[14] Kwi-Il Park, Sheng Xu, Ying Liu, Geon Tae Hwang, Suk-Joong L. Kang, Zhong Lin Wang and Keon Jae Lee* "Piezoelectric $BaTiO_3$ Thin Film Nanogenerator on Plastic Substrates", Nano Letts., 10 (2010) 4939-4943.

[15] Youfan Hu, Yan Zhang, Chen Xu, Guang Zhu and Zhong Lin Wang* "High output nanogenerator by rational unipolar-assembly of conical-nanowires and its application for driving a small liquid crystal display", Nano Letters, 10 (2010) 5025-5031.

[16] Sheng Xu, Benjamin J. Hansen and Zhong Lin Wang* "Piezoelectric-Nanowire Enabled Power Source for Driving Wireless Microelectronics", Nature Communications, vol. 1 Article Number: 93 (2010).

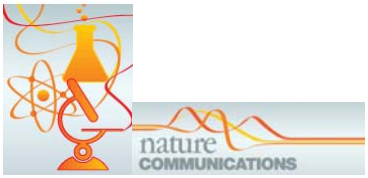

[17] Zhong Lin Wang* "Piezopotential Gated Nanowire Devices: Piezotronics and Piezo-phototronics", Nano Today, 5 (2010) 540-552.

[18] Zhong Lin Wang "Toward Self-Powered Sensor Network", Nano Today, 5 (2010) 512-514.

[19] Min-Teng Chen, Ming-Pei Lu, Yi-Jen Wu, Chung-Yang Lee, Ming-Yen Lu, Yu-Cheng Chang, Li-Jen Chou, Zhong Lin Wang and Lih-Juann Chen* "Electroluminescence from In-situ Doped p-n Homojuncitoned ZnO Nanowire Array", Nano Letters, 10 (2010) 4387-4393.

[20] Zhong Lin Wang*, Rusen Yang, Jun Zhou, Yong Qin, Chen Xu, Youfan Hu and Sheng Xu "Lateral nanowire/nanobelt based nanogenerators, piezotronics and piezo-phototronics", Mater. Sci. and Engi. Reports. R70 (No. 3-6) (2010) 320-329.

[21] Wenzhuo Wu#, Yaguang Wei# and Zhong Lin Wang* "Strain-gated piezotronic logic nanodevices ", Adv. Materials, 22 (2010) 4711-4715.

[22] Qing Yang, Xin Guo, Wenhui Wang, Yan Zhang, Sheng Xu, Der Hsien Lien, Zhong Lin Wang* "Enhancing sensitivity of a single ZnO micro/nanowire photodetector by piezo-phototronic effect", ACS Nano, 4 (2010) 6285 – 6291.

[23] 王中林 "微纳系统中的可持续自供型电源 - 能源研究中的新兴领域",《科学通报》, 55 (2010) 2472-2475.

[24] Chi-Te Huang, Jinhui Song, Chung-Min Tsai, Wei-Fan Lee, Der-Hsien Lien, Zhiyuan Gao, Yue Hao, Lih-Juann Chen,* and Zhong Lin Wang* "Single-InN-nanowire nanogenerator with up to 1 V output voltage", Adv. Mater., 36 (2010) 4008-4013.

[25] 王中林 "压电电子学和压电光电子学", 《物理》, 39 (2010) 556-557.

[26] Jinhui Song†, Huizhi Xie†, Wenzhuo Wu, V. Roshan Joseph, C. F. Jeff Wu* and Zhong Lin Wang* "Robust Optimizing of the Output Voltage of Nanogenerators by Statistical Experimental Design", Nano Research, Nano Res. 3 (2010) 613–619.

[27] Minbaek Lee Rusen Yang Cheng Li Zhong Lin Wang* "Nanowire-quantum dot hybridized cell for harvesting sound and solar energies", J. Phys. Chem. Letts., 1 (2010) 2929–2935.

[28] Yaguang Wei#, Wenzhuo Wu#, Rui Guo, Dajun Yuan, Suman Das* and Zhong Lin Wang* "Wafer-scale high-throughput ordered growth of vertically aligned ZnO nanowire arrays", Nano Letters, 10 (2010) 3414-3419.

[29] Jingbin Han, Fengru Fan, Chen Xu, Shisheng Lin, Min Wei, Xue Duan, Zhong Lin Wang* "ZnO nanotube-based dye-sensitized solar cell and its application in self-powered devices", Nanotechnology, 21 (2010) 405203.

[30] Weihua Liu, Minbaek Lee, Lei Ding, Jie Liu, Zhong Lin Wang* "Piezopotential Gated Nanowire-Nanotube-Hybrid Field-Effect-Transistor", Nano Letters, 10 (2010) 3084–3089.

[31] Guang Zhu, Rusen Yang, Sihong Wang, Zhong Lin Wang* "Flexible high-output nanogenerator based on lateral ZnO nanowire array", Nano Letters, 10 (2010) 3151–3155.

[32] Yan Zhang, Youfan Hu, Shu Xiang, and Zhong Lin Wang [a)] "Effects of Piezopotential Spatial Distribution on Local Contact Dictated Transport Property of ZnO Micro/Nanowires", Appl. Phys. Letts., 97 (2010) 033509.

[33] Benjamin J. Hansen+, Ying Liu+, Rusen Yang and Zhong Lin Wang* "Hybrid Nanogenerator for Concurrently Harvesting Biomechanical and Biochemical Energy", ACS Nano, 4 (2010) 3647-3652.

[34] Youfan Hu, Yan Zhang, Yanling Chang, Robert L. Snyder and Zhong Lin Wang* "Optimizing the Power Output of a ZnO Photocell by Piezopotential", ACS Nano. 4 (2010) 4220-4224.; Corrections: 4 (2010) 4962 - 4962.

[35] Zhou Li#, Guang Zhu#, Rusen Yang, Aurelia C. Wang, Zhong Lin Wang* "Muscle Driven In-Vivo Nanogenerator", Adv. Mater., 22 (2010) 2534-2537.

[36] Xue Bin Wang, Jin Hui Song, Fan Zhang, Cheng Yu He, Zheng Hu, and Zhong Lin Wang, "Electricity Generation Based on One-dimensional Group-III Nitride Nanomaterials", Adv. Mater., 22 (2010) 2155 – 2158.

[37] Sheng Xu[#], Yong Qin[#], Chen Xu[#], Yaguang Wei, Rusen Yang, Zhong Lin Wang* "Self-powered Nanowire Devices", Nature Nanotechnology, 5 (2010) 366-373.

[38] Z.L. Wang "Piezotronic and Piezo-phototronic Effects", The Journal of Physical Chemistry Letters, 1 (2010) 1388–1393.

[39] Chi-Te Huang, Jinhui Song, Wei-Fan Lee, Yong Ding, Zhiyuan Gao, Yue Hao, Lih-Juann Chen,* and Zhong Lin Wang* "GaN Nanowire Arrays for High-Output Nanogenerators", . *J. Am. Chem. Soc.*, **2010**, *132*, 4766–4771.

[40] Youfan Hu, Yanling Chang, Peng Fei, Robert L. Snyder and Zhong Lin Wang* "Designing the electric transport characteristics of ZnO micro/nanowire devices by coupling piezoelectric and photoexcitation effects", ACS Nano, *4* (2010) 1234–1240.

2009

[41] Zhong Lin Wang "Ten years' venturing in ZnO nanostructures: from discovery to scientific understanding and to technology applications", Chinese Science Bulletin, 54 (2009) 4021-4034.

[42] Peng Fei, Ping-Hung Yeh, Jun Zhou, Sheng Xu, Yifan Gao, Jinhui Song, Yudong Gu, Yanyi Huang [×], Zhong Lin Wang[×] "Piezoelectric-potential gated field-effect transistor based on a free-standing ZnO wire", Nano Letters, 9 (2009) 3435 - 3439.

[43] Zhiyuan Gao, Yong Ding, Shisheng Lin, Yue Hao, Zhong Lin Wang* "Dynamic Fatigue Studies of ZnO Nanowires by In-situ Transmission Electron Microscopy", physica status solidi RRL, 3 (2009) 260-262.

[44] S. S. Lin, J. H. Song, Y. F. Lu, Z. L. Wang* "Identifying individual *n*- and *p*-type ZnO nanowires by the output voltage sign of piezoelectric nanogenerator", Nanotechnology, 20 (2009) 365703.

[45] Giulia Mantini, Yifan Gao, A. D'Amico, C. Falconi, Zhong Lin Wang[×] "Equilibrium piezoelectric potential distribution in a deformed ZnO nanowire", Nano Research, 2 (2009) 624-629.

[46] Youfan Hu, Yifan Gao, Srikanth Singamaneni, Vladimir V. Tsukruk and Zhong Lin Wang* "Converse piezoelectric effect induced transverse deflection of a free-standing ZnO microbelt", Nano Letts, 9 （2009） 2661-2665.

[47] Zhiyuan Gao, Jun Zhou, Yudong Gu, Peng Fei, Yue Hao, Gang Bao, Zhong Lin Wang* "Effects of Piezoelectric Potential on the Transport Characteristics of Metal-ZnO Nanowire-Metal Field Effect Transistor", J. Appl. Physics, 105, 113707 (2009).

[48] Christian Falconi, Giulia Mantini, Arnaldo D'Amico, Zhong Lin Wang* "Studying piezoelectric nanowires and nanowalls for energy harvesting", Sensors and Actuator, B 139 (2009) 511–519.

[49] Chen Xu, Xudong Wang and Zhong Lin Wang* "Nanowire structured hybrid cell for concurrently scavenging solar and mechanical energies", JACS, *131* (2009) 5866–5872.

[50] Z.L. Wang 'Energy Harvesting Using Piezoelectric Nanowires - Comment on "Energy Harvesting Using Nanowires?" by Alexe et al.', Adv. Materials, 21 (2009) 1311-1315.

[51] Z.L. Wang, "ZnO Nanowire and Nanobelt Platform for Nanotechnology" (Review), Materials Science and Engineering Report, 64 (issue 3-4) (2009) 33-71.

[52] Ming-Pei Lu, Jinhui Song, Ming-Yen Lu, Min-Teng Chen, Yifan Gao, Lih-Juann Chen, and Zhong Lin Wang* "Piezoelectric nanogenerator using p-type ZnO nanowire arrays**",** Nano Letters, 9 (2009) 1223 - 1227.

[53] Rusen Yang, Yong Qin, Cheng Li, Guang Zhu, Zhong Lin Wang* "Converting Biomechanical Energy into Electricity by Muscle/Muscle Driven Nanogenerator", Nano Letters, 9 (2009) 1201 - 1205.

[54] Yifan Gao and Zhong Lin Wang* "Equilibrium Potential of Free Charge Carriers in a Bent Piezoelectric Semiconductive Nanowire", Nano Letters, 9 (2009) 1103 - 1110.

[55] Xudong Wang, Yifan Gao, Yaguang Wei and Zhong Lin Wang* "The Output of Ultrasonic-Wave Driven Nanogenerator in a Confined Tube", Nano Research, 2 (2009) 177-182.

[56] Rusen Yang, Yong Qin, Cheng Li, Liming Dai and Zhong Lin Wang* "Characteristics of Output Voltage and Current of Integrated Nanogenerators", Appl. Phys. Letts., 94 (2009) 022905.

[57] Rusen Yang, Yong Qin, Liming Dai and Zhong Lin Wang * "Flexible charge-pump for power generation using laterally packaged piezoelectric-wires", Nature Nanotechnology, 4 (2009) 34-39.

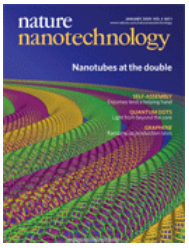

2008

[58] Sheng Xu, Yaguang Wei, Jin Liu, Rusen Yang and Zhong Lin Wang* "Integrated multilayer-nanogenerator fabricated using paired nanotip-to-nanowire brushes", Nano Letters, 8 (2008) 4027-4032.

[59] Jun Zhou, Peng Fei, Yudong Gu, Wenjie Mai, Yifan Gao, Rusen Yang, Gang Bao, Zhong Lin Wang* "Piezoelectric-potential-controlled polarity-reversible Schottky diodes and switches of ZnO wires", Nano Letters, 8 (2008) 3973-3977.

[60] Z.L. Wang "Towards self-powered nanosystems: from nanogenerators to nanopiezotronics" (feature article), Advanced Functional Materials, 18 (2008) 3553-3567.

[61] Jun Zhou, Yudong Gu, Peng Fei, Wenjie Mai, Yifan Gao, Rusen Yang, Gang Bao, Zhong Lin Wang* "Flexible piezotronic strain sensor", Nano Letters, 8 (2008) 3035-3040.

[62] Jun Zhou, Peng Fei, Yifan Gao, Yudong Gu, Jin Liu, Gang Bao, Zhong Lin Wang* "Mechanical-electrical triggers and sensors using piezolelectric microwires/nanowires", Nano Letters, 8 (2008) 2725-2730.

[63] Yi-Feng Lin, Jinhui Song, Ding Yong, Shih-Yuan Lu* and Zhong Lin Wang* "Alternating the Output of CdS-Nanowire Nanogenerator by White-Light Stimulated Optoelectronic Effect". Adv. Materials, 20 (2008) 3127-3130.

[64] Z.L. Wang "Energy harvesting for self-powered nanosystems" (review), Nano Research, 1 (2008) 1-8.

[65] Jin Liu, Peng Fei, Jun Zhou, Rao Tummala and Zhong Lin Wang* "Toward High Output-Power Nanogenerator", Appl. Phys. Letts., 92 (2008) 173105.

[66] Z.L. Wang, "Oxide Nanobelts and Nanowires - Growth, Properties and Applications" (Review), J. Nanoscience and Nanotechnology, 8 (2008) 27-55.

[67] Yong Qin, Xudong Wang and Zhong Lin Wang* "Microfiber-Nanowire Hybrid Structure for Energy Scavenging", Nature, 451 (2008) 809-813.

[68] Yi-Feng Lin, Jinhui Song, Yong Ding, Zhong Lin Wang* and Shih-Yuan Lu "Piezoelectric Nanogenerator using CdS Nanowires", Appl. Phys. Letts., **92** (2008) 022105.

[69] Zhong Lin Wang*, Xudong Wang, Jinhui Song, Jin Liu and Yifan Gao "Piezoelectric Nanogenerators for Self-Powered Nanodevices", IEEE Pervasive Computing, 7 (No. 1) (2008) 49-55.

[70] Z.L. Wang "Self-powering nanotech", Scientific American, 298 (No. 1) (2008) 82-87.

[71] Jin Liu, Peng Fei, Jinhui Song, Xudong Wang, Changshi Lao, Rao Tummala, Zhong Lin Wang* "Carrier density and Schottky barrier on the performance of DC nanogenerator", Nano Letters, 8 (2008) 328-332.

[72] Jinhui Song, Xudong Wang, Jin Liu, Huibiao Liu, Yuliang Li, Zhong Lin Wang* "Piezoelectric potential output from a ZnO wire functionalized with p-type oglimer", Nano Letters, 8 (2008) 203-207.

2007

[73] Xudong Wang, Jin Liu, Jinhui Song, Zhong Lin Wang* "Integrated Nanogenerators in Bio-Fluid", Nano Letters, 7 (2007) 2475-2479.

[74] Yifan Gao and Z.L. Wang* "Electrostatic Potential in a Bent Piezoelectric Nanowire – The Fundamental Theory of Nanogenerator and Nanopiezotronics", Nano Letters, 7 (2007) 2499-2505.

[75] Xudong Wang, Jinhui Song, Jin Liu and Zhong Lin Wang* "Direct Current Nanogenerator Driven by Ultrasonic Wave", Science, 316 (2007) 102-105.

[76] Z.L. Wang "The new field of Nanopiezotronics", Materials Today, 10 (No. 5) (2007) 20-28.

[77] Z.L. Wang "Nanopiezotronics", Adv. Mater., 19 (2007) 889-992.

[78] Jr H. He, Cheng L. Hsin, Lih J. Chen*, Zhong L. Wang* "Piezoelectric Gated Diode of a Single ZnO Nanowire", Adv. Mater., 19 (2007) 781-784.

[79] Charles M. Lieber and Zhong Lin Wang "Functional Nanowires", MRS Bulletin, 32 (2007) 99-104.

[80] Zhong Lin Wang "Piezoelectric nanostructures: from novel growth phenomena to electric nanogenerators", MRS Bulletin, 32 (2007) 109-116.

[81] Pu Xian Gao, Jinhui Song, Jin Liu and Zhong Lin Wang* "Nanowire Nanogenerators on Plastic Substrates as Flexible Power Source", Adv. Materials, *19* (2007) 67-72.

2006

[82] Xudong Wang, Jun Zhou, Jinhui Song Jin Liu, Ningsheng Xu and Zhong L. Wang* "Piezoelectric-Field Effect Transistor and Nano-Force-Sensor Based on a Single ZnO Nanowire", Nano Letters, 6 (2006) 2768-2772.

[83] Jinhui Song, Jun Zhou, Zhong Lin Wang * "Piezoelectric and semiconducting dual-property coupled power generating process of a single ZnO belt/wire – a technology for harvesting electricity from the environment", Nano Letters, 6 (2006) 1656-1662.

[84] Zhong Lin Wang* and Jinhui Song "Piezoelectric Nanogenerators Based on Zinc Oxide Nanowire Arrays", Science, 312 (2006) 242-246.

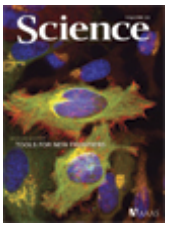

Nanogenerators

for Self-powered Devices and Systems

Zhong Lin Wang

School of Materials Science and Engineering
Georgia Institute of Technology, Atlanta GA USA

(first edition, June 2011)

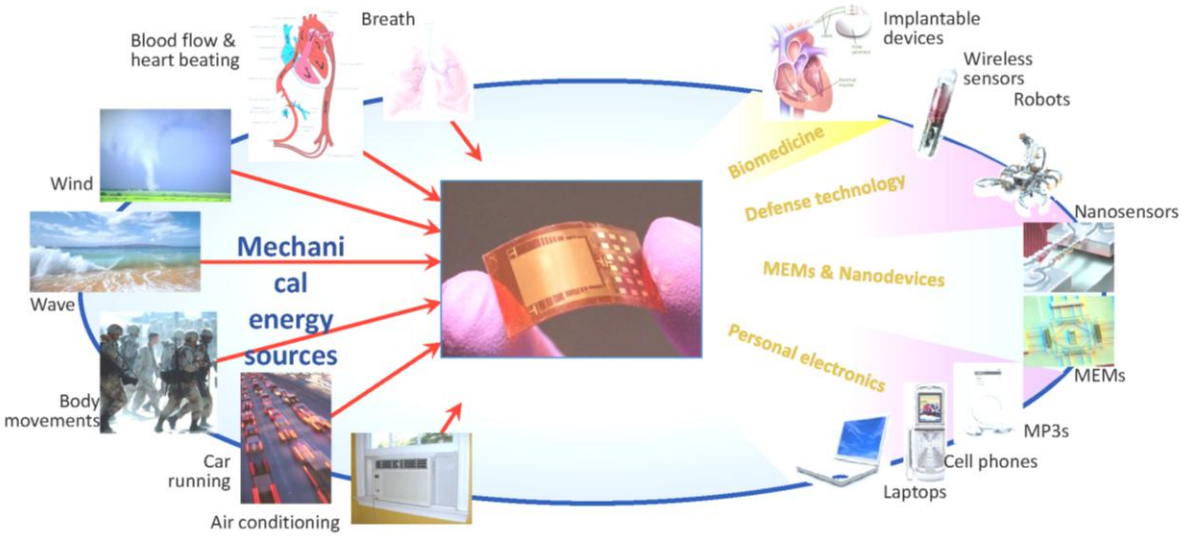

Published by

Georgia Institute of Technology, Atlanta, USA

SMARTech digital repository, 2011.

Site for down load: http://hdl.handle.net/1853/39262

ISBN 978-1-4507-8016-2